



Instituut voor Materiaal Onderzoek



Faculteit Wetenschappen

The Use of Digital Filtering Techniques in the Analysis of Spectral Data and Multicomponent Decay Curves

Proefschrift voorgelegd tot het bekomen van de graad van
Doctor in de Wetenschappen
aan het Limburgs Universitair Centrum
te verdedigen door

Sonja Schreurs

Promotor: Prof. Dr. J.-P. François
Co-promotor: Prof. Dr. P. Van Espen
(Universitaire Instelling Antwerpen)

Diepenbeek 1999

Fysica
621.38



BIBLIOTHEEK UNIVERSITEIT HASSELT



03 04 0095016 5

621.38
SCHR
1999

uhasselt

Tijdens mijn doctoraat heb ik mogen ervaren dat doctoreren eerst en vooral een opleiding is. Het verwerven van de nodige informaticakennis tijdens mijn doctoraatsopleiding heeft me dan ook een grote stap op weg geholpen. Toch is het zich eigen maken van een bepaalde manier van zelfstandig werken en kritisch denken zeker zo belangrijk. Bij aanvang lijkt een doctoraat misschien op een één-persoonsproject, toch blijkt al snel dat heel wat mensen elk op hun manier een steentje bijgedragen hebben tot het slagen van dit werk en tot mijn vorming. Daarom wil ik hier graag een woordje van dank richten tot

Prof. dr. J.-P. François, promotor van dit proefschrift, voor zijn wetenschappelijke begeleiding, zijn kritische evaluatie van dit proefschrift en voor de geboden mogelijkheden tijdens mijn onderzoek,

Prof. dr. P. Van Espen (Universitaire Instelling Antwerpen), voor het aanvaarden van het co-promotorschap van dit werk en voor zijn interesse in mijn onderzoek,

Dr. F. Janssens, voor zijn introductie in de ASDAP versie, waarmee mijn werk gestart werd,

Prof. dr. W. Krätschmer (Max Planck Institut für Kernphysik), en zijn medewerkers Dr. K. Nachtigal en Dr. G. Monninger, voor het ter beschikking stellen van hun 'ingewikkelde' IR spectra van koolstofclusters, maar ook voor hun opvolging en hulp in de ontrafeling ervan.

Dr. R. Carleer, voor het ter beschikking stellen van de ICP apparatuur en de nuttige tips tijdens dit onderzoek. In dit kader wil ik ook graag Elsy bedanken voor de aangename samenwerking en voor haar aanstekelijke, gedreven perfectie bij de voorbereidingen en de metingen van de ICP-OE spectra,

Prof. dr. M.R. Osborne en Prof. dr. G.K. Smyth, voor het bezorgen van het MatLab programma van de verbeterde Prony methode,

Eric Pauwels (KULeuven), voor zijn hulp en suggesties bij mijn eerste stappen in MatLab,

Prof. dr. M. Van der Auweraer (KULeuven), voor het ter beschikking stellen van de fluorescentie vervalcurven en van zijn resultaten in het vergelijkend onderzoek en voor de begeleiding in dit onderzoek,

Prof. dr. J. Gelan en zijn medewerkers, voor het mogelijk maken van een uitgebreide studie van FID curven, voor hun hulp bij mijn introductie tot de NMR spectroscopie en voor de vele discussies die leidden tot de succesvolle resultaten,

Dr. K. Strijckmans (INW Gent), voor de introductie in de radiochemie, voor de intensieve samenwerking zowel voor als na de opname van de radioactieve vervalcurven en voor de inspraak die mij geboden was in de voorbereiding van de experimenten.

Prof. dr. M. Aerts, en al de leden van WNI, voor hun wijze raad bij mijn statistische en wiskundige problemen en voor hun voortdurende interesse in mijn onderzoek,

Marc, Andres en Geert-Jan, voor het klaarstaan met woord en daad in de kleine en grote computerproblemen,

Magda en Adriana, voor enkele mooie illustraties die dit werk verfraaien,

Dr. E. Mathieu (UIA), voor het aanreiken van de mogelijkheden en de informatie om mijn doctoraatsopleiding te realiseren aan de UIA,

alle (ex-) collega's van groep scheikunde (doctoraatstudenten, assistenten, didactische, technische en administratieve ploeg), voor de vriendschappelijke werksfeer, de ontspannen koffiepauzes (met of zonder taart), en voor hun hartelijke steun,

mijn familie, vrienden en in het bijzonder Christophe, voor de hulp, het begrip, de steun en de vele aanmoedigingen. Zonder hun inzet was dit werk niet mogelijk geweest.

HARTELIJK BEDANKT,

Sonja

Table of contents

Introduction	1
Part I : Analysis of spectral data	4
Chapter 1 : Automated Spectral Data Analysis Program	9
1.1. Voigt profile	9
1.2. Convolution spectra	12
1.3. Automated Spectral Data Analysis Program (ASDAP)	15
1.3.1. Input	18
1.3.2. Smoothing	18
1.3.3. Background correction	18
1.3.4. Peak detection	20
1.3.5. Fitting procedure	25
1.3.6. Output	27
1.4. Appendix A : Partial derivatives of the Voigt function	28
1.4.1. Fourier integral representation of $K(x,a)$	28
1.4.2. Fourier integral representation of $L(x,a)$	29
1.4.3. Partial derivatives of the Voigt function	30
1.5. Appendix B : Partial derivatives of the reduced sum function	34
Chapter 2 : Evaluation on simulated data	37
2.1. Simulation of spectra	37
2.2. Spectral detection limit	38
2.3. Qualitative and quantitative analysis of multiplets	45
2.4. Influence of noise	47
2.5. Conclusions	49
Chapter 3 : Qualitative and quantitative applications	51
3.1. IR spectrometry of small carbon clusters trapped in noble gas matrices	51
3.1.1. Experimental set-up	59
3.1.2. Data handling	60
3.1.3. Analysis in Ar matrix	62
3.1.4. Analysis in Kr matrix	71
3.1.5. Conclusions	73
3.1.6. Appendix A : Figs 3.15 - 3.23	77
3.1.7. Appendix B : Table 3.2	86

3.2. ICP-OES	93
3.2.1. Experimental set-up	93
3.2.2. Data handling	100
3.2.3. Study of standard reference materials	105
3.2.4. Analysis of boron in steel	114
References : Part I	119
Part II : Analysis of multicomponent decay curves	125
Chapter 4 : The use of digital filtering in the analysis of multicomponent decay curves	129
4.1. An example	129
4.2. Theoretical considerations	131
Chapter 5 : The combined use of the improved methods of Gardner and Prony	137
5.1. The improved method of Gardner	137
5.1.1. Theory	137
5.1.2. Implementation	140
5.2. Improved method of Prony	143
5.2.1. Theory	143
5.2.2. Implementation	149
5.3. The combined use of the improved methods of GGM and Prony	154
5.3.1. The cubic spline function	155
5.3.2. Implementation	158
Chapter 6 : Evaluation on simulated decay curves	161
6.1. Simulation of decay curves	161
6.2. Evaluation of the improved method of Gardner	162
6.2.1. Noise-free data	162
6.2.2. Data in the presence of noise	174
6.3. Evaluation of the improved method of Prony	176
6.3.1. Noise-free data	176
6.3.2. Data in the presence of noise	179
6.4. Conclusions	179

Chapter 7 : Qualitative and quantitative applications	181
7.1. Fluorescence decay curves	181
7.1.1. Experimental set-up	183
7.1.2. Study of compound I	185
7.1.3. Study of compound II	187
7.1.4. Conclusions	191
7.2. Free induction decay analysis	192
7.2.1. Experimental set-up	193
7.2.2. Data handling	194
7.2.3. Study of isotactic polypropylene films	196
7.2.4. Study of atactic PVA grains	204
7.2.5. Conclusions	211
7.3. Radioactive decay curves	212
7.3.1. Study of positron emitters	212
7.3.2. Conclusions	224
 References : Part II	 225
 Summary and final conclusions	 229
Samenvatting en algemeen besluit	233
 Doctoraatsopleiding LUC - UIA	 237

Introduction

The second half of the twentieth century is characterized by the progress of science and technology, resulting in the development of new analytical procedures, and in the sophistication and/or speeding up (automatization) of existing ones. As a consequence, scientists and researchers could perform many accurate measurements in a short time period, and could thereby collect a huge amount of information about the studied processes. The introduction of the computer, and the spectacular evolution of computer sciences (hardware and software), lead to a breakthrough of the efficient processing of large data sets. The applied techniques should be very fast and must result in accurate, and objective solutions. Therefore, mathematics, statistics, and computer sciences have acquired an important position in other sciences. For example, in analytical chemistry, this originated in a complete new discipline called 'chemometrics'.

Chemometrics can generally be described as the application of mathematics and statistical methods in order to (1) improve chemical measurement processes, and to (2) extract more useful chemical information from the measured chemical and physical data. In their review, Workman et al. [WorJ96] emphasized the necessity of chemometrics into the realm of the chemist by the following words :

"Prior to the introduction of a formal subdiscipline of chemistry, termed chemometrics, chemists applied as much mathematics as they had available for research and problem solving, but in general, the use of statistical experimental design and data analysis were relegated to the engineer or the specialist statistician; chemists did chemistry, and life was simple. The current trend in scientific thinking across disciplines involves a multivariate approach. The world was not so simple as was once postulated, in fact it is common for scientists to approach problems realizing that there are deeply hidden relationships between variables that can be wrestled from an experiment only by the use of newer data analysis techniques; thus chemometrics becomes a necessity, not a luxury it once might have been."

Introduction

Manufactures of modern instruments took advantage of the advances in computer software and the distant attitude of operators against it. Today, instruments are designed with more features and yet they are significantly easier to use. Formerly, a skilled operator was needed to run the instruments; however, this is not the case today. Most companies have spent large amounts of time and money for developing their software for both automatization of the technique and data analysis. The implemented algorithms are usually kept secret and the operator can only use them as a black-box. Moreover, the procedures are often optimized for routine analyses, and adjustments to specific complex problems are impossible.

Nevertheless, a fraction of chemists all over the world, develops and applies their own software. Unfortunately, a satisfying solution is not found straight-away for each problem. Since chemometricians are familiar with their implemented algorithms, they can adjust and improve them to the needs of their specific research topic. As a result, the progress in one field is often limited to a select group of scientists within it and the general applicability of a successful optimization is often lost. According to recent extensive reviews [WorJ96, MobP96, BroS96], the variety of methods reached enormous dimensions.

The topic of the present work is the analysis of two data types based on digital filtering techniques. Because of the diversity of the studied data, this thesis is divided into two main parts : Part I deals with the analysis of spectral data and Part II with the unraveling of multicomponent decay curves.

The first PhD thesis realized in the Research Group Analytical Chemistry at the Limburgs Universitair Centrum on the analysis of spectral data was that of Dr. F. Janssens [JanF93]. His enthusiasm and persistence resulted in the development of a FORTRAN 77 program ASDAP (Automated Spectral Data Analysis Program). The characteristics of the implemented algorithms, based on digital filtering techniques, were evaluated on both simulated and experimental data sets [JanF93]. The aim of my work consists in a further optimization of some of these algorithms and in the general evaluation and application of ASDAP in experimental studies.

During my PhD, my attention was drawn to a completely different universal problem, the qualitative and quantitative analysis of multicomponent decay curves. Despite the many methods that are already reported in literature, none of them satisfied our norms. A first attempt to analyze multicomponent decay curves by digital filtering techniques, as they have been used in ASDAP (Part I), showed some promising results; nevertheless, it had to

be ceased. This research, presented in the first chapter of Part II, forms a transition between the topics of Part I and II.

The extensive study of two existing techniques (the methods of Gardner et al. [GarD59] and Prony [ProR95]), and their further improvements, induced the idea that the combination of both methods could result in a powerful technique for the qualitative and quantitative analysis of multicomponent decay curves. As digital filters fulfill only a small task in the improved method of Gardner, their influence upon the final result must not be underestimated. Since nowadays, MatLab is the software language of choice of many chemometricians, the combination of the improved methods of Gardner and Prony has been programmed completely in MatLab 4.2c1. Before the applicability of the developed software is illustrated in diverse experimental studies, the implemented algorithms are tested extensively on simulated data.

In each part of the present thesis, both the theory and implementation of the applied software are explained in detail; the results of the procedures are extensively tested on simulated data and are interpreted in order to formulate guide lines for a successful analysis. Finally, the applicability of the proposed methods is illustrated in several different experimental studies.

References

- [BroS96] Brown SD, Sum ST, and Despaigne F (1996) Anal Chem 68 : 21R
- [GarD59] Gardner DG, Gardner JC, and Meinke WW(1959) J Chem Phys 31 : 978
- [JanF93] Janssens F (1993) PhD 'Development of a computer program based on digital filtering techniques for qualitative and quantitative analysis of spectral data', Limburgs Universitair Centrum, B-3590 Diepenbeek
- [MobP96] Mobley PR, Kowalski BR, Workman JJ, Jr, and Bro R (1996) Appl Spectr 31 : 347
- [ProR95] Prony R (1795) Journal de l'Ecole Polytechnique 1 : 24
- [WorJ96] Workman JJ,Jr, Mobley PR, Kowalski BR, and Bro R (1996) Appl Spectr 31 : 73

Part I

Analysis of spectral data

Chapter 1 : Automated Spectral Data Analysis Program (ASDAP)

Chapter 2 : Evaluation of ASDAP

Chapter 3 : Qualitative and quantitative applications

Analysis of spectral data

Over the years, a lot of effort has been done for improving the spectroscopic measurements by optimizing some components of the applied equipment. However, some features, such as background, statistical fluctuations and interference, cannot be eliminated in a simple way. Therefore, data processing became a necessity for the qualitative and quantitative analysis of the samples. Nowadays, a huge number of approaches to the spectral data treatment are available, due to the fast growing computer facilities and the intensive use of mathematical and statistical methods in analytical chemistry, i.e. the field of chemometrics [BroS96].

In this Part I, an Automated Spectral Data Analysis Program (ASDAP) written in FORTRAN 77 is proposed. The incorporated algorithms are based on digital filtering techniques, and more specific, on the use of zero-area Gaussian filters [JanF91, JanF92, JanF93a,b]. The structure of ASDAP can be divided in two parts. The first one gives qualitative information concerning the number of lines, their positions and possible mutual interference, and is therefore called the peak and interference detection procedures. The implemented algorithms are based on the work of Janssens and François [JanF93a,b], who proposed a new set of zero area digital filters for the analysis of complex spectral data. They found that this technique has a number of advantages : (1) the constant, linear, quadratic and cubic terms in a polynomial background contribution to the signal are eliminated, (2) the resolution enhancement and the signal/noise ratio can be improved by using two identical filters and by selecting the following working interval of the filter width $M_1 : 0.25 \text{ FWHM}_s \leq M_1 \leq \text{FWHM}_s$ (FWHM_s is the full width at half maximum of the signal), (3) the broadening of the convolution signal with the combined filters for Voigt profiles is less pronounced with increasing damping constants a , (4) the use of combined filters or application of two consecutive zero-area filters is a clear improvement over a single filtering operation and even over Zimmermann's method [ZimW61] for the unraveling of multiplets composed of strongly overlapping lines. Furthermore, they illustrated the application of the digital filtering technique in ICP-OES, solid-state NMR, IR, and UV-vis absorption spectrometry.

The second part consists in the quantification of the individual spectral lines. Usually, this implies the construction of calibration lines, relating the spectral intensities and concentrations [TayP86b, WatR87]. Thus, the major problem in the quantification will be

the exact determination of the spectral intensities. A first step in this process consists in the elimination of the background contribution. Janssens and François [JanF92] introduced a new method for the optimized background correction based on the use of a digital filter and compared its performance with the procedures of Taylor and Schutyser [TayP86] and of Van der Plas et al. [VanP87]. Janssens and François concluded that their procedure performs better especially for weak signals with important statistical fluctuations and for Voigt profiles with parameters a up to 1.0, and it has the major advantage that it operates completely automatically. An important condition for the correct background calculation is the availability of a sufficient number of reference channels. The only limitation of their method is that the background should be described by a polynomial up to a third degree with a constant functional form over the selected spectral window.

After the background correction, the quantification proceeds by fitting a proper model function to the background corrected data. The choice of a suitable model function and the estimation of the starting values for the parameters are the next crucial steps. In the past, many kinds of functional forms are presented : e.g. the product function [AbrS63, PitJ66], the sum and reduced sum functions [FraR69], the Voigt function [WhiE68, HumJ79, HumJ82],.... The latter two (reduced sum and Voigt functions) have been implemented in ASDAP. Analytical expressions for their partial derivatives with respect to the parameters (I_0 , t_0 , α_G , α_L and a) have been derived and used in the fitting procedure. Starting values for the spectral lines are determined from the original (background corrected) data, the convolution signals, and Zimmermann's method [ZimW61]. The parameters are optimized using the classical Marquardt-Levenberg algorithm [MarD63, LevK44].

In the present Part, the general structure of ASDAP and the individual algorithms are explained in detail in Chapter 1. The performance of the program is tested on simulated decay curves in Chapter 2. In Chapter 3, the qualitative and quantitative analyses of ICP-OE spectra of reference materials, and of complex IR spectra of small carbon clusters trapped in solid noble gas matrices are illustrated.

Chapter 1

Automated Spectral Data Analysis Program

The basic ideas of ASDAP are mentioned in the introduction of Part I. The implemented algorithms are optimized for the detection and quantification of a number of spectral lines in a multiplet based on digital filtering techniques. Before explaining each of these algorithms in detail (Section 1.3.), the mathematical representation (the Voigt profile) of the individual lines is presented in Section 1.1, and the calculation of the convolution signals, necessary in the line and interference detection procedure of ASDAP, is treated in Section 1.2. together with the illustration of the main characteristics of the digital filters and the resulting signals.

1.1. Voigt profile

Even for very high resolution, spectral lines are not characterized by a single frequency or wavelength, but rather by an intensity distribution around a central wavelength. This physical profile, containing components with Gaussian and/or Lorentzian shapes, can be described by a Voigt profile V .

The experimental or optical profile, obtained from measurements with a dispersive element, is further given by a convolution of this physical profile with the instrumental function F_{instr} , so that $F_{eff} = V \otimes F_{instr}$. In a first approximation and for many purposes, F_{eff} can also be written as a Voigt profile [DenD28, VanH46, VanH47]. Therefore, the Voigt profile (or a good approximation of it) is commonly used to describe spectral lines originating from various techniques.

The Voigt profile is the convolution of a Gaussian and a Lorentzian distribution, and can be written as

$$V(z) = \int_{-\infty}^{+\infty} G(\xi) L(z - \xi) d\xi \quad (1.1)$$

in which z is the coordinate along the spectrum (frequency or wavelength), $G(\xi)$ and $L(z - \xi)$ are the following expressions for the Gaussian and Lorentzian distributions :

$$G(\xi) = \frac{2\sqrt{\ln 2}}{\alpha_G \sqrt{\pi}} \exp\left[-\frac{\xi^2}{(\alpha_G/2\sqrt{\ln 2})^2}\right] \quad (1.2)$$

$$L(z-\xi) = \frac{2\alpha_L}{\pi[4(z-\xi)^2 + \alpha_L^2]} \quad (1.3)$$

with α_G and α_L the Gaussian and Lorentzian full-width at half-maximum. The central maximum of these profiles is chosen at position 0. Equation (1.1) can therefore also be written as :

$$V(z) = \frac{4\sqrt{\ln 2} \alpha_L}{\sqrt{\pi^3} \alpha_G} \int_{-\infty}^{+\infty} \frac{\exp\left(-\xi^2/(\alpha_G/2\sqrt{\ln 2})^2\right)}{4(z-\xi)^2 + \alpha_L^2} d\xi \quad (1.4)$$

Introducing the substitutions (1.5 - 1.7)

$$y \equiv 2\sqrt{\ln 2} \frac{\xi}{\alpha_G} \quad (1.5)$$

$$x \equiv 2\sqrt{\ln 2} \frac{z}{\alpha_G} \quad (1.6)$$

and

$$a \equiv \sqrt{\ln 2} \frac{\alpha_L}{\alpha_G} \quad (1.7)$$

in the integral in eq. (1.4), gives the following expressions for the Voigt profile, symbolized as $V(x,a)$

$$V(x,a) = \frac{2\sqrt{\ln 2} a}{\sqrt{\pi^3} \alpha_G} \int_{-\infty}^{+\infty} \frac{\exp(-y^2)}{(x-y)^2 + a^2} dy \quad (1.8)$$

or

$$V(x,a) = \frac{2}{\alpha_G} \sqrt{\frac{\ln 2}{\pi}} K(x,a) \quad (1.9)$$

where $K(x,a)$, is the so-called Voigt function

$$K(x,a) \equiv \frac{a}{\pi} \int_{-\infty}^{+\infty} \frac{\exp(-y^2)}{(x-y)^2 + a^2} dy \quad (1.10)$$

Various numerical procedures [see the references in SchF92] have been published describing the evaluation of the Voigt function based upon various numerical expansions in different regions of the x, a space. Procedures are known which calculate only the real part of the complex probability integral [ArmB67, WhiE68, KieJ73, DrayS76, PieJ77, KarA78, DruJ85, NorR91, KunM97] or the complete probability function $W(z)$ [GauW69, GauW70, HuiA78, HumJ79, HumJ82]

$$W(z) = e^{-z^2} \left(1 + \frac{2i}{\sqrt{\pi}} \int_0^z e^{-t^2} dt \right) = e^{-z^2} \operatorname{erfc}(iz) = K(x, a) + i L(x, a) \quad (1.11)$$

where $z = x + ia$, $K(x, a)$ is given by eq. (1.10), and $L(x, a)$ is defined by the following expression

$$L(x, a) \equiv \frac{1}{\pi} \int_{-\infty}^{+\infty} \frac{(x-y) \exp(-y^2)}{(x-y)^2 + a^2} dy \quad (1.12)$$

The calculation of the complete probability function has the advantage that the imaginary part can be used for the evaluation of the partial derivatives of the Voigt function with respect to the parameters $I_{V,0}$, t_0 , α_G , α_L and a [BouP89]. If all these parameters are known, the Voigt profile can be computed using

$$I_V(t - t_0) = I_{V,0} \frac{K(x, a)}{K(0, a)} \quad (1.13)$$

where $I_V(t-t_0)$ is the intensity at any distance from the peak position t_0 , and $I_{V,0}$ is the intensity at t_0 .

Schreier [SchF92] compared different Voigt function algorithms with respect to their accuracy and computational speed. He recommended Humlicek's algorithm [HumJ79, HumJ82] as accurate, fast and flexible.

The partial derivatives of the Voigt function with respect to the parameters $I_{V,0}$, t_0 , α_G , and a are required in the fitting procedure, the Marquardt-Levenberg algorithm [MarD63, LevK44]. Calculation of these partial derivatives through their analytical expressions enhances the accuracy and speed [SchF92]. Using both the real and imaginary parts of the complex probability function, the partial derivatives of the Voigt function with respect to the parameters $I_{V,0}$, t_0 , α_G , α_L and a can be computed; the expressions are presented in Section 1.4. : Appendix A).

1.2. Digital filtering and convolution signals

Janssens and François [JanF91] proposed zero-area digital filters for peak and interference detection in automated spectral data analysis. They proved that digital filters can be useful in background elimination, peak detection and parameter estimation [JanF91, JanF93, FraJ90]. In ASDAP, the convolution spectra are obtained by applying zero-area Gaussian filters. The calculation is performed on digitized data in a discrete way by summing over a filter window. For the discrete zero-area Gaussian filter C_1 , expression (1.14) has been used :

$$C_1(\tau - t) = I_{0,c,1} \exp \left[-\frac{1}{2 \sigma_{c,1}^2} (\tau - t)^2 \right] - A_1 \quad (1.14)$$

$I_{0,c,1}$ stands for the intensity of the Gaussian distribution, $\sigma_{c,1}$ is its standard deviation, and A_1 is a constant which is determined in such a way that the total net area of the filter is zero:

$$A_1 = \frac{1}{2M_1 + 1} \sum_{\tau=-M_1}^{M_1} I_{0,c,1} \exp \left[-\frac{1}{2 \sigma_{c,1}^2} (\tau - t)^2 \right] \quad (1.15)$$

A zero-area Gaussian filter (Fig. 1.1) is characterized by two adjustable parameters, namely its width M_1 (half the convolution window) and its standard deviation $\sigma_{c,1}$ or the related full-width at half-maximum $\text{fwhm}_{c,1}$ ($= 2 \sqrt{2 \ln 2} \sigma_{c,1}$). It should be noted that the full-width at half-maximum FWHM_1 for the zero-area Gaussian filter is related to M_1 and $\sigma_{c,1}$ in the following way

$$\text{FWHM}_1 = 2 \sigma_{c,1} \left[2 \ln \left(\frac{2}{1 + \exp \left(-M_1^2 / 2 \sigma_{c,1}^2 \right)} \right) \right]^{1/2}, \quad M_1 > 0 \quad (1.16)$$

Note that

$$\lim_{M_1 \rightarrow \infty} \text{FWHM}_1 = \text{fwhm}_{c,1} \quad (1.17)$$

In ASDAP, the **R** spectrum (signal), loosely called the first order convolution spectrum (signal), is obtained by using a single zero-area Gaussian filter. The **S** spectrum (signal), called the second order convolution spectrum (signal), is the result of the consecutive application of two identical zero-area Gaussian filters $C_1(\tau-t)$ or of the use of the combination of two identical zero-area Gaussian filters $C(y)$ [JanF93] given by eq. (1.18).

$$C(y) = I_{0,c}^2 \sigma_c^2 \left\{ \left(\frac{\pi}{2} \right)^{1/2} \frac{1}{\sqrt{2} \sigma_c} \exp \left(-\frac{y^2}{4 \sigma_c^2} \right) \left[\operatorname{erf} \left(\frac{1}{\sqrt{2} \sigma_c} \left(\sqrt{2} M - \frac{|y|}{\sqrt{2}} \right) \right) \right] \right. \\ \left. + \frac{\pi}{M} \left(\operatorname{erf} \frac{M}{\sqrt{2} \sigma_c} \right) \left(\operatorname{erf} \frac{|y| - M}{\sqrt{2} \sigma_c} \right) - \frac{\pi |y|}{2 M^2} \left(\operatorname{erf} \frac{M}{\sqrt{2} \sigma_c} \right)^2 \right\} \quad (1.18)$$

where $y = \tau - t$, $M = M_1$, $\sigma_c = \sigma_{c,1}$ and $I_{0,c} = I_{0,c,1}$. This combined filter (Fig. 1.2) is no longer Gaussian and it operates over $4M$ channels.

For numerical work, it has been found that it is more efficient to use two consecutive zero-area filters than the use of the corresponding convolved filter.

Given the M_1 and FWHM_1 values of the zero-area Gaussian filter, the digital filtering techniques can be applied to the background corrected data in order to calculate the **R** and **S** signals in a discrete manner

$$R(\tau') = \sum_{t=\tau'-M_1}^{\tau'+M_1} C_1(\tau-t) D(t) \quad (1.19)$$

$$S(\tau) = \sum_{\tau'=\tau-M_1}^{\tau+M_1} C_1(t-\tau') R(\tau') = \sum_{\tau'=\tau-M_1}^{\tau+M_1} \sum_{t=\tau'-M_1}^{\tau'+M_1} C_1(t-\tau') C_1(\tau'-t) D(t) \\ = \sum_{t=\tau-2M_1}^{\tau+2M_1} C(\tau-t) D(t) \quad (1.20)$$

where C_1 and C are given by eqs (1.14) and (1.18), respectively.

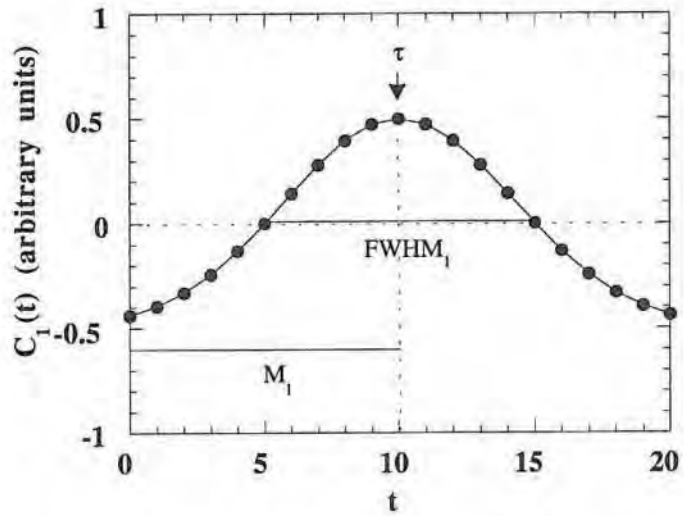


Fig. 1.1 : Zero-area Gaussian filter C_1 with characteristics $M_1 = FWHM_1 = 10$.

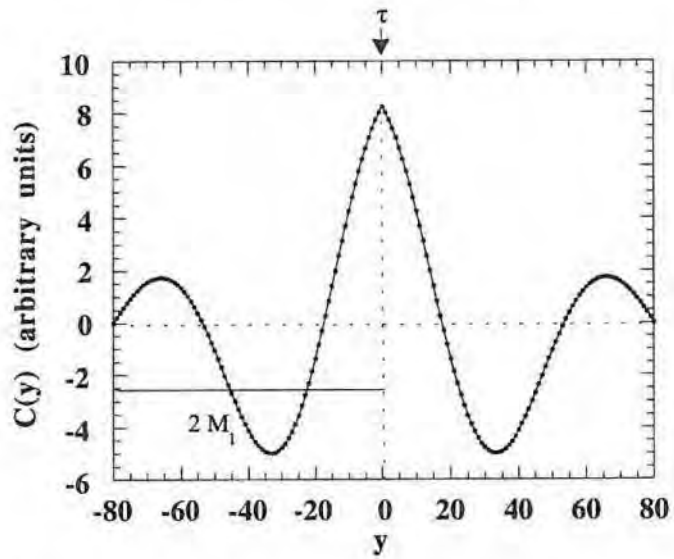


Fig. 1.2 : Combined filter C of two identical zero-area Gaussian filters with $M_1 = FWHM_1 = 40$.

Fig. 1.3 illustrates the characteristic shape of the **R** and **S** signals obtained for a Gaussian profile, with $I_0 = 10^4$ counts/channel, $\alpha_G = 10$ channels and $t_0 = 50$, by using a zero-area Gaussian filter with $\text{FWHM}_1 = M_1 = 3$ channels. In general, the **R** signal consists of a strong positive central peak, situated at the centroid of the spectral line, and two negative side lobes (one at each side of the centroid). The line width is reduced. The **S** signal has besides the strong central positive peak and the two negative minima, also two additional positive maxima (sidebands); furthermore the resolution is improved.

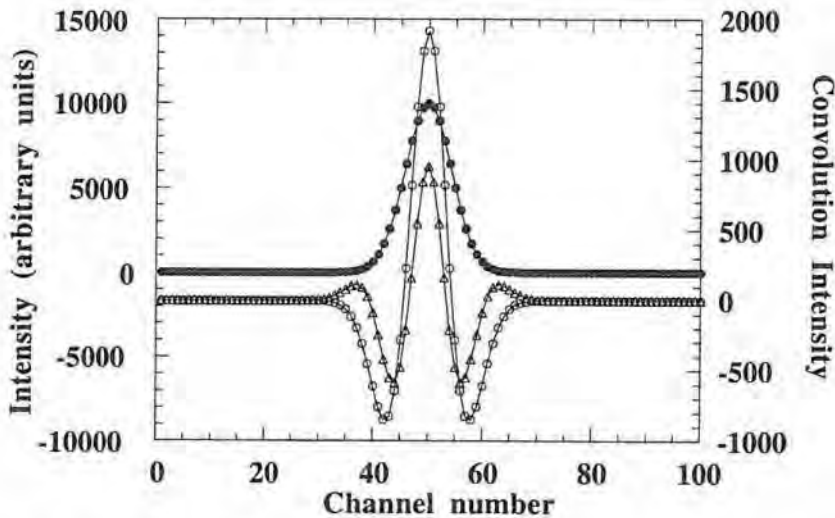
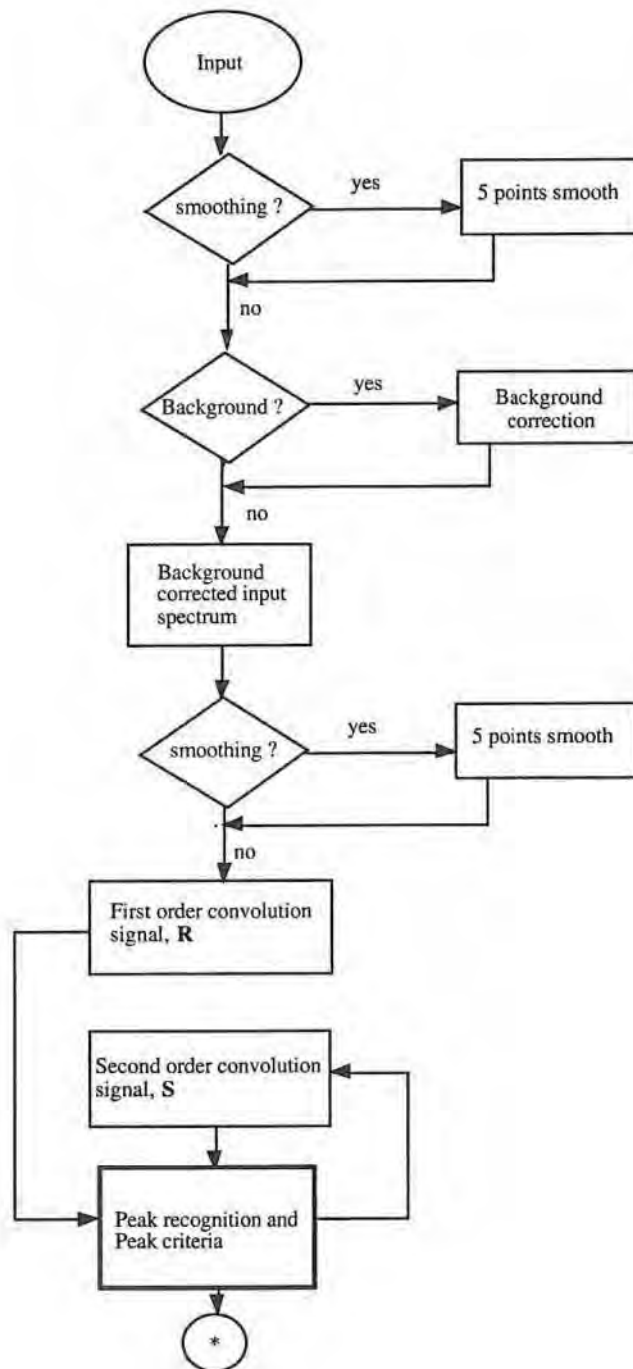


Fig. 1.3 : **R** (○) and **S** (Δ) signals obtained for a Gaussian profile (●), with $I_0 = 10^4$ counts/channel, $\alpha_G = 10$ channels and $t_0 = 50$, by using a zero-area Gaussian filter with $\text{FWHM}_1 = M_1 = 3$ channels.

1.3. Automated Spectral Data Analysis Program (ASDAP)

ASDAP is programmed in such a way that with a minimum of operator intervention a maximum of information can be extracted from the spectral data. The main steps of ASDAP are shown in the flow-chart (Fig. 1.4). The program is written in FORTRAN77. The algorithms, developed for each step, will be explained in detail furtheron.



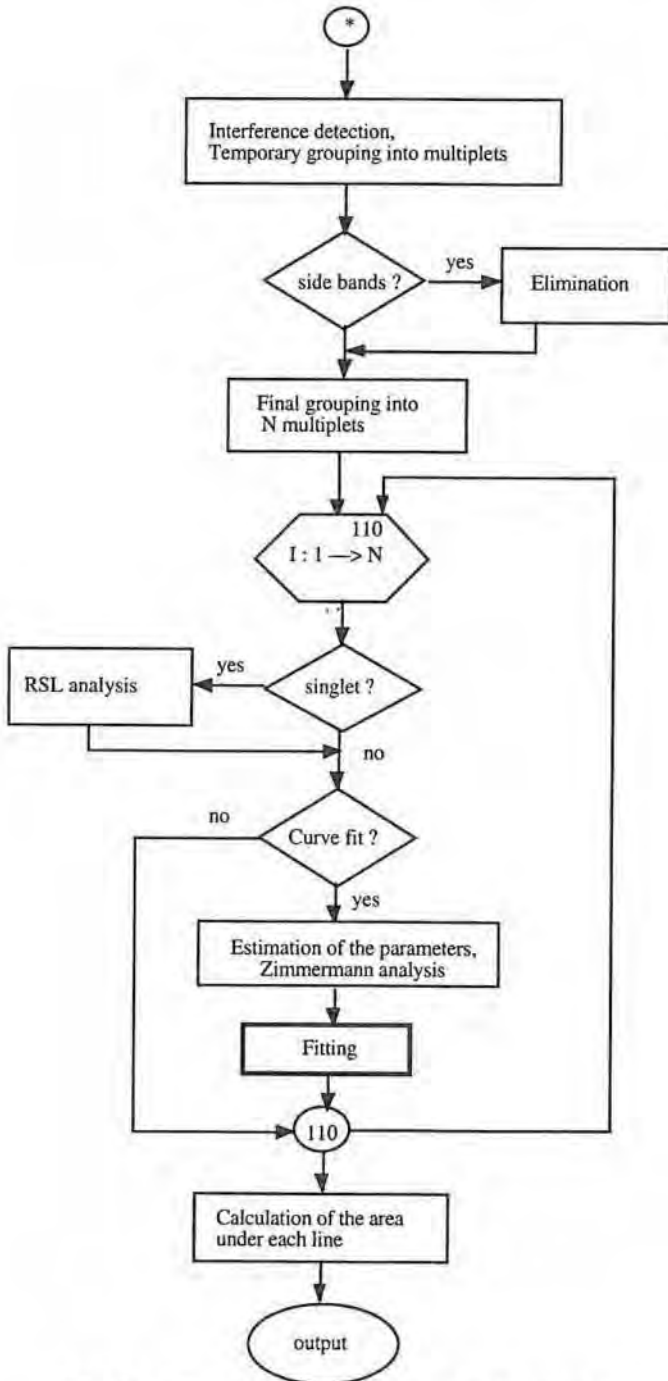


Fig. 1.4 : Flow-chart of the main steps of ASDAP.

1.3.1. Input

ASDAP reads the spectral data as columns of channel numbers and the corresponding intensities in a certain spectral window. The selection of this spectral window requires that sufficient background reference channels can be found in order to perform the background calculation correctly. In a certain sense this implies also that the operator has to make a decision whether certain lines belong to the same multiplet or not. Also a relative standard deviation *rstd* (%) will be asked, for the calculation of the absolute standard deviation of the intensity as $\text{std}(I) = (\text{rstd } I)/100$.

Input values for the FWHM_1 and M_1 of the Gaussian filter(s) are required. Since mainly two identical filters will be used as a good compromise for the *S* signal, only one set of filter parameters is needed. On the other hand, the characteristics of the filters used for both for background correction and peak detection, are mostly different. Generally, smaller filters are applied for peak detection than those used for the background correction procedure.

Before the fitting procedure, the operator is asked for the start and stop channels limiting the fitting area.

The operator is able to repeat some steps until a desired level is reached : for instance, smoothing can be repeated several times after each other, background correction and peak detection can also be restarted with different kinds of filters.

1.3.2. Smoothing

Smoothing can be applied before and after background correction using a five-point quadratic smooth given by Gorry's modification of the Savitzky-Golay algorithm [GorP90, SavA64].

1.3.3. Background correction

Since in quantitative spectral data analysis net line intensities or areas are needed, background elimination is a crucial step before peak detection and fitting procedures can be carried out.

The background correction algorithm incorporated in ASDAP is that described by Janssens and François [JanF92] and is strongly related to convolution signals. An important step here is the selection of reference channels that are affected only by the continuum background. Therefore, initial grouping of peaks into multiplets is performed.

The recognition of these peaks is based on the information supplied by the positions of the minima and maxima in the \mathbf{R} signals and their maximum intensities. The following criteria are tested :

- (a) at least one of the distances between a minimum and maximum of the convolution signal is larger than or equal to the filter width M_1 ,
- (b) $\mathbf{R}_i \geq 0$, where \mathbf{R}_i is the first order convolution intensity at position i ,
and,
- (c) $|\text{difference in intensity between maximum and deepest minimum}| > 2 \sigma_{\mathbf{R}_i}$.

After this preliminary peak detection, the lines are checked for interference, i.e. if the minima of two neighboring lines coincide in the \mathbf{R} convolution signal or if they are separated by less than 3 channels where the \mathbf{R} intensities approximate zero. If interference occurs, the channels in the region between the two (or more) peaks are excluded as reference channels.

Next, a first background estimation can be made by using all channels, except those belonging to any multiplet, that fulfil the condition

$$|\mathbf{R}_i| \leq n \sigma_{\mathbf{R}_i} \quad (1.21)$$

n is a variable, initially equal to 1.5, which is increased in steps of 0.5 until 10 channels are found or until n equals 2.5. The selected channels are fitted to a linear or quadratic polynomial, approximating best the background contributions. Then, this background estimation is used for selection of the final reference channels :

$$(a) \quad |\mathbf{R}_i| \leq n \sigma_{\mathbf{R}_i} \quad (1.21)$$

and

$$(b) \quad Y_j \leq YBE_j + n \sigma_{YBE_j} \quad (1.22)$$

Y_j represents the intensity of the original signal in channel j , YBE_j is the estimated background intensity at the same position, and σ_{YBE_j} is its standard deviation. Again n is a variable, initially equal to 1.5, and then increased in steps of 0.5 until 10 channels are found or until n equals 2.5. When these 10 channels are not found, an appropriate warning is given.

Finally, an F-test decides whether a linear, quadratic, or cubic background should be used. Once the functional form of the background has been determined, an additional test for excluding possible outliers (reference channels) may eventually be

performed in a rather simple and objective way : if the difference between the experimental intensity and the calculated one exceeds the standard deviation, the reference channel is excluded from the final background calculation.

Janssens and François [JanF92] found that the procedure outlined above, can perform correct background correction if sufficient reference channels are available and if the background can be described by a single functional form over the spectral window.

Janssens and François [JanF93] also proved that the consecutive application of two zero-area Gaussian filters or the use of the corresponding combined filter eliminates the constant (a_0), linear (a_1t), quadratic (a_2t^2), and cubic (a_3t^3) terms in the background component of the original signal.

$$B(t) = a_0 + \sum_{i=1}^n a_i t^i \quad (1.23)$$

Fig. 1.5 shows the convolution signals of a Gaussian profile with $I_0 = 1000$ counts/channel and $\alpha_G = 10$ channels superimposed on a fourth order background characterized by $a_0 = 2500$, $a_1 = a_3 = 2.5 \times 10^{-2}$, $a_2 = a_4 = -2.75 \times 10^{-4}$, obtained with a zero-area Gaussian filter with $M_1 = FWHM_1 = 5$ channels.

1.3.4. Peak detection

The peak detection procedure is based on the information in the convolution signals \mathbf{R} (eq. 1.19) and \mathbf{S} (eq. 1.20) and the background corrected spectrum. Two main parts can be distinguished : first, a peak recognition procedure is started to find all maxima in the \mathbf{R} and \mathbf{S} signals and to decide which one is related to a real peak in the original data ; secondly, these peaks are checked for interference and grouped into multiplets.

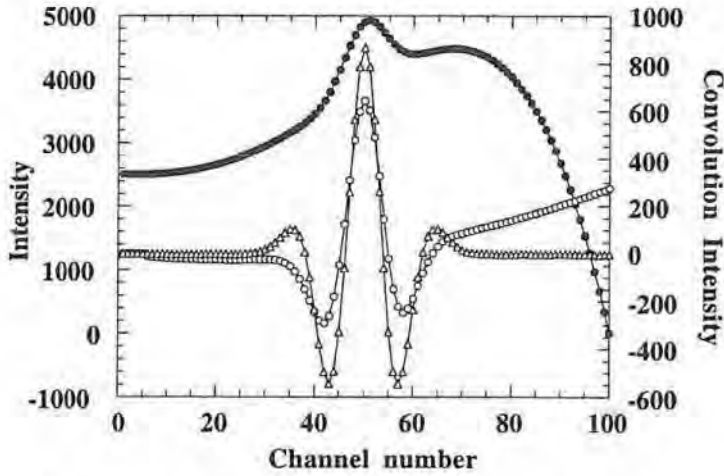


Fig. 1.5 : R (\circ) and S (Δ) signals of a Gaussian profile (\bullet) with $I_0 = 1000$ counts/channel, and $\alpha_G = 10$ channels superimposed on a fourth order background characterized by $a_0 = 2500$, $a_1 = a_3 = 2.5 \times 10^{-2}$, $a_2 = a_4 = -2.75 \times 10^{-4}$, obtained with a zero-area Gaussian filter with $M_1 = \text{FWHM}_1 = 5$ channels.

Peak recognition procedure

All maxima are searched in both the convolution signals R and S (both noted here as CS) together with the left and right minima. The minima are found in the first derivative of the CS signals calculated by a five-point quadratic derivative given by Gorry's modification of the Savitzky-Golay algorithm [GorP90, SavA64]. The maxima are tested by a set of criteria shown under the form of a flow-chart in Fig. 1.6. Various sublevels have been defined here, which will be further explained below.

* Sublevel 1

A maximum is detected at channel s based on the following inequalities between the sum of three channel contents

$$CS_{s-1} + CS_s + CS_{s+1} > CS_{s-2} + CS_{s-1} + CS_s \quad (1.24)$$

and

$$CS_{s-1} + CS_s + CS_{s+1} > CS_s + CS_{s+1} + CS_{s+2} \quad (1.25)$$

The minima are found in the first derivative of the CS signal as the positions where the first derivative changes its sign. If this criterium fails, the position at the center of two neighboring maxima is used.

* *Sublevel 2*

If the intensity of the original (background corrected) spectrum at the position of the maximum (channel s), does not exceed its standard deviation or is even smaller than zero, the maximum is rejected as a line.

* *Sublevel 3*

The line is checked whether a maximum in the CS signal corresponds to a maximum in the original (background corrected) spectrum or not.

* *Sublevel 4*

If a maximum is also found in the original spectrum at channel s , the following conditions have to be satisfied for the maximum to be accepted as a real line :

$$(a) I_s \geq 2 * \sigma_{I_s} \quad (1.26)$$

otherwise,

$$(b) CS_s \geq \sigma_{CS_s}, \text{ and} \quad (1.27)$$

$$(c) \Delta t_{\text{left}} \text{ or } \Delta t_{\text{right}} \geq M_1. \quad (1.28)$$

* *Sublevel 5*

Maxima in the CS signal that do not correspond to a maximum at the same position in the original (background corrected) spectrum can be either situated on the slope of a more intense line (sublevel 6) or may be located in a flat valley between two (or more) intense lines. The peaks in a flat valley are considered to be real.

* *Sublevel 6*

If lines are situated on the slope of more intense ones, at least three channels should be found in the background corrected spectrum with intensities exceeding their standard deviation before the minimum of the convolution signal is reached.

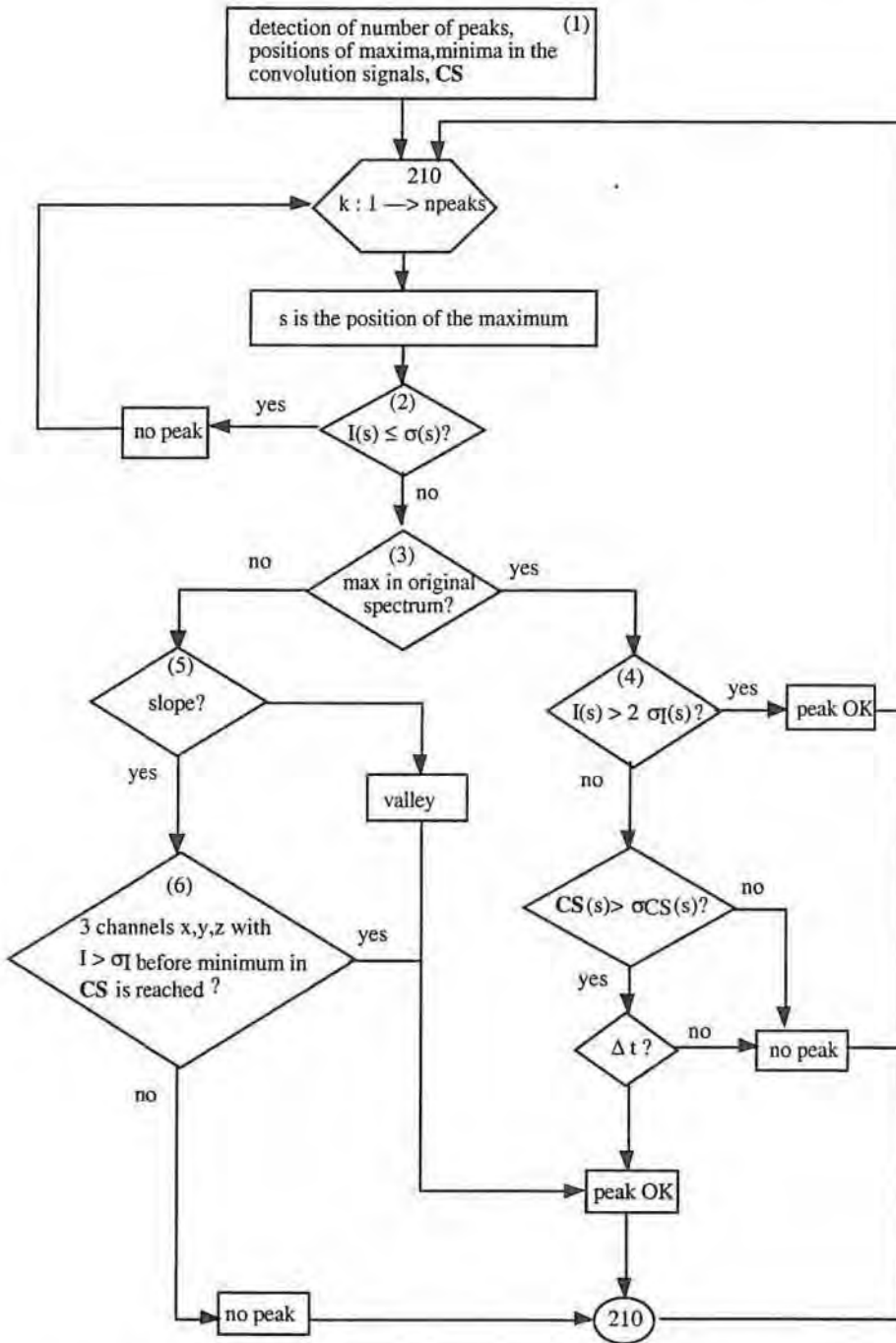


Fig. 1.6 : Flow-chart of the set of criteria at which the maxima are tested.

Interference detection procedure

Interference between two neighboring peaks in a convolution spectrum is detected if they are separated by only one minimum in the convolution spectrum. The interference detection leads to a new peak criterium. Since a positive minimum without interference at that side of the maximum cannot belong to a real maximum, the latter is rejected. Now, the interfering lines are temporary grouped into the same multiplet. The boundaries of a multiplet are determined by searching the farthest channel from the first and last maxima in this multiplet with an intensity greater than the standard deviation of the background corrected signal. Then, for each line is checked

(a) if $(s - M_1/2) \geq$ left boundary of a multiplet,

and

(b) $(s + M_1/2) \leq$ right boundary of a multiplet,

otherwise the peak is not considered to be a real one.

The number of lines in the **R** and **S** signals are compared. If the number of maxima in the second order convolution spectrum is larger than that in the first order one, this can be due to the following : (1) new real lines are detected in the more resolved **S** signal, or (2) additional sidebands are encountered. Janssens and François [JanF93] formulated a criterium for the elimination of sidebands.

If M_1 of the zero-area Gaussian filter satisfies the condition, $0.25 \text{ FWHM}_s \leq M_1 \leq \text{FWHM}_s$, the sidebands in the **S** signal are always further removed from the centroid than the side lobes in the **R** signal, as it can be seen in Fig. 1.3.

Finally, the real peaks are grouped into multiplets and the boundaries are determined. Multiplets containing only a single line are checked for non-detected interfering lines by calculation of the RSL quantity, i.e. the ratio of the intensity of the left negative side lobe to that of the right one. Because of the symmetry of the filter, symmetric data should result in a symmetric convolution signal. This means that RSL should equal unity for a single spectral line. If $|\text{RSL}|$ is smaller than 0.95, the presence of an interfering peak at the left side of the single one is supposed; if $|\text{RSL}|$ is larger than 1.05, interference at the right side is considered. In both cases, one peak is added to the multiplet.

The number of lines and multiplets are returned to the operator and he/she can decide whether the complete peak detection procedure must be repeated with a different filter (a smaller or a broader one) or not.

1.3.5. Fitting procedure

Quantitative information concerning the contribution of each line in a previously detected multiplet, is obtained by fitting the background corrected data using the classical Marquardt-Levenberg algorithm [MarD63, LevK44]. Each line is characterized by four parameters : the centroid t_0 , the intensity I_0 , at this centroid, the FWHM, and a lineshape parameter. The two last parameters depend on the model function that is selected, i.e. the Voigt function [HumJ79, HumJ82] or an approximation to it, the reduced sum function [FraR69]

$$I_{RS}(t) = I_{RS,0} \left(f \exp \left(- \ln 2 \left[\frac{2(t-t_0)}{\alpha_{RS}} \right]^2 \right) + (1-f) \left(1 + \left[\frac{2(t-t_0)}{\alpha_{RS}} \right]^2 \right)^{-1} \right) \quad (1.29)$$

with $I_{RS,0}$ the intensity at the position t_0 of the maximum of the profile, α_{RS} the FWHM of the line, and f the lineshape parameter.

Since the optimization for a Voigt profile is very sensitive to the initial estimates of the parameters, a previous fitting is done with the reduced sum function. The initial parameter values are determined by ASDAP. Since the smallest deviations from the real positions are usually found in the second order convolution signal, initial positions are taken from that signal. Due to the fact that the intensities in the convolution signals and the original spectrum are not related, at least not in a simple way, the initial I_0 values are determined as 90% of the intensity of the background corrected signal at that position.

The FWHM of the lines are also based on the background corrected data, and are determined by means of the methods of Zimmermann [ZimW61] and Mundschenk [MunH66a, MunH66b] which are closely related. The method linearizes a Gaussian curve $I_s(t)$,

$$I_s(t) = \left(\frac{A}{\sigma \sqrt{2\pi}} \right) \exp \left[- \frac{(t - t_0)^2}{2 \sigma^2} \right] \quad (1.30)$$

where A represents the area under the Gaussian curve and σ its standard deviation. The quantity $Q(t)$ is now defined as

$$Q(t) \equiv \ln \left[\frac{I_s(t-m)}{I_s(t+n)} \right] \quad ; m, n = 0, 1, 2, \dots \quad (1.31)$$

It can now readily be shown that

$$Q(t) = \frac{m+n}{\sigma^2} t + \frac{1}{2 \sigma^2} (n^2 - m^2) - \frac{1}{\sigma^2} (m+n) t_0 \quad (1.32a)$$

or

$$Q(t) = \alpha + \beta t \quad (1.32b)$$

When $Q(t)$ is plotted vs t , a straight line is obtained, which intersects the abscissa axis t at

$$\alpha = \frac{1}{2\sigma^2}(n^2 - m^2) - \frac{1}{\sigma^2}(m+n)t_0 \quad (1.33)$$

and which has a slope

$$\beta = (m+n)/\sigma^2 \quad (1.34)$$

The expressions given by Zimmermann and Mundschenk are obtained with $m = n = 1$, and $m = 0$, respectively.

François and Janssens [FraJ90] discussed the use of Zimmermann's method for the determination of the centroid t_0 and the σ value for single Gaussian profiles, and for the detection of interference through the 'kink' in the $Q(t)$ vs t curve. Even for overlapping Gaussians good t_0 and σ values can be obtained when a good choice of the fitting region is made.

Zimmermann's method has been implemented in ASDAP for obtaining the first estimates of the FWHM of lines in a multiplet. Therefore, the $Q(t)$ vs t plot is constructed with $m = n = 1$ for those regions in the background corrected spectrum corresponding to the positive parts of the S signals, for each line separately. The slope of each straight line is obtained by using a least squares linear fit and the corresponding FWHM is calculated as $(2\sqrt{2 \ln 2} \sqrt{2/\beta})$. If not enough channel contents are available, the width of the line will be determined using the foregoing and/or following lines. The smallest of all the FWHM's of the lines belonging to the same multiplet is searched and used as the initial estimate of the FWHM of each line in that multiplet.

Finally, the f values (of the reduced sum function) cannot be deduced directly from the recorded data. Therefore, a fixed value, commonly 0.5 will be used here. For the subsequent fit using the Voigt function, a good estimate for α_G can be calculated from α_{RS} using the approximation of Olivero and Longbothum [OliJ77] (eq. (1.35))

$$\alpha_V = 0.5 \left(1.0692 \alpha_L + \sqrt{0.86639 \alpha_L^2 + 4 \alpha_G^2} \right) \quad (1.35)$$

as follows.

α_V is approximated by the optimized α_{RS} of the RSF and α_L is expressed in terms of a and α_G (eq. (1.7)). From Eq. (1.35), the following expression can be deduced for α_G in terms of α_{RS} and a

$$\alpha_G = \frac{2\sqrt{\ln 2} \alpha_{RS}}{\left(1.0692 a + \sqrt{0.86639 a^2 + 4 \ln 2}\right)} \quad (1.36)$$

Furthermore, the starting value for the Voigt parameter a can be estimated from f using the formulas of Whiting [WhiE68] (eq. (1.37)), and of Van de Hulst and Reesinck [VanH47] (eq. (1.38))

$$f = 1 - (\alpha_L / \alpha_G) \quad (1.37)$$

$$\alpha_G = \sqrt{\alpha_V^2 f} \quad (1.38)$$

Expression (1.7) for the Voigt parameter a can then be written in terms of f as follows

$$a = \left(\ln 2 \frac{(1-f)^2}{f} \right)^{1/2} \quad (1.39)$$

The optimization of the parameters is done over a given spectral range. The Marquardt-Levenberg algorithm uses partial derivatives with respect to the four parameters of the model function. The analytical expressions for the partial derivatives of the Voigt function are presented in Appendix A. The partial derivatives of the reduced sum function with respect to $I_{RS,0}$, l_0 , α_{RS} , and f are given in Appendix B. After each iteration, the physical meaning of the estimated parameters is checked, and if necessary, adjusted or rejected. The optimization is stopped when the reduced chi-square becomes less than 1, or when no further significant improvement is obtained.

1.3.6. Output

ASDAP returns both qualitative and quantitative information.

* *After background correction*, the number of selected reference channels is given together with the best fitted background polynomial. The goodness of fit is shown by the obtained χ^2 value.

* *After peak and interference detection*, the number of lines found in the **R** and **S** signals are given together with their positions and the grouping in multiplets. The **R** and **S** signals, the original and background corrected intensities and the first derivatives are collected in a file. During the *fitting procedure* each multiplet is treated separately. The optimized values

after each iteration are displayed together with the corresponding reduced χ^2 values. The final optimized parameters and the calculated net line area for the detected individual lines are put in a file together with their standard deviations and goodness of fit parameters. Finally, each set of maximum 7 calculated lines is written in a file. This is necessary since Kaleidagraph, used for the visualization of the spectra, only supports eight columns (seven for intensities and one for channel numbers).

1.4. Appendix A : Partial derivatives of the Voigt profile

Using the real $K(x,a)$ and imaginary part $L(x,a)$ of the complex probability function $W(z)$ (eq. 1.11), the expressions can be derived for the partial derivatives of the Voigt function (eq. (1.13)) with respect to the parameters $I_{V,0}$, t_0 , α_G , α_L and a . But first, the Fourier integral representations of the real and imaginary parts of the complex probability function are presented, since they are required furtheron.

1.4.1. Fourier integral representation of $K(x,a)$

We start from the well known result [Gra80]

$$\int_0^{\infty} e^{-px} \cos qx \, dx = \frac{p}{p^2 + q^2} \quad , \quad p > 0 \quad (1.40)$$

Putting $p = a$ and $q = x-y$, eq. (1.10) for $K(x,a)$ can be brought into the following form

$$K(x,a) = \frac{1}{\pi} \int_0^{\infty} e^{-at} \, dt \int_{-\infty}^{+\infty} e^{-y^2} \cos(x-y)t \, dy \quad , \quad a > 0 \quad (1.41)$$

or

$$K(x,a) = \frac{1}{\pi} \left[\int_0^{\infty} e^{-at} \cos xt \, dt \int_{-\infty}^{+\infty} e^{-y^2} \cos yt \, dy + \int_0^{\infty} e^{-at} \sin xt \, dt \int_{-\infty}^{+\infty} e^{-y^2} \sin yt \, dy \right] \quad (1.42)$$

Since $e^{-y^2} \sin yt$ is an uneven function in y , eq. (1.42) simplifies as

$$K(x,a) = \frac{1}{\pi} \left[\int_0^{\infty} e^{-at} \cos xt \, dt \int_{-\infty}^{+\infty} e^{-y^2} \cos yt \, dy \right] \quad (1.43)$$

The second integral in eq. (1.43) can be computed exactly by using the following well known result [Gra80]

$$\int_0^{\infty} e^{-\beta x^2} \cos bx \, dx = \frac{1}{2} \sqrt{\frac{\pi}{\beta}} e^{-b^2/4\beta} \quad , \quad \text{real } \beta > 0 \quad (1.44)$$

The second integral can thus be transformed as

$$\int_{-\infty}^{+\infty} e^{-y^2} \cos yt \, dy = 2 \int_0^{+\infty} e^{-y^2} \cos yt \, dy = \sqrt{\pi} e^{-t^2/4} \quad (1.45)$$

Finally, the Fourier integral representation of $K(x,a)$, also known as Reiche's formula [ReiF13], is found as

$$K(x,a) = \frac{1}{\sqrt{\pi}} \int_0^{\infty} e^{-\frac{1}{4}t^2 - at} \cos xt \, dt \quad , \quad a > 0 \quad (1.46)$$

1.4.2. Fourier integral representation of $L(x,a)$

The Fourier integral representation of $L(x,a)$ (eq. (1.12)) can be derived, starting from [Gra180]

$$\int_0^{\infty} e^{-p x} \sin q x \, dx = \frac{q}{p^2 + q^2} \quad , \quad p > 0 \quad (1.47)$$

Substituting p by a , q by $(x-y)$, and introducing the resulting expression in eq. (1.12) gives the following expression for $L(x,a)$

$$L(x,a) = \frac{1}{\pi} \int_0^{\infty} e^{-at} \, dt \int_{-\infty}^{+\infty} e^{-y^2} \sin(x-y)t \, dy \quad , \quad a > 0 \quad (1.48)$$

or

$$L(x,a) = \frac{1}{\pi} \left[\int_0^{\infty} e^{-at} \sin xt \, dt \int_{-\infty}^{+\infty} e^{-y^2} \cos yt \, dy + \int_0^{\infty} e^{-at} \cos xt \, dt \int_{-\infty}^{+\infty} e^{-y^2} \sin yt \, dy \right] \quad (1.49)$$

Since $e^{-y^2} \sin yt$ is an uneven function in y , the last term in eq. (1.49) vanishes. With the aid of eq. (1.45) the Fourier integral representation of $L(x,a)$ is finally obtained :

$$L(x,a) = \frac{1}{\sqrt{\pi}} \int_0^{\infty} e^{-\frac{1}{4}t^2 - at} \sin xt \, dt \quad , \quad a > 0 \quad (1.50)$$

1.4.3. Partial derivatives of the Voigt function

a. with respect to $I_{V,0}$

$$\boxed{\frac{\partial I_V(t-t_0, a)}{\partial I_{V,0}} = \frac{K(x, a)}{K(0, a)}} \quad (1.51)$$

b. with respect to t_0

$$\frac{\partial I_V(t-t_0, a)}{\partial t_0} = \frac{I_{V,0}}{K(0, a)} \frac{\partial K(x, a)}{\partial t_0} = \frac{I_{V,0}}{K(0, a)} \frac{\partial K(x, a)}{\partial x} \frac{\partial x}{\partial t_0} \quad (1.52)$$

Using eq. (1.6) with $z = t - t_0$ gives

$$\frac{\partial x}{\partial t_0} = \frac{\partial}{\partial t_0} \left(2\sqrt{\ln 2} \frac{t-t_0}{\alpha_G} \right) = \frac{-2\sqrt{\ln 2}}{\alpha_G} = -\frac{x}{t-t_0} \quad (1.53)$$

Eq. (1.52) becomes

$$\frac{\partial I_V(t-t_0, a)}{\partial t_0} = -\frac{x}{t-t_0} \frac{I_{V,0}}{K(0, a)} \frac{\partial K(x, a)}{\partial x} \quad (1.54)$$

Using the Fourier integral representation of $K(x, a)$ (eq. (1.46)), the partial derivative of $K(x, a)$ with respect to x can be readily found as

$$\frac{\partial}{\partial x} K(x, a) = \frac{1}{\sqrt{\pi}} \int_0^{\infty} e^{-\frac{1}{4}t^2 - at} \frac{\partial}{\partial x} \cos xt \, dt = -\frac{1}{\sqrt{\pi}} \int_0^{\infty} t e^{-\frac{1}{4}t^2 - at} \sin xt \, dt \quad (1.55)$$

or

$$\frac{\partial}{\partial x} K(x, a) = 2[a L(x, a) - x K(x, a)] \quad (1.56)$$

Indeed, substituting the Fourier integral representations for $K(x, a)$ and $L(x, a)$ in eq. (1.56) gives

$$\begin{aligned} \frac{\partial}{\partial x} K(x, a) &= \frac{2}{\sqrt{\pi}} \left[a \int_0^{\infty} e^{-\frac{1}{4}t^2 - at} \sin xt \, dt - x \int_0^{\infty} e^{-\frac{1}{4}t^2 - at} \cos xt \, dt \right] \\ &= \frac{2}{\sqrt{\pi}} \left[- \int_0^{\infty} e^{-\frac{1}{4}t^2} \sin xt \, d e^{-at} - x \int_0^{\infty} e^{-\frac{1}{4}t^2 - at} \cos xt \, dt \right] \\ &= \frac{2}{\sqrt{\pi}} \left\{ - \left[e^{-\frac{1}{4}t^2 - at} \sin xt \right]_0^{\infty} + \int_0^{\infty} e^{-at} d \left(e^{-\frac{1}{4}t^2} \sin xt \right) - x \int_0^{\infty} e^{-\frac{1}{4}t^2 - at} \cos xt \, dt \right\} \end{aligned}$$

$$= \left[0 - \frac{2}{\sqrt{\pi}} \frac{1}{2} \int_0^{\infty} t e^{-\frac{1}{4}t^2 - at} \sin xt \, dt + \int_0^{\infty} x e^{-\frac{1}{4}t^2 - at} \cos xt \, dt - x \int_0^{\infty} e^{-\frac{1}{4}t^2 - at} \cos xt \, dt \right]$$

$$= -\frac{1}{\sqrt{\pi}} \int_0^{\infty} t e^{-\frac{1}{4}t^2 - at} \sin xt \, dt$$

Combination of eqs (1.54) and (1.56) gives finally the desired partial derivative

$$\boxed{\frac{\partial I_V(t-t_0, a)}{\partial t_0} = \frac{2x I_{V,0}}{(t-t_0) K(0, a)} [x K(x, a) - a L(x, a)]} \quad (1.57)$$

c. with respect to α_G

$$\frac{\partial I_V(t-t_0, a)}{\partial \alpha_G} = I_{V,0} \frac{\partial}{\partial \alpha_G} \frac{K(x, a)}{K(0, a)} = I_{V,0} \frac{K(0, a) \frac{\partial K(x, a)}{\partial \alpha_G} - K(x, a) \frac{\partial K(0, a)}{\partial \alpha_G}}{[K(0, a)]^2} \quad (1.58)$$

in which

$$\frac{\partial K(x, a)}{\partial \alpha_G} = \frac{\partial K(x, a)}{\partial x} \frac{\partial x}{\partial \alpha_G} + \frac{\partial K(x, a)}{\partial a} \frac{\partial a}{\partial \alpha_G} \quad (1.59)$$

Using eqs (1.6) and (1.7), i.e. the definitions of x and a , respectively, it can be found that

$$\frac{\partial x}{\partial \alpha_G} = -\frac{x}{\alpha_G} \quad (1.60)$$

$$\frac{\partial a}{\partial \alpha_G} = -\frac{a}{\alpha_G} \quad (1.61)$$

Substitution of eqs (1.60) and (1.61) in eq. (1.59) results in

$$\frac{\partial K(x, a)}{\partial \alpha_G} = -\frac{1}{\alpha_G} \left(x \frac{\partial K(x, a)}{\partial x} + a \frac{\partial K(x, a)}{\partial a} \right) \quad (1.62)$$

with $\partial K(x, a)/\partial x$ given by eq. (1.55), and

$$\frac{\partial}{\partial a} K(x, a) = \frac{1}{\sqrt{\pi}} \int_0^{\infty} \frac{\partial}{\partial a} \left(e^{-\frac{1}{4}t^2 - at} \right) \cos xt \, dt = -\frac{1}{\sqrt{\pi}} \int_0^{\infty} t e^{-\frac{1}{4}t^2 - at} \cos xt \, dt \quad (1.63)$$

This can also be written as

$$\frac{\partial}{\partial a} K(x, a) = 2 \left[x L(x, a) + a K(x, a) - \frac{1}{\sqrt{\pi}} \right] \quad (1.64)$$

Indeed,

$$\begin{aligned}
 \frac{\partial}{\partial a} K(x, a) &= \frac{2}{\sqrt{\pi}} \left[x \int_0^{\infty} e^{-\frac{1}{4}t^2 - at} \sin xt \, dt + a \int_0^{\infty} e^{-\frac{1}{4}t^2 - at} \cos xt \, dt - 1 \right] \\
 &= \frac{2}{\sqrt{\pi}} \left[x \int_0^{\infty} e^{-\frac{1}{4}t^2 - at} \sin xt \, dt - \int_0^{\infty} e^{-\frac{1}{4}t^2} \cos xt \, dt e^{-at} - 1 \right] \\
 &= \frac{2}{\sqrt{\pi}} \left\{ x \int_0^{\infty} e^{-\frac{1}{4}t^2 - at} \sin xt \, dt - \left[e^{-\frac{1}{4}t^2 - at} \cos xt \right]_0^{\infty} + \int_0^{\infty} e^{-at} d \left(e^{-\frac{1}{4}t^2} \cos xt \right) - 1 \right\} \\
 &= \frac{2}{\sqrt{\pi}} \left[x \int_0^{\infty} e^{-\frac{1}{4}t^2 - at} \sin xt \, dt + 1 - \frac{1}{2} \int_0^{\infty} t e^{-\frac{1}{4}t^2 - at} \cos xt \, dt - x \int_0^{\infty} e^{-\frac{1}{4}t^2 - at} \sin xt \, dt - 1 \right] \\
 &= -\frac{1}{\sqrt{\pi}} \int_0^{\infty} t e^{-\frac{1}{4}t^2 - at} \cos xt \, dt
 \end{aligned}$$

Now, the second term in the 'nominator' of eq. (1.58), contains the partial derivative of $K(0, a)$ with respect to α_G :

$$\frac{\partial K(0, a)}{\partial \alpha_G} = \frac{\partial K(0, a)}{\partial a} \frac{\partial a}{\partial \alpha_G} = -\frac{a}{\alpha_G} \frac{\partial K(0, a)}{\partial a} \quad (1.65)$$

$K(0, a)$ is given by

$$K(0, a) = \frac{a}{\pi} \int_{-\infty}^{+\infty} \frac{\exp(-y^2)}{y^2 + a^2} \, dy = \frac{2a}{\pi} \int_0^{\infty} \frac{\exp(-y^2)}{y^2 + a^2} \, dy = e^{a^2} \operatorname{erfc} a \quad (1.66)$$

and

$$\frac{\partial K(0, a)}{\partial a} = \frac{\partial}{\partial a} e^{a^2} \operatorname{erfc} a = 2 \left(a e^{a^2} \operatorname{erfc} a - \frac{1}{\sqrt{\pi}} \right)$$

or

$$\frac{\partial K(0, a)}{\partial a} = 2 \left(a K(0, a) - \frac{1}{\sqrt{\pi}} \right) \quad (1.67)$$

Eq. (1.58) can be transformed as follows using eqs. (1.62) and (1.65)

$$\frac{\partial I_V(t - t_0, a)}{\partial \alpha_G} = I_{V,0} \left\{ \frac{-1}{K(0, a) \alpha_G} \left[\left(x \frac{\partial K(x, a)}{\partial x} + a \frac{\partial K(x, a)}{\partial a} \right) - a \frac{K(x, a)}{K(0, a)} \frac{\partial K(0, a)}{\partial a} \right] \right\} \quad (1.68)$$

and

$$x \frac{\partial K(x,a)}{\partial x} + a \frac{\partial K(x,a)}{\partial a} = 4 a x L(x,a) - 2(x^2 - a^2)K(x,a) - \frac{2a}{\sqrt{\pi}} \quad (1.69)$$

After substitution of eqs (1.67) and (1.69) in eq. (1.68), the final expression for the partial derivative with respect to α_G , is obtained

$$\frac{\partial I_V(t-t_0,a)}{\partial \alpha_G} = \frac{2 I_{V,0}}{\alpha_G K(0,a)} \left[x^2 K(x,a) - 2ax L(x,a) + \frac{a}{\sqrt{\pi}} \left[1 - \frac{K(x,a)}{K(0,a)} \right] \right] \quad (1.70)$$

Boumans [BouP89] obtained the following expression for $\partial I_V(t-t_0,a)/\partial \alpha_G$

$$\frac{\partial I_V(t-t_0,a)}{\partial \alpha_G} = I_{V,0} \left\{ \frac{-1}{K(0,a) \alpha_G} \left[x \frac{\partial K(x,a)}{\partial x} + a \frac{\partial K(x,a)}{\partial a} \right] \right\} \quad (1.71a)$$

or

$$\frac{\partial I_V(t-t_0,a)}{\partial \alpha_G} = \frac{-I_{V,0}}{K(0,a) \alpha_G} \left[4ax L(x,a) - 2(x^2 - a^2)K(x,a) - \frac{2a}{\sqrt{\pi}} \right] \quad (1.71b)$$

It can be seen that Boumans neglected the term $\partial K(0,a)/\partial a$ given by eq. (1.67).

d. with respect to a

$$\frac{\partial I_V(t-t_0,a)}{\partial a} = I_{V,0} \frac{\partial}{\partial a} \frac{K(x,a)}{K(0,a)} = I_{V,0} \frac{K(0,a) \frac{\partial K(x,a)}{\partial a} - K(x,a) \frac{\partial K(0,a)}{\partial a}}{[K(0,a)]^2} \quad (1.72)$$

Substitution of $\partial K(x,a)/\partial a$ (eq. (1.64)) and $\partial K(0,a)/\partial a$ (eq. (1.67)), in eq. (1.72) gives

$$\frac{\partial I_V(t-t_0,a)}{\partial a} = \frac{2 I_{V,0}}{K(0,a)} \left[x L(x,a) - \frac{1}{\sqrt{\pi}} \left[1 - \frac{K(x,a)}{K(0,a)} \right] \right] \quad (1.73)$$

e. with respect to α_L

The applied optimization method (Marquardt-Levenberg algorithm) does not require the partial derivative of the Voigt function with respect to α_L ; nevertheless, its expression is deduced in order to check the correctness of the expression published by Boumans [BouP89].

$$\frac{\partial I_V(t-t_0,a)}{\partial \alpha_L} = I_{V,0} \frac{\partial}{\partial \alpha_L} \frac{K(x,a)}{K(0,a)} = I_{V,0} \frac{K(0,a) \frac{\partial K(x,a)}{\partial \alpha_L} - K(x,a) \frac{\partial K(0,a)}{\partial \alpha_L}}{[K(0,a)]^2} \quad (1.74)$$

where

$$\frac{\partial K(x,a)}{\partial \alpha_L} = \frac{\partial K(x,a)}{\partial a} \frac{\partial a}{\partial \alpha_L} \quad (1.75)$$

In the last equation, $\partial K(x,a)/\partial a$ is given by eq. (1.64), and since a is defined by eq. (1.7), the following equation holds,

$$\frac{\partial a}{\partial \alpha_L} = \frac{\sqrt{\ln 2}}{\alpha_G} \quad (1.76)$$

Furthermore,

$$\frac{\partial K(0,a)}{\partial \alpha_L} = \frac{\partial K(0,a)}{\partial a} \frac{\partial a}{\partial \alpha_L} = \frac{\sqrt{\ln 2}}{\alpha_G} \frac{\partial K(0,a)}{\partial a} \quad (1.77)$$

Hence

$$\frac{\partial I_V(t-t_0,a)}{\partial \alpha_L} = I_{V,0} \left(\frac{1}{K(0,a)} \frac{\sqrt{\ln 2}}{\alpha_G} \frac{\partial K(x,a)}{\partial a} - \frac{K(x,a)}{[K(0,a)]^2} \frac{\sqrt{\ln 2}}{\alpha_G} \frac{\partial K(0,a)}{\partial a} \right)$$

or

$$\frac{\partial I_V(t-t_0,a)}{\partial \alpha_L} = \frac{2\sqrt{\ln 2}}{\alpha_G} \frac{I_{V,0}}{K(0,a)} \left[x L(x,a) - \frac{1}{\sqrt{\pi}} \left[1 - \frac{K(x,a)}{K(0,a)} \right] \right] \quad (1.78)$$

where the eqs (1.64) and (1.67) have been used.

The expression for the $\partial I_V(t-t_0,a)/\partial \alpha_L$ derived by Boumans [BouP89] is

$$\frac{\partial I_V(t-t_0)}{\partial \alpha_L} = 2 \frac{I_{V,0}}{K(0,a)} \frac{\sqrt{\ln 2}}{\alpha_G} \left(x L(x,a) + a K(x,a) - \frac{1}{\sqrt{\pi}} \right) \quad (1.79)$$

In this expression, Boumans neglected also the second term in the nominator of eq. (1.74), which is again related to $\partial K(0,a)/\partial a$.

1.5. Appendix B : Partial derivatives of the reduced sum function

The reduced sum function [FraR69] (eq. (1.29)) has the following partial derivatives with respect to the parameters $I_{RS,0}$, t_0 , α_{RS} , and f . Since the derivations of the expressions are elementary, only the final results are presented.

a. with respect to $I_{RS,0}$

$$\frac{\partial I_{RS}(t)}{\partial I_{RS,0}} = f \exp \left(- \ln 2 \left[\frac{2(t-t_0)}{\alpha_{RS}} \right]^2 \right) + (1-f) \left(1 + \left[\frac{2(t-t_0)}{\alpha_{RS}} \right]^2 \right)^{-1} \quad (1.80)$$

b. with respect to t_0

$$\frac{\partial I_{RS}(t)}{\partial t_0} = I_{RS,0} \left\{ \frac{8 \ln 2 f (t-t_0)}{\alpha_{RS}^2} \exp \left(-\ln 2 \left[\frac{2(t-t_0)}{\alpha_{RS}} \right]^2 \right) + \frac{8(1-f)(t-t_0)}{\alpha_{RS}^2 \left(1 + \left[\frac{2(t-t_0)}{\alpha_{RS}} \right]^2 \right)} \right\} \quad (1.81)$$

c. with respect to α_{RS}

$$\frac{\partial I_{RS}(t)}{\partial \alpha_{RS}} = I_{RS,0} \left\{ \frac{8 \ln 2 f (t-t_0)^2}{\alpha_{RS}^3} \exp \left(-\ln 2 \left[\frac{2(t-t_0)}{\alpha_{RS}} \right]^2 \right) + \frac{8(1-f)(t-t_0)^2}{\alpha_{RS}^3 \left(1 + \left[\frac{2(t-t_0)}{\alpha_{RS}} \right]^2 \right)} \right\} \quad (1.82)$$

d. with respect to f

$$\frac{\partial I_{RS}(t)}{\partial f} = I_{RS,0} \left(\exp \left(-\ln 2 \left[\frac{2(t-t_0)}{\alpha_{RS}} \right]^2 \right) - \left(1 + \left[\frac{2(t-t_0)}{\alpha_{RS}} \right]^2 \right)^{-1} \right) \quad (1.83)$$

Chapter 2

Evaluation of ASDAP

An extensive evaluation of ASDAP has been performed by Janssens [JanF93b]. However, in the present work, the analyses of numerous simulations were necessary in order to get an idea of the impact of some improvements and additions of ASDAP, like e.g. the use of analytical expressions for the partial derivatives of the Voigt and reduced sum functions, the implementation of the Humlicek algorithm for the calculation of the Voigt profile, the determination of minima in the convolution signals using a five-point quadratic derivative given by Gorry's modification of the Savitzky-Golay's algorithm, and some trial and error optimizations of the peak criteria and of the fitting procedure. It would be an impossible task to present this complete study here since that would require very long lists with numerical data. Instead, in the present chapter, the performance of ASDAP on special selected simulated data is shown in order to illustrate some specific features. The present study is basically divided into two parts as it is already the case in ASDAP. First, the procedures for determining the correct number of spectral lines are examined, resulting in the determination of the so-called '**spectral detection limit**' of ASDAP (Section 2.2.). Second, after illustration of the peak and interference detection for **complex multiplets** containing up to 6 lines, the fitting results are evaluated (Section 2.3.). Finally, the **influence of noise** on the final results is discussed in Section 2.4..

2.1. Simulation of spectra

The characteristics and mathematical representation of spectral lines have already been given in Chapter 1.

In our simulations, Humlicek's algorithm [HumJ79, HumJ82] has been used for the calculation of the individual spectral line profiles in multiplets, given the parameters ($I_{V,0}$, α_G , t_0 and a) for each line. These individual profiles are then summed in order to obtain the complete spectrum. In order to approximate the experimental situations as good as possible, and Gaussian distributed noise, generated by a random number generator [NAG87], has been introduced on the final spectrum..

2.2. Spectral detection limit

The key problem in spectral data analysis appeared to be the determination of the correct number of lines under a spectral envelop. The procedures incorporated in ASDAP for considering this point are the background correction, the peak and interference detection, and the grouping in multiplets. All these procedures are more or less based on the characteristics of the **R** and **S** signals. In Fig. 1.3, the **R** and **S** signals for a single Gaussian profile are shown. The question now is the following : how do **R** and **S** signals change for Voigt profiles with $a > 0$? Figs 2.1a,b show the convolution signals obtained from Voigt profiles with $I_0 = 10^4$ counts/channel, $\alpha_G = 10$ channels, $t_0 = 50$, and $a = 0.0, 0.4$ and 0.8 , with a zero-area Gaussian filter with $M_1 = \text{FWHM}_1 = 3$ channels. As the Voigt parameter a increases, the maximum intensity of the first order convolution signal **R** (Fig. 2.1a) diminishes, its width broadens, its negative side lobes are further displaced from the centroid t_0 and are less pronounced. The same trends can be seen for the **S** signal (Fig. 2.1b); moreover, the positive sidebands almost disappear as the Voigt parameter a approaches 0.8 . Shortly, it can be stated that the convolution signals loose their characteristic shape. This is caused by the broadening of the signal as the Voigt parameter increases. As a result, the characteristic M_1 of the zero-area Gaussian filter does not match the condition $0.25 \text{ FWHM}_s \leq M_1 \leq \text{FWHM}_s$ (see Section 1.3.4.).

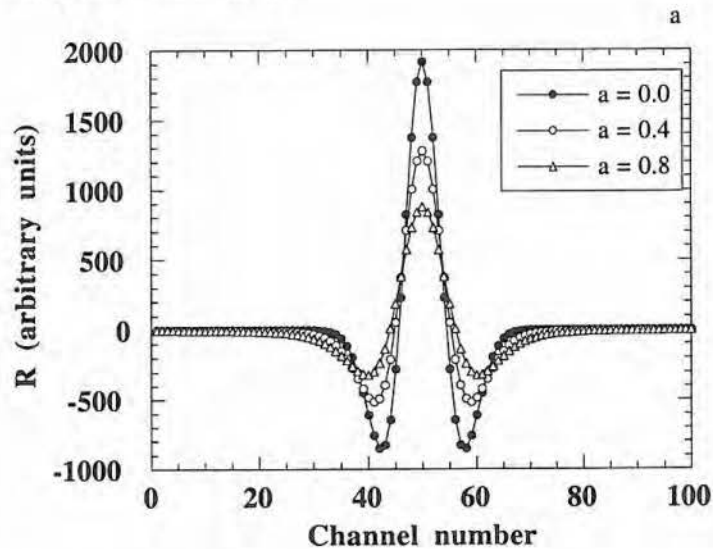


Fig. 2.1a : **R** signals obtained from Voigt profiles, with $I_0 = 10^4$ counts/channel, $\alpha_G = 10$ channels, $t_0 = 50$, and $a = 0.0, 0.4$ and 0.8 , with a zero-area Gaussian filter with $M_1 = \text{FWHM}_1 = 3$ channels.

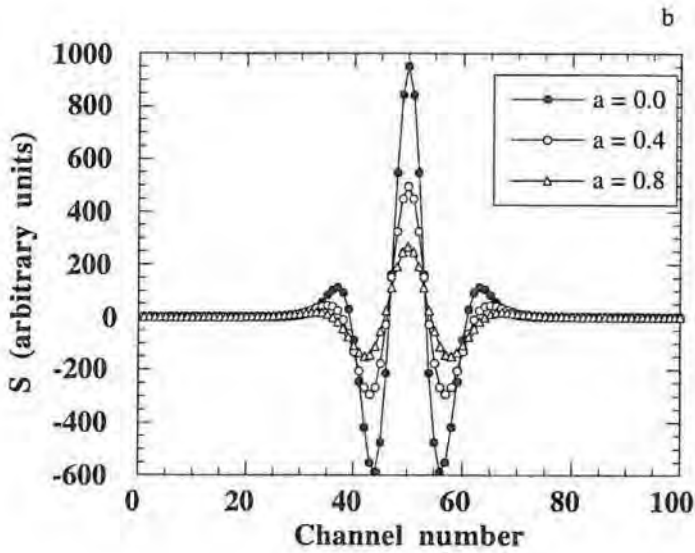


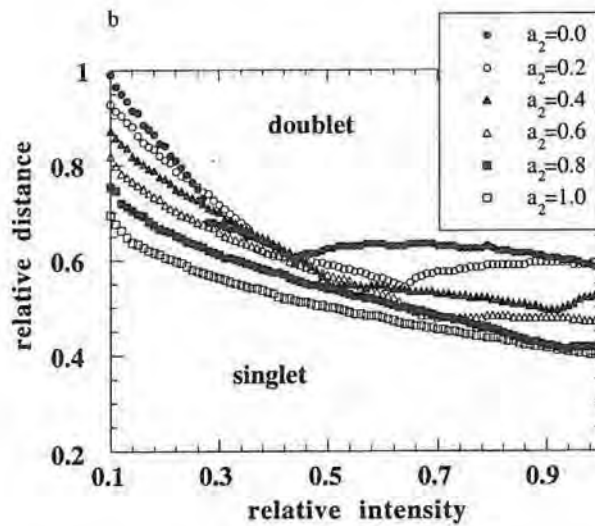
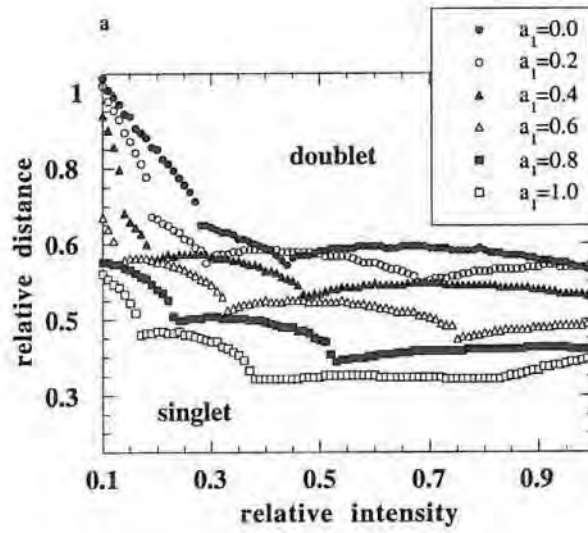
Fig. 2.1b : S signals obtained from Voigt profiles, with $I_0 = 10^4$ counts/channel, $\alpha_G = 10$ channels, $t_0 = 50$, and $a = 0.0, 0.4$ and 0.8 , with a zero-area Gaussian filter with $M_1 = \text{FWHM}_1 = 3$ channels.

The detection of interfering lines has been evaluated in an extensive simulation study in which two Voigt profiles approach each other in small steps until they are no longer distinguishable by the peak and interference detection procedures of ASDAP. The RSL analysis of ASDAP is not encountered here since this procedure is only used in special cases, i.e. when only a single line is detected. Two identical zero-area Gaussian filters are used with $M_1 = \text{FWHM}_1 = 3$ channels for the generation of the R and S signals.

Figs 2.2a-c show the limits for detection as a doublet or singlet in relation to the relative intensities $I_{0,2}/I_{0,1}$ and distances $\Delta_{1,2} = (t_{0,2} - t_{0,1})/\langle\alpha_V\rangle$ of two approaching lines with specified Voigt parameters. $\langle\alpha_V\rangle$ is the average full width at half maximum of both Voigt profiles.

$$\langle\alpha_V\rangle = \frac{\alpha_{V,1} + \alpha_{V,2}}{2} \quad (2.1)$$

The smallest relative distance when two approaching Voigt profiles can still be detected as a doublet is defined here as the spectral detection limit. It can be stated in general that if the relative intensity of the two lines diminishes, the distances between two centroids must be larger in order to resolve both lines.



Figs 2.2a,b : Spectral detection limits related to the relative intensities $I_{0,2}/I_{0,1}$ and relative distances $\Delta_{1,2} = (t_{0,2} - t_{0,1}) / \langle \alpha_V \rangle$ of the two peaks with fixed shapes :
 (a) the approach of a Gaussian line towards a Voigt profile,
 (b) the approach of a Voigt profile towards a Gaussian one.

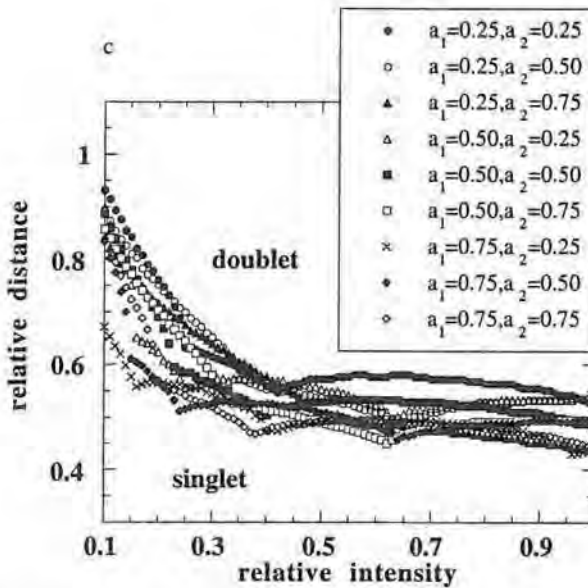
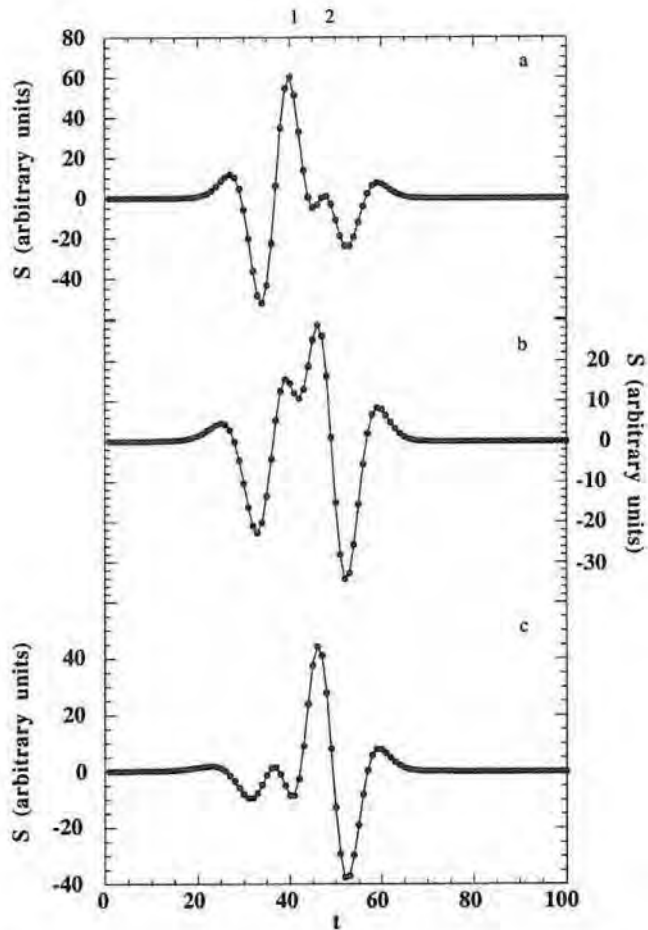


Fig. 2.2c : Spectral detection limits related to the relative intensities $I_{0,2}/I_{0,1}$ and relative distances $\Delta_{1-2} = (t_{0,2} - t_{0,1})/\langle\alpha_V\rangle$ of the two peaks with fixed shapes :
(c) the approach of two Voigt profiles.

Fig. 2.2a shows the spectral detection limits for the approach of a Gaussian line towards Voigt profiles with increasing Voigt parameters. For $a = 0.0$ and a relative intensity larger than 0.3, the spectral detection limits are between 0.6 and 0.7. Since the Voigt parameter alters especially the wings of the profile, it could be expected that a larger Lorentz contribution in the profile would deteriorate the spectral detection limit. However, it can be seen that for larger a values, the Gaussian line can approach the Voigt profile closer before they cannot be resolved. For $a = 1.0$ and a relative intensities larger than 0.3, the spectral detection limits are between 0.3 and 0.4.

The explanation is found by considering the S signals. Figs 2.3a-c show the S signals obtained in the analysis of doublets with characteristics : $I_{0,1} = 1000$ counts/channel, $I_{0,2} = 600$ counts/channel, $\alpha_{G,1} = \alpha_{G,2} = 10$ channels, $t_{0,1} = 40$, $t_{0,2} = 46.5$, $a_1 = 0.0$ (a), 0.4 (b), 0.8 (c), and $a_2 = 0.0$. The second order convolution spectra change as follows : a clear maximum at position 1 in Fig. 2.3a ($a_1 = 0.0$) changes to a doublet (1 and 2) in Fig. 2.3b ($a_1 = 0.4$) and finally to a distinct maximum at position 2 in Fig. 2.3c ($a_1 = 0.8$). This can be attributed to a reduction of the S signals at position 1 in Figs 2.3a-c for increasing Voigt parameters. This effect has already been shown in Fig. 2.1b. As a consequence ASDAP has to evaluate S spectra with different relative maxima for the same relative

intensities $I_{0,2}/I_{0,1}$ and distances Δ_{1-2} . In Fig. 2.3a, the S signal for the second line is very small compared to the first and can hardly be distinguished by ASDAP. Therefore the spectral detection limit is almost reached. On the other hand, in Fig. 2.3c, the S signal for the first peak is still large enough to be detected by ASDAP, so that the spectral detection limit will occur at lower relative distances for the same relative intensity as compared to two Gaussian peaks.



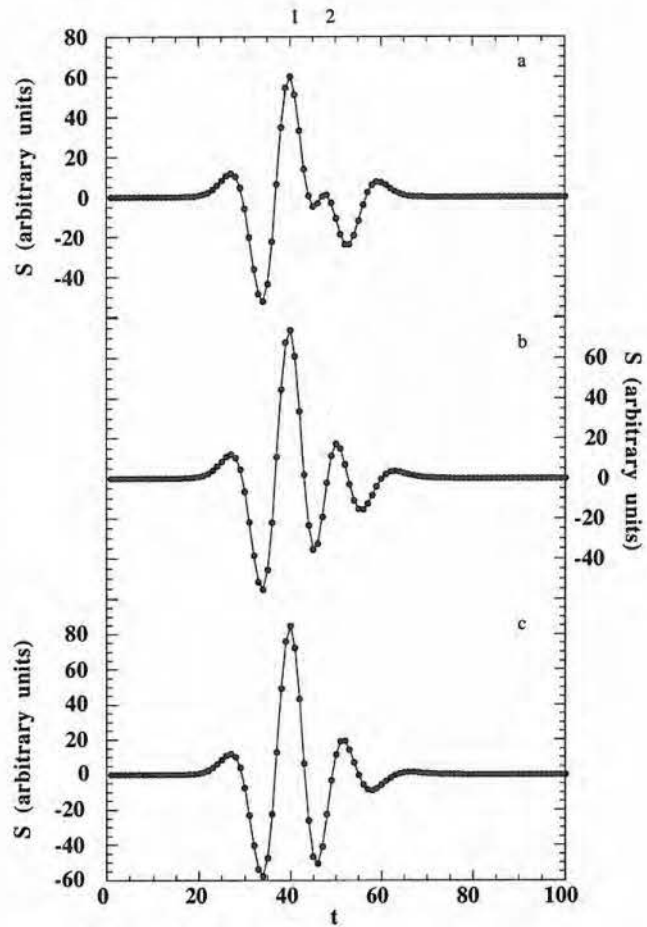
Figs 2.3a-c : S signals of doublets with characteristics $I_{0,1} = 1000$ counts/channel, $I_{0,2} = 600$ counts/channel, $\alpha_{G,1} = \alpha_{G,2} = 10$ channels, $t_{0,1} = 40$, $t_{0,2} = 46.5$, $a_1 = 0.0$ (a), 0.4 (b), 0.8 (c), and $a_2 = 0.0$.

Fig. 2.2b shows the doublet and singlet detection limits for the approach of a Voigt profile towards a Gaussian one. The improvements in detection limits for higher Voigt parameter are less pronounced than in Fig. 2.1a.

Figs 2.4a-c show the S signals obtained in the analysis of doublets with the following characteristics : $I_{0,1} = 1000$ counts/channel, $I_{0,2} = 600$ counts/channel, $\alpha_{G,1} = \alpha_{G,2} = 10$ channels, $t_{0,1} = 40$, $t_{0,2} = 46.5$, $a_1 = 0.0$, and $a_2 = 0.0$ (a), 0.4 (b), 0.8 (c). It can be seen that the maximum at position 2 coincides with the minimum of the line at position 1. The intensities of the S signals at the centroids of Voigt profiles decrease for increasing a parameters; at the same time their FWHM enlarges (see behavior in Fig. 2.1b). However, this effect does not drastically change the global shape of the S spectra (Fig 2.4a-c) which have to be analyzed by ASDAP. The second order convolution spectra have all a clear maximum at position 1 and a small maximum at position 2 (located at the minimum of the right of the first line) moving to higher channel numbers for increasing Voigt parameters. Therefore, the Voigt profile can approach the first Gaussian line closer before they are detected as a single line.

In Fig. 2.2c, the spectral detection limits are depicted for the approach of two Voigt profiles. It can be stated that the interference of small peaks ($I_{0,2} = 0.1 I_{0,1}$) can be detected if the relative distances between the peaks are 0.7 - 1.0. More intense interfering lines ($I_{0,2} > 0.4 I_{0,1}$) are already detected at relative distances of 0.5 - 0.6.

It can be concluded that the higher the values of the Voigt parameters of the two approaching profiles, the further these lines can approach each other before they will be detected by ASDAP as one signal.



Figs 2.4a-c :S signals of doublets with characteristics $I_{0,1} = 1000$ counts/channel, $I_{0,2} = 600$ counts/channel, $\alpha_{G,1} = \alpha_{G,2} = 10$ channels, $t_{0,1} = 40$, $t_{0,2} = 46.5$, $a_1 = 0.0$, and $a_2 = 0.0$ (a), 0.4 (b), 0.8 (c).

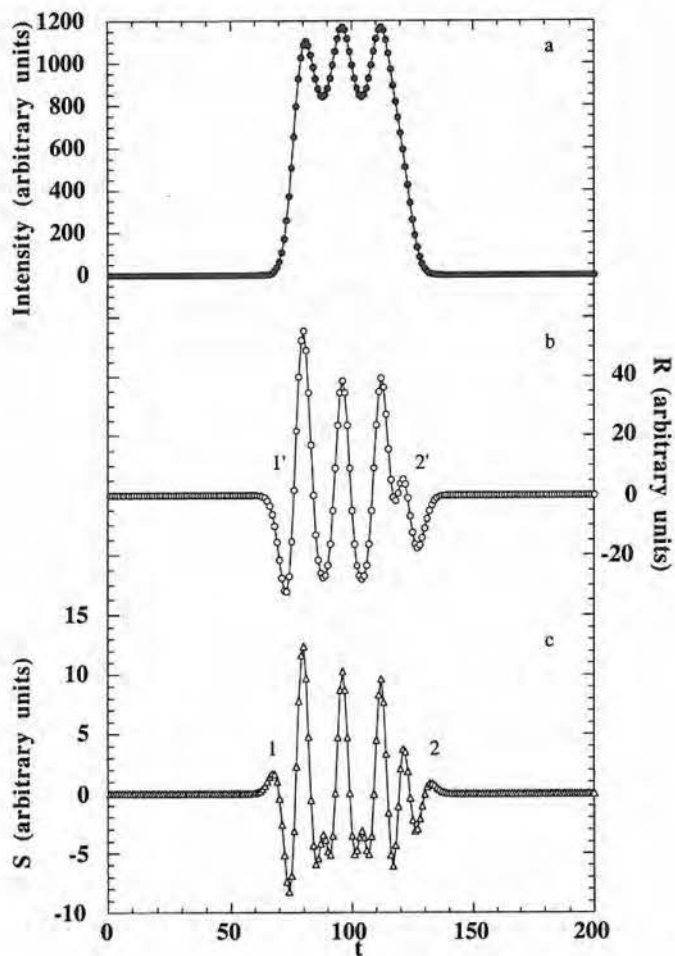
2.3. Qualitative and quantitative analysis of multiplets

The spectral detection limits of ASDAP are related to the minimum distances for which two neighboring lines can still be resolved. In spectral data analysis, more complex situations can occur in which many lines belong to the same multiplet. Visually, the interference on a singlet can easily be detected by inspecting the (asymmetric) shape of the profile. In a multiplet, the number of inflection points divided by two can give an indication for the minimum number of spectral lines present under the envelop. However, small peaks may be hidden between larger ones and are therefore not detected. The resolution enhancement procedures incorporated in ASDAP are then required. This is illustrated in the analysis of a simulated multiplet with six Gaussian lines; the parameters of each peak are stated in Table 2.1.

Table 2.1 : Input parameter for the simulation of the multiplet with six Gaussian lines

peak	I_0 counts/channel	α_G channels	t_0
1	1000	10	80
2	500	10	88
3	1000	10	96
4	500	10	104
5	1000	10	112
6	500	10	120

Figs 2.5a-c show the original multiplet (a) and the convolution signals **R** (b) and **S** (c) obtained with zero-area Gaussian filters with $M_1 = FWHM_1 = 3$ channels. The first order convolution signal **R** has three large maxima at channel numbers 80, 96, 112, and a small one at position 120. The **S** signal consists of the same three large maxima and two small ones located between them at channel numbers 88 and 104; a pronounced maximum at position 120 can also be seen. The side bands (1 and 2) of the first and last lines in the **S** signal are eliminated because they are further removed from the centroid than the side lobes (1' and 2') in the **R** signal (see Section 1.3.4.). The peak and interference detection procedures of ASDAP were able to determine the correct number of lines as well as their positions.



Figs 2.5a-c : Multiplet (a) with 6 Gaussian profiles (parameters are presented in Table 2.1) and the convolution signals **R** (b) and **S** (c) obtained with a zero-area Gaussian filter with $M_1 = FWHM_1 = 3$ channels.

The quantification (with the fitting procedure) proceeds in each multiplet separately. Each line in a multiplet, detected in the peak and interference procedures, is quantified by fitting a model function to the background corrected data using the Marquardt-Levenberg algorithm [MarD63, LevK44]. The parameters of the model function for a line

(centroid t_0 , intensity I_0 at this centroid, FWHM, and a lineshape parameter) are estimated using information from the convolution signals and Zimmermann's method (see Chapter 1). Since the direct optimization using the Voigt profile is very sensitive to the initial estimates of the parameters, a previous fitting is done with the reduced sum function (eq. 1.29). The optimized values for the parameters of the reduced sum function are transformed (eqs 1.35 - 1.39) into more accurate starting values for the Voigt function (eq. 1.13) and a second optimization is started. As an example the multiplet of six lines, mentioned above, is fitted with the reduced sum and Voigt functions over a channel number range 50 to 150.

The optimized parameters for both optimizations are given in Tables 2.2 and 2.3, together with the relative error (%), defined as follows.

$$RE(\%) \equiv \frac{\text{Surface of the fitted line} - \text{Surface of the simulated line}}{\text{Surface of the simulated line}} \quad (2.2)$$

(range : $t_0 \pm 10$) (range : $t_0 \pm 10$)

With the reduced sum function, large relative errors are obtained for the contributions of the third and fourth peak. The results of the fitting with the Voigt function are much better.

2.4. Influence of noise

The influence of noise has been evaluated for Voigt doublets. The parameters of the simulated lines are : $I_{0,1} = 1000$ counts/channel, $I_{0,2} = 500$ counts/channel, $\alpha_{G,1} = \alpha_{G,2} = 10$ channels, $a_1 = 0.5$, and $a_2 = 0.25$. The positions of the centroids depend on the relative distance $\Delta_{1,2}$ between the two lines as follows.

$$t_{0,2} - t_{0,1} = \Delta_{1,2} \langle \alpha_V \rangle \quad (2.3)$$

For each $\Delta_{1,2}$ (given in Table 2.4), 10 spectra are analyzed that have been generated by a superposition of 3% noise with a pseudo random generator (see Section 2.1) [NAG87] on the same basic noise-free doublet. The individual spectra are analyzed using ASDAP and the RE's and relative standard deviations (RSD's) of the areas of each line are calculated (Table 2.4). The model function used in the fitting procedure is the reduced sum function. As a reference, the results that are obtained from the same spectrum in the absence of noise and under the same analysis conditions (filter, fitting area, smoothing and model function) are also presented. In all cases, ASDAP could retrieve the two components and optimize their parameters. Only for small relative distances, the presence of noise has an effect on the RE(%) of the areas under the individual lines. On the other hand, the results show that the

RSD(%) of the results, representing the precision of the method, are more affected than the RE(%) of the results, representing the accuracy. This indicates that reliable results can be obtained for rather noisy spectra when repeated data under the same conditions are available.

Table 2.2 : Results obtained from the Marquardt-Levenberg algorithm using the reduced sum function as model function

peak	I_0 counts/channel	α_{RS} channels	t_0	f	RE (%)
1	998.972	10.008	80.007	1.000	-0.02
2	525.733	10.204	88.262	1.000	+7.07
3	888.036	9.553	95.804	0.997	-14.94
4	586.865	11.748	103.753	1.000	+34.57
5	932.119	9.805	112.182	0.982	-8.32
6	504.933	10.041	119.925	1.000	+1.14

Table 2.3 : Results obtained from the Marquardt-Levenberg algorithm using the Voigt function as model function

peak	I_0 counts/channel	α_G channels	t_0	a	RE (%)
1	1007.770	10.059	80.060	0.000	+1.32
2	507.904	9.810	88.230	0.021	+1.19
3	971.263	9.749	95.948	0.000	-5.31
4	514.461	10.137	103.694	0.000	+4.03
5	1008.996	10.094	111.985	0.001	+1.54
6	493.054	9.972	120.051	0.000	-1.64

Table 2.4 : Fitting of simulated Voigt doublets with the reduced sum function

Δ_{1-2}	without noise		with 3% noise			
	RE(%)		RE(%)		RSD(%)	
			line 1	line 2	line 1	line 2
0.948	+0.5	-0.1	-0.2	-0.3	2.7	7.2
0.869	-0.02	+1.1	-0.5	+0.4	3.6	9.4
0.790	-1.3	+4.1	-1.7	+2.8	5.4	13.6
0.711	-4.3	+10.7	-1.9	+4.1	7.7	18.1
0.632	+1.9	-4.0	-8.2	+18.3	6.6	11.8

2.5. Conclusions

The peak and interference detection techniques and the fitting procedures incorporated in ASDAP are evaluated individually using simulated spectra.

The evaluation of the peak and interference detection procedures, based on the construction of the first and second order convolution signals using zero-area Gaussian filters, resulted in the definition and visualization of an important characteristic of ASDAP, namely the ability of determining the exact number of lines under a spectral envelop. This characteristic is expressed in terms of the so-called spectral detection limit defined as the smallest relative distance when two approaching Voigt profiles with a specific relative intensity can still be detected as a doublet. For the approach of two Voigt profiles in a doublet, it can be stated that the interference of small peaks on large ones ($I_{0,2} = 0.1 I_{0,1}$) can be detected if the relative distances between the peaks are 0.7 - 1.0. More intense interfering lines ($I_{0,2} > 0.4 I_{0,1}$) are already detected at relative distances of 0.5 - 0.6. Furthermore, it has been found that the higher the values of the Voigt parameters of the two approaching profiles, the further these lines can approach each other before they will be detected by ASDAP as a single signal.

The qualitative evaluation of a complex multiplet with six interfering lines showed that the peak and interference detection procedures of ASDAP were able to determine the correct number of lines as well as their positions.

The multiplet with six interfering lines, mentioned above, has also been used for the evaluation of the fitting procedures incorporated in ASDAP. The influence of the model function has been studied and it has been found that the results obtained with the Voigt function were much better than those obtained with the reduced sum function.

The influence of noise on the quantitative results is also studied. It has been observed that reliable results could be obtained for rather noisy spectra (3%) when repeated data under the same conditions are available.

Chapter 3

Qualitative and quantitative applications

3.1. IR spectrometry of small carbon clusters trapped in noble gas matrices

Carbon clusters have been the subject of extensive theoretical and experimental studies, even before the discovery of the fullerene [CurR97, KroH97, Smar97, DreM96], due to their importance in many fields such as astrophysics, material science and combustion processes [WelW89, WelW90, KroH91, KroH92]. As early as 1971, Thompson, DeKock and Weltner (TDW) [ThoK71] recorded IR spectra in an argon matrix and attempted assignments of bands to specific linear C_n ($3 \leq n \leq 9$) species. Subsequent, quantum chemical calculations have shown that the TDW assignments should be completely revised. Many of these new assignments have been confirmed experimentally by FTIR spectroscopy and high-resolution tunable diode laser IR spectroscopy (a complete list of references is presented in Table 3.1). Still several IR features are left unassigned.

The search for new assignments was preceded by extensive theoretical and experimental studies to reveal the ground state structures of the carbon clusters. Some general conclusions can be drawn. The small odd-numbered clusters of C_3 to C_9 (Fig. 3.1) exist exclusively as cumulenic linear chains, whereas the even-numbered clusters of C_4 , C_6 and C_8 (Fig. 3.2) have nearly isoenergetic structural isomers : a linear chain and a planar monocyclic ring for C_6 and C_8 [MarJ96a] and a rhombic structure for C_4 [MarJ96b]. From C_{10} onwards the cyclic form appears to have a lower energy with respect to the linear, as already predicted by Hoffmann [HofR66] in 1966. Ab initio studies [MarJ95a] show that the even numbered C_n species can be divided in two groups : the C_{4n+2} clusters ($1 \leq n \leq 4$) have cumulenic structures (like C_6 and C_{10} in Fig. 3.2) and the C_{4n} ($2 \leq n \leq 4$) have polyenyic structures (like C_8 in Fig. 3.2). The structure (linear or cyclic) with lowest energy could not be identified unambiguously for odd C_n species in the range $n=11-13$ [MarJ91c, BleR94, GieT94, VonG93a, SlaZ92a, SlaZ94]. Very recently, Martin et al. [MarJ96c] concluded in their study of the structures and relative energetics of C_{2n+1} ($n=2-7$) species that from C_{11} onwards, these molecules prefer cyclic structures and that no indication appears to exist for the presence of either cyclic C_7 and C_9 or linear C_{11} and C_{13} in matrix

IR spectra of graphite vapor. Ion mobility measurements indicate that a rich variety of structures begins to form above C_{20} , including planar monocyclic and polycyclic rings [BowM93, VonG93b, VonG93c].

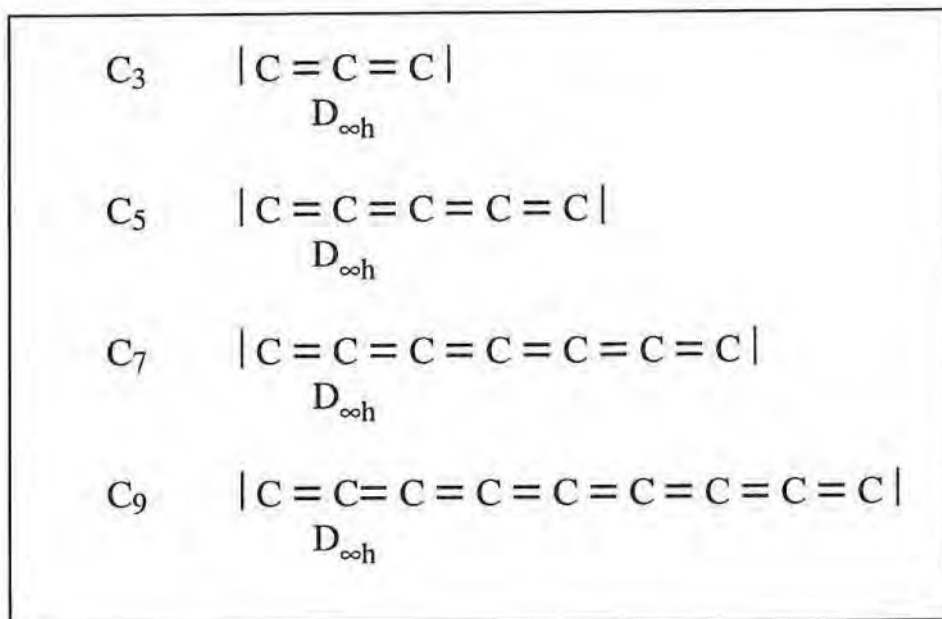


Fig. 3.1 : Structures of small odd-numbered clusters of C_3 to C_9 : cumulenenic linear chains (${}^1\Sigma_g^+$ ground states).

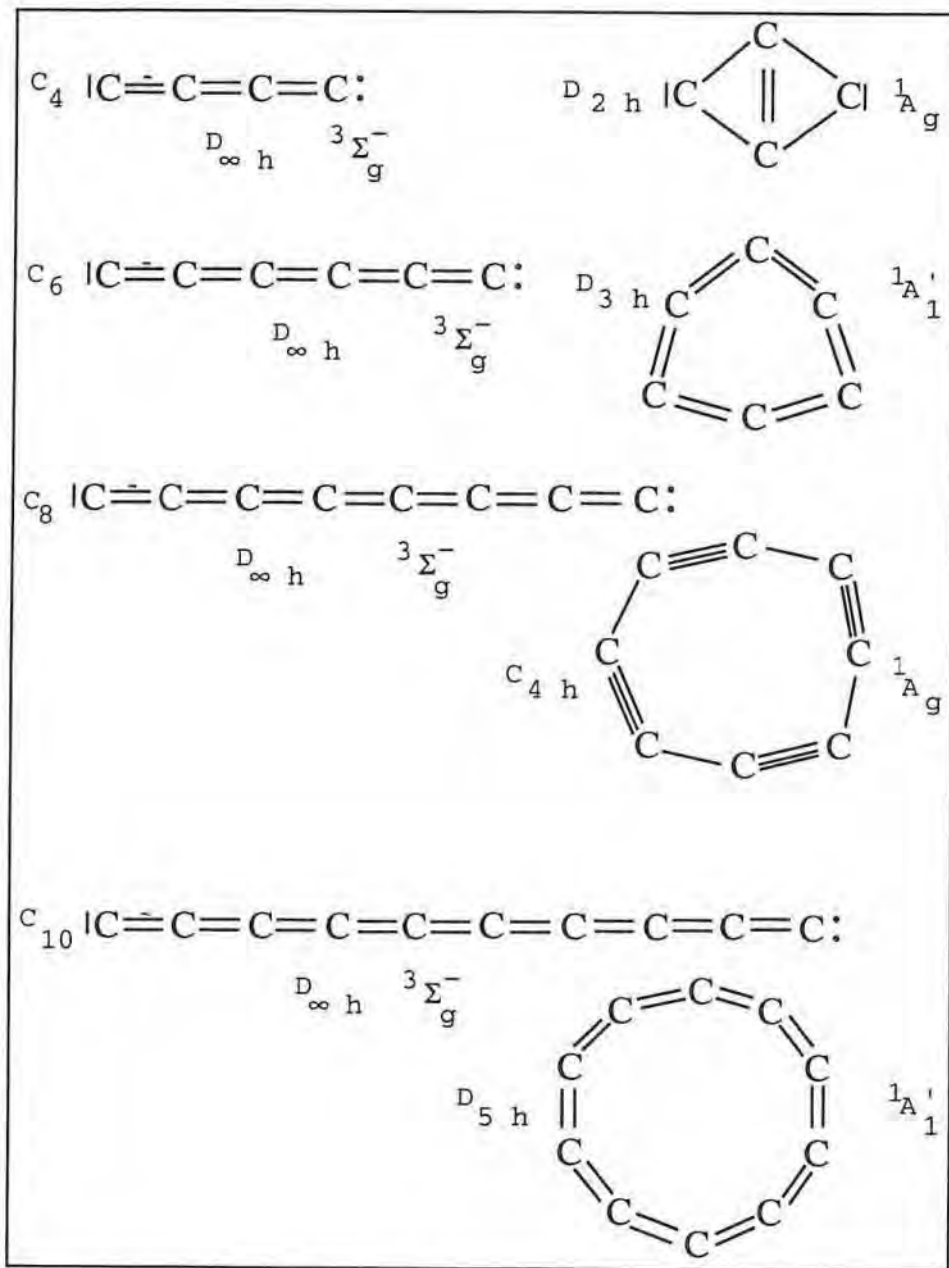


Fig. 3.2 : Structural isomers of the even-numbered clusters C_4 to C_{10} : cumulenlic linear chains and planar monocyclic rings C_6 to C_{10} ; cyclic C_4 shows a rhombic structure.

Table 3.1 : Overview of the IR features in the 1150-2280 cm^{-1} range, together with the TDW assignments and the latest revisions

Wave-number (cm^{-1}) ^(a)	TDW [ThoK71] assignment	Revised assignment *	Quantum chemical calculations	FT IR	Tunable diode laser IR	IR
1197	C ₆	C ₆ (l)	MarJ91a MarJ90a	KraR93a		
1284		C ₄ (c)	MarJ91b WatJ92 MarJ96b			
1346		?				
1447	C ₉	C ₅ (l)	MarJ96a BotP89	KraR92		
1477		?				
1489		?				
1544	C ₅	C ₄ (l)	MarJ96a MarJ95a MicD87 BerD88	SheL89	HeaJ91a	
1578						
1590		C ₉ (l) ^{†*}	MarJ96a MarJ95a	KraR95		
1601						
1695		C ₆ (c)*	MarJ96a	PreJ97 WanS97		
1715		C ₁₁ (c)* C ₈ (l)*	MarJ91c MarJ96a MarJ95a HutJ94			SzcJ96
1747		?				
1804		C ₁₁ (c)*	MarJ91c MarJ95b			
1818		C ₁₀ (c)* C ₁₁ (l)* C ₈ (c)*	MarJ91c MarJ95b MarJ96a MarJ95a			
1844		C ₁₁ (c)*	MarJ91c MarJ95b			
1896	C ₉	C ₇ (l)	MarJ91 MarJ90a	KraR96	HeaJ91b HeaJ91c	

Wave-number (cm ⁻¹) ^(a)	TDW [ThoK71] assignment	Revised assignment •	Quantum chemical calculations	FT IR	Tunable diode laser IR	IR
1915		C ₇ (c) C ₁₀ (c)*	SlaZ92a MarJ96a MarJ96b			
1921		C ₁₈ (c)*	MarJ95a			
1947		C ₁₄ (c)*	MarJ95a			
1952	C ₅	C ₆ (l)	MarJ90a MarJ91 MarJ95a MarJ96a	ValM90a KraR93b		
1999	C ₆	C ₉ (l)	MarJ90a MarJ91 MarJ95a MarJ96a		HeaJ90b HeaJ93	
2036		?				
2041	C ₃	C ₃ (l)			MatK88	WeiW64
2053		C ₅ ⁺ (c)#		ValM90a		
2053-2080		C ₈ (l), C ₉ (l) ‡*	MarJ95a MarJ96a MarJ96b			
2128	C ₉	C ₇ (l)	MarJ90a MarJ91 MarJ95a MarJ96a	KraR96	HeaJ90b HeaJ91b	
2164	C ₄	C ₅ (l)	MarJ89 BotP89	ValM89	MoaN89a MoaN89b HeaJ89	
2180-2214		?				
2218-2227		?				
2247		?				
2253		?				

(a) In a solid Ar matrix

• (l) linear, (c) cyclic ; * tentatively ; # probably not correct ;
‡ one band in the multiplet is assigned to this specific carbon cluster species

Over the past several years, great attention has been devoted to the question : "Which is the smallest stable fullerene?". A fullerene is defined as a closed trivalent C_n cage containing only pentagonal and hexagonal rings. It can be shown that the number of pentagons is 12 and the number of hexagons $n/2 - 10$. The smallest possible fullerene is C_{20} containing only 12 pentagons. The relative energies of the bowl, ring and cage structures (Fig. 3.3) of C_{20} are considered in many theoretical studies [ParV91, SlaZ92b, BraC92, RagK93, TayP95, GroJ95, MarJ96d]. In the most recent study [MarJ96d], it has been found that the corannulene like bowl structure is the lowest in energy. However, a fullerene structure is quite close in energy [ParV91, SlaZ92b, BraC92, RagK93, TayP95, GroJ95, MarJ96d].

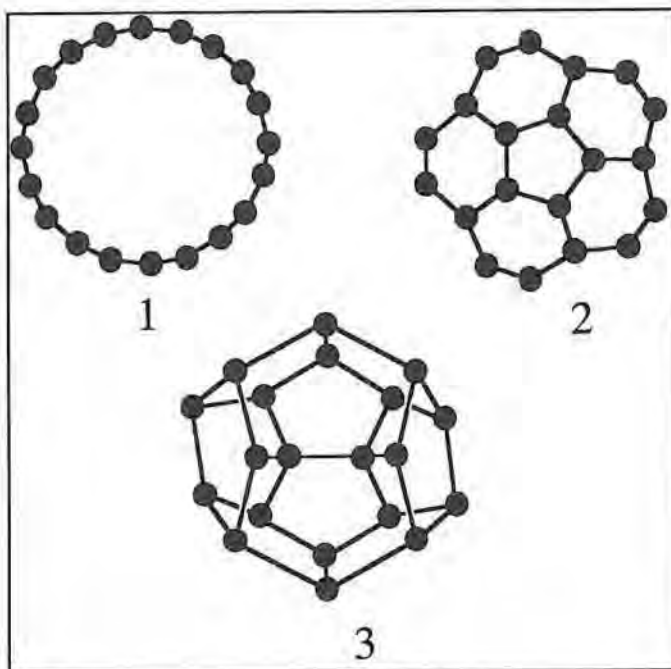


Fig 3.3. : Ring (1), bowl (2) and cage (3) structures of C_{20} .

Seven possible structures of C_{24} (Fig. 3.4) [see [MarJ96e] and references therein] are investigated : a coronene like planar sheet, a monocyclic and bicyclic ring, two kinds of corannulene like bowl structures and fullerenes. Martin et al. [MarJ96e] concluded that the coronene like planar sheet (which corresponds to a graphite sheet fragment) and a D_6 fullerene cage are comparable in energy, followed by a polyenyic ring and a bowl structure derived from the C_{20} bowl by adding an extra 6-ring to it. At high temperatures, the ring will benefit from its high vibrational entropy.

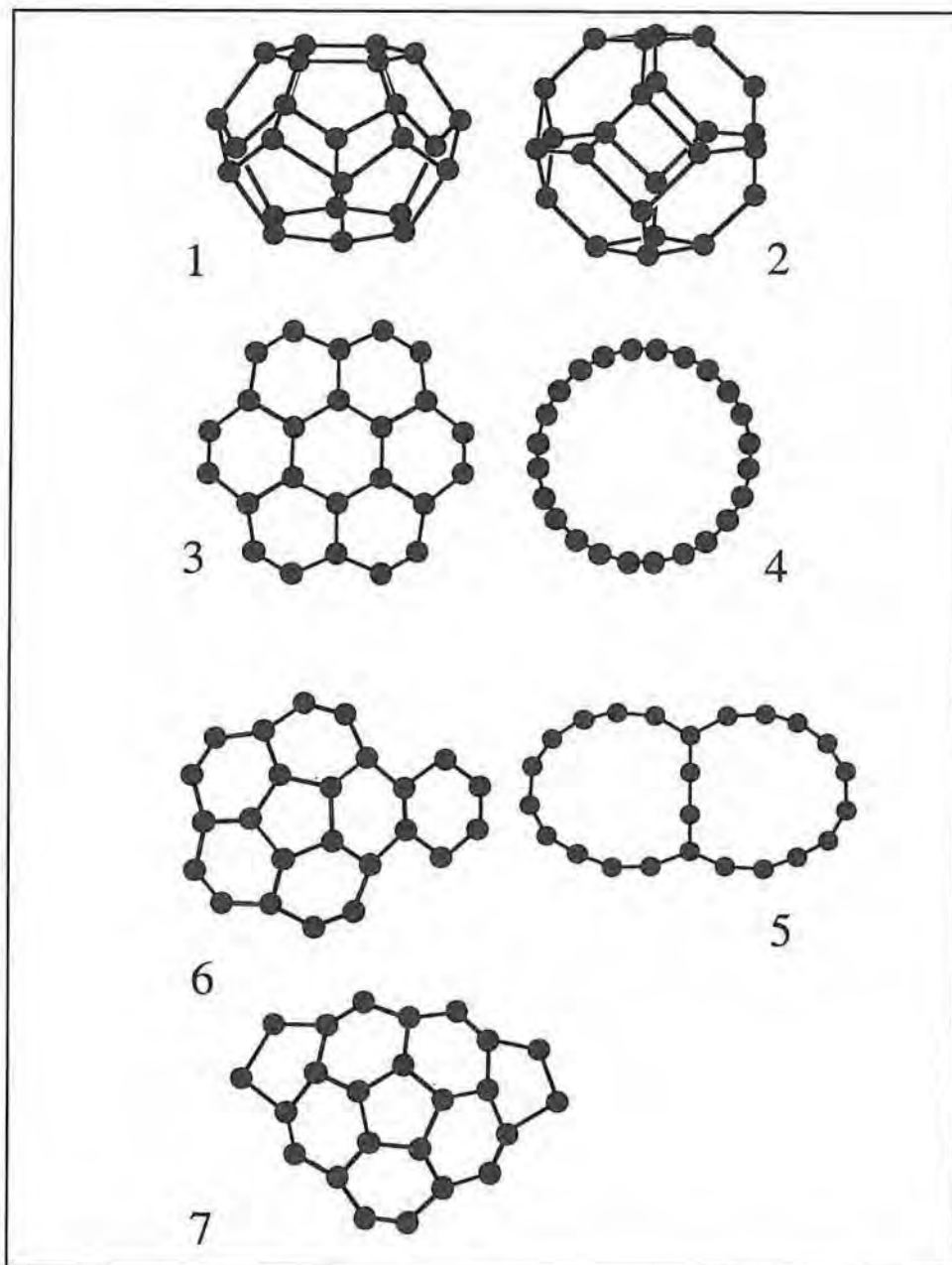


Fig 3.4. : Seven possible structures of C_{24} : two kinds of fullerenes (1 , 2), a coronene like planar sheet (3), a monocyclic (4) and bicyclic (5) ring, and two kinds of corannulene like bowl structures (6 , 7).

Experimentally, $U@C_{28}$ fullerene has been observed by using a cluster FT-ICR apparatus [GuoT92]. Kroto [KroK87] proposed a fullerene like structure in 1987. Feyereisen et al. [FeyM92] found the ring and fullerene structures to be of comparable energy. Very recently, quantum chemical calculations of Martin [MarJ96f] pointed out that the fullerene structure (Fig. 3.5) is the most stable structure, followed by a graphite sheet fragment and a ring structure.

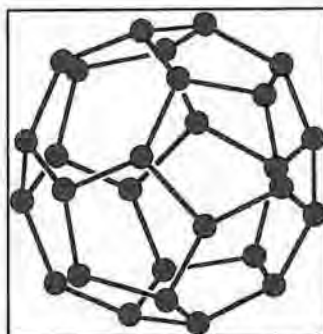


Fig. 3.5. : C_{28} fullerene structure.

It should be mentioned that the frequencies obtained from quantum chemical methods are usually harmonic ones. They differ from experimental frequencies, measured in the gas phase (e.g. by tunable diode laser IR spectroscopy) by anharmonicity contributions. IR frequencies resulting from measurements of C_n species, trapped in noble gas matrices, deviate from those in the gas phase by the following effects : (i) interactions of the C_n species with the matrix, and (ii) spectral shifts due to the solid matrix. It can be found that by plotting ν (quantum theory) versus ν (solid matrix) for features were an exact assignment could be made (e.g. C_2 ($^1\Sigma_g^+$) 1828; C_2 ($a^3\Pi_u$) 1641; C_3 (lin) 2039; C_4 (lin) 1544; C_7 (lin) 1895, 2128 cm^{-1}) a linear relationship exists. These relationships have been used in quantum chemical studies establishing a number of assignments (see Tabel 3.1).

Since a large variety of structures of small carbon clusters exist, a complex IR spectrum of carbon vapor can be expected. Krätschmer and Nactigall [KraW87, NacK87] published an interesting study on the IR spectra of carbon species trapped in noble gas matrices (Ar and Kr). The spectra in Ar have been recorded at 13, 30 and 35 K (annealing

experiments were carried out at the two last temperatures). Carbon of natural isotopic abundance was used in the experiments. Their background corrected IR spectra were put at our disposal in digitized form. These IR spectra are characterized by a large number of lines and by excessive overlapping of bands in certain spectral regions.

In the present section, the complete quantitative analysis of these recorded spectra is discussed in detail in Sections 3.1.3 (Ar) and 3.1.4. (Kr). The spectra are analyzed by using the ASDAP program. The assignments of the IR bands to specific C_n cluster species are based on data obtained from quantum chemical computations and from tunable diode laser IR spectroscopy of C_n species in the gas phase as referred to in the literature. The growth behavior of some spectral features and the influence of the matrix are discussed.

3.1.1. Experimental set-up

The technique used by Krätschmer and Nachtigall [KraW87, NacK87] to isolate larger carbon molecules in matrices is as follows : initially, the lighter molecules of carbon vapor (i.e. C, C_2 and C_3) are trapped in an inert matrix. Upon thermal annealing, the lighter species start to diffuse through the matrix and to react with each other, e.g. according to $C_m + C_n = C_{m+n}$. One finally obtains a mixture of matrix isolated heavy carbon molecules.

Experimentally, carbon molecules has been produced by a carbon evaporator (resistively heated carbon rods) and deposited along with the matrix gas (purity Ar : 99.9999%, Kr : 99.99%) onto a cryogenically cooled KBr window. The initial temperature of the window is 15K and is raised to 25-35K for the annealing process. The matrix deposition rates ranged between 1.5 and 4 $\mu\text{m}/\text{min}$. The amount of carbon evaporated is derived from the thickness of the film cooled on the observation window, The manually controlled burning and thus the carbon evaporation is not very steady. The derived concentrations of carbon in the matrix are average values and may be in local regions significantly higher than the average (between 0.1 and 1 mol%) suggests. After the sample deposition, a first IR spectrum is recorded using a Beckmann IR 11 spectrometer in the spectral range of 650 to 2015 cm^{-1} , and a second one in the range of 1980 to 4000 cm^{-1} ($\Delta x = 0.5 \text{ cm}^{-1}$). The IR spectra are characterized by a large number of lines and by excessive overlapping of bands in certain spectral regions. Then, the matrix is warmed up until changes in the absorption features could be noticed, re-cooled again to the initial temperature, and the next spectrum recorded. They are characterized by an increase or decrease of the intensities of specific spectral lines, or even by the appearance of new IR features.

The data handling (Section 3.1.2.) of these spectra consists of the merging of the two spectral regions, the background correction and the final qualitative and quantitative analysis. The first two steps were already performed by Krätschmer and Nachtigall.

3.1.2. Data handling

The spectrometer provides three kinds of data for each spectral range (I : 650 - 2015 cm^{-1} , II : 1980 - 4000 cm^{-1}), i.e. the measured signal of the sample at each wavelength (x_i, y_i), the reference signal of the KBr pellet (x_r, y_r), and the background signal measured with closed slits (x_0, y_0). In a first step, the absorbance a_i at each x_i is calculated as

$$a_i = -\log \frac{y_i - y_0}{y_r - y_0} \quad (3.1)$$

Thus, two new data sets ($x_i, a_{i,I}$) and ($x_i, a_{i,II}$) are created, one for each spectral range. These are now merged using the following algorithm :

- 1) Search of the mean value C of the difference between the signals of both data sets in each point of the region 1980 - 1990 cm^{-1} ($\Delta x = 0.5 \text{ cm}^{-1}$), i.e.

$$C = \frac{\sum (a_{i,I} - a_{i,II})}{21} \quad (3.2)$$

- 2) Calculation of

$$A_{i,I} = a_{i,I} + C \quad \text{for } x_i \leq 1980 \text{ cm}^{-1} \quad (3.3a)$$

$$A_{i,II} = a_{i,II} \quad (3.3b)$$

- 3) Collection of these corrected absorbances in one data set (x_i, A_i).

In the background correction procedure, a maximum of fifteen reference channels x_i is chosen randomly. In the region ($x_i \pm 20$) around each of these data points, minima are selected after three smoothings [GorP90, SavA64] of the data (x_i, A_i). A polynomial of degree 3 is fitted in each of the regions between these minima. For example, in the interval $[x_{\min,i}, x_{\min,i+1}]$, the functional form of the fitted polynomial is obtained by first calculating the variables

$$AF = 0.5 [A(x_{\min,i}) + A(x_{\min,i+1})] \quad (3.4)$$

$$DF = 0.5 [A(x_{\min,i}) - A(x_{\min,i+1})] \quad (3.5)$$

$$S_i = 0.5 \{ [A(x_{\min,i+1}) - A(x_{\min,i})] / [x_{\min,i+1} - x_{\min,i}] + [A(x_{\min,i}) - A(x_{\min,i-1})] / [x_{\min,i} - x_{\min,i-1}] \} \quad (3.6)$$

$$S_{i+1} = 0.5 \{ [A(x_{\min,i+2}) - A(x_{\min,i+1})] / [x_{\min,i+2} - x_{\min,i+1}] \\ + [A(x_{\min,i+1}) - A(x_{\min,i})] / [x_{\min,i+1} - x_{\min,i}] \} \quad (3.7)$$

$$\text{AFS} = 0.5 (S_i + S_{i+1}) \quad (3.8)$$

$$\text{DFS} = 0.5 (S_i - S_{i+1}) \quad (3.9)$$

$$x_M = 0.5 (x_{\min,i} + x_{\min,i+1}) \quad (3.10)$$

$$x_1 = (x_{\min,i} - x_M) \quad (3.11)$$

The mathematical form of the polynomial describing the background in the interval $[x_{\min,i}, x_{\min,i+1}]$ can be written as

$$y_b(x) = A (x - x_M)^3 + B (x - x_M)^2 + C (x - x_M) + D \quad (3.12)$$

$$\text{with } A = 0.5 [\text{AFS } x_1 - \text{DF}] / x_1^3 \quad (3.13a)$$

$$B = \text{DFS} / (2 x_1) \quad (3.13b)$$

$$C = 0.5 [3 \text{DF} / x_1 - \text{AFS}] \quad (3.13c)$$

$$D = \text{AF} - 0.5 \text{DFS } x_1 \quad (3.13d)$$

Finally, the background corrected signal Y_i at wavelength x_i is obtained as

$$Y_i = A_i - y_b(x_i) \quad (3.14)$$

These final background corrected IR spectra have been put at our disposal (in the range 1260 - 2260 cm^{-1}) in digitized form.

The IR spectra of carbon species trapped in argon matrices are analyzed [SchS96] in a total spectral range of 1260-2260 cm^{-1} . Because of the complexity of the spectra and the dimensions of the individual data sets, the spectra were first divided in smaller regions of about 100 cm^{-1} . Further, the background corrected intensities are multiplied by a factor of 10^4 before they have been analyzed with ASDAP (the arbitrary factor of 10^4 has been introduced for computational ease). For each of the subsets, several combinations of input parameters (number of smoothings, $\text{FWHM}_1 = M_1$ of the zero-area Gaussian filter, fitting area) were tried in order to obtain the most plausible solution. Both the reduced sum and Voigt functions have been used as model functions for the spectral profiles. Since $\Delta x = 0.5 \text{ cm}^{-1}$, the area under the optimized components of the multiplet is calculated over a spectral range of $(x_{0,s} \pm 5 \text{ cm}^{-1})$.

The final results obtained for the IR spectra resulting from the annealing experiments in solid Ar matrix are presented in Section 3.1.3.. A brief overview of remarkably changes in the IR features recorded in solid Kr matrix are presented in Section 3.1.4.

3.1.3. Analysis in Ar matrix

The IR spectra of C_n clusters trapped in the solid Ar matrix at 13, 30 and 35 K are analyzed in a spectral region of 1260 - 2260 cm^{-1} . In order to obtain an idea of the complexity of the analyses, an example is given in Fig. 3.6. The **R** and **S** signals were obtained in the 2110 - 2160 cm^{-1} range by using a small zero-area Gaussian filter with $M_1 = FWHM_1 = 3$ channels. Even for this small spectral region (50 cm^{-1} or 100 data points) no less than 12 peaks were found in the **S** signal, of which still 11 ones remained after the fitting procedure (full lines under the experimental points (*) of Fig. 3.6).

All the original data and the resolved bands obtained with ASDAP at the three different temperatures (13, 30 and 35K) are superimposed in the Figs 3.15 - 3.23 collected in Appendix A. The calculated areas (range $x_{0,s} \pm 5$ cm^{-1}) for each optimized component *s*, are collected in Table 3.2 of Appendix B (together with the results for the Kr matrix). Many of the resolved IR bands could be assigned to specific carbon species using theoretical and experimental data (see Table 3.1). The thermal behavior of some IR lines is illustrated and compared with other known IR bands of the same carbon species. These results are presented and discussed for each of the smaller regions.

a. 1260 - 1360 cm^{-1}

Fig. 3.15 shows that due the large fluctuations, the spectra in this region are difficult to analyze. Therefore, the analysis has been performed with three consecutive smoothings and with a very small zero-area Gaussian filter ($M_1 = FWHM_1 = 2$). However, in the spectrum recorded at 13 K, no significant bands can be distinguished. In the spectra obtained after annealing to 30 and 35 K, two IR features at 1284 and 1346 cm^{-1} can be noticed.

Martin et al. [MarJ91b] suggested, based on quantum chemical computations that the absorption at 1284 cm^{-1} belongs to cyclic C_4 . Afterwards, Watts et al. [WatJ92] predicted an intense band for this species at 1400 cm^{-1} . Recently, Martin et al. [MarJ96b] confirmed their earlier assignment at 1284 cm^{-1} based on more accurate calculations in which they computed the anharmonicity for rhombic C_4 .

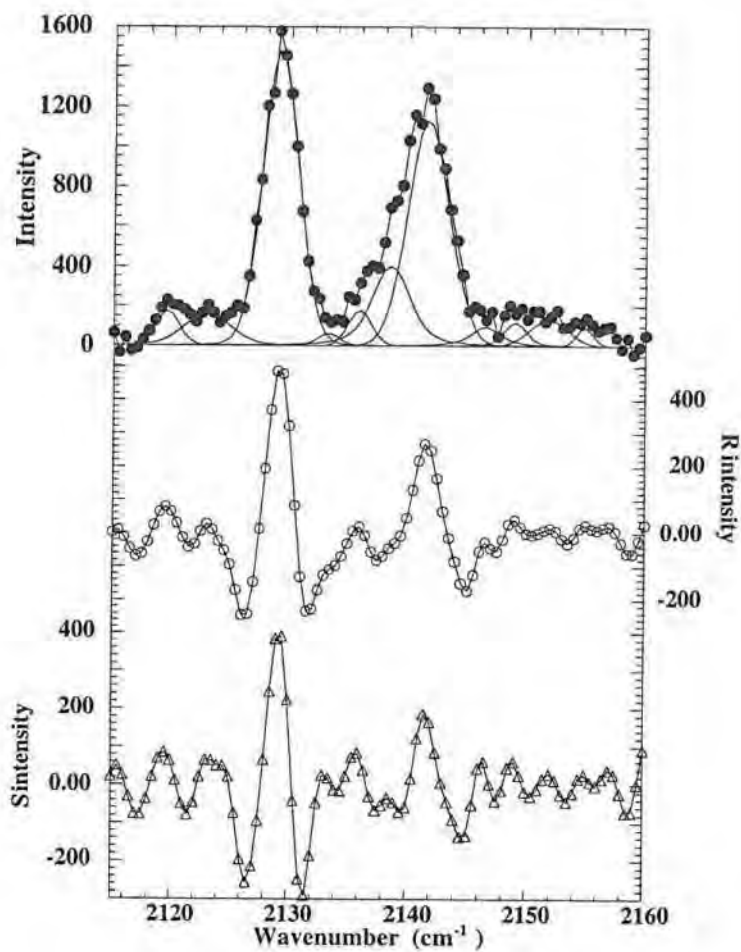


Fig. 3.6 : IR spectrum(•)of carbon clusters in an Ar matrix at 35K in the 2110 - 2160 cm^{-1} range, individual fitted components (full lines), and corresponding $R(o)$ and $S(\Delta)$ signals obtained by using zero-area Gaussian filters with $M_1 = \text{FWHM}_1 = 3$ channels.

b. 1420 - 1520 cm⁻¹

The detection of the individual components, present in the 1420 - 1520 cm⁻¹ region, is performed by using a zero-area Gaussian filter with $M_1 = \text{FWHM}_1 = 3$ after three smoothings in order to reduce the noise (Fig. 3.16). After annealing to 30 and 35 K, three weak infrared bands (1447, 1477 and 1489 cm⁻¹) become visible.

The early assignment by TDW [ThoK71] of the 1447 cm⁻¹ feature to the C₉ cluster should be revised as it has been proved in several theoretical studies [MarJ96a, BotP89] and reassigned to the linear C₅ species. The annealing behavior of the 1447 and the 2164 cm⁻¹ bands of linear C₅, illustrated in Fig. 3.7, seems to contradict this assignment. The 1447 cm⁻¹ feature increases strongly upon annealing while the 2164 cm⁻¹ line decreases. A Fourier transform infrared study of C₅ in an Ar matrix at 10 K by Kranze and Graham [KraR92] resulted in the first identification of the $\nu_4(\sigma_u)$ stretching mode at 1446.6 cm⁻¹.

The weak infrared features at 1477 and 1489 cm⁻¹ are still unassigned to any C_n species.

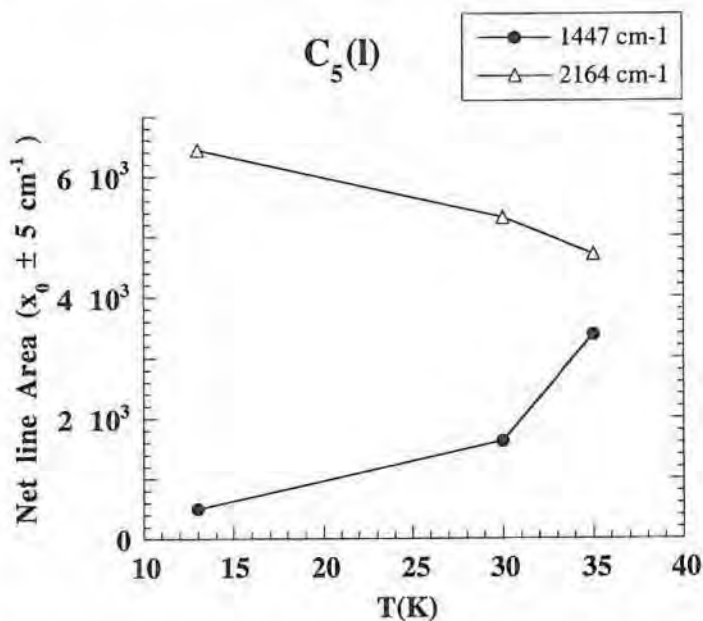


Fig. 3.7 : Plot of the computed intensities of the IR bands at 1447 and 2164 cm⁻¹, both belonging to linear C₅, versus the annealing temperature.

c. 1520 - 1650 cm⁻¹

The 1520 - 1650 cm⁻¹ region is characterized by some major IR bands (Fig. 3.17). Several consecutive smoothings (3 times at 13 and 30K ; 5 times at 35K) and a small zero-area Gaussian filter ($M_1 = \text{FWHM}_1 = 3$) were necessary in order to unravel the spectra due to the large number of spectral lines (especially at 35K) and important fluctuations.

The intensity of a first peak at 1544 cm⁻¹ decreases upon annealing. Theoretical [MarJ96a, MarJ95a, MicD87, BerD88] and experimental evidence [SheL89, HeaJ91a] are given that this absorption is due to linear C₄.

The IR features at 1578, 1590 and 1601 cm⁻¹ have all the same thermal behavior. Martin et al. [MarJ95a, MarJ96a] concluded from their quantum chemical results that one of these features should be assigned to linear C₉. Recently, Kranze et al. [KraR95] observed for the first time a second stretching fundamental $\nu_7(\sigma_u)$ of linear C₉ at 1601 cm⁻¹ from a FTIR investigation in solid Ar at 10 K. Fig. 3.8 shows the relation between the intensities of the 1998 cm⁻¹ feature, assigned earlier to linear C₉ by Heath and Saykally [HeaJ90a], and the 1578, 1590 and 1601 cm⁻¹ features at 13, 30 and 35 K. The intensities obtained in the analyses of the 1570 - 1580 cm⁻¹ bands are summed. The relative growths of the features from 13 to 35 K is 5.0, 2.7, 14.2 and 4.3 for the 1998, 1578, 1590 and 1601 cm⁻¹ respectively when the temperature is raised from 13 to 35 K. Hence, the most likely candidate for linear C₉ is the 1601 cm⁻¹ feature.

No conclusive evidence can be given for an assignment of the small IR band at 1625 cm⁻¹.

d. 1680 - 1780 cm⁻¹

Fig. 3.18 shows a complex multiplet around 1700 cm⁻¹ in which two IR bands (1695 and 1715 cm⁻¹) are growing fast upon annealing. A single smoothing combined with a zero-area Gaussian filter ($M_1 = \text{FWHM}_1 = 3$) was sufficient for the analysis of this spectrum. The spectra obtained at 30 and 35K were three times smoothed before they were analyzed using a zero-area Gaussian filter with $M_1 = \text{FWHM}_1 = 3$ at 30K and $M_1 = \text{FWHM}_1 = 2$ at 35K.

The 1695 cm⁻¹ feature has been assigned to the cyclic C₆ by Martin and Taylor [MarJ96a]. Recently, Wang et al. [WanS97] identified cyclic C₆ for the first time in FTIR spectra of products from the laser evaporation of graphitic rods trapped in Ar at ~ 10K. The assignment of the most intense infrared active mode of cyclic C₆ at 1694.9 cm⁻¹ was based

on excellent agreement of the frequency, isotopic shifts, and their relative intensities with the theoretical predictions. At almost the same time, Presilla-Márquez et al. [PreJ97] identified in their FTIR study of matrix-isolated carbon vapor a small cyclic carbon cluster, C_6 .

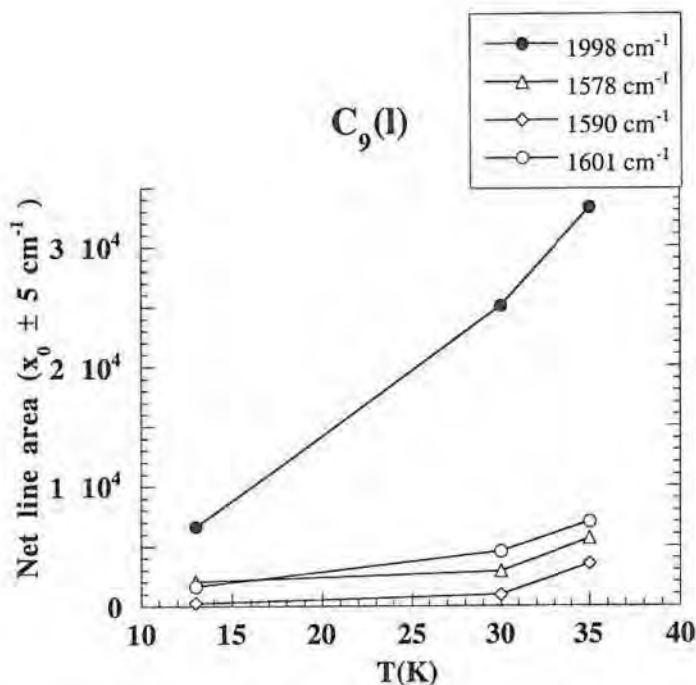


Fig. 3.8 : Plot of the computed intensities of the IR bands at 1998 cm^{-1} , belonging to linear C_9 , and the IR bands at 1578 , 1590 and 1601 cm^{-1} , versus the annealing temperature.

Martin et al. [MarJ91c] concluded in 1991 that one of the detectable IR bands of cyclic C_{11} is the 1715 cm^{-1} feature. In later quantum chemical studies of Martin et al. [MarJ96a, MarJ95a], they concluded that both the 1695 and 1715 cm^{-1} bands could be candidates for assignment to linear C_8 . In a thermal annealing study of Szczepanski et al. [Szc96], this assignment has been revised to 1710.5 cm^{-1} , which matches closely the theoretical prediction of 1703 cm^{-1} by Hutter et al. [HutJ94]. In addition to their pioneering work concerning the identification of cyclic C_6 , Presilla-Márquez et al. [PreJ97] also confirmed the assignment of a band at 1710.3 cm^{-1} to linear C_8 .

e. 1780 - 1880 cm^{-1}

Fig. 3.19 shows the complex analyses of the IR spectra in the spectral range of 1780 - 1880 cm^{-1} . A large number of spectral lines has been found with ASDAP using a zero-area Gaussian filter ($M_1 = \text{FWHM}_1 = 3$) after three consecutive smoothings of the spectra recorded at 13 and 30K and a single smoothing of the spectrum obtained at 35K. The spectra are clearly dominated by three fast growing bands at 1804, 1818 and 1844 cm^{-1} which have shoulders at both sides.

Martin et al. [MarJ91c] have tentatively assigned the 1804 and 1844 cm^{-1} bands to cyclic C_{11} and the 1818 cm^{-1} band to cyclic C_{10} and linear C_{11} . Martin and Taylor [MarJ95b] performed higher level ab initio calculations on C_{11} yielding results in good agreement with the previous published ones [MarJ91c]. Fig. 3.9 shows the influence of annealing upon the intensities of the 1715 [MarJ91c], 1804 and 1844 cm^{-1} features of cyclic C_{11} . It is found that the 1715 cm^{-1} line shows a much smaller growth (almost a factor 10) upon annealing than the 1804 and the 1844 cm^{-1} features. This confirms the revision of the assignment of the 1715 cm^{-1} feature to linear C_8 [MarJ96a, MarJ95a, SzcJ96, HutJ94].

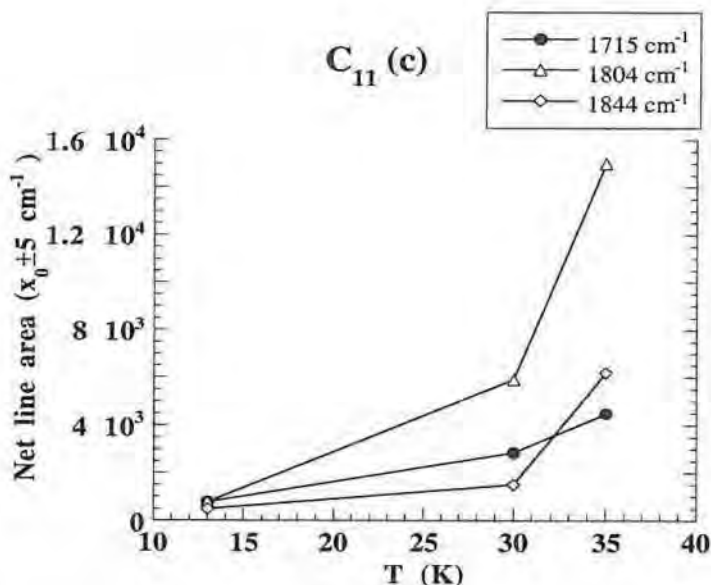


Fig. 3.9 : Plot of the computed areas of the IR bands at 1715 cm^{-1} , belonging to cyclic C_{11} , and the IR bands at 1804 and 1844 cm^{-1} , against the annealing temperature.

In their more recent theoretical studies of small carbon clusters, Martin et al. [MarJ95a, MarJ96a] suggested that the 1818 cm^{-1} band appears to be the most likely candidate for cyclic C_8 .

f. 1880 - 1980 cm^{-1}

The detection of the many individual components present in the 1880 - 1980 cm^{-1} region is performed using a small zero-area Gaussian filter with $M_1 = \text{FWHM}_1 = 3$ for the spectra obtained at 30 and 35K, and with $M_1 = \text{FWHM}_1 = 2$ for the spectrum recorded at 13K (Fig. 3.20). Three smoothings of the original signals was necessary in order to reduce the large fluctuations present in each of the spectra.

It can be seen from Table 3.1 that a first peak at 1896 cm^{-1} has been assigned to linear C_7 based on quantum chemical work [MarJ91, MarJ90a]. Also a lot of experimental studies confirm this assignment. Heath and coworkers [HeaJ91b, HeaJ91c] have assigned an absorption at 1898 cm^{-1} to the second ν_5 (σ_u) antisymmetric stretch of linear C_7 using high resolution diode laser spectroscopy. In a neon matrix, the ν_5 (σ_u) mode has been observed at 1897.5 cm^{-1} [SmiA94]. A FTIR ^{13}C isotopic study has been performed by Kranze et al. [KraR96] in order to identify the ν_5 (σ_u) fundamental at 1894.3 cm^{-1} by trapping the products of the evaporation of graphite in solid Ar at 10K. Fig. 3.10 shows the thermal behavior of the ν_5 (σ_u) fundamental at 1898 cm^{-1} and the ν_4 (σ_u) fundamental at 2128 cm^{-1} of the linear C_7 cluster. A similar behavior can be observed for the temperatures of 13 and 30 K. At 35 K the area under the 1896 cm^{-1} feature decreases, but the area under the 2129 cm^{-1} feature slightly increases. A closer look at the intensities at the 2129 cm^{-1} position in Fig. 3.23 shows that the intensity at the maximum of this peak also decreases. Thus the increase of the area is due to a small broadening of the line at 35 K.

The 1915 cm^{-1} line, with a shoulder at 1921 cm^{-1} , grows strongly upon annealing. Slanina et al. [SlaZ92a] concluded that the 1915 cm^{-1} band is the most obvious experimental candidate for cyclic C_7 . Martin et al. [MarJ96b, MarJ96a] suggested that one of the components of the doublet observed at 1915 and 1921 cm^{-1} belongs to cyclic C_{10} .

In their extensive theoretical study of structures and vibrational spectra of carbon clusters C_n ($n=2-10, 12, 14, 16, 18$) Martin et al. [MarJ95a] proposed tentative assignments of the 1921 and 1947 cm^{-1} bands to cyclic C_{18} and cyclic C_{14} , respectively.

The large feature at 1952 cm^{-1} , which is already strongly present at 13K, has been assigned to linear C_6 by Martin et al. [MarJ90a, MarJ91, MarJ95a, MarJ96a] based on ab initio calculations. In an experimental study of linear C_6 formed by trapping the products

of laser ablation of graphite in solid Ar, Vala and co-workers [ValM90a] assigned the ν_4 (σ_u) stretching mode of $C_6(\text{lin})$ to an absorption at 1952 cm^{-1} . Also Kranze and Graham [KraR93b] confirmed the ν_4 (σ_u) assignment at 1952 cm^{-1} in their FTIR ^{13}C isotopic study of linear C_6 .

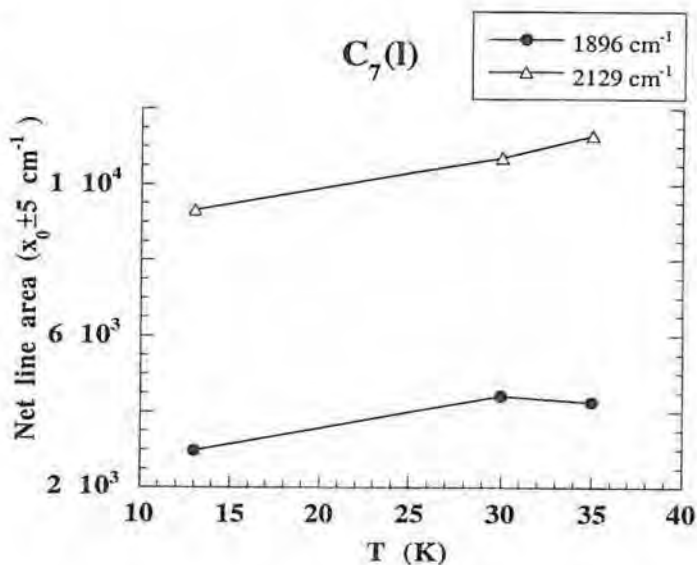


Fig. 3.10 : Plot of the computed intensities of the IR bands at 1896 and 2129 cm^{-1} , both belonging to linear C_7 , versus the annealing temperature.

g. $1980 - 2020\text{ cm}^{-1}$

The spectra in the $1980 - 2020\text{ cm}^{-1}$ region have been analyzed using a small zero-area Gaussian filter ($M_1 = \text{FWHM}_1 = 2$) although there are only a few lines (Fig. 3.21). It has been found that only one important multiplet is present. Nevertheless, the intensities of these components were large and the fluctuations in the base line (some intensities below zero, probably as a result of an incorrect background correction) made the use of three smoothings necessary.

The central peak around 2000 cm^{-1} grows strongly upon annealing. TDW [ThoK71] assigned this band to the C_6 cluster species. Vala and coworkers [ValM90b] reassigned the 1998 cm^{-1} feature to C_8 . This assignment was again challenged by Martin et al. [MarJ91, MarJ90a, MarJ95a, MarJ96a] who proposed that the 1998 cm^{-1} line should be attributed to C_9 based on the results of quantum chemical work. Heath and Saykally [HeaJ90a] identified a gas phase band at 2014.3 cm^{-1} as the ν_6 (σ_u) antisymmetric stretching

mode of linear C₉ using diode laser spectroscopy. Taking into account the linear relation between the gas-to-Ar matrix shift [HeaJ93] and the size of the linear cluster, they predicted that this band would appear at 1998 cm⁻¹ in an Ar matrix. The relationship between the ν_7 and ν_6 frequencies has already been shown in Fig. 3.8.

The interfering peaks in the wings of the central line are still unassigned.

h. 2020 - 2100 cm⁻¹

The analyses of the IR spectra in the 2020 - 2100 cm⁻¹ spectral region are presented in Fig. 3.22. They result from the optimizations of the peaks found with zero-area Gaussian filters ($M_1 = \text{FWHM}_1 = 2$ for the spectrum obtained at 13K, and $M_1 = \text{FWHM}_1 = 3$ for the spectra obtained at 30 and 35K). Only for the spectrum recorded at 30K, a single smoothing of the data sufficed. The spectra obtained at 13 and 35K needed three consecutive smoothings to obtain the optimized components.

The origin of some small lines at 2026 and 2029 cm⁻¹ is still unknown. The intensities of the doublet at 2036 and 2041 cm⁻¹ decrease upon annealing. Experimental evidence for the assignment of the 2040 cm⁻¹ band to the C₃ species was already given by Weltner and McLeod [WelW64] in 1964. Matsumura et al. [MatK88] concluded also in their infrared diode laser spectroscopic study that the strong band around 2040 cm⁻¹ belongs to the ν_3 band of linear C₃.

At higher temperatures a band at 2053 cm⁻¹ becomes visible. This IR feature was previously assigned to the cyclic C₅⁺ species by Vala and coworkers [ValM90a]. More recently, extensive evidence is given by Szczepanski et al. [SzcJ95] that the 2053 cm⁻¹ band belongs to the C₃⋯H₂O complex.

After analysis of a broad feature at 2073 - 2080 cm⁻¹ with ASDAP, it seems to be composed of three bands. According to Martin and Taylor [MarJ95a, MarJ96a, MarJ96b] some of them belong to linear C₈ and C₉. Van Orden and coworkers [VanA96] have observed the ν_5 antisymmetric stretching vibration of C₉ using direct infrared diode laser absorption spectroscopy of a pulsed supersonic cluster beam at 2079.7 cm⁻¹. Szczepanski et al. [SzcJ96] found also that the observed 2078 cm⁻¹ feature correlates with the two known linear C₉ bands at 1601 and 1998 cm⁻¹.

i. 2100 - 2260 cm^{-1}

A lot of spectral lines is concentrated in the 2100 - 2260 cm^{-1} region of the IR spectra (Fig. 3.23) and that complex region could be unraveled using three smoothings and a zero-area Gaussian filter with $M_1 = \text{FWHM}_1 = 3$.

Martin et al. [MarJ91, MarJ90a, MarJ95a, MarJ96a] concluded in their theoretical studies that the 2128 cm^{-1} feature should be assigned to the linear C_7 cluster. Heath and coworkers [HeaJ90b, HeaJ91b] have found a corresponding absorption at 2138.3 cm^{-1} for the second ν_4 (σ_u) antisymmetric stretch of linear C_7 in the gas phase. In a neon matrix the ν_4 (σ_u) mode has been reported at 2134.6 cm^{-1} [SmiA94]. Kranze et al. [KraR96] identified the ν_4 (σ_u) fundamental at 2127.8 cm^{-1} in solid Ar at 10K.

The line at 2140 cm^{-1} comes from the almost unavoidable contamination of CO [KraW87].

The large 2164 cm^{-1} feature at the beginning of a broad multiplet was theoretically proven to belong to the linear C_5 carbon cluster by Martin et al. [MarJ89] and Botschwina and Sebald [BotP89]. Experimentally, Vala et al. [ValM89], Moazzen-Ahmadi et al. [MoaN89a, MoaN89b] and Heath et al. [HeaJ89] have confirmed this new assignment.

Fig. 3.23 shows also a complex multiplet between 2180 and 2230 cm^{-1} that grows strongly upon annealing. Because of this annealing behavior it can be expected that the appearance of these bands is due to the formation of large cyclic C_n ($n > 10$) clusters. However, until now none of them can be assigned to a specific carbon species. Also, the origin of the two bands arising at 2247 and 2253 cm^{-1} is still unknown.

3.1.4. Analysis in Kr matrix

The IR spectra of C_n clusters trapped in a solid Kr matrix at 35 K are analyzed in a spectral region of 1250 - 2250 cm^{-1} . The calculated areas of the individual components found in these IR spectra are collected in the last column but one of Table 3.2 in Appendix B.

The positions of IR bands in the matrix phase are shifted compared to their positions in the gas phase due to the influence of the solid matrix. The matrix-induced shift was for the first time quantified by Heath and Saykally [HeaJ93] for the antisymmetric stretching modes of linear C_n clusters trapped in an argon matrix. They found that the

matrix-induced red shift was proportional to the size of the carbon cluster n , namely approximately equal to $2.5 (n - 3) \text{ cm}^{-1}$. From the results of our analyses of IR spectra of carbon clusters trapped in noble gas matrices, we can calculate the shifts and plot them against the size of carbon cluster n in Fig. 3.11. This plot shows that we obtain exact the same expression as Heath and Saykally in an Ar matrix and that we find a similar linear relationship for carbon clusters trapped in a Kr matrix, namely $(0.6 + 2.2 n) \text{ cm}^{-1}$. The slopes of both lines are almost the same; however, due to the larger intercept, the matrix-induced red shifts in a Kr matrix are larger than in an Ar matrix.

Besides the matrix shift, the spectrum recorded in a Kr matrix differs at some specific wavelengths from those recorded in Ar matrices. Some new and rather large features are present as can be seen in Figs 3.12a-c : a small doublet at about $1850 - 1852 \text{ cm}^{-1}$ (a), a large doublet at $2003 - 2005 \text{ cm}^{-1}$ (b), and a singlet at 2079 cm^{-1} (c).

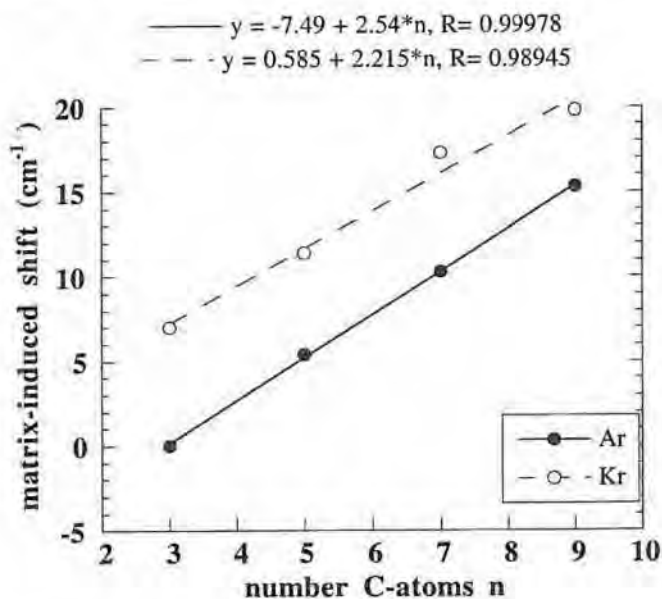


Fig. 3.11 : Matrix induced shifts in a solid Ar and Kr matrix against the size of carbon cluster n .

In Fig. 3.13a, the IR band at 1489 cm^{-1} that can be observed in the IR spectrum in an Ar matrix at 35 K (Fig. 3.16) cannot be clearly distinguished in the spectrum recorded in a Kr matrix. Instead, a broad multiplet with low intensities is present. This could indicate that the spectrum is recorded at a lower temperature than 35 K or that the structure of this species is not present in a Kr matrix. Fig. 3.13b shows that the 1695 cm^{-1} feature, assigned

to cyclic C_6 by Martin and Taylor [MarJ96a], is strongly decreased compared to the high intensity of the 1710 cm^{-1} band that increased strongly upon annealing in an Ar matrix (Fig. 3.18).

Comparing of the IR bands in the 1520 to 1650 cm^{-1} region recorded in Ar (Fig. 3.17) and in Kr matrices (Fig. 3.14a) shows that the components of the multiplet at $1570 - 1620\text{ cm}^{-1}$ in a solid Kr matrix are much less resolved than in a solid Ar matrix. The opposite trend can be observed for the multiplet in the $1930 - 1970\text{ cm}^{-1}$ region which is more resolved in the spectrum obtained in Kr (Fig. 3.14b) than in Ar (Fig. 3.20).

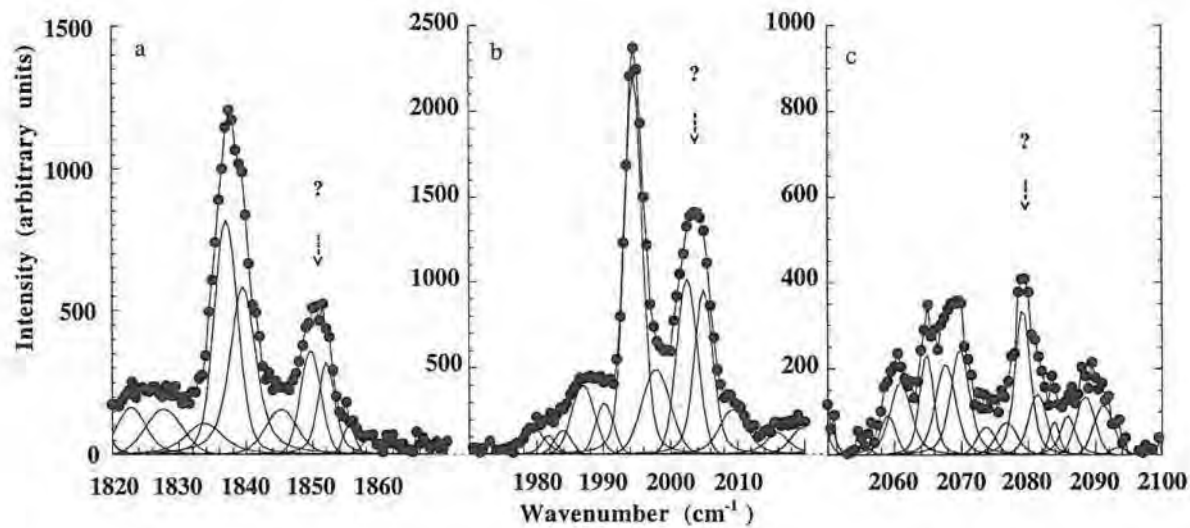
3.1.5. Conclusions

It was demonstrated that ASDAP can analyze both qualitatively and quantitatively the complex IR spectra of carbon cluster trapped in Ar and Kr matrices at temperatures of 13, 30 and 35K. The resolved IR bands could be assigned to specific C_n cluster species based on data obtained via quantum chemical computations and from tunable diode laser IR spectroscopy of C_n species in the gas phase as referred to in literature.

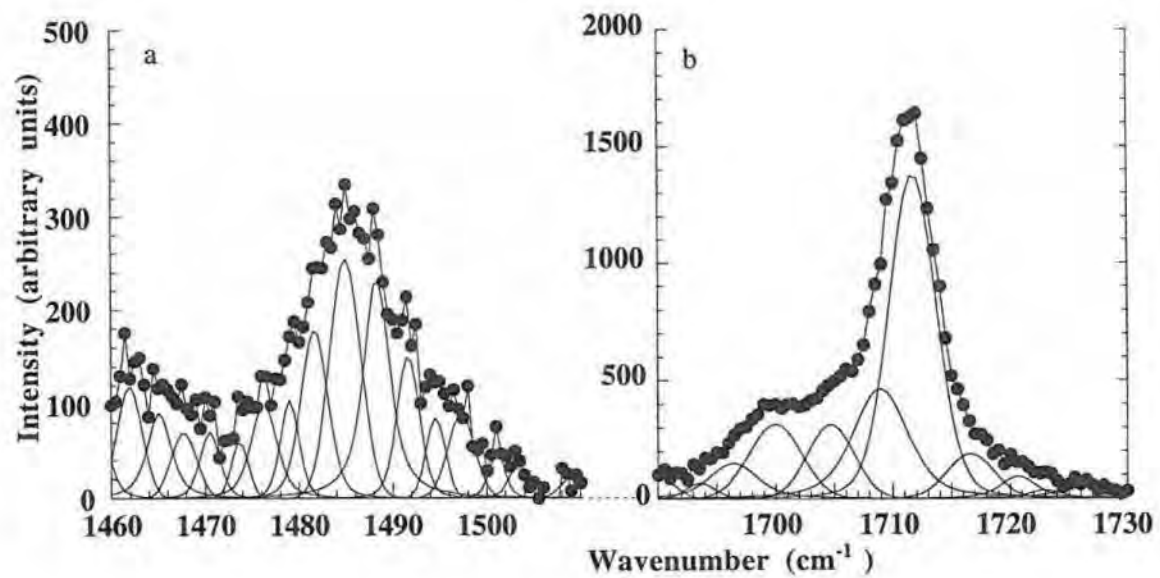
The theoretical assignment of different spectral features to the same carbon species could be confirmed based on the similar growth behavior of the specific lines at the three recorded temperatures in Ar.

The relationship between the matrix-induced red shift and the size of the carbon cluster n , was found to be equal to the one published by Heath and Saykally [HeaJ93] in Ar matrix. A similar one was found in a Kr matrix, namely $(0.6 + 2.2 * n)\text{ cm}^{-1}$. The slopes of both lines are almost the same, however the matrix-induced red shifts in a Kr matrix are larger than in an Ar matrix.

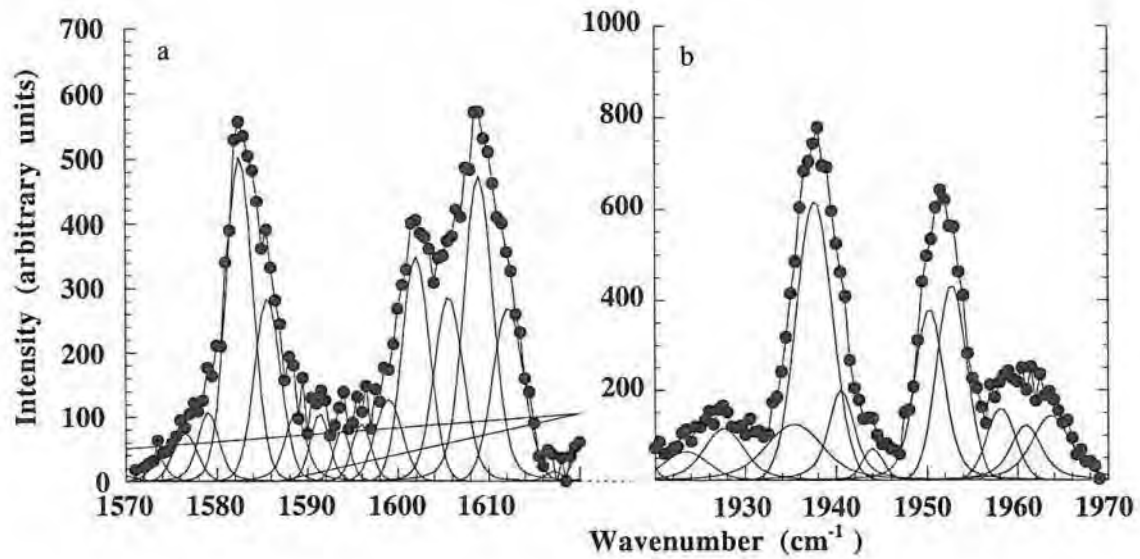
Finally, the differences between the spectrum recorded in a krypton matrix and the ones obtained in an Ar matrix are discussed. Some new features were found to be present in a Kr matrix : a small doublet at about $1850 - 1852\text{ cm}^{-1}$ (a), a large doublet at $2003 - 2005\text{ cm}^{-1}$ (b) and singlet at 2079 cm^{-1} (c). The intensity of other spectral features (1489 cm^{-1} and 1710 cm^{-1}) was found to be decreased. Also the resolution of $1570 - 1620\text{ cm}^{-1}$, and $1930 - 1970\text{ cm}^{-1}$ bands were different from the corresponding bands in an Ar matrix.



Figs 3.12a-c : New IR features present in Kr matrix : a small doublet at about 1850 - 1852 cm⁻¹ (a), a large doublet at 2003 - 2005 cm⁻¹ (b) and singlet at 2079 (c) cm⁻¹



Figs 3.13a,b : IR bands near 1489 cm⁻¹ and 1695 cm⁻¹.



Figs 3.14a,b : IR bands in the spectral region of 1520 - 1650 cm⁻¹, and 1930 - 1970 cm⁻¹

3.1.6. Appendix A : Fig. 3.15 - 3.23 : Details of the analysis of the IR spectra of C_n clusters trapped in Ar matrix at 13, 30 and 35K.

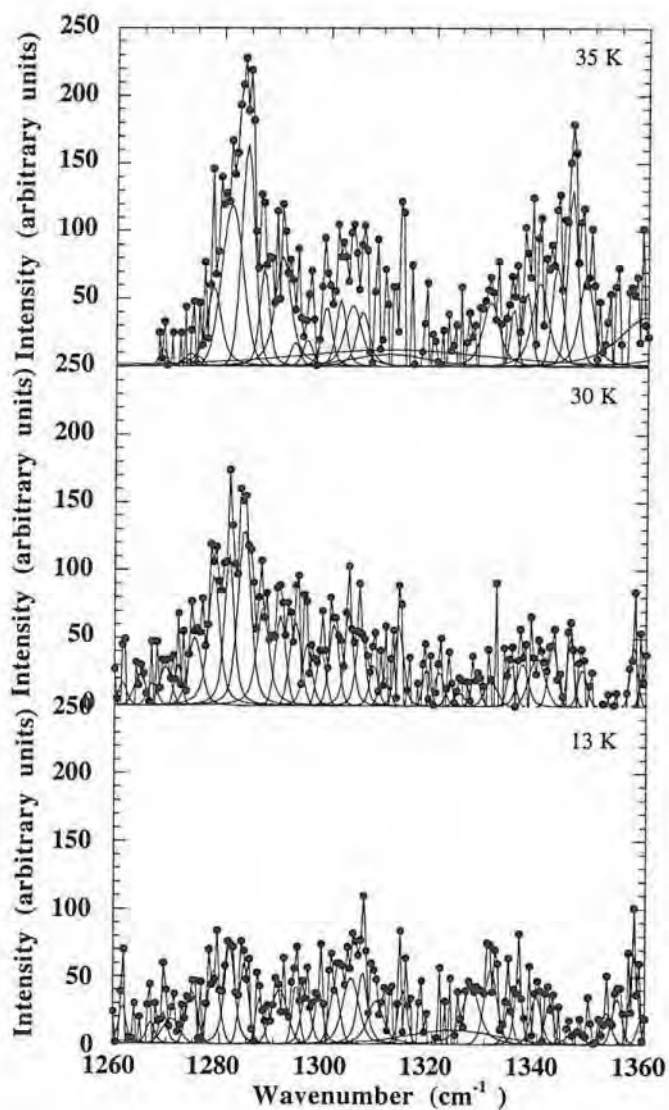


Fig. 3.15 : Detail of the IR spectrum (•) in the 1260 - 1360 cm^{-1} region in an Ar matrix at 13, 30 and 35 K, with the individual components (full lines).

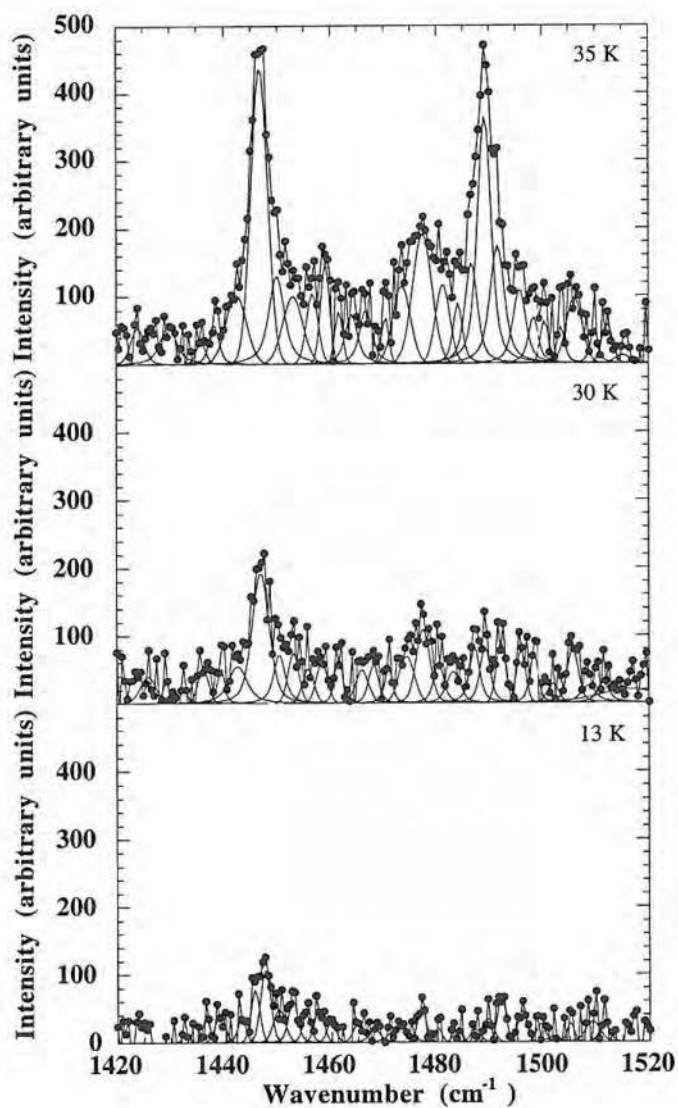


Fig. 3.16 : Detail of the IR spectrum (●) in the 1420 - 1520 cm^{-1} region in an Ar matrix at 13, 30 and 35 K, with the individual components (full lines).

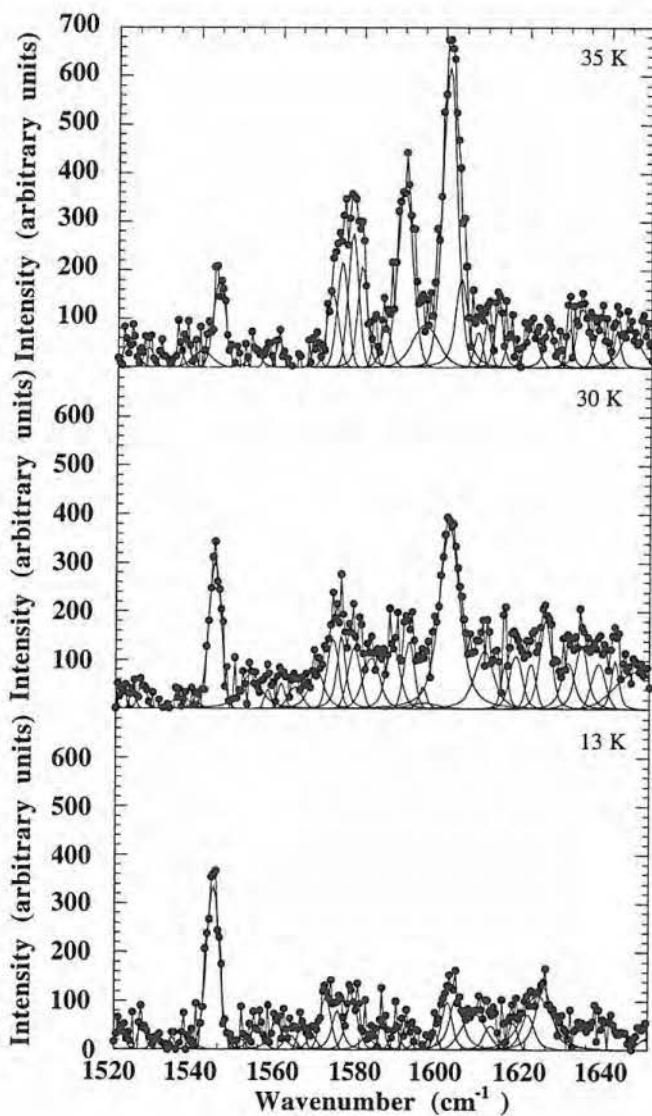


Fig. 3.17 : Detail of the IR spectrum (•) in the 1520 - 1650 cm⁻¹ region in an Ar matrix at 13, 30 and 35 K, with the individual components (full lines).

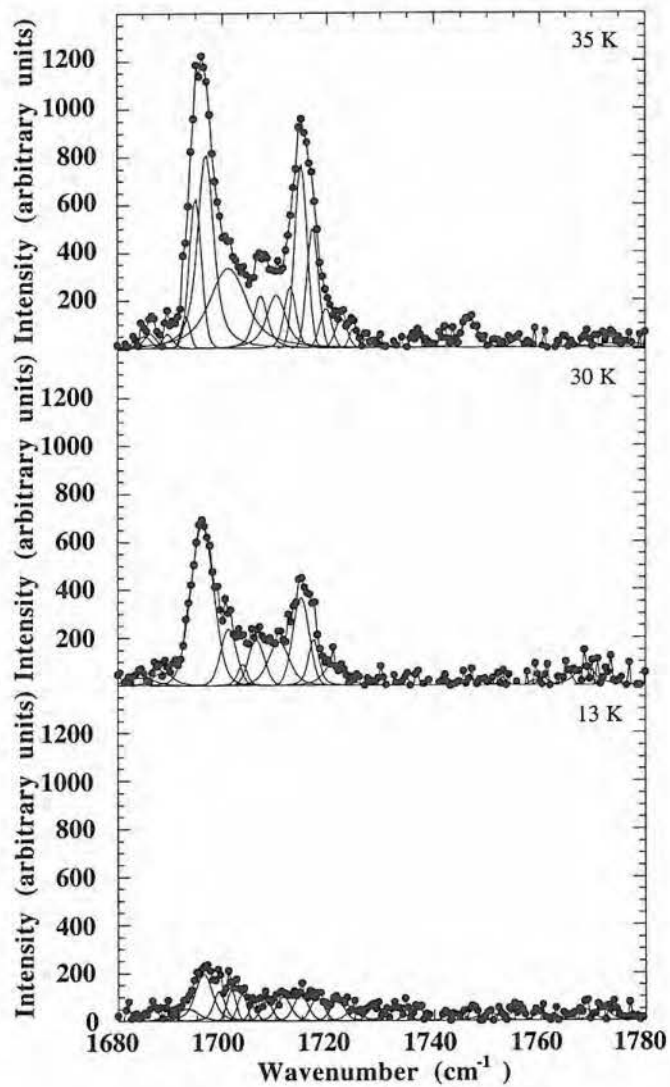


Fig. 3.18 : Detail of the IR spectrum (●) in the 1680 - 1780 cm⁻¹ region in an Ar matrix at 13, 30 and 35 K, with the individual components (full lines).

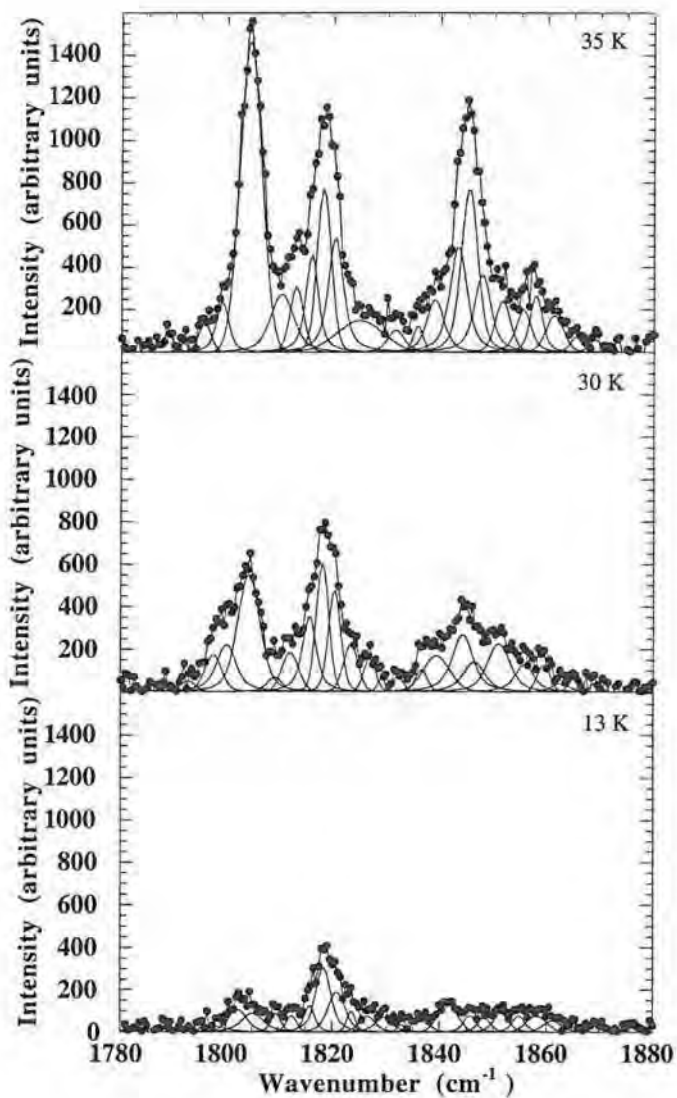


Fig. 3.19 : Detail of the IR spectrum (●) in the 1780 - 1880 cm⁻¹ region in an Ar matrix at 13, 30 and 35 K, with the individual components (full lines).

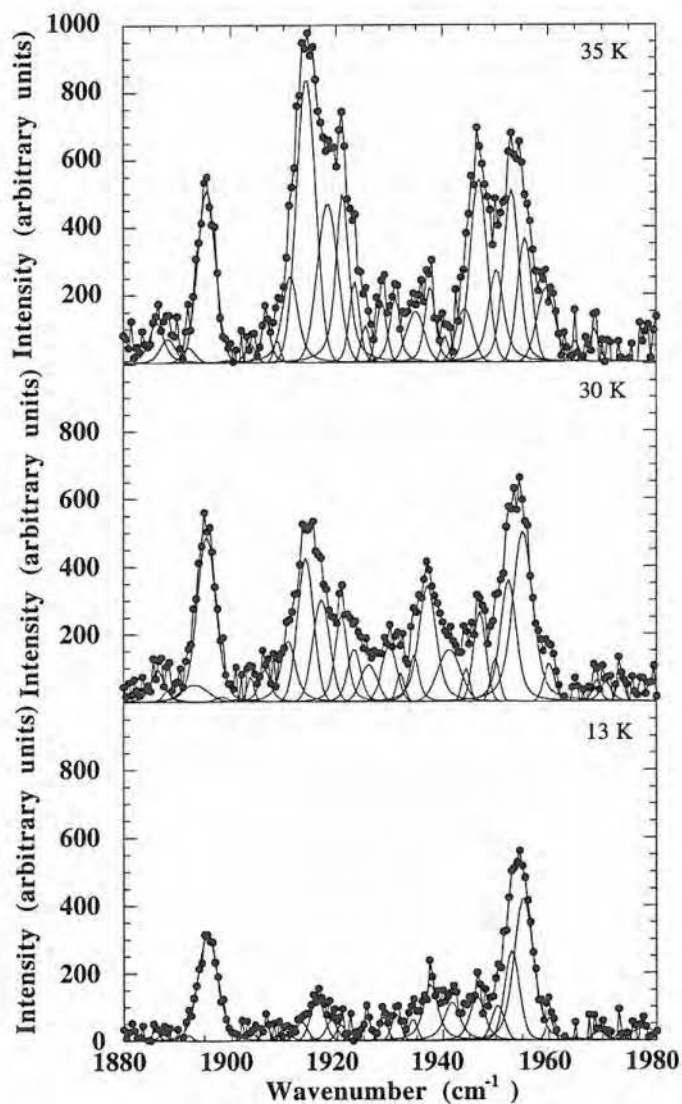


Fig. 3.20 : Detail of the IR spectrum (•) in the 1880 - 1980 cm⁻¹ region in an Ar matrix at 13, 30 and 35 K, with the individual components (full lines).

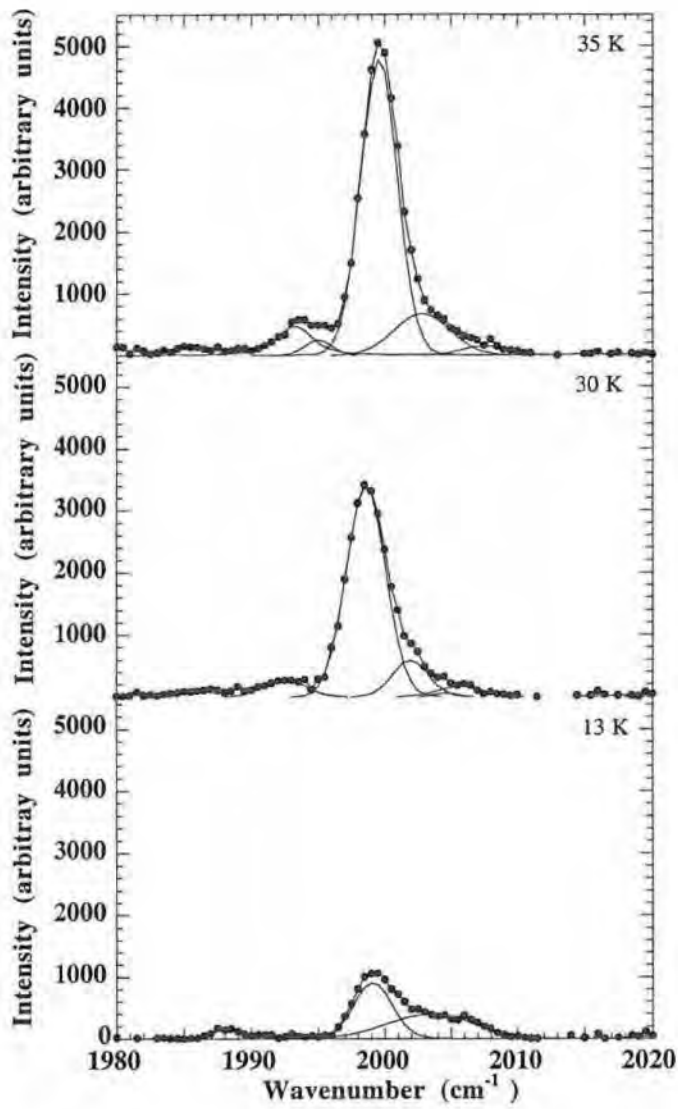


Fig. 3.21 : Detail of the IR spectrum (\bullet) in the 1980 - 2020 cm^{-1} region in an Ar matrix at 13, 30 and 35 K, with the individual components (full lines).

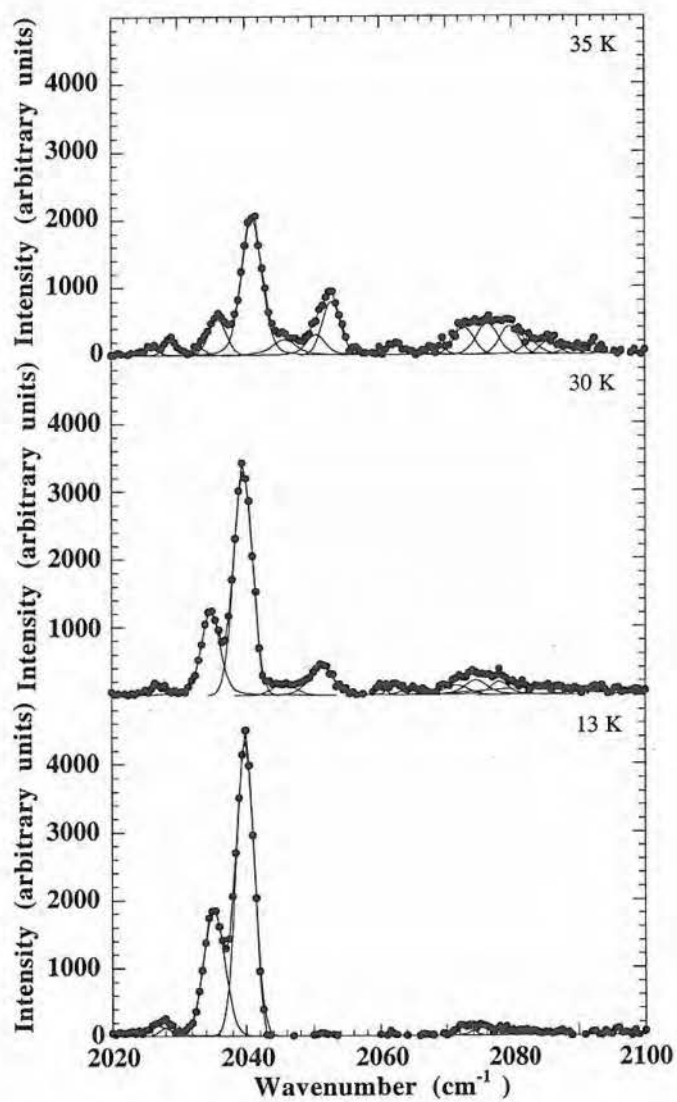


Fig. 3.22 : Detail of the IR spectrum (●) in the 2020 - 2100 cm⁻¹ region in an Ar matrix at 13, 30 and 35 K, with the individual components (full lines).

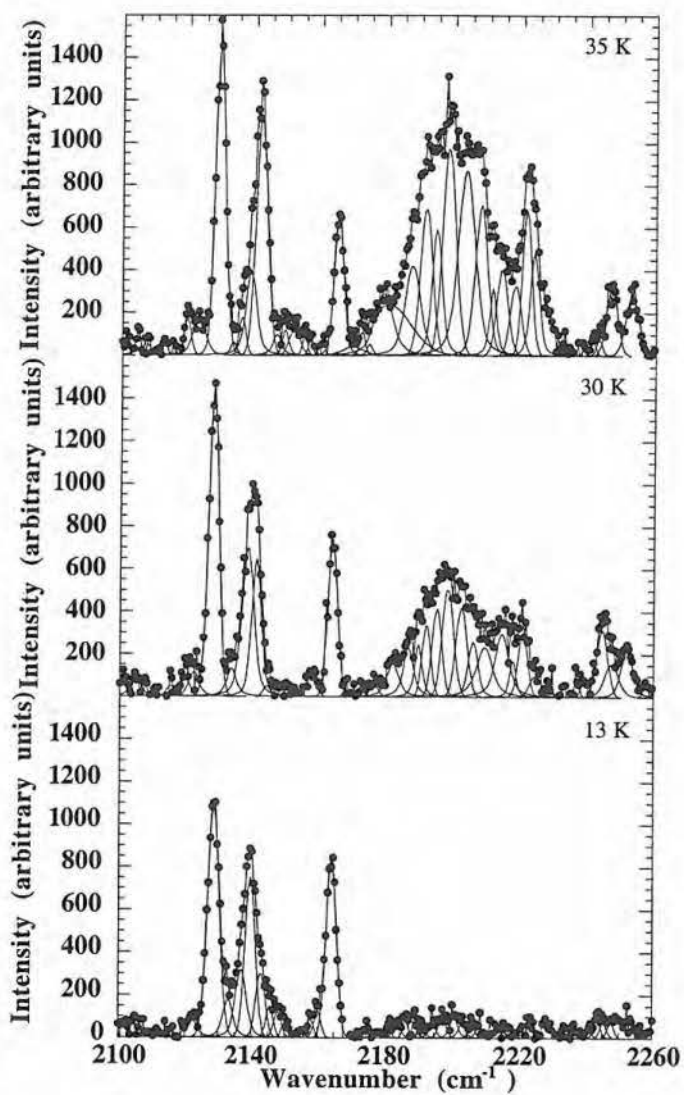


Fig. 3.23 : Detail of the IR spectrum (●) in the 2100 - 2260 cm⁻¹ region in an Ar matrix at 13, 30 and 35 K, with the individual components (full lines).

3.1.6. Appendix B : Table 3.2 : Complete analysis of the IR-spectra of C_n- clusters in the 1250-2250 cm⁻¹ range

Argon matrix						Krypton matrix	
13K		30K		35K		λ(cm ⁻¹)	Area
λ(cm ⁻¹)	Area	λ(cm ⁻¹)	Area	λ(cm ⁻¹)	Area		
1278.9	307.3	1278.6	603.7	1278.2	446.6	1299.3	1019.8
1281.9	402.3	1281.5	584.4	1281.6	1185.6	1302.5	890.8
1284.6	254.3	1284.3	863.7	1284.5	1042.2	1306.1	493.5
1287.5	119.2	1287.8	486.6	1287.6	368.0		
1291.2	304.3	1291.1	331.3	1291.0	674.1		
1301.6	213.3	1301.1	288.1	1302.0	262.1	1320.6	1084.3
1304.6	402.3	1303.9	325.0	1304.3	393.5	1324.0	1979.5
1306.8	295.2	1306.2	282.9	1306.2	283.3	1328.1	388.5
1309.3	266.5	1308.7	130.4				
1327.5	388.8						
1331.2	349.9	1331.0	115.6	1330.6	421.8	1354.7	764.8
1334.7	117.9	1334.8	116.1	1334.8	146.1		
1336.4	194.2	1336.9	182.5	1337.4	242.1	1357.8	974.2
1339.8	197.1	1339.6	268.8	1339.8	531.2	1362.2	647.4
1342.3	124.7	1342.7	196.8	1343.1	397.1	1364.9	355.6
		1346.0	164.4	1345.9	662.6	1367.5	316.0
		1348.2	115.3	1348.5	510.2	1376.2	436.6
		1442.5	518.1	1442.4	957.3		
1445.6	320.0						
1447.5	504.0	1446.7	1623.2	1446.7	3381.1	1445.9	5716.4
1450.0	279.5	1450.3	465.7	1449.9	1075.5	1452.6	2163.7
1452.6	303.6	1452.9	382.2	1452.9	942.6	1458.5	577.8
1455.2	179.2	1455.7	276.9	1456.6	577.1		
1457.5	214.1	1458.3	323.0	1459.0	635.7	1461.9	501.8
1459.9	132.7	1461.4	287.3	1464.0	497.2	1464.9	767.3
1465.1	152.5	1465.8	306.9	1466.7	539.9	1467.9	524.2
1468.1	122.5	1468.0	219.1				

1472.7	215.3	1474.2	495.8	1473.4	956.2	1473.7	255.7
1476.9	207.0	1477.4	737.7	1477.4	1751.8	1476.1	497.7
1480.0	71.7	1480.3	324.6	1481.2	789.9	1479.0	555.7
1483.7	73.9	1483.1	329.0	1484.1	453.6		
1487.0	93.7	1487.1	453.5	1486.6	1001.6	1481.7	1302.2
1489.6	163.3	1489.1	542.4	1489.1	2602.9	1485.0	2454.3
1492.0	264.6	1492.1	401.7	1491.5	1342.7	1488.4	1623.3
1496.0	190.2	1495.9	335.1	1495.7	757.0	1491.5	623.3
1499.5	119.5	1498.4	338.7	1498.4	385.5	1494.6	779.1
1505.1	93.8	1505.7	447.2	1506.1	722.7	1497.7	439.4
1509.3	204.0					1501.0	167.3
				1540.5	371.7	1539.4	449.3
1544.0	2633.6	1544.0	2246.2	1544.5	1345.9	1541.3	238.7
1554.5	351.8	1553.0	893.9	1553.2	292.7		
1559.7	502.7						
1563.1	213.9	1563.8	377.9				
		1569.1	774.0	1568.1	258.2	1576.6	498.0
1571.7	707.6	1573.1	983.7	1572.3	1079.1	1579.1	678.8
1574.5	574.3	1575.1	934.8	1574.7	1441.7	1582.6	3738.0
1578.2	777.7	1578.3	976.1	1577.4	1805.2	1585.6	2091.1
1581.8	237.0	1582.5	1096.3	1579.6	1303.7	1588.7	696.2
1585.6	284.3					1591.4	568.9
						1593.8	375.1
		1587.9	1168.6	1585.4	575.0	1596.0	489.0
1588.9	311.3			1590.1	3513.1	1599.0	953.9
1591.7	247.4	1591.8	909.1	1595.1	1246.0	1602.0	2657.7
1601.6	677.6	1601.6	4547.9	1601.0	5549.9	1605.7	2362.1
1603.8	956.1			1603.9	1463.5	1608.9	3883.2
1607.9	989.5	1609.9	1363.6	1610.0	415.3	1612.2	2301.7
1611.8	420.1	1614.9	453.8	1612.8	726.9	1623.8	218.1
1617.3	293.0	1617.5	878.7	1615.5	327.1	1634.7	1100.9
1620.7	636.3	1621.2	564.1	1620.6	620.6		
1624.6	1337.1	1624.7	1423.8	1624.9	535.3		
		1630.1	849.3	1629.8	380.9		
		1633.4	1096.5	1633.0	968.3		

1826.8	713.8	1826.9	883.7			1819.0	507.1
1832.8	300.3	1832.3	385.9	1831.6	889.2	1822.9	1814.8
1836.6	546.5	1836.5	608.9			1827.7	2042.1
		1839.4	2061.2	1839.0	2180.8		
1841.7	1175.4						
		1844.2	2772.8	1843.2	4252.9	1833.8	1449.6
1845.7	487.6	1846.3	1520.4	1845.2	6203.8	1837.1	7313.5
1848.4	571.7			1847.7	3204.9	1839.6	5891.9
1851.5	607.7	1851.0	2513.1	1851.5	1819.9	1845.3	1834.1
1854.7	548.9	1855.8	1276.0	1855.4	1562.8	1849.7	2803.6
1858.2	812.9	1859.4	785.6	1857.8	1754.3	1852.1	2203.6
1861.2	435.6	1862.5	380.8	1861.3	1490.1	1855.4	457.1
1865.2	255.9	1865.0	319.0	1865.3	443.1	1858.4	260.1
		1893.2	634.6			1887.7	582.6
1895.6	2983.4	1895.4	4423.5	1895.5	4260.9	1890.8	3041.6
		1906.4	595.7	1906.6	650.8		
1909.8	204.0	1910.8	1416.1	1911.2	2083.6	1906.8	1005.1
1913.3	321.2	1914.1	3273.2	1914.3	7635.7	1909.5	1181.1
1916.2	828.0						
		1917.1	2422.3	1918.3	4555.5	1912.1	2293.5
1918.9	372.9						
1920.6	216.7	1920.8	1673.8	1921.1	3494.4	1914.9	3042.8
		1923.3	1037.4	1923.4	1231.9	1917.6	1307.8
1925.6	270.5	1926.1	846.3	1925.5	428.4		
1928.7	282.9	1929.9	1174.8	1828.5	857.5	1923.5	768.6
1931.1	350.5	1932.0	327.5	1931.0	1072.2	1927.6	1303.7
1934.3	261.8	1934.6	741.5	1934.9	1247.6		
1937.6	1317.2	1937.1	3015.2	1937.7	1257.5		
1941.7	958.0	1941.3	1628.3				
		1944.4	360.2	1944.2	1243.0	1935.4	1785.3
1946.5	1005.7	1947.0	1556.1	1946.9	4355.0	1937.6	6099.0
1950.4	641.7	1949.9	517.2	1950.2	2184.7	1940.6	1578.4
						1944.0	416.6
1953.0	1922.1	1952.4	2908.0	1953.0	3875.6	1950.3	3210.1
1955.3	3980.8	1955.1	4910.4	1955.6	2501.9	1952.8	3592.1
						1958.2	1278.0

1960.2	255.9	1960.1	581.0	1959.6	1960.1	1960.9	1131.8
1988.3	1170.6					1963.8	1570.9
		1992.5	2178.8	1993.3	3584.4	1979.6	1244.3
				1995.0	1275.1	1981.8	644.8
1999.1	6641.4	1998.6	25034.5	1999.6	33228.0	1983.9	857.7
2003.5	5881.6	2002.0	3932.7			1986.9	3439.0
		2005.8	1353.1	2002.8	6970.6	1990.1	1957.7
				2007.6	715.5	1994.5	15339.9
2026.7	1481.0	2027.0	908.5	2026.0	725.8	2002.5	7872.3
2028.1	578.9			2028.9	1145.2	2005.0	6983.8
2035.2	14469.5	2034.8	8909.1	2033.5	409.6	2009.3	2711.6
2039.9	28318.0	2039.7	22703.6	2036.0	3541.7	2015.9	1162.5
				2041.0	15707.2	2019.7	1384.7
		2045.6	1402.8	2045.9	2238.0	2026.8	1908.3
		2051.1	4325.7	2050.5	2392.0	2030.4	1671.0
				2052.8	5429.5	2032.8	6179.7
		2060.0	373.2	2056.8	400.2	2036.6	3655.4
		2062.2	883.3			2039.2	2201.1
		2065.2	658.0	2062.4	953.4	2044.8	2666.2
		2069.5	328.7	2067.4	353.6	2047.4	1355.5
2072.6	843.8	2071.5	1008.8	2069.4	508.5	2059.0	540.7
2075.4	967.1	2074.3	2224.5	2072.8	3057.7	2061.0	1443.8
						2064.8	1345.2
2078.5	410.9	2077.6	2301.9	2076.3	3756.2	2067.7	1689.5
2081.3	359.4	2081.4	676.1			2069.8	1878.8
2084.1	422.5	2084.5	434.4	2079.6	3111.4	2073.7	447.8
				2085.8	1349.9	2076.8	617.3
2087.6	212.8	2087.2	681.2			2079.2	2125.1

2092.7	147.6	2089.7	251.7	2089.5	795.6	2081.4	1013.6
2095.7	362.7	2092.9	461.0	2092.5	594.6	2085.9	583.0
2104.8	542.8	2104.7	564.9	2104.7	585.9	2088.5	963.1
						2091.2	848.9
2122.0	833.7	2119.6	628.5	2119.5	893.8		
2128.5	9313.0	2122.2	969.1	2122.9	1631.5	2121.2	8279.6
2133.0	1509.4	2127.9	10705.1	2129.1	11290.1	2125.1	1966.4
2136.9	2765.0	2133.5	1109.4			2132.4	4622.2
2139.6	5695.5	2138.3	6496.9	2135.9	882.6	2137.0	10758.6
				2138.5	3421.1	2144.2	1153.8
2142.7	2165.3	2141.0	4495.0			2146.8	685.9
				2141.7	9768.9		
2145.5	827.9	2144.2	307.5	2146.4	721.1		
2148.0	697.5						
		2149.4	248.9	2148.9	634.5		
2150.2	339.8						
2157.9	400.1	2157.9	767.6	2151.8	1060.6		
2160.0	684.2			2156.5	259.5		
2164.1	6438.4	2163.9	5309.8	2165.0	4705.3	2157.5	5039.7
				2169.3	580.6		
2174.7	154.7	2173.0	210.0	2172.3	480.3		
2179.2	106.6	2176.7	353.9	2178.6	3835.4		
2181.7	204.7	2182.3	1547.6	2180.4	4513.7	2166.5	324.0
2184.1	382.5					2172.6	5074.3
2186.7	374.2	2187.0	1942.4	2187.4	4858.0	2178.8	2176.1
2189.6	350.0	2189.9	1538.4	2191.4	6279.0	2182.5	2589.1
2191.6	248.7	2192.3	2151.6			2184.5	1899.4
2194.6	458.0	2195.4	3094.5	2194.6	4782.3	2188.4	8063.0
2197.7	556.0	2198.7	4277.8	2198.2	9511.0	2193.9	12578.5
2201.0	624.0					2199.7	6318.3
2203.4	374.0	2202.6	3393.7	2203.2	10391.9	2202.6	1427.0
2206.3	265.6	2205.9	1924.5				
2208.2	265.9	2209.3	2806.3	2207.5	6581.1	2207.3	5504.0

2214.1	405.4	2214.5	3199.2	2211.0	1931.9	2212.3	7464.8
2221.1	196.7	2217.8	935.9	2213.8	3478.1	2218.2	1255.7
2223.4	335.9	2220.7	2127.7	2217.8	2685.0	2223.1	875.9
2235.9	202.3	2224.4	870.1	2221.1	4810.3	2226.5	1346.1
2241.4	145.0	2237.8	607.6	2223.4	3546.8	2241.1	6967.2
2243.6	465.9	2244.5	2626.1	2227.0	1901.9	2245.4	3136.9
2245.4	391.3	2247.4	1664.6	2241.2	274.8		
2247.6	358.8	2252.1	2066.0	2243.0	370.8		
2249.8	412.8	2257.5	220.5	2246.7	2675.2		
2252.4	440.4			2252.8	2806.3		
2254.4	247.7						
2256.8	150.7						
2259.6	180.3						
2269.1	345.8						

3.2. ICP-OES analysis

Besides the progress in computer sciences, improved technology resulted in the development of high-tech measuring instruments, equipped with software for the control of the apparatus as well as for the direct and rapid analysis of the spectral data. In a first part of the present section, certified reference materials are analyzed with a recent ICP-OE spectrometer (JY-138 Ultrace). Analyses are performed using the standard software (JYESS version 4.0) delivered with the instrument, and with our program ASDAP. The results are compared with the certified values. Furthermore, a careful comparison has been made with the values obtained by Janssens [JanF93b] on an older ICP-OE spectrometer (JY 38VHR). To enable this comparison, the same strategy is followed : the samples are treated in duplo, and the spectral measurements (at the same wavelengths) are repeated three times for each of them, and for each of the mono-element standard solutions. However, microwave digestion has been used instead of the time consuming conventional dissolution techniques. Finally, solid sample analysis of analogous reference materials combined with solid multi-element standard materials has also been performed using spark ablation. The final results of the solid sample analyses are critically evaluated in the present section.

The second part of this section deals with the determination of boron in a certified steel sample. Six spectral lines for boron have been selected. Five samples of the reference material are prepared using microwave digestion. Each of the samples are measured five times on each of the six selected spectral lines. The same measurement procedure has been followed for the mono-element reference solutions with specific concentrations. Calibration curves are constructed with both weighted and non-weighted linear regression using the results of ASDAP. The sensitivity for the selected spectral lines is discussed, and the detection limits are determined. The best procedures related to the final choice of the most sensitive spectral lines, reproducibility,... for the determination of B in steel are discussed.

3.2.1. Experimental set-up

3.2.1.1. Microwave apparatus

The power of the microwave Milestone 1200 mls mega apparatus is 1200 W with 1000 W delivered inside the working chamber. The power emission can be changed between 10 and 1000 W with 10 W increments. The microwave frequency is 2450 Mhz, equivalent to a wavelength of 12.25 cm. Several heating programs can be applied. The apparatus allows simultaneous digestion of 10 samples in high pressure vessels (up to 110 bar).

3.2.1.2. Preparation of solutions

a. Reagents

- Merck suprapur hydrochloric, nitric and hydrofluoric acid are used for the preparation of standard solutions and the dissolution of the samples.

- Water - deionized (Millipore, Milli Q).

b. Reference solutions

The calibration curves have been determined with reference solutions covering a concentration range of typically 2 or 3 orders of magnitude. These reference solutions have been prepared by dilution of mono-element standard solutions (Merck, of 1000 ppm) with the same concentration of acids used for the sample dissolution. The reference solutions always contained only one element of interest.

c. Steel AISI 4340 standard reference material 361 and steel AISI 94B17 standard reference material 362

The samples have been treated as follows : transfer 0.1 gram of the sample in a high pressure vessel for microwave digestion, and add slowly, in small portions of 0.25 ml, 3 ml HCl, 3 ml HNO₃ and 2 ml HF. Put the closed vessels in the microwave, and program the following scheme : 5 min. at 250W, 5 min. at 450W, 5 min. at 650W, and 5 min. at 250W. Let it cool down for 30 min. in a water bath. Dilute to 50 ml.

The addition of HF is necessary in order to obtain a complete dissolution of the samples.

d. Steel standard reference material ECRM287-1C

Several dissolution methods for the analysis of B in steel have been published [CoeA93, CoeA96, HlaI89]. After transferring 0.25 gram of the sample in a high pressure vessel for microwave digestion, three procedures presented in Table 3.3. are followed in order to obtain a complete dissolution. With procedures I [CoeA96] and II, a precipitate remained after the microwave digestion. After filtering and diluting to 100 ml, a preliminary analysis of the samples, showed that a substantial amount of boron was lost. Only with the third procedure [CoeA93] a complete dissolution of the steel ECRM287-1C sample could be realized.

Table 3.3. : Procedures for the microwave digestion of B in steel samples.

	Procedure I [CoeA96]	Procedure II	Procedure III [CoeA93]
solvents	1 ml HCl 0.5 ml HNO ₃ 5 ml H ₂ O 0.35 ml H ₂ SO ₄	5 ml HCl 2 ml HNO ₃ 10 ml H ₂ O	5 ml HCl 2 ml HNO ₃ 10 ml H ₂ O 0.5 ml HF
microwave conditions	30 min. at 400W	30 min. at 400W	30 min. at 400W
dilution	to 100 ml.	to 100 ml.	to 100 ml.

3.2.1.2. ICP-OE spectrometer

A Jobin-Yvon 138 ultrace ICP-OE spectrometer has been used for all analyses. It includes the following components : a sample introduction system, an electrical generator, an optical system, and a signal processing system. Each of these components will be discussed briefly.

a. Sample introduction system

Liquid sample introduction

Fig 3.24 shows the general sample introduction system. The sample is pumped with an identical and reproducible uptake rate for sample and standards into the nebulizer using a peristaltic pump. At the exit of the nebulizer, an Ar flow creates a primary aerosol and transports it through the spray chamber. Here, this primary aerosol is modified as it passes through the spray chamber because of evaporation, impact and drop shattering, inertial deposition, and gravitational settling. Hence, a secondary aerosol is created with a more homogenous droplet size distribution. At the end of the spray chamber, the largest drops are drained off. The secondary aerosol is then carried to the plasma through a sheathing device to the torch. The sheathing device envelops the aerosol with Ar gas in order to reduce problems of memory effects, pollution and crystallization in the injector. Furthermore, by varying the gas flow, the time that the sample spends in the plasma can be manipulated.

The torch, which is fully removable, consists of three concentric tubes creating three channels for argon flow. Through the external channel, flows the so-called cooling gas

which forms a thermic shield between the plasma and the outer tube, and forms also the bulk mass of the plasma and sustains it. The intermediate channel is used for the auxiliary gas that lifts the plasma away from the injector (central tube). This Ar gas is only used for the analysis of organic solutions. Finally, the aerosol carrier gas flows through the internal channel. The tube assembly is coaxially situated in the inductor or induction coil.

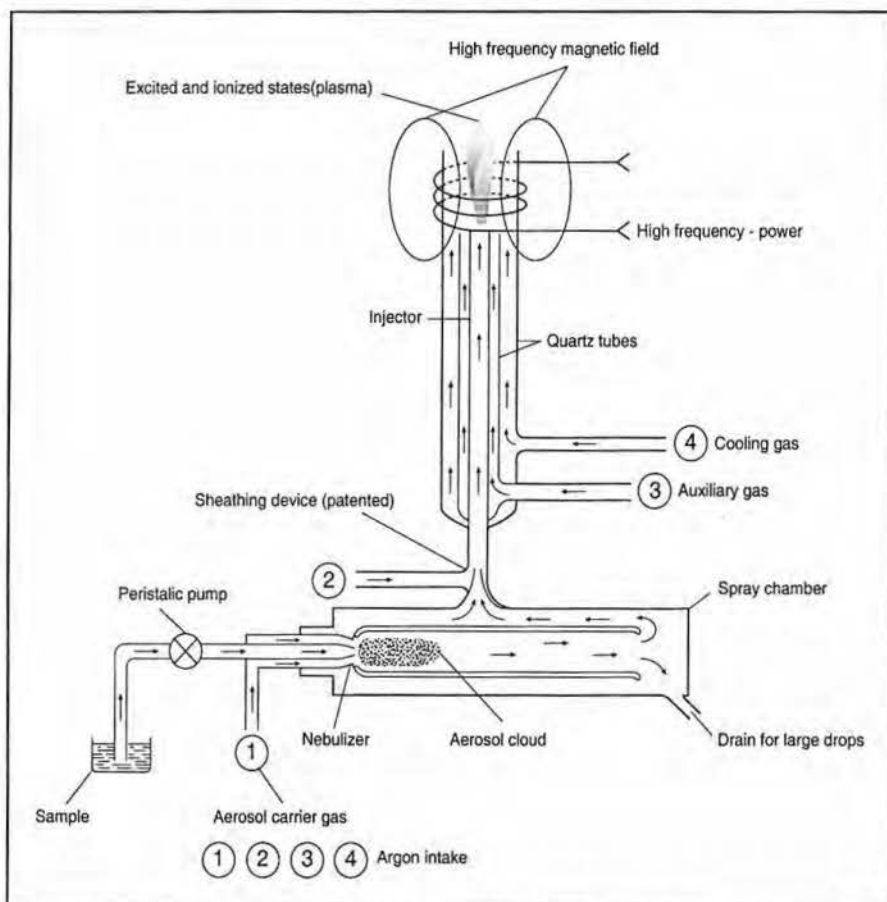


Fig. 3.24 : General liquid sample introduction system

A single drop of sample aerosol undergoes several processes as it travels through the plasma. As the drop is heated, solvent evaporates and leaves a solid analyte particle behind. After this particle is sufficiently heated, it begins to vaporize, atomize and sometimes ionize. A small fraction of the atoms and ions becomes excited, and emit light for ICP-OES.

Since the solutions contain hydrofluoric acid (see par 3.2.1.1.), a special introduction system (the HF cassette) is used including a cross flow nebulizer to create an aerosol, a black spray chamber to sort the droplets, a black sheath to envelop the aerosol with Ar gas, and a torch that carries the aerosol into the plasma.

The experimental conditions, like sample uptake, Ar gas flows and pressure,... are collected in Tabel 3.4.

Solid sample introduction

After extensive polishing of the discs, spark ablation sampling was carried out. The small particles sputtered from the surface of the disc are carried by a separate Ar gas flow through two traps, so that only the smallest particles are transported directly to the torch of the spectrometer. The rate of the separate Ar gas flow is 3 l min^{-1} , and its pressure is 4.4 bar. The sputtering process heats the discs and after a small number of sparks, the surface must be polished again.

Table 3.4 : Experimental conditions used in the present work

Sample uptake		1 ml min^{-1}
Gas flow rate (l min^{-1})	cooling	13
	sheating	0.23
	carrier	0.25
Ar pressure		3 bar
Observation height (mm)		15 mm
Power		1000 W
Anode current		0.40 A
Grid tension		150 mV
High voltage		4 kV

b. Generator

A tuned line RF generator (JY 2300) delivers the power required to obtain and maintain the plasma. It consists of three parts : a power supply unit delivering the power, an oscillator transforming the power into RF power at a frequency of 40.68 MHz, and a plasma box (or tuning box) on which the coil, which transfers the RF power to the plasma, is mounted.

The radio-frequency signal creates a changing magnetic field inside the coil in the flowing argon gas (Fig 3.25). The lines of the magnetic field are axially oriented inside the coil and take elliptical configuration outside it. A changing magnetic field induces a circulating current of charged particles (electrons and ions) in a conductor, which in turn heats the conductor due to the collision of the charged particles with other atoms. At room temperature, Ar is not a conductor, but it can be made electrically conductive if it is heated. To start the ICP discharge, a pilot electrical discharge absorbs energy from the magnetic field and turns rapidly into a stable plasma (self-sustaining).

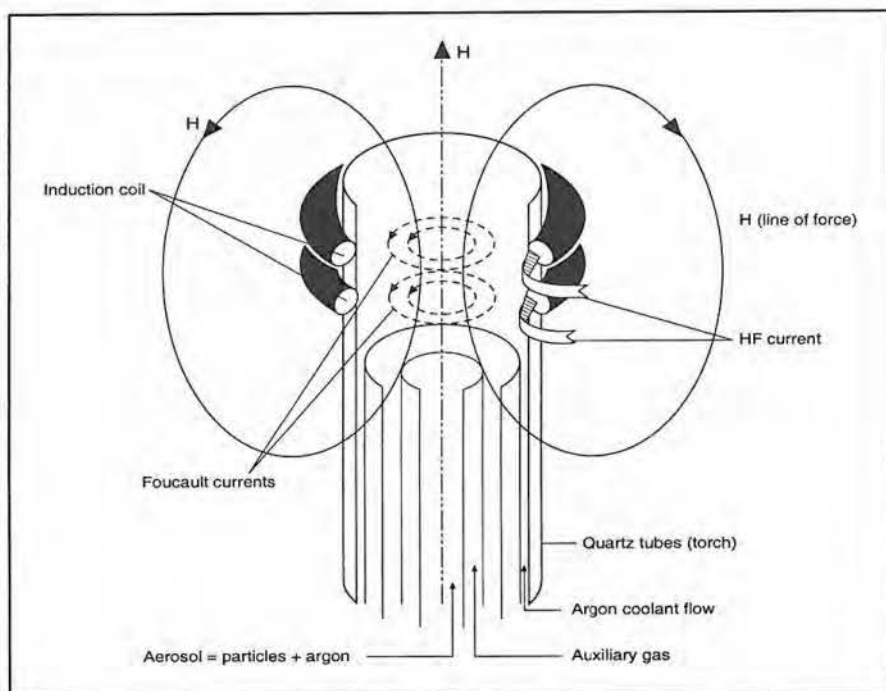


Fig. 3.25 : ICP discharge

c. Optical system

The light emitted by the plasma is guided to the monochromator entrance slit by a system of two lenses. The monochromator (Fig. 3.26) is of the Czerny-Turner type, with a fixed space between the input slit S1 and output slit S2, a planar grating G to diffract the light, and two mirrors (M1 and M2). A first one (M1) is located at the focal length (0.64 m) from the input slit, and reflects the beam on the grating, which rotates about its vertical axis. The diffracted light from the grating is focused by the second mirror (M2) to the output slit.

At this point, the light is collected in a photomultiplier where it is transformed into an electrical current.

The specific monochromator used in our Jobin-Yvon 138 ultrace ICP-OE spectrometer is a HR 1000 type. The high resolution grating has 2400 grooves per mm, and is used in second order. A spectral range between 160 and 800 nm can be studied with this grating. Two entrance slits of 8 and 17 μm , and two output slits of 17 and 78 μm are present.

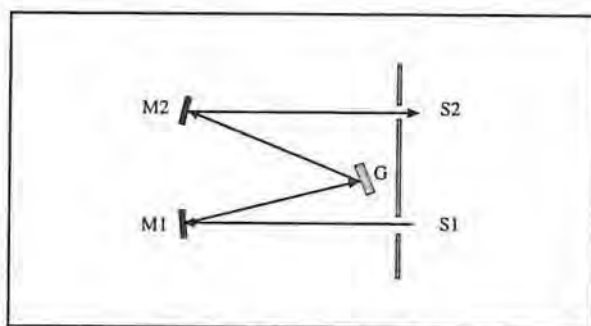


Fig 3.26 : Czerny-Turner configuration

Janssens [JanF93b] showed that Zimmermann's method (described in Chapter 1, eqs 1.32 - 1.34) is well suited for the determination of the t_0 and σ (or FWHM) values of the Gaussian component (central part) of a spectral line. In order to get an idea of the resolution of the spectrometer, which is related to the σ values of the resulting spectral profiles, the Mn(II) 2576.10 \AA spectral line of a 1 ppm standard solution is measured. The construction of the $Q(t)$ (eq. 1.32) and the linearization by Zimmermann method is presented in Fig. 3.27. From the slope of the fitted straight line, a σ value of $2.64 \cdot 10^{-3}$ nm is found using eq. 1.33. Janssens [JanF93b] obtained in a similar experiment on the older ICP-OE spectrometer (JY 38VHR, grating of 3600 grooves/mm used in first order), a σ value of $3.67 \cdot 10^{-3}$ nm. Hence, only a small resolution improvement is achieved with the JY-138 Ultrace.

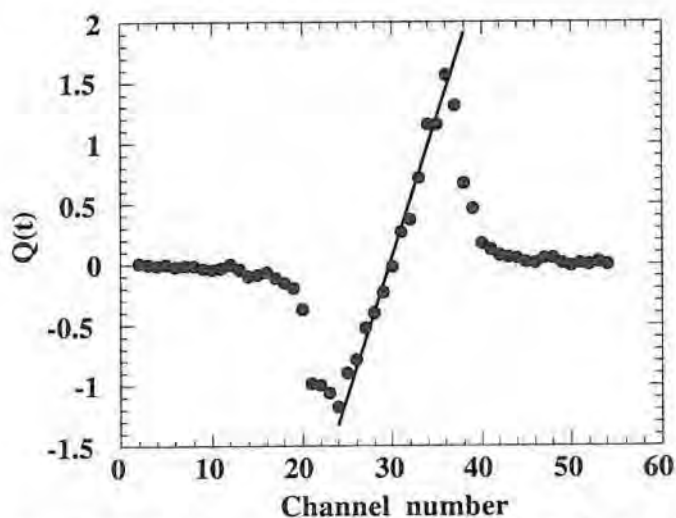


Fig. 3.27 : Linearization of the central part of the Mn(II) 2576.10 Å spectral line using Zimmermann's method. $Q(t)$ is defined by eq. 1.23.

3.2.2. Data handling

Two different strategies (A, B) for the measurements and for the data acquisition are applied for the quantification of the analytes in the studied samples.

A) The standard Jobin Yvon software searches first the position of the selected spectral line and optimizes the voltage of the photomultiplier. Then, it calculates the background, and fits a Gaussian function through the background corrected intensities of 7 points (the maximum and 3 points at each side). Finally, the value of the intensity at the position of the maximum is calculated. This is repeated five times (standard procedure) consecutively for each reference solution, and the mean value is stored in order to construct the calibration curve. This calibration curve is calculated using a linear least squares regression. The optional weighting is not performed. Finally, the unknown samples are measured in the same way, and the concentrations and standard deviations are displayed. The standard deviation is calculated from the values of the corresponding concentrations resulting from each of the five measurements.

B) The procedure, which precedes the analysis with ASDAP, is more complex. First the maximum of the selected spectral line is searched. It is positioned in the center of the selected window (60 channel numbers). Three spectra (in the analysis of the steel standard reference materials) or five spectra (in the analysis of boron in steel) for each of the

reference solutions and the unknown samples are recorded consecutively, and stored in different files. These files are transferred one by one to the DEC ALPHA 3000-800 central computer. They are analyzed separately by ASDAP using optimal digital filters for background correction and peak detection. After quantification of the net line areas of the selected spectral lines in the fitting procedure, these net line areas are given as input to MatLab 4.2c1, where the calibration curves are constructed using linear least squares procedures (non-weighted in the analysis of standard reference solutions, weighted in the analysis of boron in steel). Subsequently, the same program determines the concentrations and the corresponding 95% confidence intervals using the equations stated in Section 3.2.2.1. The program, developed for the analysis of boron in steel, using a weighted linear least squares regression is presented in Fig. 3.28.

```

% calibration ICP ANALYSES of boron in steel
% based on weighted linear least squares regression
% concentration of standards (ppm)
X = [1 4 10 20 40 100]
% input of the data set for the construction of the calibration curve
load file1.dat;
F=file1;
[n,s]=size(F);
sumF=sum(F);
meanF=mean(F);
stdF=std(F);
stdF2=stdF.^2;
weight=1./stdF2;
sumweight=sum(weight);
% Cochran test
maxstdF2=max(stdF2);
sumstdF2=sum(stdF2);
C=maxstdF2/sumstdF2
% Calibration curve
% a0 = intercept
% a1 = slope
% R = correlation coefficient
meanwX=(X*weight)/sumweight;
meanwF=(meanF*weight)/sumweight;
a1_a = X-meanwX;
a1_b = meanF-meanwF;
a1_c = weight.*a1_a.*a1_b;
suma1_c=sum(a1_c);
a1_d = weight.*a1_a.^2;
suma1_d=sum(a1_d);
a1=suma1_c/suma1_d
a0=meanwF-a1*meanwX
R=corcoef([X' meanF'])
e2=(meanF-(a1*X+a0)).^2;
sdc=((1/(s-2))*(e2*weight))^0.5;

```

```

T=[12.706 4.303 3.182 2.776 2.571 2.447 2.365 2.306 2.262 2.228 2.201 2.179
2.160 2.145 2.131 2.120 2.110 2.101 2.093 2.086 2.080 2.074 2.069];
% input of the unknown sample data
load sample.dat;
YS=sample;
[ns,ss]=size(YS);
meanYS=mean(YS);
stdYS=std(YS);
stdYS2=stdYS.^2;
weightYS=1./stdYS2;
X2=X.^2;
sumwX2=X2*weight;
sumwX=(X*weight).^2;
XS=(meanYS-a0)/a1
bi_a=1./(weightYS*ns);
bi_b=1/sumweight;
bi_c=(meanYS-meanwF).^2;
bi_d=bi_c.*sumweight;
bi_e=sumweight*sumwX2-sumwX;
bi_f=a1^2*bi_e;
bi_g=(bi_a+bi_b+(bi_d/bi_f)).^0.5;
bi_h=T(s-2).*sde./a1;
bi=bi_h.*bi_g
load exactmass.dat;
EM=exactmass;
% determination of concentration (ww%) and 95% confidence limits
yconc=XS.*100./(10.*EM)
clyconc=bi.*100./(10.*EM)
end;

```

Fig. 3.28 : MatLab program for calibration based on weighted linear least squares regression.

3.2.2.1. Calibration

Emission spectroscopy is not an absolute technique for the determination of analyte concentrations. However, the linear relationship (eq. 3.3) between the net line intensity (net line area) I of a spectral line and the concentration c of the emitting species enables its quantification through the construction of calibration curves.

$$I = a_0 + a_1 c \quad (3.3)$$

The linearity of these curves is ensured over a wide concentration range in ICP-OES.

Since the errors made in preparing the standards are significantly smaller than the measuring errors, it is usually assumed that the c values are not subject to error. The linear function (calibration curve) between the net line intensity (net line area) and the concentration can be determined using a linear least squares method. In the least squares method, it is assumed that the residuals e_i (deviations of the measurements I_i from their values predicted

by the calibration curve \hat{I}_i) are normally distributed random numbers, are mutually independent, and have all the same variance σ^2 (homoscedasticity). The latter condition is not always fulfilled. Homoscedasticity can be tested, for example, by Cochran's criterion. Therefore, replicate measurements are required to estimate the variances of the responses at the different c_i values. Cochran's criterion is based on comparing s_{\max}^2 with all other variances

$$C = \frac{s_{\max}^2}{\sum_j s_j^2} \quad (3.4)$$

Then, this C value is compared to a critical value C_{crit} [MasD97]. If C is smaller than C_{crit} , homoscedasticity can be assumed. In the case of heteroscedasticity, weighted least squares regression is required to overcome this problem. Here, weighting factors inversely proportional to the variances, are introduced.

$$w_i = 1/s_{\hat{I}_i}^2 \quad (3.5)$$

So that for all data points (c_i, I_i) , used to construct the calibration line, the most importance is given to the most precise points. The slope a_1 and the intercept a_0 of this line are found as

$$a_1 = \frac{\sum_i w_i (c_i - \bar{c}) (I_i - \bar{I})}{\sum_i w_i (c_i - \bar{c})^2} \quad (3.6)$$

$$a_0 = \bar{I} - a_1 \bar{c} \quad (3.7)$$

$$\text{with } \bar{c} = \frac{\sum_i w_i c_i}{\sum_i w_i} \quad (3.8)$$

$$\text{and } \bar{I} = \frac{\sum_i w_i I_i}{\sum_i w_i} \quad (3.9)$$

The standard deviations of the slope and the intercept are given by eqs. (3.10) and (3.11)

$$s_{a_1}^2 = \frac{s_{\hat{I}/c}^2}{\sum_i w_i (c_i - \bar{c})^2} \quad (3.10)$$

$$s_{a_0}^2 = s_{I/c}^2 \left(\frac{1}{n} + \frac{\bar{c}^2}{\sum_i w_i (c_i - \bar{c})^2} \right) \quad (3.11)$$

$$\text{with } s_{I/c}^2 = \frac{\sum_i w_i (I_i - \hat{I}_i)^2}{n-2} \quad (3.12)$$

and where $n-2$ is the number of degrees of freedom; n is the number of calibration points.

Using the expression of the standard deviation of a point on the calibration curve,

$$s_I^2 = s_{I/c}^2 \left(\frac{1}{n} + \frac{w_i (c_i - \bar{c})^2}{\sum_i w_i (c_i - \bar{c})^2} \right) \quad (3.13)$$

the corresponding confidence interval of that point is found as

$$\hat{y}_0 \pm t_{0.025;n-2} \left[s_{I/c}^2 \left(\frac{1}{n} + \frac{w_0 (c_0 - \bar{c})^2}{\sum_i w_i (c_i - \bar{c})^2} \right) \right]^{1/2} \quad (3.14)$$

The confidence limits that apply for the whole regression line are obtained by replacing $t_{0.025;n-2}$ by $\sqrt{2F_{0.05;2,n-2}}$ in eq. (3.14). These confidence curves are hyperbola and the area between them is called the Working-Hotelling confidence band. Fig. 3.29 shows the calibration curve for the Al (I) 3961.52Å line, obtained in Section 3.2.3.2, together with the Working-Hotelling confidence band.

The most important application of the calibration curve is the prediction of the concentration of an analyte in a sample c_s and its confidence interval, from the mean \bar{I}_s of N replicate determinations of I . It is found as

$$\frac{\bar{I}_s - a_0}{a_1} \pm t_{0.025;n-2} \left[\frac{s_{I/c}^2}{a_1^2} \left(\frac{1}{w_s N} + \frac{1}{\sum_i w_i} + \frac{(\bar{I}_s - \bar{I})^2 \sum_i w_i}{a_1^2 \left(\sum_i w_i \sum_i w_i c_i^2 - \left(\sum_i w_i c_i \right)^2 \right)} \right) \right]^{1/2} \quad (3.15)$$

with w_s the weighting factor applied for the sample measurement \bar{I}_s , and $t_{0.025, n-2}$ is the tabled t-value (one-sided) with $n-2$ degrees of freedom for a 95% confidence interval of c_s .

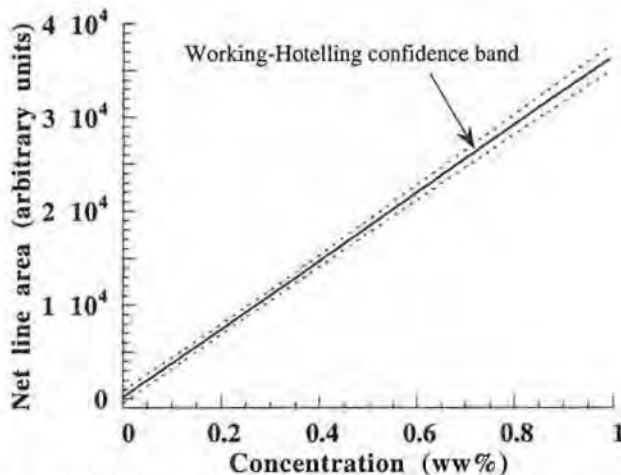


Fig.3.29 : Calibration curve of Al (I) 3961.52Å line together with the Working-Hotelling confidence band

3.2.3. Study of standard reference materials

In this section, we present the analysis of ICP-OE spectra obtained in the study of standard reference materials SRM 361 and SRM 362. The quantitative analyses are performed automatically using the standard Jobin Yvon software and independently with our program ASDAP. The results are compared with the certified values, and with the values obtained by Janssens [JanF93b] on the older JY38 VHR spectrometer. The analysis of spectra obtained after a liquid sample introduction of the prepared solutions and standard solutions, are presented in section 3.2.3.1., these of the spectra obtained after a solid sample introduction are discussed in section 3.2.3.2..

3.2.3.1. Liquid sample introduction

The unknown concentrations of the analytes in the samples, are determined by using calibration curves, which are constructed using the results for one-element reference solutions, as stated above. It has already been mentioned that each solution is measured only three times. From the statistical point of view, the mean of a small random check is not representative. Therefore, each net line area, resulting from the analysis of these spectra, represents one point at the calibration curve instead of the mean of the three measurements.

Subsequently, a MatLab program for linear least squares regression calculates the calibration curves, unknown concentrations, and the corresponding confidence intervals. The final results are collected in Tables 3.5 and 3.6, together with the results obtained with the Jobin Yvon software and the reported earlier results by Janssens [JanF93b].

Table 3.5. : Analysis (ww%) of standard reference material 361 (Steel AISI 4340)

Element	Wavelength (Å)	Certified	Jobin Yvon software	ASDAP	ASDAP [JanF93b]
Al (I)	3961.52	0.021 ± 0.005	0.022 ± 0.0007	0.021 ± 0.006	0.021 ± 0.004
Co (II)	2363.79	0.032 ± 0.001	0.14 ± 0.01	0.11 ± 0.002	*
	2286.16		0.032 ± 0.001	0.033 ± 0.004	0.028 ± 0.001
Cr (II)	2677.20	0.69 ± 0.005	0.69 ± 0.01	0.70 ± 0.004	0.66 ± 0.01
	2835.63		0.72 ± 0.02	0.69 ± 0.01	0.49 ± 0.03
Cu (I)	3247.54	0.042 ± 0.001	0.045 ± 0.0006	0.042 ± 0.0009	0.043 ± 0.002
Mn (II)	2576.10	0.66 ± 0.01	0.63 ± 0.006	0.63 ± 0.03	0.56 ± 0.02
Ni (II)	2216.47	2.0 ± 0.1	1.95 ± 0.06	1.97 ± 0.04	1.98 ± 0.03
Ti (II)	3349.41	0.020 ± 0.001	0.021 ± 0.0005	0.024 ± 0.007	0.014 ± 0.001

(*) no satisfying results or convergence could be obtained.

Table 3.6. : Analysis (ww%) of standard reference material 362 (Steel AISI 94B17)

Element	Wavelength (Å)	Certified	Jobin Yvon software	ASDAP	ASDAP [JanF93b]
Al (I)	3961.52	0.083 ± 0.001	0.076 ± 0.003	0.079 ± 0.006	0.080 ± 0.008
As (I)	2288.12	0.092 ± 0.005	0.089 ± 0.001	0.086 ± 0.003	0.092 ± 0.003
Co (II)	2363.79	0.30 ± 0.01	0.40 ± 0.008	0.36 ± 0.004	0.28 ± 0.01
	2286.16		0.30 ± 0.006	0.30 ± 0.008	0.28 ± 0.01
Cr (II)	2677.20	0.30 ± 0.01	0.31 ± 0.003	0.30 ± 0.003	0.30 ± 0.002
	2835.63		0.32 ± 0.004	0.31 ± 0.01	0.24 ± 0.01
Cu (I)	3247.54	0.50 ± 0.01	0.50 ± 0.004	0.48 ± 0.01	0.48 ± 0.003
Mn (II)	2576.10	1.04 ± 0.01	1.01 ± 0.003	1.02 ± 0.03	1.00 ± 0.02
Ni (II)	2216.47	0.59 ± 0.01	0.56 ± 0.04	0.57 ± 0.03	0.57 ± 0.14
Ti (II)	3349.41	0.097 ± 0.001	0.102 ± 0.002	0.120 ± 0.007	*

(*) no satisfying results or convergence could be obtained.

Since only mono-element reference solutions are used for the construction of the calibration curves, the corresponding spectra are simple; they are only hard to analyze for very small concentrations due to the background and noise. An example is shown in Fig. 3.30, where the spectrum of a 0.1 ppm As reference solution around the 2288.12 Å line is shown. Nevertheless, a good calibration curve can be constructed, as can be seen in Fig. 3.31, due to better signal/noise ratios for the spectra obtained for more concentrated As solutions.

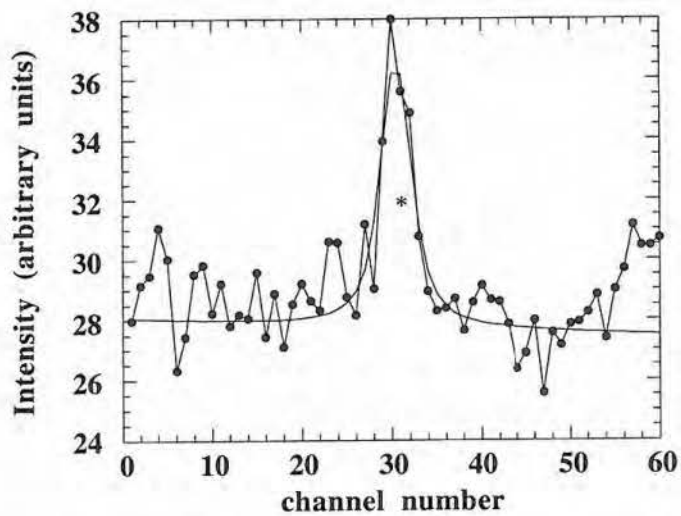


Fig. 3.30 : As(I) 2288.12 Å line, indicated by *, of a 0.1 ppm aqueous As solution. The full line represents the fitted As (I) 2288.12 Å line, increased by the polynomial background.

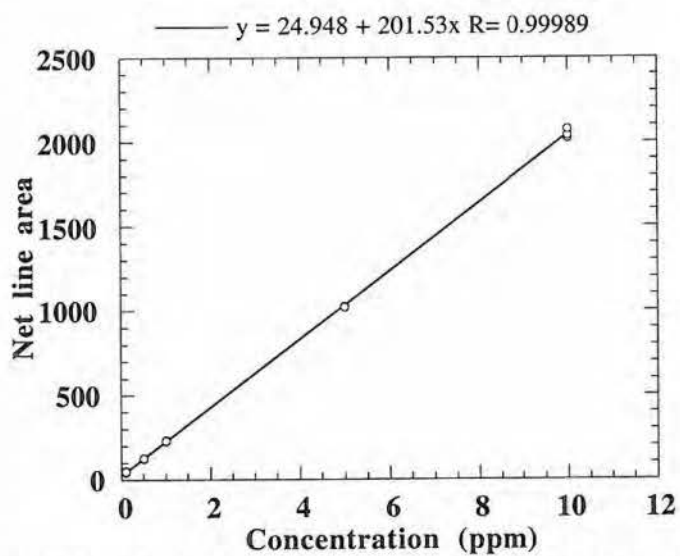


Fig 3.31 : Calibration curve for the determination of As (I) 2288.12 Å.

However, the limiting factor in this ICP-OES study is the analysis of the complex spectra resulting from the steel samples themselves. Figs 3.32a,b show the recorded spectra of the 2363.79 Å line of Co (II) in the steels SRM361 (a) and SRM362 (b), together with the individual lines computed by ASDAP. Tables 3.5 shows that even for ASDAP no satisfying results could be obtained for the determination of Co in the SRM361 steel using the 2363.79 Å line. The analyte line could not be completely resolved from the large interference at the right side of this line. As a consequence, an overestimation of the area under the spectral line was found which resulted in a too large concentration compared to the certified value. A ten times larger concentration of Co in the steel SRM 362, could be determined more accurately (see Table 3.6). Nevertheless, still a positive deviation of 20% was found. Figs 3.33a,b show that the 2286.16 Å line of Co (II) is much more appropriate for the determination of the Co concentration in the steels SRM 361 (a) and SRM 362 (b) (see Tables 3.5 and 3.6).

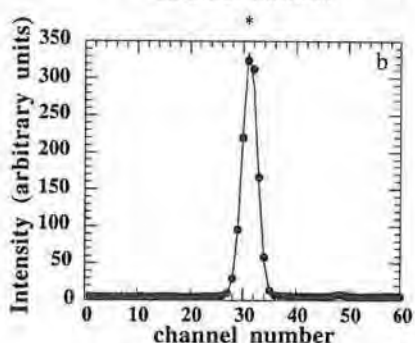
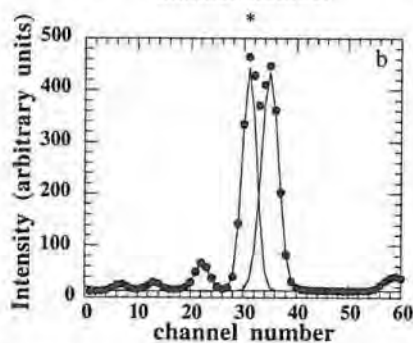
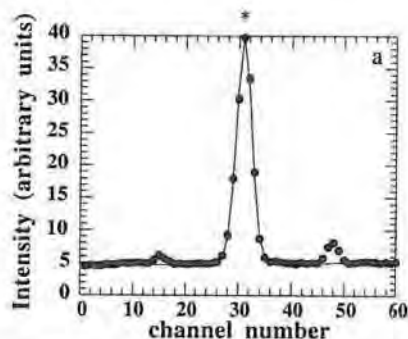
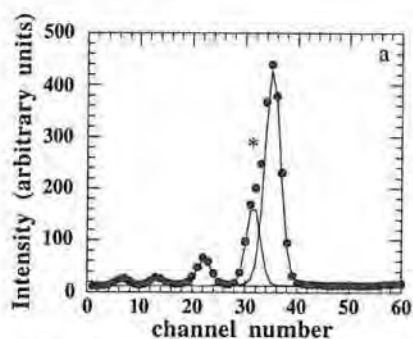


Fig. 3.32a,b : Co (II) 2363.79 Å line, indicated by *, in the steel SRM 361 (a), and SRM 362 (b), which is seriously interfered.

Fig 3.33a,b : Co (II) 2286.16 Å line, indicated by *, in the steel SRM 361 (a), and SRM 362 (b).

The two lines, 2677.20 Å and 2835.63 Å, of Cr (II) were found to be both suitable for the determination of the Cr concentration. Janssens [JanF93b], on the other hand, found a seriously lower concentration with the 2835.63 Å line.

Furthermore, he found no satisfying results or convergence for the quantification of Ti in SRM 362, and a much too small concentration in the SRM 361 steel. The contribution of this element could be determined successfully using the new Jobin Yvon software. ASDAP however, found too high concentrations.

3.2.3.2. Solid sample introduction

The major advantage of solid sample introduction is reduced contamination, since no dissolution and little sample preparation is generally required. However, a price must be paid. An absolute requirement is that the solid material should be conductive; insulators can be made conductive for the electric current by the addition of e.g. ultrapure graphite. Also a large set of solid standard reference materials, covering a wide concentration range of many analytes, is required in order to construct good calibration curves. In addition, the complexity of the recorded spectra can be different, since the standards can be composed of different interfering species, even in very different concentrations.

Furthermore, it was found that the reproducibility was not so good, compared to the recorded spectra after liquid sample introduction. For each selected spectral line, the standards and the unknown samples are analyzed three times consecutively at the same spot. Polishing was required after a small number of sparks which is also time consuming. The quantification of the analytes is discussed below.

As a consequence of the above mentioned difficulties, the correlation coefficients of the calibration curves, listed in Table 3.7, are all worse than those obtained for the liquid sample introduction. Furthermore, for some of the curves, the certified value of concentration of the analyte is situated near the edge of the calibration curve. Since the widths of the confidence intervals (eq. 3.15) are the smallest at the mean of the x-values, and increase away from it, predictions at the edges of a calibration curve must be calculated with caution. Together with the larger fluctuations in the calculated net line area of a spectral line (reproducibility), this results in larger confidence intervals for the predicted concentrations, as can be seen in Tables 3.8 and 3.9. Accurate results are obtained with ASDAP, however the corresponding 95% confidence intervals are large. Those resulting from the Jobin Yvon software are much smaller, since they are calculated from the standard deviation of the derived concentration, given a number of intensities measured from the sample at the

maximum of the specific spectral line and the calculated calibration curve. They do not at all depend on the reliability of the fitted calibration curve.

Fig 3.34 shows one of the three recorded ICP-OE spectra of the 2835.63 Å Cr (II) line in steel SRM 362 which contains 0.30 ww% Cr. Fig 3.35 represents also one of the three recorded ICP-OE spectra of a solid standard containing 0.443 ww% Cr. It reflects clearly the complexity of the spectra resulting from the solid standard, and the large fluctuations between consecutively measured data.

Table 3.7. : Correlation coefficients R of the calibration curves obtained using the spectra recorded after liquid sample introduction (LSI) and after solid sample introduction (SSI).

	Al (I) 3961.52 Å	Cr (II) 2677.20 Å	Cr (II) 2835.63 Å	Cu (I) 3247.54 Å	Mn (II) 2576.10 Å	Ni (II) 2216.47 Å	Ti (II) 3349.41 Å
LSI	0.99948	0.99996	0.99962	0.99999	0.99956	0.99935	0.99920
SSI	0.99868	0.99867	0.99780	0.99390	0.99824	0.99876	0.99944

Table 3.8. : Analysis (ww%) of standard reference material 361

	Wavelength (Å)	Certified	Jobin Yvon software	ASDAP
Al (I)	3961.52	0.021 ± 0.005	0.021 ± 0.001	0.021 ± 0.02
Cr (II)	2677.20	0.69 ± 0.05	0.67 ± 0.002	0.69 ± 0.05
	2835.63		0.68 ± 0.02	0.75 ± 0.07
Cu (I)	3247.54	0.042 ± 0.005	0.045 ± 0.002	0.042 ± 0.05
Mn (II)	2576.10	0.67 ± 0.05	0.66 ± 0.009	0.66 ± 0.08
Ni (II)	2216.47	2.0 ± 0.5	1.88 ± 0.13	1.97 ± 0.07
Ti (II)	3349.41	0.020 ± 0.005	0.021 ± 0.002	0.022 ± 0.009

Table 3.9. : Analysis (ww%) of standard reference material 362

	Wavelength (Å)	Certified	Jobin Yvon software	ASDAP
Al (I)	3961.52	0.081 ± 0.002	0.082 ± 0.001	0.088 ± 0.02
Cr (II)	2677.20	0.30 ± 0.01	0.30 ± 0.007	0.31 ± 0.06
	2835.63		0.28 ± 0.01	0.31 ± 0.07
Cu (I)	3247.54	0.51 ± 0.01	0.51 ± 0.06	0.47 ± 0.04
Mn (II)	2576.10	1.05 ± 0.01	1.03 ± 0.09	1.10 ± 0.1
Ni (II)	2216.47	0.59 ± 0.01	0.56 ± 0.04	0.54 ± 0.07
Ti (II)	3349.41	0.10 ± 0.004	0.10 ± 0.009	0.10 ± 0.009

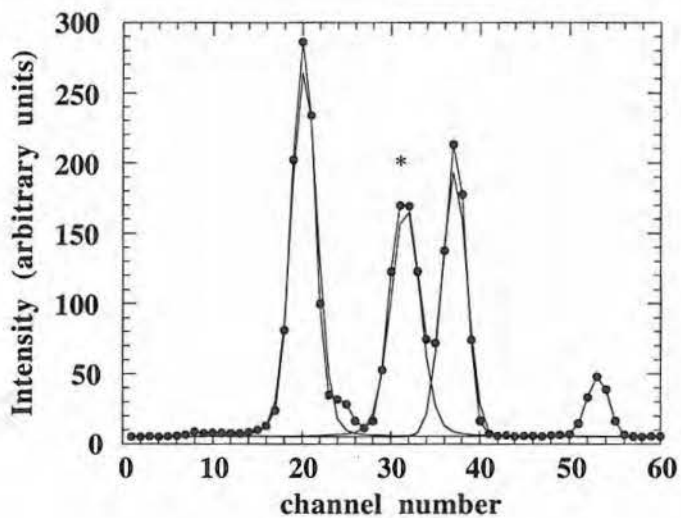


Fig. 3.34 : ICP-OE spectrum of solid steel SRM 362 containing 0.30 ww% Cr. The full lines represent the individual calculated components, the Cr (II) 2835.63 Å line, is indicated by *.

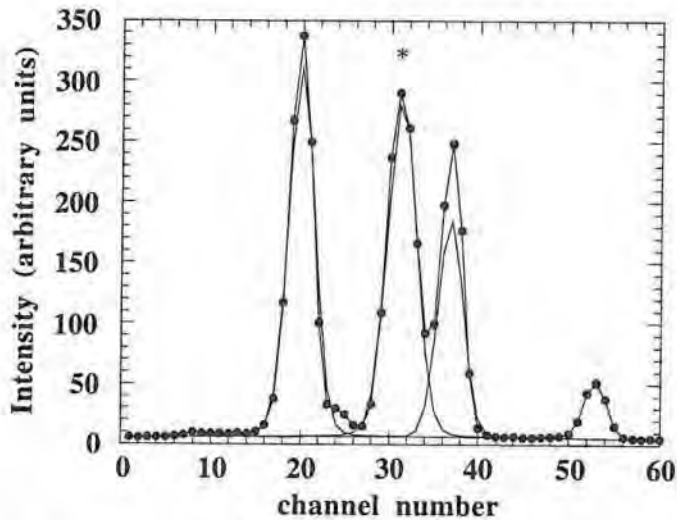


Fig. 3.35 : ICP-OE spectrum of a solid standard containing 0.443 ww% Cr. The full lines represent the individual calculated components , the Cr (II) 2835.63 Å line, is indicated by *.

3.2.3.3. Conclusions

From the study of ICP-OE spectra of standard reference materials, we can conclude the following :

- the quality of the ICP-OE spectra obtained with the JY-138 Ultrace is very good. The software delivered with the instrument produced good results in the absence of interferences. However, the calculation of the 95% confidence limits is only based on the precision of the measurements of the sample, not on the reliability of the calibration curves, resulting in underestimated values. The analysis performed with ASDAP, resulted in accurate determinations of the analyte concentrations, compared to the corresponding certified values. More realistic 95% confidence limits are obtained using the MatLab program based on linear least squares regression.

- solid sample introduction (of conducting materials) has the advantage to be a fast technique, with a minimum of preparations. However, it has been illustrated that the complexity of the spectra resulting from standard materials and the low reproducibility hamper the success of this technique.

3.2.4. Analysis of boron in steel

The boron concentration in steel is an important quantity since it influences certain mechanical properties, such as hardenability, hot workability, creep resistance, etc. Boron suppresses the occurrence of the intergranular fracture and consequently improves resistance to secondary embrittlement. Therefore, the precise and accurate determination of this element is required. Boron can be present in steels as various borides of iron, nickel, and chromium ; nitrides ; and carbides.

In the present study, the determination of the B concentration in a certified reference material ECRM287-1C, containing 0.89 ww% B, has been performed using calibration curves which have been constructed using one-element reference solutions. For each of the six spectral lines (1825.29, 1825.83, 2088.93, 2089.59, 2496.78, and 2497.73Å) that are considered, the results obtained with ASDAP are used to construct the calibration curves in three different ways :

- (1) each point is the mean of the analysis of five spectra,
weighted linear least squares regression
- (2) each point corresponds to the analysis of one spectrum,
linear least squares regression, no weights
- (3) each point is the mean of the analysis of five spectra,
linear least squares regression, no weights

A criterium (Cochran test) for the detection of non-constant variance is presented in section 3.2.2.1.. C-values for the six lines are calculated using the s_i^2 values resulting from the net line areas obtained by ASDAP : $C_{1825.29\text{Å}} = 0.51$, $C_{1825.83\text{Å}} = 0.50$, $C_{2088.93\text{Å}} = 0.66$, $C_{2089.59\text{Å}} = 0.78$, $C_{2496.78\text{Å}} = 0.91$, $C_{2498.091\text{Å}} = 0.59$. The critical C value for these experiments is equal to 0.48. This indicates non-constant variance, and weighted regression (1) should be performed. However, linear regression without weighting is performed on each of the individual measurements (2) and on each of the mean values resulting from the analysis of five spectra. The calibration procedure developed for the ICP software is based on non-weighted linear regression, and the corresponding confidence limits for an unknown concentration are calculated from the variance of the calculated concentrations using each of the measured intensities. It does not take any reliability of the computed calibration curve into account.

The results for each of the six lines are presented in Table 3.10. The deviations between the uncertainties calculated with the Jobin Yvon software, and computed following the calibration procedures (1) to (3) using the net line areas obtained with ASDAP, are small.

This is caused by the excellent quality of the calibration curves : very good reproducible spectra resulting in a small variances for the line intensities, and a good choice of reference solutions around the predicted concentrations.

Table 3.10. : Analysis (ww%) of boron in steel ECRM287-1C

Wavelength (Å)	Jobin Yvon software	(1)	ASDAP (2)	(3)
1825.29	0.79 ± 0.008	0.81 ± 0.008	0.82 ± 0.014	0.82 ± 0.018
1825.83	0.81 ± 0.007	0.82 ± 0.010	0.83 ± 0.015	0.83 ± 0.013
2088.93	0.82 ± 0.014	0.85 ± 0.018	0.86 ± 0.015	0.86 ± 0.026
2089.59	0.86 ± 0.008	0.85 ± 0.007	0.85 ± 0.013	0.85 ± 0.008
2496.78	0.88 ± 0.013	0.88 ± 0.009	0.88 ± 0.020	0.88 ± 0.015
2497.73	0.89 ± 0.006	0.87 ± 0.013	0.88 ± 0.013	0.88 ± 0.017

The first three lines do not result in an accurate prediction of the concentration. Fig. 3.36 shows a superposition of the six calibration curves. It can be seen that the sensitivity S , defined as the slope of the calibration curve, of the first three lines is low compared to that of the last three lines.

The detection limit c_L is defined as the concentration, derived from the smallest signal y_L that can be detected with a reasonable certainty for a given analytical procedure, where

$$y_L = y_{bl} + k s_{bl} \quad (3.16)$$

with y_{bl} the response of the blank, s_{bl} the standard deviation of the blank responses and k a constant. The detection limit c_L is now found as

$$c_L = k s_{bl} / S \quad (3.17)$$

with S , the sensitivity of the analytical method, corresponding to the slope of the calibration curve. IUPAC [IUPAC78] strongly recommends to use a value of $k = 3$.

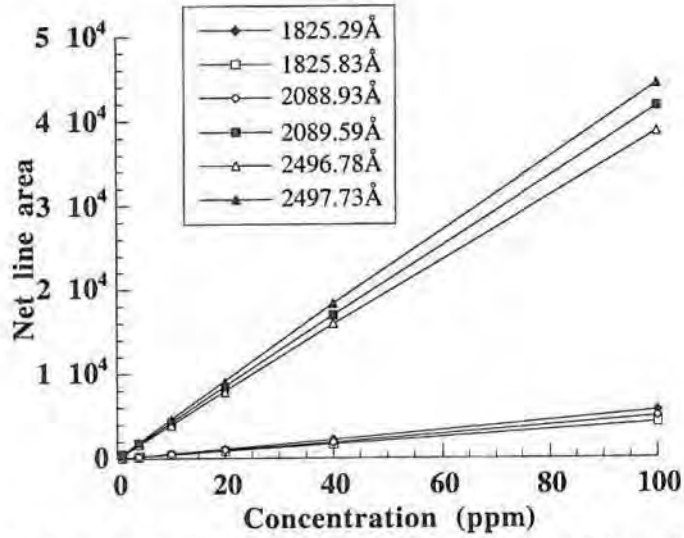


Fig 3.36 : Calibration curves for the determination of B in steel.

The detection limits are determined in ICP-OES as

$$c_L = k s_{bl} * c_n / y_n \quad (3.18)$$

with s_{bl} = standard deviation resulting from 10 measurements of the blank, y_n the net response corresponding to the concentration c_n .

Introducing the quantity BEC (Background Equivalent Concentration) defined as the concentration of an analyte that yields a net signal equal to the background intensity, or

$$BEC = y_{bl} * c_n / y_n = | \text{intercept of the calibration curve} | \quad (3.19)$$

In practice, BEC is determined by constructing a calibration curve using 10 repetition measurements of the lowest and the highest standard. BEC is then equal to the absolute value of the intercept of this calibration curve.

Finally, the detection limit determined in ICP-OES is found as

$$c_L = (k RSD_{bl} BEC) / 100 \quad (3.20)$$

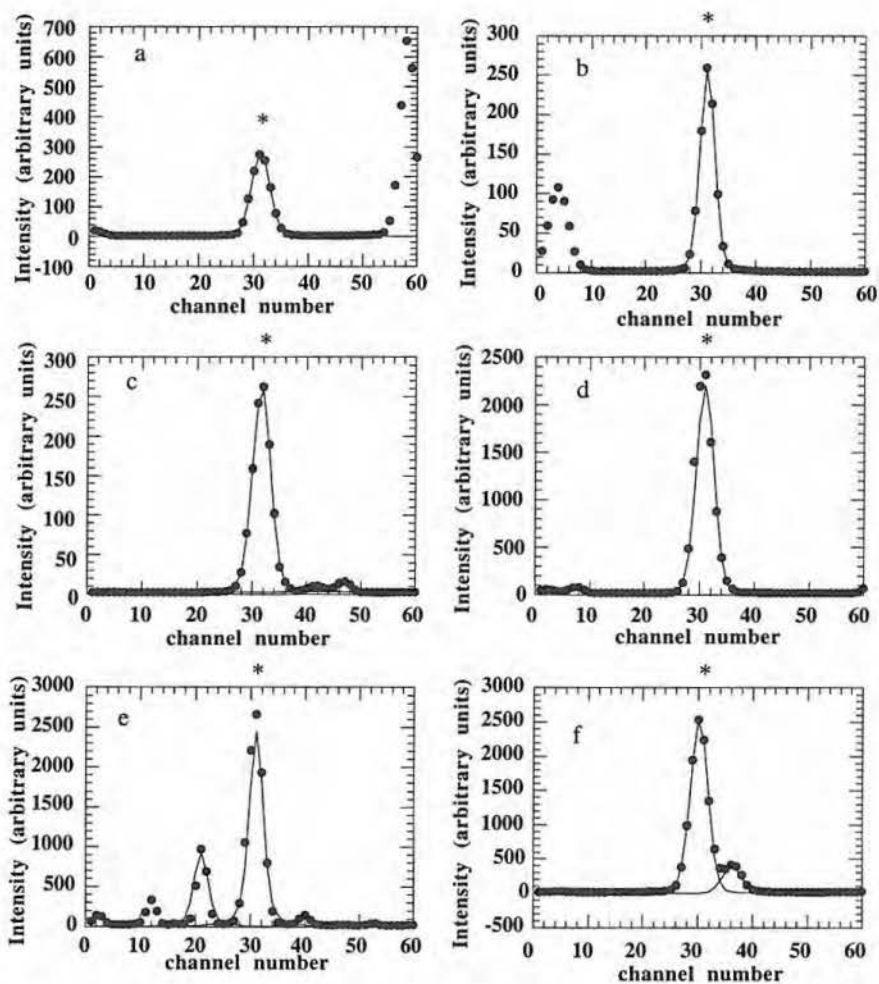
with $RSD_{bl} = 100 * s_{bl} / y_{bl}$ the relative standard deviation resulting from 10 measurements of the blank.

Table 3.11 shows the detection limits for the determination of B using each of the six spectral lines. It should be noted that the constant k is set equal to 3, nevertheless the Jobin Yvon software uses $k = 2$. The detection limits for the 1825.29, 2089.59, 2496.78, and 2497.73 Å lines are low (ppb).

Table 3.11. : Detection Limits for B

line (Å)	1825.29	1825.83	2088.93	2089.59	2496.78	2497.73
DL(ppb)	6.3	23.7	19.7	2.7	4.4	6.2

Figs 3.37a-f show the recorded and analyzed spectra for one sample in each spectral window around the selected spectral line. It can be seen that only for the two last spectral lines (e) 2496.78 Å, and (f) 2497.73 Å, problems can arise during the quantitative analysis of the corresponding spectra. The 2496.78 Å line is surrounded by three peaks diminishing the number of candidates for the background reference channels. As a consequence, the background polynomial is calculated using only a small number of points. Interference of a small peak in the right flank of the 2497.73 Å line can cause computational errors in the determination of the net line area of this peak. However, Table 3.10 shows that these problems do not seriously hamper the quantification of B in the steel sample under study. Hence, it can be concluded that the 2089.59, 2496.78 and 2497.73 Å lines are the most suitable spectral lines for the quantitative determination of B in steel.



Figs 3.37a-f : ICP-OE spectra (●) recorded of the certified reference material ECRM287-1C at the six spectral lines of B : (a) 1825.29, (b) 1825.83, (c) 2088.93, (d) 2089.59, (e) 2496.78, and (f) 2497.73 Å. The full lines represent the individual calculated components by ASDAP.

References Part I

- [AbrS63] Abramowitz S, and Bauman RP (1963) *J Chem Phys* 39 : 2757
- [ArmB67] Armstrong BH (1967) *J Quant Spectrosc Radiat Transfer* 7 : 61
- [BerD88] Bernholdt DE, Magers DH, and Bartlett RJ (1988) *J Chem Phys* 89 : 3612
- [BleR94] Bleil R, Tao FM, and Kais S (1994) *Chem Phys Letters* 229 : 491
- [BotP89] Botschwina P, and Sebald P (1989) *Chem Phys Lett* 160 : 485
- [BouP89] Boumans PWJM, ZhiZhuang H, Vrakking JJAM, Tielrooy JA, and Maessen FJM (1989) *Spectrochim Acta* 44B : 31-93
- [BowM93] Bowers MT, Kemper PR, Von Helden G, and Van Koppen M (1993) *Science* 260 : 1446
- [BraC92] Brabec CJ, Anderson E, Davidson BN, Kajihara SA, Zhang QM, Bernhole J, and Tomanek D (1992) *Phys Rev B* 46 : 7326
- [BroS96] Brown SD, Sum ST, and Despaigne F (1996) *Anal Chem* 68 : 21R
- [CurR97] Curl RF (1997) *Reviews Mod Phys* 69 : 691
- [DenD28] Dennison DM (1928) *Phys Rev* 31 : 503
- [DraS76] Drayson SR (1976) *J Quant Spectrosc Radiat Transfer* 16 : 611
- [DreM96] Dresselhaus MS, Dresselhaus G and Eklund PC (1996) *Science of Fullerenes and Carbon Nanotubes*, Academic Press, San Diego
- [DruJ85] Drummond JR, and Steckner M (1985) *J Quant Spectrosc Radiat Transfer* 34 : 517
- [FeyM92] Feyereisen M, Gutowski M, Simons J, and Almlöf J (1992) *J Chem Phys* 96 : 2926
- [FraD91a] Franco DV, Gelan J, Martens H, and Vanderzande DJ-M (1991) *Fuel* 70 : 811
- [FraD91b] Franco DV, Gelan J, Martens H, and Vanderzande DJ-M (1991) *Energy & Fuel* 5-6 : 527
- [FraJ90] François JP, and Janssens F (1990) *Spectrochim Acta* 45B : 177
- [FraR69] Fraser RDB, and Suzuki E (1969) *Anal Chem* 41 : 37
- [GauW69] Gautschi W (1969) *Comm ACM* 12 : 635
- [GauW70] Gautschi W (1970) *SIAM J Num Anal* 7 : 187
- [GieT94] Giesen TF, Van Orden A, Hwang HJ, Fellers RS, Provencal RA, and Saykally RJ *Science* (1994) 265 : 756
- [GorP90] Gorry PA (1990) *Anal Chem* 62 : 570
- [GraI80] Gradshteyn IS and Ryzhik IM (1980) *Table of Integrals, Series and Products*, Academic Press (corrected and enlarged edition)
- [GroJ95] Grossman JC, Mitas L, and Raghavachari K (1995) *Phys Rev Letters* 75 : 3870

References Part I

- [GuoT92] Guo T, Diener MD, Chai Y, Alford MJ, Haufler, McClure SM, Ohno T, Weaver JH, Scuseria GE, and Smalley RE (1992) *Science* 257 : 1661
- [HeaJ89] Heath JR, Cooksy AL, Gruebele MHW, Schmuttenmaer CA, and Saykally RJ (1989) *Science* 244 : 564
- [HeaJ90a] Heath JR, and Saykally RJ (1990) *J Chem Phys* 93 : 8392
- [HeaJ90b] Heath JR, Sheeks RA, Cooksy AL, and Saykally RJ (1990) *Science* 249 : 895
- [HeaJ91a] Heath JR, and Saykally RJ (1991) *J Chem Phys* 94 : 3271
- [HeaJ91b] Heath JR, and Saykally RJ (1991) *J Chem Phys* 94 : 1724
- [HeaJ91c] Heath JR, Van Orden A, Kuo E, and Saykally RJ (1991) *Chem Phys Lett* 182 : 17
- [HeaJ93] Heath JR, and Saykally RJ (1993) 'On clusters and clustering : from atoms to fractals', Edited by PJ Reynolds, Elsevier Amsterdam, and references therein
- [HofR66] Hoffmann R (1966) *Tetrahedron* 22 : 521
- [HuiA78] Hui AK, Armstrong BH, and Wray AA (1978) *J Quant Spectrosc Radiat Transfer* 19 : 509
- [HumJ79] Humlicek J (1979) *J Quant Spectrosc Radiat Transfer* 21 : 309
- [HumJ82] Humlicek J (1982) *J Quant Spectrosc Radiat Transfer* 27 : 437
- [HutJ94] Hutter J, Lüthi HP, and Diederich F (1994) *J Am Chem Soc* 116 : 750
- [IUPAC78] International Union of Pure and Applied Chemistry (1978) *Spectrochim Acta* 33 : 241
- [JanF91] Janssens F, and François JP (1991) *Anal Chem* 63 : 320
- [JanF92] Janssens F, and François JP (1992) *Appl Spectrosc* 46 : 283
- [JanF93a] Janssens F, and François JP (1993) *Anal Chem* 65 : 3098
- [JanF93b] Janssens F (1993) PhD 'Development of a computer program based on digital filtering techniques for qualitative and quantitative analysis of spectral data' Limburgs Universitair Centrum, B-3590 Diepenbeek
- [KarA78] Karp AH (1978) *J Quant Spectrosc Radiat Transfer* 20 : 379
- [KieJ73] Kielkopf JF (1973) *J Quant Spectrosc Radiat Transfer* 63 : 987
- [KraR92] Kranze RH, and Graham WRM (1992) *J Chem Phys* 64 : 2517
- [KraR93a] Kranze RH, and Graham RM (1993) *J Chem Phys* 98 : 71
- [KraR93b] Kranze RH, and Graham WRM (1993) *J Chem Phys* 98 : 71
- [KraR95] Kranze RH, Withey PA, Rittby CML, and Graham WRM (1995) *J Chem Phys* 103 : 6841
- [KraR96] Kranze RH, Rittby CML, and Graham WRM (1996) *J Chem Phys* 105 : 5313
- [KraW87] Krätschmer W, and Nachtigall K (1987) *Polycyclic aromatic hydrocarbons and astrophysics*, Edited by A Léger, L d'Hendecourt and N Boccarda, Reidel, Dordrecht

- [KroH87] Kroto HW (1987) *Nature* 329 : 529
- [KroH91] Kroto HW, Allaf AW, and Balm SP (1991) *Chem Rev* 91 : 1213
- [KroH92] Kroto HW (1992) *Angew Chem Int Ed Engl* 31 : 111
- [KroH97] Kroto HW (1997) *Reviews Mod Phys* 69 : 703
- [KunM97] Kuntz M (1997) *J Quant Spectrosc Radiat Transfer* 57(6) : 819
- [LevK44] Levenberg K (1944) *Quart Appl Maths* 2 : 164
- [MarD63] Marquardt DW (1963) *J Soc Indust Appl Maths* 11 : 431
- [MarJ89] Martin JML, François JP, and Gijbels R (1989) *J Chem Phys* 80 : 3403
- [MarJ90a] Martin JML, François JP, and Gijbels R (1990) *J Chem Phys* 93 : 8850
- [MarJ91a] Martin JML, François JP, and Gijbels R (1991) *J Comp Chem* 12 : 52
- [MarJ91b] Martin JML, François JP, and Gijbels R (1991) *J Chem Phys* 94 : 3753
- [MarJ91c] Martin JML, François JP, Gijbels R and Almlöf (1991) *Chem Phys Letters* 187 : 367
- [MarJ95a] Martin JML, El-Yazal J, and François JP (1995) *Chem Phys Letters* 242 : 570
- [MarJ95b] Martin JML, and Taylor PR (1995) *Chem Phys Lett* 240 : 521
- [MarJ96a] Martin JML, and Taylor PR (1996) *J Phys Chem* 100 : 6047
- [MarJ96b] Martin JML, Schwenke DW, Lee TJ, and Taylor PR (1996) *J Chem Phys* 104 : 4657
- [MarJ96c] Martin JML, El-Yazal J, and François JP (1996) *Chem Phys Letters* 252 : 9
- [MarJ96d] Martin JML, El-Yazal J, and François JP (1996) *Chem Phys Letters* 248 : 345
- [MarJ96e] Martin JML, El-Yazal J, and François JP (1996) *Chem Phys Letters* 255 : 7
- [MarJ96f] Martin JML (1996) *Chem Phys Letters* 255 : 1
- [MasD97] Massart DL, Vandeginste BGM, Buydens LMC, De Jong S, Lewi PH, and Smeyers-Verbeke J (1997) *Handbook of Chemometrics and Qualimetrics Part A*, Elsevier, Amsterdam
- [MatK88] Matsumura K, Kanamori H, Kawaguchi K, and Hirota E (1988) *J Chem Phys* 89 : 3491
- [MicD87] Michalska D, Chojnacki H, Hess BA, Jr, and Schaad LJ (1987) *Chem Phys Lett* 141 : 376
- [MoaN89a] Moazzen-Ahmadi N, Mc Kellar ARW, and Amano T (1989) *Chem Phys Lett* 157 : 1
- [MoaN89b] Moazzen-Ahmadi N, Mc Kellar ARW, and Amano T (1989) *J Chem Phys* 91 : 2140
- [MunH66a] Mundschenk H (1966) *Nucl Instrum Meth* 44 : 325
- [MunH66b] Mundschenk H (1966) *Nucl Instrum Meth* 45 : 77
- [NacK87] Nachtigall K (1987) *Infrarotspektroskopie an Kohlenstoffmolekülen (Diplomarbeit)* Max-Planck-Institut für Kernphysik, Heidelberg

References Part I

- [NAG87] NAG FORTRAN library, Numerical algorithms Group Limited, NAG Central Office, Oxford (1987)
- [NorR91] Norton RH, and Rinsland CP (1991) *Appl Opt* 30 : 389
- [OliJ77] Olivero JJ, and Longbothum RL (1977) *J Quant Spectrosc Radiat Transfer* 17 : 233
- [ParV91] Parasuk V, and Almlöf J (1991) *Chem Phys Letters* 144 : 187
- [PieJ77] Pierluissi JH, Vanderwood PC, and Gomez RB (1977) *J Quant Spectrosc Radiat Transfer* 18 : 555
- [PitJ66] Pitha J, and Jones RN (1966) *Can J Chem* 44 : 3031
- [PreJ97] Presilla-Márquez JD, Sheehy JA, Mills JD, Carrick PG, and Larson CW (1997) *Chem Phys Letters* 274 : 439
- [RagK94] Raghavachari K, Strout DL, Odom GK, Scuseria GE, Pople JA, Johnson BG, and Gill PMW (1994) *Chem Phys Letters* 214 : 357
- [ReiF13] Reiche F (1913) *Verhandlungen der Deutschen Physikalischen Gesellschaft* 15 : 3
- [SavA64] Savitsky A, and Golay MJE (1964) *Anal Chem* 36 : 1627
- [SchF92] Schreier F (1992) *J Quant Spectrosc Radiat Transfer* 48 : 743
- [SchS96] Schreurs S, and François JP (1996) *Fres J Anal Chem* 355 : 726
- [SheL89] Shen LS, and Graham WRM (1989) *J Chem Phys* 91 : 5115
- [SlaZ92a] Slanina Z, Kurtz J, and Adamowicz L (1992) *Chem Phys Lett* 196 : 208
- [SlaZ92b] Slanina Z, and Adamowicz L (1992) *Thermochem Acta* 205 : 299
- [SlaZ94] Slanina Z, Lee SL, François JP, Kurtz J, Adamowicz L, and Smigel M (1994) *Mol Phys* 81 : 1489
- [SmaR97] Smalley RE (1997) *Reviews Mod Phys* 69 : 723
- [SmiA94] Smith AM, Agreiter J, Hartle M, Engel C, and Bondybey VE (1994) *Chem Phys* 189 : 315
- [SzcJ95] Szczepanski J, Ekern S, and Vala M (1995) *J Phys Chem* 99 : 8002
- [SzcJ96] Szczepanski J, Ekern S, Chapo C, and Vala M (1996) *Chem Phys* 221 : 359
- [TayP86a] Taylor P, and Schutyser P (1986) *Spectrochim Acta* 41B : 81
- [TayP86b] Taylor P, and Schutyser P (1986) *Spectrochim Acta* 41B : 1055
- [TayP95] Taylor PR, Bylaska E, Weare JH, and Kawai R (1995) *Chem Phys Letters* 235 : 558. Note that the tables in this paper contain a number of significant misprints ; for corrections see the comments in the file at the URL
<ftp://ftp.sdsc.edu/pub/sdsc/chemistry/structures/C20/README>
- [ThoK71] Thompson KR, DeKock RL, and Weltner W, Jr (1971) *J Am Chem Soc* 93 : 4688
- [ValM89] Vala M, Chandrasekhar TM, Szczepanski J, Van Zee R, and Weltner W, Jr (1989) *J Chem Phys* 90 : 595

- [ValM90a] Vala M, Chandrasekhar TM, Szczepanski J, and Pellow R (1990) *J Mol Structure* 222 : 209
- [ValM90b] Vala M, Chandrasekhar TM, Szczepanski J, and Pellow R (1990) *High Temp Sci* 27 : 19
- [VanA96] Van Orden A, Provencal RA, Keutsch FN, and Saykally RJ (1996) *J Chem Phys* 105 : 6111
- [VanH46] Van de Hulst HC (1946) *Bull Insts Netherlds* 10 : 79
- [VanH47] Van de Hulst HC, and Reesinck JJM (1947) *Astrophys J* 106 : 121
- [VanP87] Van der Plas, Uitbeijerse E, deLoos - Vollebregt LTC, and De Galan L (1987) *Spectrochim Acta* 42B : 1027
- [VonG93a] Von Helden G, Gotts NG, and Bowers MT (1993) *Chem Phys Letters* 212 : 241
- [VonG93b] Von Helden G, Hsu MT, Gotts NG, and Bowers MT (1993) *J Phys Chem* 97 : 8182
- [VonG93c] Von Helden G, Hsu MT, Gotts NG, Kemper PR, and Bowers MT (1993) *Chem Phys Letters* 204 : 15
- [WanS97] Wang SL, Rittby CML, and Graham WRM (1997) *J Chem Phys* 16 : 6032
- [WatJ92] Watts JD (1992) *J Chem Phys* 97 : 2372
- [WatR87] Watters RL, Carroll RJ, and Spiegelman CH (1987) *Anal Chem* 59 : 1639
- [WelW64] Weltner W, Jr, and McLeod D, Jr (1964) *J Chem Phys* 40 : 1305
- [WelW89] Weltner W, Jr, and Van Zee RJ (1989) *Chem Rev* 89 : 1713
- [WelW90] Weltner W, Jr, and Van Zee RJ (1990) *J Molec Struc* 222 : 201
- [WhiE68] Whiting EE (1968) *J Quant Spectrosc Radiat Transfer* 8 : 1379
- [ZaiA70] Zaidel AN, Prokof'ev VK, Raiskii SM, Slavnyi VA, and Shreider EY (1970) *Tables of Spectral lines*, IFI/PLENUM, NY-London
- [ZimW61] Zimmermann W (1961) *Rev Sci Instr* 32 : 1063

Part II

Analysis of multicomponent decay curves

Chapter 4 : The use of digital filtering in the analysis of multicomponent decay curves

Chapter 5 : The combined use of the improved methods of Gardner and Prony

Chapter 6 : Evaluation on simulated decay curves

Chapter 7 : Qualitative and quantitative applications

Analysis of multicomponent decay curves

The analysis of exponential decay curves has been the subject of many theoretical and practical studies. A lot of different techniques have been developed based on e.g. graphical extraction [ManP70], linear [HunG69, PaaP69] and non linear [VarJ85] least squares methods, singular value decomposition [KunS83, BarH87, LupM95], Fourier transformations [GarD59, SchJ73, SmiM74, CohS75a, CohS75b], and Prony's method [ProR95, OsbM75, OsbM91, OsbM95]. Unfortunately, the success of these techniques is often hampered by the ill conditioning property of the exponential-sum fitting problem. Furthermore, the final results seem to depend strongly upon the input of the correct number of exponential components n , and upon the initial estimates of the pre-exponential factors N_i^0 and decay constants λ_i . Many of these methods were further optimized and adjusted to specific problems so that the general applicability of a successful optimization is often lost.

As a challenge, we tried to use digital filters (proposed in Part I) in the analysis of multicomponent decay curves. It seemed to us that their use could reveal some valuable information about the number of components present in the decay curve and their corresponding decay constants. This primary detection procedure was a strategy that was used successfully in the analysis of spectral data (see Part I). Unfortunately, in Chapter 4, it will be shown that zero area Gaussian filters are not able to give a simple solution for the analysis of multicomponent decay curves. Even the use of square wave filters resulted in expressions which are very difficult to handle.

In the literature, a method was described which could reveal information about the number of components and the corresponding decay constants, i.e. the method of Gardner and co-workers [GarD59], which will be furtheron denoted as the GGM method. In 1795, the method of Prony [ProR95] was developed for the quantification of the parameters N_i^0 and λ_i using the number of components n . Each of these methods have been extensively improved in the past.

In 1959, Gardner and coworkers [GarD59] published a method to analyze a multicomponent decay curve composed as a sum of independent exponential functions, based on non linear transformations of the variables and on Fourier transformations. At that time, the method did not gain much success as the numerical evaluation of these Fourier transformations was difficult and tedious. After the development of the Fast Fourier Transform (FFT) technique [CooJ65], the method was improved by Schlesinger [SchJ73]

and, independently, by Smith and Cohn-Sfetcu [SmiM74, CohS75a, CohS75b, SmiM76]. Additionally, Schlesinger and the Cohn-Sfetcu group combined the technique with an adequate low-pass filter in order to decrease the effects of computational noise and of the high frequency noise normally present in experimental data. The best results were obtained with a Gaussian low-pass filter. They also showed that the improved method of Gardner et al. was able to analyze all kinds of multicomponent decay curves as long as the model functions were known. The improved method results in a continuous spectrum in which the number of real peaks is equal the number of components n , their positions are good estimates for the decay constants λ_i and the intensities are proportional to the pre-exponential factors N_i^0 each divided by the corresponding decay constant λ_i .

The method of Prony [ProR95, OsbM75, OsbM91, OsbM95] was published for the first time in 1795 [ProR95]. The technique is based on a separation of the linear N_i^0 and non linear parameters λ_i . The original version was extensively evaluated by Lanczos [LanC56]. He showed that the method was numerically unstable, was not able to analyze a tri-exponential function unambiguously, and failed completely in the presence of noise. Two hundred years after Prony, Osborne and coworkers [OsbM91, OsbM95] published two versions of an improved method of Prony, namely the recurrence and the difference versions. Osborne et al. published a detailed mathematical study of these new versions of Prony's method in which they proved the asymptotic stability of the method. They compared the technique with the Marquardt-Levenberg algorithm [MarD63, LevK44] on simulated decay curves, and concluded that the improved methods of Prony converge rapidly and are remarkably tolerant for poor starting values.

The original methods of Gardner et al. and Prony and their improvements are discussed and evaluated by Schreurs [SchS96]. Furthermore, the practical applicability of the combined use of both methods was illustrated in a preliminary analysis of free induction decay (^1H NMR) curves in order to detect the number of phases in polymer systems.

In the present part, it will be shown that the combination of these methods results in a powerful technique for the analysis of multicomponent decay curves. The theory and implementation of these improved methods of Gardner et al. and Prony are discussed in detail in Chapter 5. The combination of both methods is realized by the implementation of a cubic spline interpolation method. The characteristics of the methods are revealed after an extensive evaluation of their performance on simulated decay curves in Chapter 6. And finally, in Chapter 7, the applicability of their combined use is illustrated in the analyses of multicomponent decay curves obtained in fluorescence spectrometry, solid state ^1H NMR spectrometry, and radiochemistry [SchS98, SchSx1, SchSx2].

Chapter 4

The use of digital filtering in the analysis of multicomponent decay curves

Digital filters and more specifically zero-area Gaussian filters, are proposed in Part I in order to unravel complex spectral data. The transformation of the original spectrum into the first and second order convolution spectra has the advantage that with a proper choice of filter parameters, the resolution and signal/noise ratio can be enhanced in order to perform a more accurate qualitative analysis (number of peaks and their positions). As a result of a better peak detection procedure, the subsequent fitting procedure can yield a better quantitative analysis. This technique has been applied with success in the analysis of IR and ICP-OE spectra.

In the present part, a complete different problem is handled, namely the analysis of multicomponent decay curves. The above mentioned idea of transforming the original data, was the incentive for using digital filters on these data. Curious about the appearance of the transformed spectra, exponential decay curves were simulated and the first and second order convolution signals calculated using a simple zero-area square wave filter. This filter is a symmetric rectangular (square) fold-in function with unit intensity in both the positive central (size : M) and negative side windows (size : $M/2$).

The discussion of the results, in Section 4.1., shows that it could be possible to obtain some valuable information about the number of components present in the decay curve and their corresponding decay constants. The theoretical considerations in order to quantify this information is presented in Section 4.2.. It will further be shown that even the use of a simple zero-area square wave filter results in a difficult evaluation.

4.1. Examples

Digital filtering using a square wave filter is performed on simulated decay curves with the following characteristics : the decay curves have been calculated at discrete points in time t_i so that x_i , equal to $\ln t_i$, varies from 0 to 10, in equal steps $\Delta x = 0.25$.

$$f(t) = 100 \exp (-0.02 t) \quad (4.1)$$

$$f(t) = 100 [\exp (-0.5 t) + \exp (-0.1 t) + \exp (-0.02 t) + \exp (-0.004 t)] \quad (4.2)$$

Fig. 4.1 shows the calculated **R** and **S** signals obtained in the analysis of the data set resulting from a mono-exponential decay curve (eq. (4.1)). Both first and second order convolution signals are characterized by a single minimum at the same position but with one difference, namely that the shape of the **R** signal is asymmetric while that of the **S** signal is symmetric.

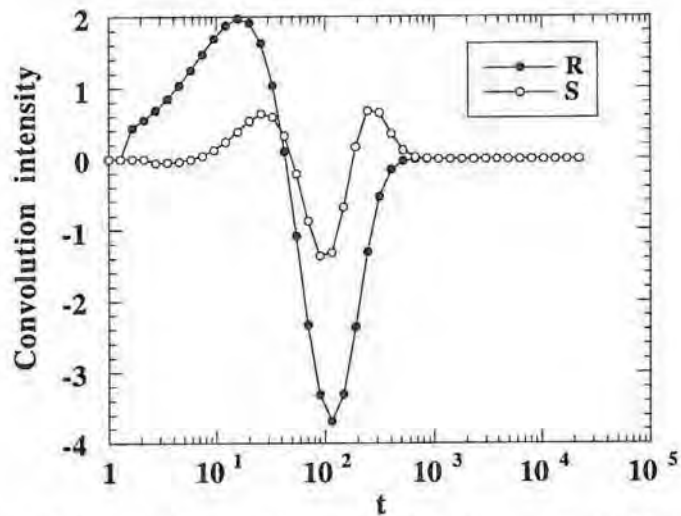


Fig. 4.1 : **R** and **S** signals obtained in the analysis of the data set obtained from eq. (4.1), with a square wave filter with $M = 2$ channels.

The **R** and **S** signals resulting from the analysis of a multicomponent decay curve (eq. (4.2)) are presented in Fig. 4.2. Here, the **R** signal has 4 minima, each situated at a lower intensity. The four minima of the **S** signal are better separated and they have approximately the same intensity.

It can thus be concluded that the number of minima in the **S** signal corresponds to the number of components in the decay curve and that components with similar pre-exponential factors will have similar **S** intensities.

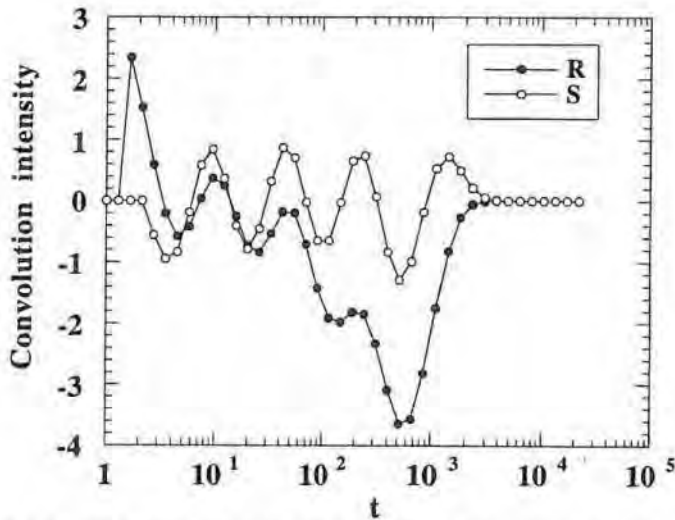


Fig. 4.2 : R and S signals obtained in the analysis of the data set obtained from eq. (4.2), with a square wave filter with $M = 2$ channels.

The following question naturally arises : is there a simple relationship between the value of the decay constants and the positions of the minima? Hence, the mathematical expressions for the R and S signals are needed.

4.2. Theoretical considerations

Let us first consider the following mono-exponential decay curve

$$N = N^0 \exp(-\lambda t) \tag{4.3}$$

In Section 4.1., data sets have been calculated at n_x discrete points in time t_i on a constant logarithmic scale. Hence,

$$t = \exp(a x) \tag{4.4}$$

where a is a constant, and x takes on the values $0, 1, 2, \dots, \theta, \dots$. Here, θ represents the value on the x axis where a minimum in the first order convolution signal R is found. It corresponds to a value $\tau = \exp(a \theta)$ on the t axis.

In this section, we will try to find a relationship between the τ (or θ) value and the unknown λ value of the original decay curve.

Using a square wave filter with width M (Fig 4.3), the expression for the R signal can be written as

$$R(\theta) = - \sum_{x=\theta-M}^{\theta-M/2} N^0 e^{-\lambda e^{ax}} + \sum_{x=\theta-M/2}^{\theta+M/2} N^0 e^{-\lambda e^{ax}} - \sum_{x=\theta+M/2}^{\theta+M} N^0 e^{-\lambda e^{ax}} \quad (4.5)$$

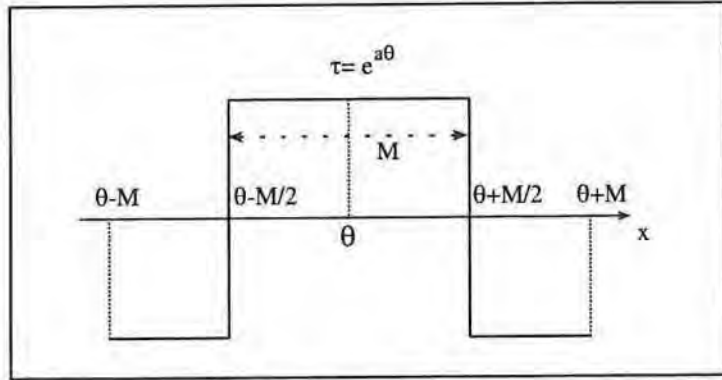


Fig. 4.3 : Square wave filter.

The expression for a continuous SWF is given by

$$R(\theta) = - \int_{\theta-M}^{\theta-M/2} N^0 e^{-\lambda e^{ax}} dx + \int_{\theta-M/2}^{\theta+M/2} N^0 e^{-\lambda e^{ax}} dx - \int_{\theta+M/2}^{\theta+M} N^0 e^{-\lambda e^{ax}} dx \quad (4.6)$$

Making the substitution $z = \lambda e^{ax}$, eq. (4.6) can be transformed as

$$R(\tau) = \frac{N^0}{a} \left(- \int_{\lambda \tau e^{-aM}}^{\lambda \tau e^{-aM/2}} \frac{e^{-z}}{z} dz + \int_{\lambda \tau e^{-aM/2}}^{\lambda \tau e^{aM/2}} \frac{e^{-z}}{z} dz - \int_{\lambda \tau e^{aM/2}}^{\lambda \tau e^{aM}} \frac{e^{-z}}{z} dz \right) \quad (4.7)$$

or

$$R(\tau) = \frac{N^0}{a} \left(E_1(\lambda \tau e^{aM}) - E_1(\lambda \tau e^{-aM}) + 2E_1(\lambda \tau e^{-aM/2}) - 2E_1(\lambda \tau e^{aM/2}) \right) \quad (4.8)$$

where

$$E_1(z) \equiv \int_z^{\infty} \frac{e^{-u}}{u} du$$

is the usual notation for the exponential integral.

In Section 4.1, it has been found that the number of exponentials is equal to the number of minima in the R signal. The relationship between the positions of these minima

and the corresponding values for the decay constants λ can be found by calculating the first derivative of R with respect to τ :

$$\frac{dR(\tau)}{d\tau} = \frac{N^0}{a\tau} \left(e^{-\lambda\tau} e^{-aM} - e^{-\lambda\tau} e^{aM} - 2e^{-\lambda\tau} e^{-aM/2} + 2e^{-\lambda\tau} e^{aM/2} \right) \quad (4.9)$$

The minima can be found from the condition

$$\frac{dR(\tau)}{d\tau} = 0$$

or from

$$e^{-\lambda\tau} e^{-aM} - e^{-\lambda\tau} e^{aM} = 2 \left(e^{-\lambda\tau} e^{-aM/2} - e^{-\lambda\tau} e^{aM/2} \right) \quad (4.10)$$

The R signal obtained with a square wave filter with $M = 2$ channels, and the corresponding first derivative of the data set simulated from eq. (4.1), is shown in Fig. 4.4.

In practice, the positions of the minima can be obtained from the graphical representation of the R signal. The value for the decay constant λ can be calculated from eq. (4.10). It is found that no simple relationship can be deduced between the position of a minimum in the R signal and the corresponding value for the decay constant λ .

The evaluation becomes even more complex for a multicomponent decay curve

$$N = \sum_{i=1}^n N_i^0 e^{-\lambda_i t} \quad (4.11)$$

where N_i^0 and λ_i represent the pre-exponential factor and decay constant of the i th component, respectively.

The first order convolution signal R can now be written as (cfr eq. (4.6))

$$R(\theta) = \sum_{i=1}^n N_i^0 \left(- \int_{\theta-M}^{\theta-M/2} e^{-\lambda_i e^{ax}} dx + \int_{\theta-M/2}^{\theta+M/2} e^{-\lambda_i e^{ax}} dx - \int_{\theta+M/2}^{\theta+M} e^{-\lambda_i e^{ax}} dx \right) \quad (4.12)$$

or

$$R(\tau) = \frac{1}{a} \sum_{i=1}^n N_i^0 \left(E_1(\lambda_i \tau e^{aM}) - E_1(\lambda_i \tau e^{-aM}) + 2E_1(\lambda_i \tau e^{-aM/2}) - 2E_1(\lambda_i \tau e^{aM/2}) \right) \quad (4.13)$$

The expression for the first derivative is given by

$$\frac{dR(\tau)}{d\tau} = \frac{1}{a\tau} \sum_{i=1}^n N_i \left(e^{-\lambda_i \tau} e^{-aM} - e^{-\lambda_i \tau} e^{aM} - 2e^{-\lambda_i \tau} e^{-aM/2} + 2e^{-\lambda_i \tau} e^{aM/2} \right) \quad (4.14)$$

and the condition for finding the minima is again $\frac{dR(\tau)}{d\tau} = 0$

Since the individual terms in the sum in eq. (4.14) can become negative, eq. (4.14) cannot be separated into n independent equations of the type (4.10) and eq. (4.14) must be solved completely, which cannot be done in a closed form.

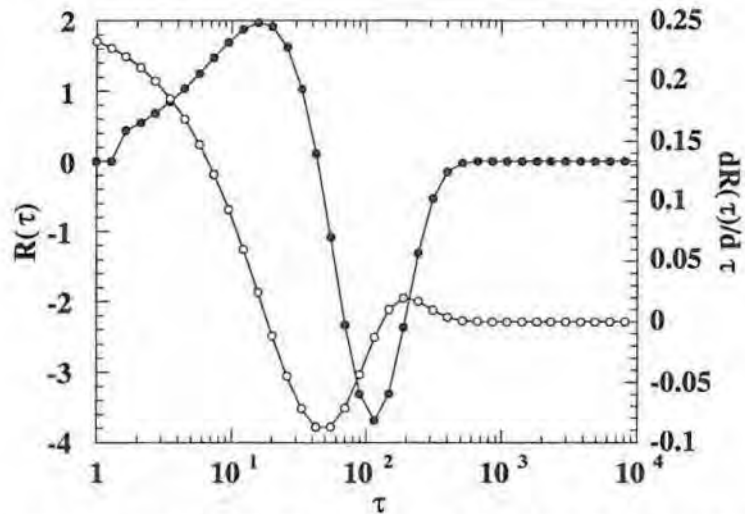


Fig. 4.4 : $R(\bullet)$ signal obtained with a square wave filter with $M = 2$ channels, and the corresponding first derivative (o) of the data set simulated from eq. (4.1).

The second order convolution signal S obtained with a square wave filter is given by eq. (4.15)

$$S(\theta) = - \sum_{\theta'=\theta-M}^{\theta-M/2} R(\theta') + \sum_{\theta'=\theta-M/2}^{\theta+M/2} R(\theta') - \sum_{\theta'=\theta+M/2}^{\theta+M} R(\theta') \quad (4.15)$$

or in continuous form as

$$S(\theta) = - \int_{\theta-M}^{\theta-M/2} R(\theta') d\theta' + \int_{\theta-M/2}^{\theta+M/2} R(\theta') d\theta' - \int_{\theta+M/2}^{\theta+M} R(\theta') d\theta' \quad (4.16)$$

The evaluation of $\frac{d S(\theta)}{d \theta}$ and the solution of the equation

$$\frac{d S(\theta)}{d \theta} = 0$$

is extremely complex and will not be considered further.

Principally, the **R** signal can be used to determine the number of components n present in a multicomponent decay curve. However, it was not possible to derive relationships between the minima in the **R** or **S** signals and the corresponding decay constants. Hence, this approach was abandoned and other methods were explored to unravel exponential decay curves. These methods are presented in the following chapters.

Chapter 5

The combined use of the improved methods of Gardner and Prony

In the introduction of Part II, a combination of two improved methods, namely the GGM method and Prony's method, is introduced as a powerful technique for the qualitative and quantitative analysis of multicomponent decay curves. In the present chapter, the theory and implementation (Sections 5.1. and 5.2.) of the latest revisions of these methods is presented in detail. In Section 5.3., the importance of a cubic interpolation method for the combination of the above mentioned methods is stressed.

5.1. Improved method of Gardner et al.

5.1.1. Theory

The original method of Gardner et al. [GarD59] considered a multicomponent exponential decay curve $f(t)$

$$f(t) = \sum_{i=1}^n N_i^0 \exp(-\lambda_i t) \quad ; \quad t > 0 \quad (5.1)$$

as a special form of the Laplace integral equation

$$f(t) = \int_0^{\infty} \exp(-\lambda t) g(\lambda) d\lambda \quad ; \quad t > 0 \quad (5.2)$$

provided

$$g(\lambda) = \sum_{i=1}^n N_i^0 \delta(\lambda - \lambda_i) \quad (5.3)$$

where $\delta(\lambda)$ is Dirac's delta function. GGM used a non linear transformation of the variables, $x = \ln(t)$ and $\lambda = \exp(-y)$, and Fourier transforms in order to obtain the solution of eq. (5.2):

$$g(e^{-x}) = \mathcal{F}^{-1} \left[\frac{\mathcal{F} [e^x f(e^x)]}{\mathcal{F} [e^x e^{(-e^x)}]} \right] \quad (5.4)$$

\mathcal{F} is the Fourier transform operator. The resulting spectrum $g(e^{-x})$ vs x is equivalent to the spectrum of $g(\lambda)/\lambda$ vs λ . The number of peaks in the continuous spectrum equals the number of components n , the positions of the peaks correspond to the decay constants λ_i , and the intensities of the peaks are proportional to N_i^0/λ_i .

Schlesinger [SchJ73] showed that the cumbersome numerical evaluations of the Fourier integrals were no longer needed after the development of the Fast Fourier algorithm [CooJ65]. The GGM technique was further improved by using a low-pass filter [SchJ73, SmiM74, CohS75a, CohS75b, SmiM76] in order to reduce the effect of experimental and computational noise. The best results could be obtained with a Gaussian low-pass filter

$$H(\mu) = \exp\left(-\frac{\mu^2}{\mu_d^2}\right) \quad (5.5)$$

characterized by its parameter μ_d .

An example of such a filter with $\mu_d = 1.2$, is shown in Fig. 5.1. $H(\mu)$ is calculated in the values

$$\mu(k) = k/(2 \ n_x \ \Delta) \quad \text{with } k = -n_x+1, \dots, n_x \quad (5.6)$$

The value of $\mu(k)$ is situated in the interval $[-1/(2\Delta), 1/(2\Delta)[$. For the calculation of the filter in Fig. 5.1, the value of Δ is equal to 0.1 and the $2 \ n_x$ elements of the vector μ are sorted in the same way as they are used in the implementation of the method (see Section 5.1.2.), i.e.

$$\mu_1 = 0, \dots, \mu_{n_x} = 5.0, \mu_{n_x+1} = -5.0, \dots, \mu_{2n_x-1} = -0.1.$$

The intensity of $H(\mu)$ decreases gently from 1 to 0 for μ changing from 0 to the highest frequency (5) and increases gently again as μ changes from the lowest frequency (-5) to (-0.1).

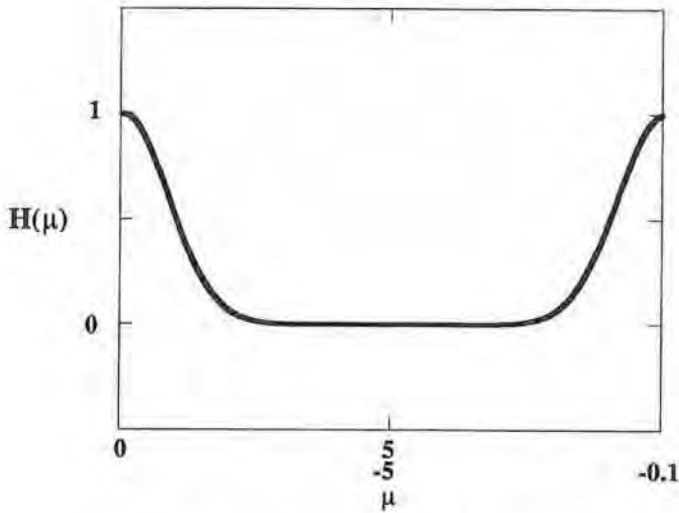


Fig. 5.1 : Gaussian low-pass filter with $\mu_d = 1.2$.

Smith et al. [SmiM76] recognized that the solution offered by GGM implies a mapping of the integral equation (5.2) into the convolution integral equation (5.7)

$$ff(x) = gg(x) \otimes kk(x)$$

$$= \int_{-\infty}^{+\infty} gg(z) kk(x-z) dz \quad (5.7)$$

with $ff(x) = e^x f(e^x) \quad (5.8)$

$$gg(x) = g(e^{-x}) \quad (5.9)$$

and the model function

$$kk(x) = e^x \exp(-e^x). \quad (5.10)$$

This equation can be deconvolved for $gg(x)$ by applying Fourier Transform techniques :

$$gg(x) = \mathcal{F}^{-1} \left\{ \frac{\mathcal{F}[ff(x)]}{\mathcal{F}[kk(x)]} \right\} \quad (5.11)$$

The Gaussian low-pass filter, mentioned above (eq. (5.5)), is multiplied with the quotient $\text{quot} = \mathcal{F}[ff]/\mathcal{F}[kk]$ before the inverse Fourier transform is calculated.

Cohn-Sfetcu et al. [CohS75a, CohS75b] proved that this method can also be used to analyze multicomponent Gaussian, Lorentzian, and $\sin x/x$ type functions by using a

suitable model function $kk(x)$. For example, a superposition of Gaussian functions can be deconvolved by using the model function

$$kk(x) = e^x \exp(-e^{(x^2)}) \quad (5.12)$$

Cohn-Sfetcu et al. [CohS75b] applied the improved GGM method in the analysis of pulsed NMR measurements.

5.1.2. Implementation

The MatLab 4.2c1 program 'gardner.m' for the deconvolution of multicomponent decay curves with the improved GGM's method combined with a Gaussian low pass filter is shown in Fig. 5.2. The main steps of the program are explained below.

As an input the program requires a file with the nx data $(t(i), yf(i))$ so that $x(i) = \ln(t(i)) = (i-1)\Delta$ for $i = 1, \dots, nx$ and Δ is a constant interval. The value of Δ (delta) and the μ_d (mud) value for the Gaussian low-pass filter are also required.

First, the program calculates the function ff , given by eq. (5.8), and the function kk (given by eqs. (5.10) or (5.12) for an exponential or Gaussian model function, respectively) is calculated in the points x_i , so that

- (a) the values $0 \leq x_i < \Delta$ correspond to those with $1 \leq i \leq nx$,
 - (b) the values of x_i in the interval $]-\Delta, nx; 0[$ correspond to $nx+2 \leq i \leq 2 nx$,
- and
- (c) the value $i = nx+1$ corresponds to $x = -\Delta$ and $x = \Delta$

In practice, the calculation of ff proceeds as follows :

- (a) for $1 \leq i \leq nx$: $ff(i)$ is found by multiplying the values of t_i and f_i in each point,
- (b) for $nx+2 \leq i \leq 2 nx$: the values of the function f must be calculated for each $0 \leq t_i \leq 1$, by extrapolation of the function f using a polynomial of degree 2 through the first 3 measured points,
- (c) for $i = nx+1$ is $ff(nx+1) = e^{nx \Delta} f(e^{nx \Delta}) = e^{-nx \Delta} f(e^{-nx \Delta})$. If Δ is small, $ff(nx+1) = 0$.

Analogously, $kk(i)$ can be calculated for each value of i from 1 to $2 nx$. The calculation of the model function $kk(i)$ for exponential components (eq. (5.10)) is given in the MatLab program 'gardner'; for the calculation of $kk(i)$ for Gaussian components the expression after the '%' on the same line must be used.

The FFT of *ff* and *kk* returns vectors with $2 \times n_x$ components in the values

$$\mu(k) = k/(2 \times n_x \Delta) \quad \text{with } k = -n_x+1, \dots, n_x \quad (5.6)$$

These values of $\mu(k)$ are required in the expression of the Gaussian low-pass filter (5.5) and are therefore already calculated. The value of $\mu(k)$ is situated in the interval $[-1/(2\Delta), 1/(2\Delta)]$.

The resulting vectors of *ff*, *kk*, and μ , and the value of the parameter μ_d are given as input to a separate M - file 'mgardner.m' (Fig. 5.3). Here the FFT's of the functions *ff* are calculated followed by those of *kk*. Their quotient is then multiplied by the Gaussian low-pass filter given in eq. (5.5). Finally, the function *g* is found as the inverse FFT.

The values of the function *g* are returned to the main program 'gardner.m' as a vector $g(x_j)$ with $x_j = j \Delta$. According to the theory, a plot of the function $g(x_j)$ vs x_j is equivalent to a plot of $g(\lambda_j)/\lambda_j$ vs λ_j with $\lambda_j = \exp(-x_j)$. The real part of the function *g* is saved in a data file and $g(\lambda_j)/\lambda_j$ is plotted versus λ_j on a semilogarithmic scale for λ_j . The number of peaks in this spectrum is equal to the number of components *n* in the decay curve. The positions of the peaks are good estimates for the decay constants λ_j when the correct model function is used.

The program supposes that all values of λ_j are smaller than unity. For values larger than 1, the extrapolation, needed for the calculation of the last n_x components of *ff* and *kk*, is inadequate. This problem can be avoided by the following transformation of the scale $t' = \alpha t$ with $\alpha > 1$.

```
% gardner.m
% method of gardner using FFT
% uses the function mgardner.m

% Input
load expx.dat;
F=expx;
[ny cy]=size(F);
n=input('aantal punten = ');
delta=input('afstand in log t = ');
t=F(1:ny,1);
f=F(1:ny,2);
if n>ny,
for i=ny+1:n,
    ti=exp(i*delta);
    f(i,1)=0.;
    t(i,1)=ti;
end;
end;
```

```

% Calculation of f1 and f2
x1=t(1:3)
y1=yr(1:3)
p=polyfit(x1,y1,2)
noem=2*n*delta;
for i=1:n,
    f1(i)=t(i)*yr(i);
    f2(i)=t(i)*exp(-t(i));           % f2(i)=t(i)*exp(-t(i).^2);
    mu(i)=(i-1)/noem;
end;
s=size(mu)
f1(n+1)=0.;
f2(n+1)=0.;
mu(n+1)=n/noem;
for i=n+2:2*n,
    tinv=exp((i-1-2*n)*delta);
    finv=polyval(p,tinv);
    fi1(i)=tinv*finv;
    fi2(i)=tinv*exp(-tinv);         % fi2(i)=tinv*exp(-tinv.^2);
    mu(i)=(i-1-2*n)/noem;
end;
f1=fi1(1:2*n);
f2=fi2(1:2*n);
mud=input('waarde voor mu(d) ');
% calculation of g(e^-X) = invFFT [FFT(f1) / FFT(f2)]
% in gardner.m
[g]=mgardner(f1,f2,mu,mud);
% output : plot g(λ)/λ vs λ
[np nq]=size(g);
d=0:np-1;
x=d.*delta;
xas=exp(-x);
semilogx(xas,real(g,'b'));
axis([0.001 1 -2000 3000]);
end;

```

Fig. 5.2 : MatLab-program 'gardner.m' for the improved GGM method.

```

function [g]=mgardner(fi,gi,mu,mud);
% g(e-y) = inversefourier [ FFT(f)/FFT(g)]
ff=fft(fi);
gg=fft(gi);
quot=ff./gg;
hh=exp(-mu.^2./mud.^2);
quoth=quot.*hh';
g=ifft(quoth);
end;

```

Fig. 5.3 : MatLab-function 'mgardner.m' needed in the program 'gardner.m'.

5.2. Improved method of Prony

5.2.1. Theory

The improved method of Prony [ProR95, OsbM75, OsbM91, OsbM95] is based on two formalisms. The *first* states that the coefficients of the differential equation (5.13), with characteristic polynomial $P_{\xi}(z)$ (5.14),

$$\sum_{i=1}^{n+1} \xi_k D^{k-1} f(t) = 0 \quad (5.13)$$

where D is the usual notation for the differential operator and ξ_k are constant coefficients.

$$P_{\xi}(z) = \sum_{k=1}^{n+1} \xi_k z^{k-1} \quad (5.14)$$

comprise a more stable parameterization than those of eq. (5.1). The characteristic polynomial has n roots $-\lambda_j$, and the general solution for $f(t)$ is a sum of exponential functions (eq. (5.1)). Eq. (5.13) can also be written as

$$\left[\prod_{j=1}^n (D + \lambda_j I) \right] f(t) = 0 \quad (5.15)$$

with I the identity operator.

In practice, $f(t)$ is often known in a finite number N of discrete points t_1, \dots, t_N in a finite interval. Assuming that the interval is $]0,1[$ then $t_i = i/N$ for $i = 1, \dots, N$. Osborne et al. represented eq. (5.15) in two equivalent discrete formulations, namely in the difference and recurrence versions. Therefore, they defined a forward shift operator Π and a divided difference operator Δ such that

$$\Pi f(t) \equiv f(t+1/N) \quad (5.16)$$

$$\Delta \equiv N (\Pi - I) \quad (5.17)$$

and

$$\begin{aligned} D f(t) &= \frac{f(t+1/N) - f(t)}{1/N} \\ &= N (\Pi - I) f(t) = \Delta f(t) \end{aligned} \quad (5.18)$$

Now, eq. (5.15) can be formulated in a discrete manner using the divided difference operator Δ

$$\left[\prod_{j=1}^n (\Delta + \zeta_j I) \right] f(t) = 0 \quad (5.19)$$

Using the explicit notation for eq. (5.19) and keeping in account the commutativity of the operators, we find that $\zeta_j = N(1 - \exp(-\lambda_j/N))$. Indeed :

$$\left[(\Delta + \zeta_1 I) \dots (\Delta + \zeta_j I) \dots (\Delta + \zeta_n I) \right] \sum_{i=1}^n N_i^0 \exp(-\lambda_i t) = 0 \quad (5.20)$$

This is true, if it can be proved that for a given ζ_j

$$(\Delta + \zeta_j I) e^{-\lambda_j t} = 0 \quad (5.21)$$

$$\Rightarrow N \left(e^{-\lambda_j(t+1/N)} - e^{-\lambda_j t} \right) + \zeta_j e^{-\lambda_j t} = 0$$

$$\Rightarrow N \left(e^{-\lambda_j t} e^{-\lambda_j/N} - e^{-\lambda_j t} \right) + \zeta_j e^{-\lambda_j t} = 0$$

$$\Rightarrow N \left(e^{-\lambda_j/N} - 1 \right) + \zeta_j = 0$$

$$\Rightarrow \zeta_j = N \left(1 - e^{-\lambda_j/N} \right) \quad (5.22)$$

So, $f(t)$ is a solution of eq. (5.19) and if the ζ_j are given by eq. (5.22), eq. (5.19) can also be written as a sum

$$\sum_{k=1}^{n+1} \gamma_k \Delta^{k-1} f(t) = 0 \quad (5.23)$$

where the γ_k represent the difference Prony parameters. Eq. (5.23) converges to eq. (5.13) for $N \rightarrow \infty$, so that $\zeta_j \rightarrow \lambda_j$ and $\gamma_k \rightarrow \xi_k$.

The characteristic polynomial $P_\gamma(z)$ becomes

$$P_\gamma(z) = \sum_{k=1}^{n+1} \gamma_k z^{k-1} \quad (5.24)$$

and has n roots $\zeta_j = N(1 - \exp(-\lambda_j/N))$.

Eq. (5.15) can also be transformed using the forward shift operator Π

$$\left[\prod_{j=1}^n (\Pi - \rho_j I) \right] f(t) = 0 \quad (5.25)$$

where the parameters ρ_j are given by $\exp(-\lambda_j/N)$, so that $f(t)$ is a solution of eq. (5.25). Therefore, by analogy with eq. (5.21), the following statement must be proven :

$$(\Pi - \rho_j I) e^{-\lambda_j t} = 0 \quad (5.26)$$

It is found that

$$\Rightarrow e^{-\lambda_j(t+1/n)} - \rho_j e^{-\lambda_j t} = 0$$

so that,

$$\rho_j = e^{-\lambda_j/N} \quad (5.27)$$

Eq. (5.25) can be written as a sum :

$$\sum_{k=1}^{n+1} \delta_k \Pi^{k-1} f(t) = 0 \quad (5.28)$$

where δ_k represent the recurrence Prony parameters. If $N \rightarrow \infty$, $\rho_j \rightarrow 1$ and the parameters δ_k converges to a multiple of the binomial coefficients $(-1)^{n-k+1} \binom{n}{k-1}$. This limit is independent of λ_j .

The corresponding characteristic polynomial $P_\delta(z)$ for the recurrence version is

$$P_\delta(z) = \sum_{k=1}^{n+1} \delta_k z^{k-1} \quad (5.29)$$

and has n roots $\rho_j = e^{-\lambda_j/N}$.

The problem is now to find the optimal set of Prony parameters in the difference (5.23) or recurrence (5.28) equations, followed by the calculation of the roots of the corresponding polynomials $P_\gamma(z)$ (eq. (5.24)) or $P_\delta(z)$ (eq. (5.29)).

Mathematically, a relationship between the difference and recurrence parameters can be deduced by equating

$$\sum_{k=1}^{n+1} \gamma_k \Delta^{k-1} = \sum_{k=1}^{n+1} c_k \Pi^{k-1} \quad (5.30)$$

which, when solved for the c_k , gives

$$c_j = \sum_{k=j}^{n+1} (-1)^{k-j} \binom{k-1}{j-1} N^{k-1} \gamma_k \quad (5.31)$$

In matrix notation, this can be noted as $\mathbf{c} = \mathbf{U}\gamma$ with \mathbf{U} a non singular matrix, given by the following expression

$$\mathbf{U} = \begin{bmatrix} 1 & -1 & 1 & \dots & (-1)^n \\ & 1 & -2 & & \vdots \\ & & 1 & & \\ & & & \ddots & \\ & & & & 1 & -\binom{n}{1} \\ & & & & & 1 \end{bmatrix} \begin{bmatrix} 1 \\ N \\ \dots \\ N^n \end{bmatrix}$$

and

$$\mathbf{c} = (c_1, \dots, c_{n+1})^T$$

\mathbf{c} and δ are rescaled versions of each other and the notational convention will be used that \mathbf{c} represents the above function of γ while δ is a function of the decay constants λ_j with normalized elements. We will henceforth confine the further discussion to the case of the recurrence equations (5.28). An analogous version in terms of the difference parameters can be deduced using the above relationship.

The recurrence equations (5.28) can also be stated in matrix notation. Let $f_i = f(t_i)$, $i = 1, \dots, N$, $\mathbf{f} = (f_1, \dots, f_N)^T$, and let \mathbf{X}_δ be the $N \times (N - n)$ matrix

$$\mathbf{X}_\delta = \begin{bmatrix} \delta_1 & & & \\ \vdots & \ddots & & \\ \delta_{n+1} & & \delta_1 & \\ & \ddots & \vdots & \\ & & & \delta_{n+1} \end{bmatrix} \quad (5.32)$$

where δ_k are the recurrence parameters, then \mathbf{f} satisfies

$$\mathbf{X}_\delta^T \mathbf{f} = \mathbf{0} \quad (5.33)$$

The method that Osborne et al. [Osbm91, Osbm95] developed for finding the optimal set of Prony parameters is based on the treatment of the exponential fitting problem as a separable regression. This constitutes the *second* formalism. By definition, a least squares problem is called separable if the fitting function can be written as a linear combination of functions involving further parameters in a non linear manner.

The model function f in eq. (5.1) can also be written as

$$\mathbf{f} = \mathbf{A}(\lambda) \mathbf{N}^\circ \quad (5.34)$$

where $\mathbf{f} = (f_1, \dots, f_N)^T$, \mathbf{A} is a $(N \times n)$ matrix function of λ with elements $A_{ij} = e^{-\lambda_j t_i}$, and $\mathbf{N}^\circ = (N_1^\circ, \dots, N_n^\circ)^T$.

Osborne [Osbm75] showed that such a separable problem can be transformed to a minimization problem with one equality condition involving the non linear parameters only. Let $\mathbf{y} = (y_1, \dots, y_N)^T$ be the vector of observations that can be represented best by the model function f in eq. (5.34). For any fixed value of λ , the sum of squares

$$\Phi(\mathbf{N}^\circ, \lambda) = (\mathbf{y} - \mathbf{A}(\lambda) \mathbf{N}^\circ)^T (\mathbf{y} - \mathbf{A}(\lambda) \mathbf{N}^\circ) \quad (5.35)$$

is minimized by

$$\hat{\mathbf{N}}^\circ(\lambda) = (\mathbf{A}^T \mathbf{A})^{-1} \mathbf{A}^T \mathbf{y} \quad (5.36)$$

Substituting this back into Φ gives the reduced sum of squares

$$\begin{aligned} \Psi(\lambda) &= \Phi(\hat{\mathbf{N}}^\circ(\lambda), \lambda) \\ &= \mathbf{y}^T \left(\mathbf{I} - \mathbf{A} (\mathbf{A}^T \mathbf{A})^{-1} \mathbf{A}^T \right) \mathbf{y} \\ &= \mathbf{y}^T (\mathbf{I} - \mathbf{P}_A) \mathbf{y} \end{aligned} \quad (5.37)$$

where \mathbf{P}_A is the orthogonal projection onto the column space of \mathbf{A} . The least squares problem may be solved by minimizing Ψ with respect to λ , and recovering the least squares estimate of \mathbf{N}° from eq. (5.36). Note that $\mathbf{X}^T \mathbf{A} = \mathbf{0}$ so that the columns of \mathbf{X} and \mathbf{A} span orthogonal spaces. Therefore, eq. (5.37) can be rewritten in terms of the Prony parameters

$$\Psi = \mathbf{y}^T \mathbf{P}_X \mathbf{y} \quad \text{with} \quad \mathbf{P}_X = \mathbf{X} (\mathbf{X}^T \mathbf{X})^{-1} \mathbf{X}^T \quad (5.38)$$

where P_X is the orthogonal projection onto the column space of X_δ . Hence, Ψ is a function of the recurrence Prony parameters δ_k . The derivative of Ψ with respect to δ can be written as

$$\dot{\Psi}_\delta = 2 B_\delta(\delta) \delta \quad (5.39)$$

with B_δ a symmetric $(n + 1) \times (n + 1)$ matrix function of δ with elements

$$B_{\delta_{ij}} = y^T X_{\delta_i} (X_\delta^T X_\delta)^{-1} X_{\delta_j}^T y - y^T X_\delta (X_\delta^T X_\delta)^{-1} X_{\delta_i}^T X_{\delta_j} (X_\delta^T X_\delta)^{-1} X_\delta^T y \quad (5.40)$$

and with $X_{\delta_j} = \partial X_\delta / \partial \delta_j$. Each X_{δ_j} is a constant matrix representing the $(j - 1)$ th order divided difference operator. The function Ψ is now minimized with respect to the Prony parameters δ with an additional constraint $\delta^T \delta = 1$ so that the elements of δ are normalized.

The necessary condition for a stationary value δ^* leads to a non-linear eigenvalue problem :

$$\begin{aligned} (B(\delta) - vI)\delta &= 0 \\ \delta^T \delta &= 1 \\ \text{in } \delta &= \delta^* \end{aligned} \quad (5.41)$$

Let $W(\delta, v) = \Psi(\delta) + v(1 - \delta^T \delta)$ be the Lagrange auxiliary function with v the Lagrange multiplier for the constraint and $\dot{W}_\delta = 2 B(\delta)\delta - 2v\delta = 0$. Because Ψ does not depend on $\|\delta\|$, $\dot{\Psi}(\delta)$ must be in a direction orthogonal to δ , so that

$$\delta^T \dot{\Psi}(\delta) = 2 \delta^T B(\delta)\delta = 0 \quad (5.42)$$

Premultiplying $\dot{W}_\delta = 0$ by δ^T and using eq. (5.42) leads to the result that $v = 0$. Thus, the non-linear eigenvalue problem (5.31) can be solved iteratively as a linear eigenvalue problem.

Given δ^k , solve the linear eigenvalue problem

$$\begin{cases} (\mathbf{B}(\delta^k) - v^{k+1}\mathbf{I})\delta^{k+1} = \mathbf{0} \\ \delta^{k+1T}\delta^{k+1} = 1 \end{cases} \quad (5.43)$$

for δ^{k+1} and v^{k+1} , with v^{k+1} the nearest to zero of such solutions.

Convergence can be accepted when

$$v^{k+1} \ll \|\mathbf{B}\|$$

This iterative scheme is the improved Prony algorithm for the recurrence equations. An exactly analogous version of the algorithm can be developed in terms of the difference parameters. The difference and recurrence versions are two different algorithms with the same stationary values. The convergence and stability are discussed in detail by Osborne and Smyth [OsbM91, OsbM95]. They compared the technique with the Marquardt-Levenberg algorithm [MarD63, LevK44] on simulated decay curves, and concluded that the improved methods of Prony converge rapidly and are remarkably tolerant for poor starting values.

5.2.2. Implementation

The program 'prony.m' has been written in Matlab 4.2c1. It uses the function 'mprony.m', based on the recurrence version of Prony's improved method and was communicated to us by Osborne and Smyth. An explanation of the main steps in the program is given in the present section. The MatLab-program 'prony.m' is presented in Fig. 5.4 and that of 'mprony.m' in Fig. 5.5.

As an input, 'prony.m' requires the data file of the N observations (t_i, y_i) with $t_i = i \Delta t$, and $i = 1, \dots, N$, the number of exponentials n , and optionally, the starting values of the decay constants λ_i .

Afterwards, the function $[b, a, \mu] = \text{mprony}(y, t, n, \text{bstart})$, implemented in a separate M file 'mprony.m' (see Fig 5.5), is called with or without starting values for the decay constants (-bstart). The main steps are :

First, a matrix \mathbf{Y} is defined as

$$\mathbf{Y} = \begin{bmatrix} y_1 & y_2 & \cdots & y_{n+1} \\ y_2 & y_3 & \cdots & y_{n+2} \\ \vdots & \vdots & \ddots & \vdots \\ y_{N-n} & y_{N-n+1} & \cdots & y_N \end{bmatrix} \quad (5.44)$$

so that

$$\mathbf{X}_\delta^T \mathbf{y} = \mathbf{Y} \mathbf{c} \quad (5.45)$$

These $\mathbf{X}_{\delta_j}^T \mathbf{y}$ are 'windowed shifts' of \mathbf{y} as can be noticed from the columns of \mathbf{Y} .

Now, the starting values \mathbf{c} are calculated :

(a) no starting values for the decay constants are given :

The starting values of \mathbf{c} (δ) are found as the eigenvector belonging to the smallest eigenvalue l of $\mathbf{Y}^T \mathbf{Y}$.

(b) starting values for the decay constants are given as input :

The starting values of \mathbf{c} are found as the coefficients of the polynomial $P_c(z)=0$ (eq. 5.29) of degree n with roots $z_j = \rho_j = \exp(-\lambda_j/N)$.

Then the parameters \mathbf{c} are divided by a factor (norm \mathbf{c}). These are the normalized starting values of δ .

In the next part, the elements of $\mathbf{B}(\delta)$ are calculated as

$$B_{\delta_{ij}} = \mathbf{y}^T \mathbf{X}_{\delta_i} (\mathbf{X}_\delta^T \mathbf{X}_\delta)^{-1} \mathbf{X}_{\delta_j}^T \mathbf{y} - \mathbf{y}^T \mathbf{X}_\delta (\mathbf{X}_\delta^T \mathbf{X}_\delta)^{-1} \mathbf{X}_{\delta_i}^T \mathbf{X}_{\delta_j} (\mathbf{X}_\delta^T \mathbf{X}_\delta)^{-1} \mathbf{X}_{\delta_j}^T \mathbf{y} \quad (5.46)$$

using the scheme

$$* \mathbf{X} = \begin{bmatrix} \bar{c}_1 & & & & \\ \bar{c}_2 & \bar{c}_1 & & & \\ \vdots & \bar{c}_2 & \ddots & & \\ \bar{c}_{n+1} & \vdots & \ddots & \bar{c}_1 & \\ & \bar{c}_{n+1} & \ddots & \bar{c}_2 & \\ & & \ddots & \vdots & \\ & & & \bar{c}_{n+1} & \end{bmatrix} = \mathbf{X}_\delta$$

where \mathbf{X} is a $N \times (N-n)$ matrix with $n+1$ bands.

With the optimal set \mathbf{c} (δ) values, the decay constants λ_j can be derived from the roots of the polynomial $P_\delta(z) = 0$, i.e. $z_j = \rho_j = \exp(-\lambda_j/N)$ with $1/N$ equal to Δt , the constant time interval.

The fitted y-values are stored in the variable **mu**. The optimized decay constants (**b**), pre-exponential factors (**a**), and the fitted y-values (**mu**) are returned to the main program 'prony.m' where the first two are displayed.

```
% prony.m
% uses function mprony.m
% file.dat : t,y data equidistant
% input
load file.dat;
a=file;
y=a(:,2);
t=a(:,1);
p=input('number of exp ');
opt=input('with(1) or without(0) starting values ');
if opt==0,
    % without bstart values
    [b,n,mu]=mprony(y,t,p);
else
    % with bstart values
    bstart=[-landa1 -landa2,...,'];
    [b,n,mu]=mprony(y,t,p,bstart);
end;
% output
disp(b);
disp(n);
end;
```

Fig. 5.4 : Matlab-program 'prony.m': the recurrence version of Prony's improved method.

```
function [b,a,mu] = mprony(y,t,p,bstart);
%
[n cy]=size(y);
dt=t(2)-t(1);
% form Y
Y=zeros(n-p,p+1);
i=1:(n-p);
for j=1:p+1,
    Y(:,j)=y(i+j-1);
end;
% starting values
if nargin < 4,
    [x d]=eig(Y'*Y); [l jmin]=min(diag(d)); c=x(:,jmin);
else
    c=poly(exp(bstart*dt)); c=c(:);
    c=c(p+1:-1:1)/norm(c);
end;
```

```

% form B
%X=zeros(n,n-p);
X=sparse( [],[],[],n,n-p,(n-p)*(p+1) );
for j=1:n-p,
    X(j+j*p,j)=conj(c);
end;
MY=(X*X)\Y;
v=MY*c;
V=zeros(n,p+1);
for j=1:p+1,
    V(j:n-p+j-1,j)=v;
end;
B=( Y'*MY-V'*V )./(n-p);
% initial eigenvalues
lold=inf;
[x d]=eig(B); [l jmin]=min(diag(d)); c=x(:,jmin);
lfirst=l;
tol=10^(-15+log(n));
iter=0;
while (abs((l-lold)/lfirst) > 1e-5) & (rcond(B) > tol) & (iter<40);
    iter=iter+1;
    if iter==40;
        disp('MProny. Max iterations reached.');
```

```

end;
% form B
for j=1:n-p,
    X(j+j*p,j)=conj(c);
end;
MY=(X*X)\Y;
v=MY*c;
V=zeros(n,p+1);
for j=1:p+1,
    V(j:n-p+j-1,j)=v;
end;
B=( Y'*MY-V'*V )./(n-p);
% inverse iteration
lold=l;
[x d]=eig(B); [l jmin]=min(diag(d)); c=x(:,jmin);
end;
% extract rate constants
b=log(roots( c(p+1:-1:1) ))/dt;
```

```

if nargout > 1,
    A=exp(t*b);
    a=A\y;
    mu=A*a;
end;
```

Fig. 5.5 : MatLab-function 'mprony.m' used
in the Matlab-program 'prony.m'.

5.3. The combined use of the improved methods of GGM and Prony

The combined use of the improved methods of GGM and Prony on the same experimental data introduces an additional difficulty because the input of the GGM method requires a data set gathered at constant logarithmic time intervals, while Prony's method uses a data set measured at constant time intervals. Hence, one data set must be generated from the other one. From a practical point of view, the sampling of a data set at constant time intervals is much more convenient. Thus, we opted for an interpolation of this data set in order to calculate the values at constant logarithmic time intervals.

Smith et al. [SmiM76] used an interpolation method, after the transformation of the data set $(t, f(t))$ in a semi-logarithmic space $(t, \ln f(t))$, based on the fitting of a polynomial of the third degree over a time period of ca $3/2$ of the smallest time constant. When the parameters of the fit differ from those that could be expected for a multi-exponential decay, two options could be taken : either enlarge the interval or reduce the degree of the polynomial to two. An example of such an abnormality is the presence of a positive derivative when the exponential function itself consists of only positive pre-exponential factors. The technique of Smith and Buckmaster [SmiM75] was used for the determination of the t_i value from where the function was pure mono-exponentially. The remaining data were then fitted using the method of Moore and Yalcin [MooW73] or using a weighted least squares method. The polynomial interpolation has the further advantage that besides the interpolation also a smoothing effect is achieved. However, an important disadvantage is the fact that the interpolated polynomials over neighboring intervals can be different due to the different $f(t)$ values that are used to calculate their coefficients. As a consequence, the neighboring polynomials will not be completely connected at the joint border points of the interpolation intervals, and the first and higher derivatives at these points are thus discontinuous.

An alternative method is spline interpolation, also suggested by Smith et al. [SmiM76]. A spline is a piecewise polynomial of degree p between the data points. Furthermore, a spline of degree p is a continuous function with $(p-1)$ continuous derivatives inside the interpolation interval as well as at the border points of it. The most common used splines are the cubic splines ($p=3$). These are discussed in Section 5.3.1..

5.3.1. The cubic spline function

A function $S(x)$ is a spline function of degree 3 if

1. the domain of $S(x)$ is an interval $[a,b]$;
2. $S(x)$, $S'(x)$, and $S''(x)$ are continuous in $[a,b]$;

and

3. there exists nodes $a = x_0 < x_1 < \dots < x_n = b$, so that $S(x)$ is a polynomial $S_i(x)$ of degree ≤ 3 on the subinterval $[x_{i-1}, x_i]$, for $i = 1, \dots, n$. Hence, $S(x)$ is a group of piecewise polynomials $S_i(x) = a_i x^3 + b_i x^2 + c_i x + d_i$, and has $4n$ unknown coefficients.

According to this definition, the function $S(x)$ satisfies the following conditions :

$$S_i(x_i) = y_i \quad i = 1, \dots, n \quad (5.47a)$$

$$S_i(x_{i-1}) = y_{i-1} \quad i = 1, \dots, n \quad (5.47b)$$

$$S'_i(x_i) = S'_{i+1}(x_i) \quad i = 1, \dots, n-1 \quad (5.47c)$$

$$S''_i(x_i) = S''_{i+1}(x_i) \quad i = 1, \dots, n-1 \quad (5.47d)$$

The conditions in eqs (5.47a-d) totals $4n-2$. For the determination of the $4n$ coefficients, two additional conditions are to be satisfied. The two most commonly used are :

$$\text{Suppose that} \quad S''(a) = S''(b) = 0, \quad (5.47e)$$

$$\text{and that} \quad S'(a) = f'(a) \text{ and } S'(b) = f'(b) \quad (5.47f)$$

The cubic spline satisfying the conditions (5.47a-e) is called a natural cubic spline.

Since $S_i(x)$ is a polynomial of the third degree, $S''_i(x)$ is linear in $[x_{i-1}, x_i]$ and can therefore be written as

$$S''_i(x) = \frac{z_i}{h_i}(x - x_{i-1}) + \frac{z_{i-1}}{h_i}(x_i - x) \quad (5.48a)$$

$$\text{with} \quad z_i = S''(x_i) \quad (5.48b)$$

$$\text{and} \quad h_i = x_i - x_{i-1} \quad (5.48c)$$

After a double integration of eq. (5.48a), the following expression for $S_i(x)$ is found

$$S_i(x) = \frac{z_i}{6h_i}(x - x_{i-1})^3 + \frac{z_{i-1}}{6h_i}(x_i - x)^3 + C_i^* x + D_i^* \quad (5.49)$$

where C_i^* en D_i^* are integration constants.

By adjusting these integration constants, eq. (5.49) becomes

$$S_i(x) = \frac{z_i}{6h_i}(x - x_{i-1})^3 + \frac{z_{i-1}}{6h_i}(x_i - x)^3 + C_i(x - x_{i-1}) + D_i(x_i - x) \quad (5.50)$$

Using the conditions (5.47a and b) in the endpoints, the constants C_i en D_i can be determined as

$$S_i(x_i) = \frac{z_i}{6}h_i^2 + C_i h_i = y_i \quad \Rightarrow \quad C_i = \frac{y_i}{h_i} - \frac{h_i}{6} z_i \quad (5.51a)$$

$$S_i(x_{i-1}) = \frac{z_{i-1}}{6}h_i^2 + D_i h_i = y_{i-1} \quad \Rightarrow \quad D_i = \frac{y_{i-1}}{h_i} - \frac{h_i}{6} z_{i-1} \quad (5.51b)$$

After substitution of the eqs (5.51) in eq. (5.50), the expression for the cubic spline over the interval $[x_{i-1}, x_i]$ is obtained

$$S_i(x) = \frac{z_i}{6h_i}(x - x_{i-1})^3 + \frac{z_{i-1}}{6h_i}(x_i - x)^3 + \left(\frac{y_i}{h_i} - \frac{h_i}{6} z_i\right)(x - x_{i-1}) + \left(\frac{y_{i-1}}{h_i} - \frac{h_i}{6} z_{i-1}\right)(x_i - x) \quad (5.52)$$

The derivative of $S_i(x)$ is given by eq. (5.53) :

$$S'_i(x) = \frac{z_i}{2h_i}(x - x_{i-1})^2 - \frac{z_{i-1}}{2h_i}(x_i - x)^2 + \left(\frac{y_i}{h_i} - \frac{h_i}{6} z_i\right) - \left(\frac{y_{i-1}}{h_i} - \frac{h_i}{6} z_{i-1}\right) \quad (5.53)$$

Analogously, the expression for the derivative of the cubic spline $S_{i+1}(x)$, can be derived over the neighboring interval $[x_i, x_{i+1}]$:

$$S'_{i+1}(x) = \frac{z_{i+1}}{2h_{i+1}}(x - x_i)^2 - \frac{z_i}{2h_{i+1}}(x_{i+1} - x)^2 + \left(\frac{y_{i+1}}{h_{i+1}} - \frac{h_{i+1}}{6} z_{i+1}\right) - \left(\frac{y_i}{h_{i+1}} - \frac{h_{i+1}}{6} z_i\right) \quad (5.54)$$

Both derivatives are defined in the same border point x_i

$$S'_i(x_i) = \frac{h_i}{6} z_{i-1} + \frac{h_i}{3} z_i + \frac{y_i - y_{i-1}}{h_i} \quad (5.55)$$

$$S'_{i+1}(x_i) = -\frac{h_{i+1}}{3} z_i - \frac{h_{i+1}}{6} z_{i+1} + \frac{y_{i+1} - y_i}{h_{i+1}} \quad (5.56)$$

According to the condition (5.47c), eq. (5.55) is equal to eq. (5.56), so that

$$h_i z_{i-1} + 2(h_i + h_{i+1})z_i + h_{i+1} z_{i+1} = 6 \left(\frac{y_{i+1} - y_i}{h_{i+1}} - \frac{y_i - y_{i-1}}{h_i} \right) \quad (5.57)$$

Put $u_i \equiv 2(h_i + h_{i+1})$,

and $v_i \equiv 6 \left(\frac{y_{i+1} - y_i}{h_{i+1}} - \frac{y_i - y_{i-1}}{h_i} \right)$

then, eq. (5.57) can be rewritten as

$$h_i z_{i-1} + u_i z_i + h_{i+1} z_{i+1} = v_i \quad (5.58)$$

In the case of natural cubic splines, the z_i 's are found as the solutions of the linear system

$$\begin{cases} z_0 & = 0 \\ h_i z_{i-1} + u_i z_i + h_{i+1} z_{i+1} & = v_i \quad \text{with } i = 1, \dots, n-1 \\ z_n & = 0 \end{cases} \quad (5.59)$$

In matrix notation :

$$\begin{bmatrix} 1 & 0 & 0 & \dots & 0 \\ h_1 & u_1 & h_2 & 0 & \dots & 0 \\ 0 & h_2 & u_2 & h_3 & 0 & \dots & 0 \\ \vdots & & \ddots & \ddots & \ddots & & \vdots \\ 0 & \dots & 0 & h_{n-1} & u_{n-1} & h_n & 0 \\ 0 & \dots & & 0 & 0 & 1 & 0 \end{bmatrix} \begin{bmatrix} z_0 \\ z_1 \\ \vdots \\ z_{n-1} \\ z_n \end{bmatrix} = \begin{bmatrix} 0 \\ v_1 \\ \vdots \\ v_{n-1} \\ 0 \end{bmatrix} \quad (5.60)$$

If a cubic spline satisfies the conditions formulated in the eqs (5.47a-d) and (5.47f), then the z_i 's are the solutions of the following system :

$$\begin{cases} 2h_1 z_0 + h_1 z_1 & = 6(b_1 - f'(a)) \\ h_i z_{i-1} + u_i z_i + h_{i+1} z_{i+1} & = v_i \quad \text{with } i = 1, \dots, n-1 \\ h_n z_{n-1} + 2h_n z_n & = 6(f'(b) - b_n) \end{cases} \quad (5.61)$$

In matrix notation :

$$\begin{bmatrix} 2h_1 & h_1 & 0 & & \dots & & 0 \\ h_1 & u_1 & h_2 & 0 & \dots & & 0 \\ 0 & h_2 & u_2 & h_3 & 0 & \dots & 0 \\ \vdots & & \ddots & \ddots & \ddots & & \vdots \\ 0 & \dots & 0 & h_{n-1} & u_{n-1} & h_n & z_{n-1} \\ 0 & \dots & & 0 & h_n & 2h_n & z_n \end{bmatrix} \begin{bmatrix} z_0 \\ z_1 \\ \vdots \\ z_{n-1} \\ z_n \end{bmatrix} = \begin{bmatrix} 6(b_1 - f'(a)) \\ v_1 \\ \vdots \\ v_{n-1} \\ 6(f'(b) - b_n) \end{bmatrix} \quad (5.62)$$

The both symmetric tri-diagonal systems of linear equations (5.60) and (5.62) need $O(N)$ operations in order to calculate their solutions.

5.3.2. Implementation

In all analyses, natural cubic splines are used for the interpolation of the data set with N observations (t_i, y_i) so that $t_i = i \Delta t$, for $i = 1, \dots, N$ and Δt a constant time interval, in order to obtain n_x data points $(t(i), yf(i))$ so that $x(i) = \ln(t(i)) = (i-1)\Delta$, for $i = 1, \dots, n_x$ and Δ a constant interval. A small program 'fspline.m' (Fig. 5.6) in MatLab 4.2c1 is written which uses the MatLab function 'interp1', a standard function for the calculation yf at x using a natural cubic spline on the data set (t, y) .

As input the program requires the original data set (t, y) of N observations, the maximum value n_x for x (within the limits of the data set (t, y)) and the value Δx of Δ . A vector $\mathbf{x_d}$ contains the values of $x(i)$. Then, the elements of the vector $\mathbf{y_f}$ are calculated at each point of the vector $\mathbf{x_d}$.

The program returns a plot with an overlay of the original and interpolated data. Finally, the name of the output file is asked, and the interpolated data are stored.

```
% program fspline
% interpolation of dataset (t,y) to (xf,yf) using cubic splines
% with xf on a constant logarithmic time scale
% input
load input.dat;
F=input;
nx=input('limiet voor x = ');
deltax=input('delta x = ');
% interpolation
t=F(:,1);
yr=F(:,2);
xd=0:deltax:nx;
x=exp(xd);
yf=interp1(t,yr,xf,'spline');
% overlay plot
plot(t,yr,'+',xf,yf)
xlabel('t'),ylabel('y')
% output
xf=xf;
yf=yf;
[np nq]=size(yf)
yout(np,2)=0.;
for i=1:nq,
    yout(i,1)=xf(i);
    yout(i,2)=yf(i);
end;
filename=input('outputfile = ','s');
fid=fopen(filename,'w');
count=fprintf(fid,'%16.10f %16.10f\n',yout);
status=fclose(fid);
end;
```

Fig. 5.6 : Matlab-program 'fspline.m'

Chapter 6

Evaluation on simulated decay curves

The improved methods of Gardner et al. and Prony are first individually evaluated on simulated decay curves. The influence of their specific parameters has been studied in order get an idea about the applicabilities of the methods (order of complexity of the problem, influence of noise, experimental conditions, ...), and in order to predict some rules for the experimental gathering and computational treatment of the data.

6.1. Simulation of decay curves

First, the improved methods of Gardner et al. and Prony are evaluated on simulated decay curves in the *absence* of noise. The following decay curves are calculated at discrete points in time :

$$f(t) = 100 \exp(-0.02 t) \quad (6.1)$$

$$f(t) = 1000 \exp(-0.1 t) + 100 \exp(-0.01 t) \quad (6.2)$$

$$f(t) = 100 \exp(-0.1 t) + 100 \exp(-0.01 t) \quad (6.3)$$

$$f(t) = 3750 \exp(-0.5 t) + 1000 \exp(-0.1 t) + 100 \exp(-0.02 t) + 100 \exp(-0.01 t) \quad (6.4)$$

$$f(t) = 1000 \exp(-(t/10)^2) + 100 \exp(-t/100) \quad (6.5)$$

$$f(t) = 1000 \exp(-1.386 t) + 100 \exp(-0.1386 t) \quad (6.6)$$

For the evaluation of the improved method of Gardner et al., these functions are calculated at times t_i so that x_i , equal to $\ln t_i$, varies from 0 to a given x_0 value, in equal steps Δx .

The following points influencing the resulting $g(\lambda)/\lambda$ vs λ spectrum are studied :

- a. Influence of the Gaussian low-pass filter (eq. (5.5), Fig. 5.1);
- b. Performance on multicomponent decay curves;
- c. Influence of the model function $kk(x)$;
- d. Choice of the time scale.

For the evaluation of the improved method of Prony, data sets for all the functions (6.1 - 6.4), are generated at constant time intervals ($\Delta t = 20$) over a time period from 0 to t_0 .

The impact of some input variables on the final analysis has been studied :

- a. Input of the number of components n ;
- b. Influence of the starting values;
- c. Influence of the number of data points.

One of the most important application of decay curve analysis is found in nuclear and radiochemistry. All counting processes are accompanied by a *Poisson distributed noise* so that the standard deviation $\sigma(c)$ equals \sqrt{c} , where c is the number of counts. For that reason, a Poisson random number generator [VanR93] has been used in order to superimpose noise on the following mono-exponential decay curves :

$$f(t) = 10^6 \exp(-0.01 t) \quad , \quad \text{initially 0.1 \% noise} \quad (6.7)$$

$$f(t) = 10^4 \exp(-0.01 t) \quad , \quad \text{initially 1.0 \% noise} \quad (6.8)$$

The impact of these initial noise levels of 0.1 and 1.0 % has been checked for both improved methods.

6.2. Evaluation of the improved method of Gardner et al.

6.2.1. Noise-free data

a. Influence of the Gaussian low-pass filter

A mono-exponential decay curve has been simulated using eq. (6.1)

$$f(t) = 100 \exp (-0.02 t) \quad (6.1)$$

for times t_i so that x_i , equal to $\ln t_i$, varies from 0 to 10 in steps of 0.1. This decay curve is analyzed using the MatLab program 'gardner.m'. Fig. 6.1 shows the resulting $g(\lambda)/\lambda$ vs λ spectrum. It is characterized by a large maximum at the position of the decay constant $\lambda = 0.02$. Unfortunately, additional noise signals (ripples) are also present. These ripples will hamper the detection of small maxima near larger ones for more complex (more than one component) situations.

The signal to noise ratio is defined here as the intensity of the real maximum divided by that of the largest noise ripple. In the example presented in Fig. 6.1, the signal to noise ratio is almost 6. In Chapter 5, it was mentioned that the GGM method could be improved by using a Gaussian low-pass filter (eq.(5.5)) in order to reduce the effects of experimental and computational noise.

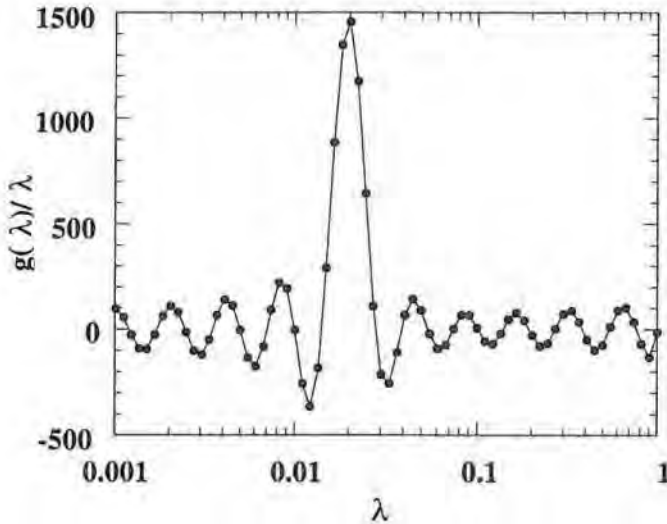


Fig. 6.1 : $g(\lambda)/\lambda$ vs λ spectrum for the analysis of the data set generated from eq. (6.1) using the improved GGM method.

The influence of filters has been studied by considering the data set generated from eq. (6.1). Fig. 6.2 shows an overlay plot of the $g(\lambda)/\lambda$ vs λ spectra when no Gaussian low-pass filter is used, and when a filter is introduced with a μ_d value of 1.2 and 0.6. All the resulting spectra have a maximum at $\lambda = 0.02$, and are characterized by additional noise signals (ripples). However, it can be seen that with the use of a Gaussian low-pass filter the intensities of the noise ripples strongly decrease.

The influence of the filter can be explained by comparing the behavior of the quotient $quot = \mathcal{F}[ff]/\mathcal{F}[kk]$ before and after the multiplication with the Gaussian low-pass filter. Figs 6.3a,b, show the quotients $quot$ obtained in the analyses of the data set generated from eq. (6.1) by using the improved GGM method without (a) and in combination with (b) a Gaussian low-pass filter ($\mu_d = 1.2$). Schreurs [SchS96] found that the elimination of the largest fluctuations (near $i = 30$ and 170) can improve the method significantly. The shape of

a Gaussian filter is depicted in Fig. 5.1. Multiplication of the filter with the function quot in Fig 6.3a will alter the latter not only in the central part (the high frequencies), but will also influence the low frequencies (Fig. 6.3b). This deformation depends on the characteristic parameter μ_d of the Gaussian low-pass filter. The smaller the μ_d value, the larger the effect on the low frequencies. The fluctuations in the function quot are eliminated after multiplication with $H(\mu)$ (Fig. 6.3b).

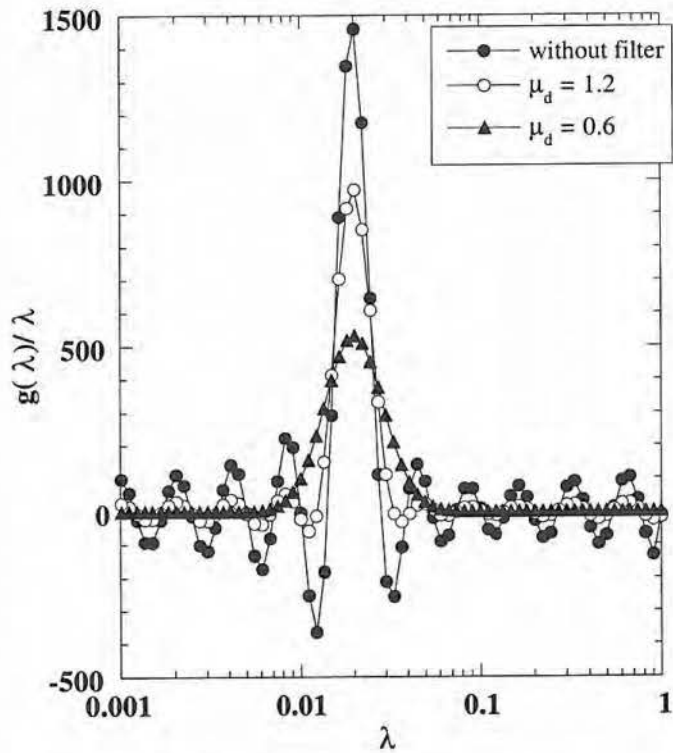
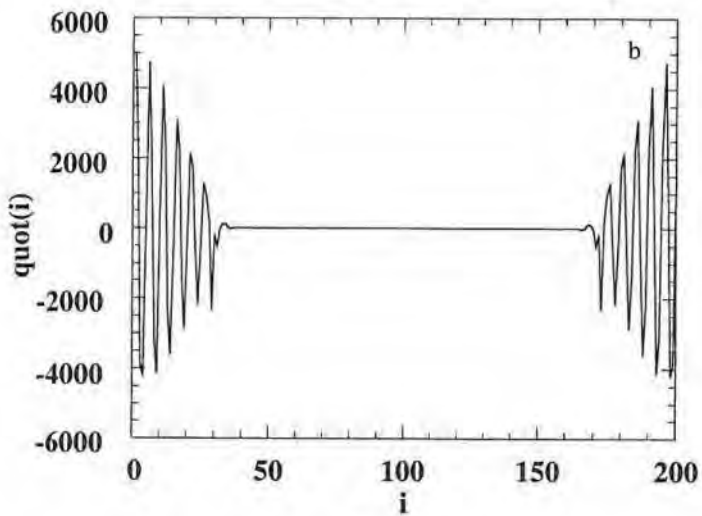
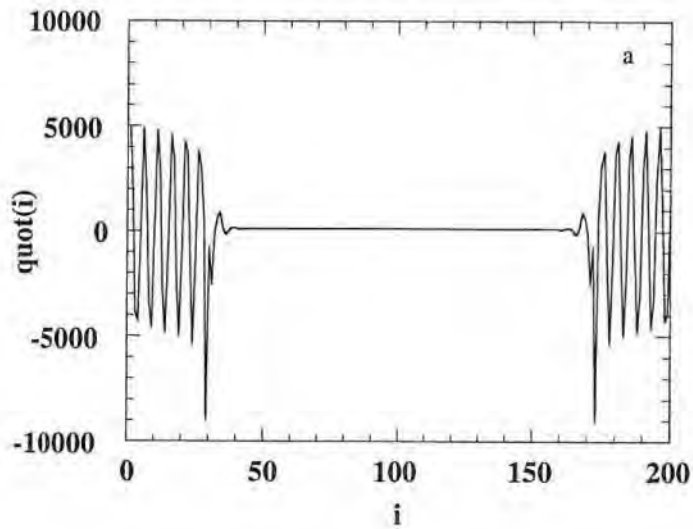


Fig. 6.2. : Overlay plot of the $g(\lambda)/\lambda$ vs λ spectra for the analyses of the data set generated from eq. (6.1) using the improved GGM method without a Gaussian low-pass filter, and with a filter characterized by a μ_d value of 1.2 and 0.6.



Figs 6.3a,b : Function $quot(i)$ obtained in the analysis of the data set from eq. (6.1) : without (a) and with (b) the combination of a Gaussian low-pass filter ($\mu_d = 1.2$).

The influence of the μ_d value of the Gaussian low-pass filter on the signal to noise ratio has been studied further in detail and the results are presented in Fig. 6.4. In the detail plot, it can be seen that from $\mu_d = 5.0$ on, no significant improvement is obtained. If the μ_d value decreases, it can clearly be seen that the signal to noise ratio improves exponentially. However, Fig. 6.2 shows also that the introduction of a Gaussian low-pass filter broadens the peak and, unfortunately, diminishes the resolution. This effect becomes even larger for a smaller μ_d value. A compromise between both effects leads to an optimum choice of the μ_d value.

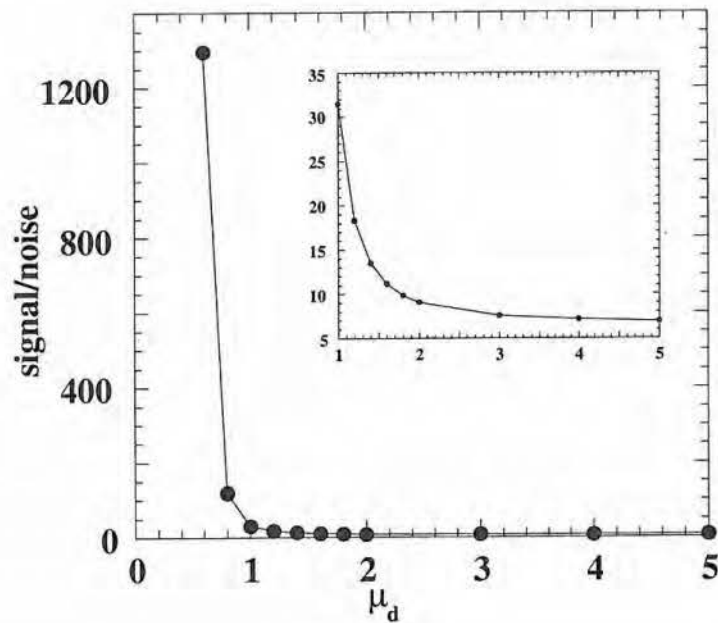


Fig. 6.4 : Influence of the μ_d value of the Gaussian low-pass filter on the signal to noise ratio.

b. Analysis of multicomponent decay curves

Two bi-exponential functions, eqs (6.2) and (6.3), are simulated for $0 \leq x \leq 10$, with $\Delta x = 0.1$, and are analyzed using the improved GGM method combined with a Gaussian low-pass filter with $\mu_d = 1.0$. The $g(\lambda)/\lambda$ vs λ spectra are depicted in Figs 6.5a,b.

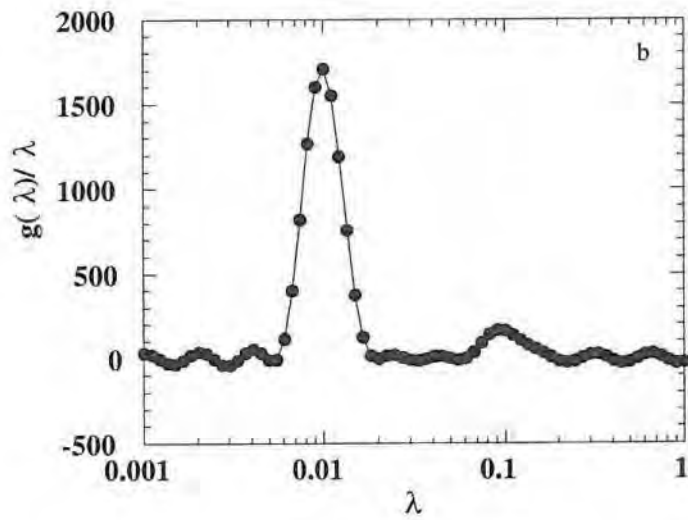
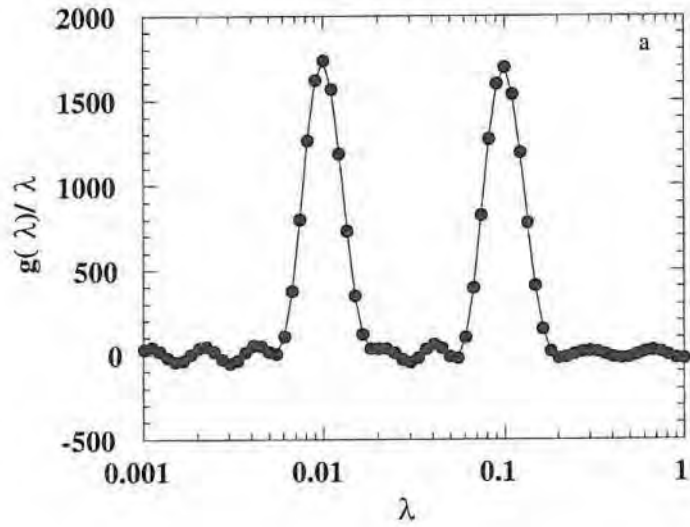
GGM [GarD59] already pointed out that the intensities of the peaks in the $g(\lambda)/\lambda$ vs λ spectrum are proportional to the ratios N_i^0/λ_i for each component i . For the data set originating from eq. (6.2), the ratios are equal to 10^4 for both peaks. The resulting spectrum in Fig. 6.5a has therefore also two peaks of equal size. However, for the data set, simulated from eq. (6.3), the ratio of the first peak is ten times smaller than that of the second one. Its intensity at the corresponding λ value in the spectrum (Fig. 6.5b) is therefore also ten times smaller and can hardly be distinguished from the noise ripples.

The analysis of a more complex decay curve is illustrated by using the function (6.4)

$$f(t) = 3750 \exp(-0.5 t) + 1000 \exp(-0.1 t) + 100 \exp(-0.02 t) + 100 \exp(-0.01 t) \quad (6.4)$$

where the x range is between 0 and 10 at intervals of length 0.1. The $g(\lambda)/\lambda$ vs λ spectrum obtained with the improved GGM method, combined with a Gaussian low-pass filter with $\mu_d = 1.0$, is shown in Fig. 6.6. The four components can be retrieved at the correct λ positions. In eq. (6.4), the ratios are $N_1^0/\lambda_1 = 7500$, $N_2^0/\lambda_2 = N_4^0/\lambda_4 = 10^4$, and $N_3^0/\lambda_3 = 5000$. It can be seen from Fig. 6.6, that the intensities of the second and fourth components are the same, and the intensity of the third component is a factor of two smaller than the intensities of the second and fourth components. Fig. 6.6 also shows that some of the peaks could not be completely resolved. The peaks at $\lambda = 0.02$ and 0.01 , belonging to the third and fourth components, respectively, interfere because the desintegration constants are not sufficiently different (a factor of two).

As a result, in an experimentally observed multicomponent exponential decay curve, the improved GGM method, combined with a Gaussian low-pass filter, will only be able to retrieve components with similar N_i^0/λ_i ratios, and the N_i^0/λ_i value should be large compared to the expected signal to noise ratio.



Figs. 6.5a,b : $g(\lambda)/\lambda$ vs λ spectrum obtained with the improved GGM method combined with a Gaussian low-pass filter ($\mu_d = 1.0$) in the analysis of the data set generated by eqs (6.2) and (6.3).

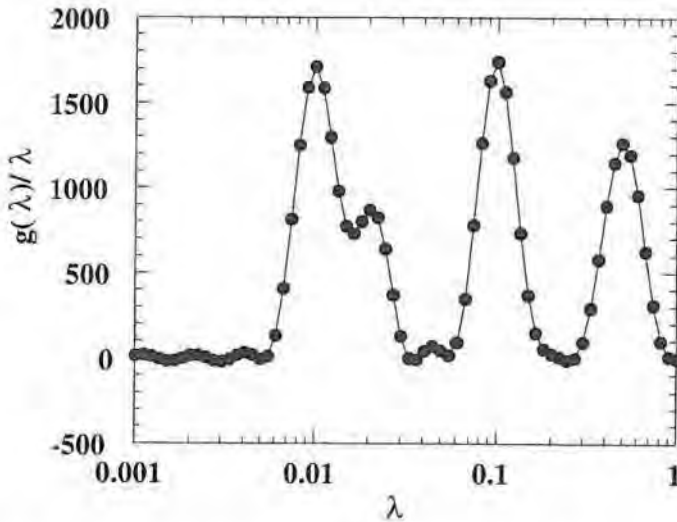


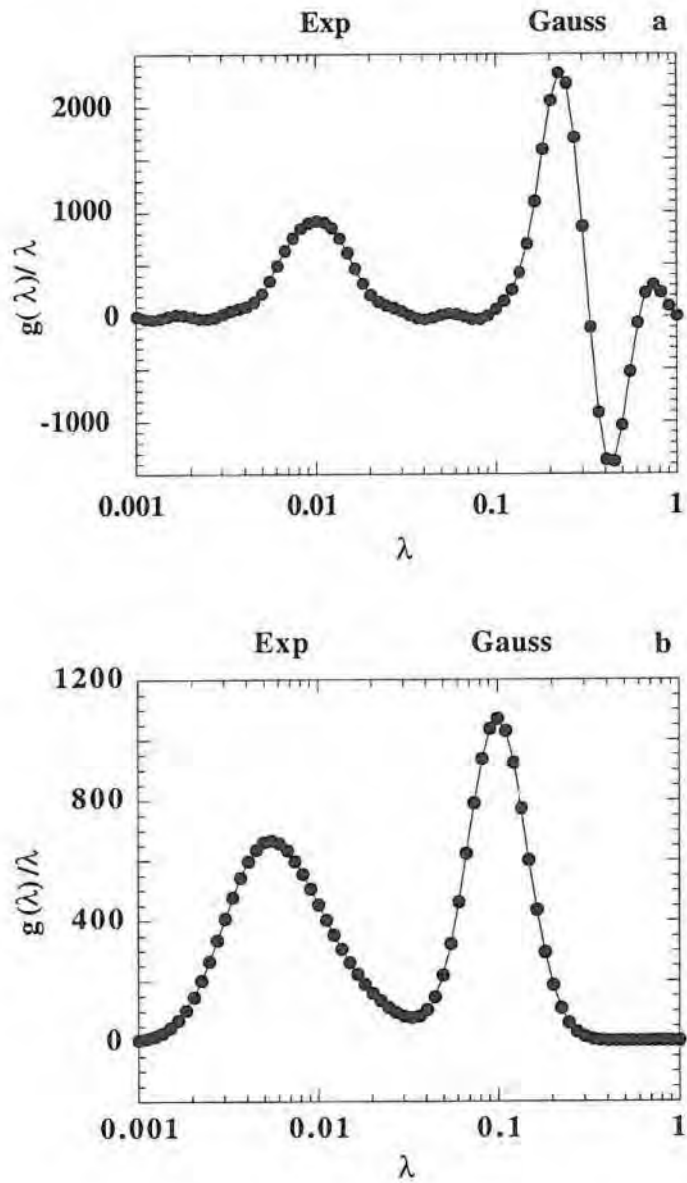
Fig. 6.6 : $g(\lambda)/\lambda$ vs λ spectrum obtained with the improved GGM method combined with a Gaussian low-pass filter ($\mu_d = 1.0$) in the analysis of the data set generated by eq. (6.4).

c. Choice of the model function $kk(x)$

Cohn-Sfetcu et al. [CohS75] showed that the improved GGM method can also be used to analyze multicomponent Gaussians, Lorentzians and $\sin x/x$ type functions by using another model function $kk(x)$ (eq. 5.10). The positions of the peaks are only good estimates for the decay constants when the correct model function is used. For example, Figs 6.7a,b show the $g(\lambda)/\lambda$ vs λ spectra obtained in the analysis of a multicomponent decay curve $f(t)$ composed of a Gaussian and an exponential function (eq.(6.5)) :

$$f(t) = 1000 e^{-(t/10)^2} + 100 e^{-t/100} \quad (6.5)$$

Fig. 6.7a is obtained by using the model function $kk(x) = \exp(-\exp(x))$. Two peaks are present : a symmetric one at $\lambda = 0.01$, corresponding to the decay constant of the exponential component, and an asymmetric one, belonging to the Gaussian component, with a large negative lobe at the right side. Fig. 6.7b is the output of the improved GGM method by using the model function $kk(x) = \exp(-\exp(x^2))$. Again two peaks are seen : a symmetric one at $\lambda = 0.1$, belonging to the Gaussian component, and a broader and asymmetric peak originating from the exponential function. Thus, if the model function $kk(x)$ is chosen correctly, a symmetric peak can be found at the corresponding λ value in the $g(\lambda)/\lambda$ vs λ spectrum.



Figs 6.7a,b : $g(\lambda)/\lambda$ vs λ spectra obtained in the analysis of a multicomponent decay curve composed of a Gaussian and an exponential function (eq. (6.5)) using the model function (a) $kk(x) = \exp(-\exp(x))$, and (b) the model function $kk(x) = \exp(-\exp(x^2))$.

e. Influence of the time scale

An other problem can occur when not all the decay constants are less than unity. Indeed, due to a poor extrapolation in the $]0,1[$ interval for fast decaying components, large computational errors occur and the real peaks are indistinguishable from the error ripples. In Section 5.1.2., the implementation of the GGM method the following about the calculation of the function $f(i)$:

for $n_x+2 \leq i \leq 2*n_x$: the values of the function f must be calculated for each $0 \leq t_i \leq 1$ by extrapolation of the function f using a polynomial of degree 2 through the first 3 measured points.

However if a certain λ_j is larger than 1, an extrapolation using a polynomial of the second degree does not give accurate f value in the last n_x-1 points. A simple solution for this problem is to use a smaller time scale for gathering the experimental data.

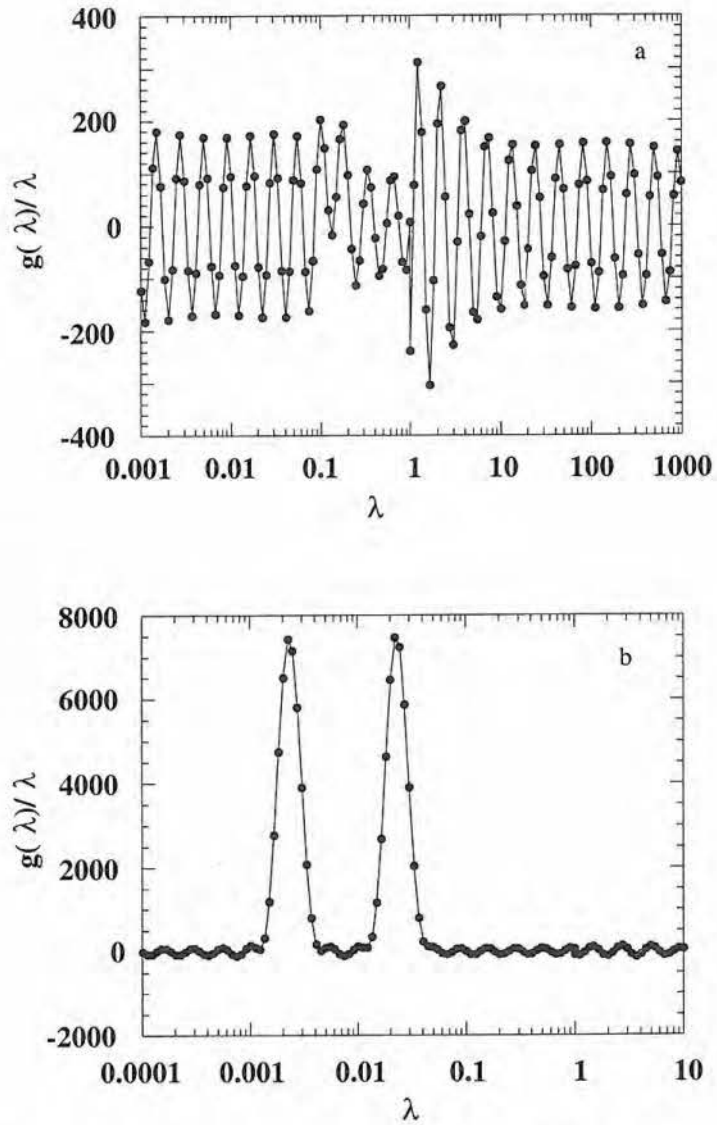
For example, if a mixture of two radionuclides with half lives of 0.5 and 5 hours is measured, the activity $f(t)$ can be represented by eq. (6.6) when the time unit is one hour, or by eq. (6.9) when the time is expressed in minutes :

$$f(t) = 1000 \exp(-1.386 t) + 100 \exp(-0.1386 t) \quad (6.6)$$

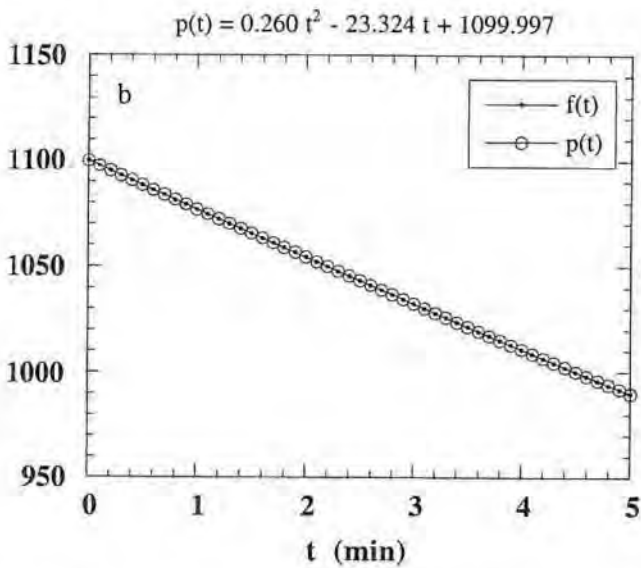
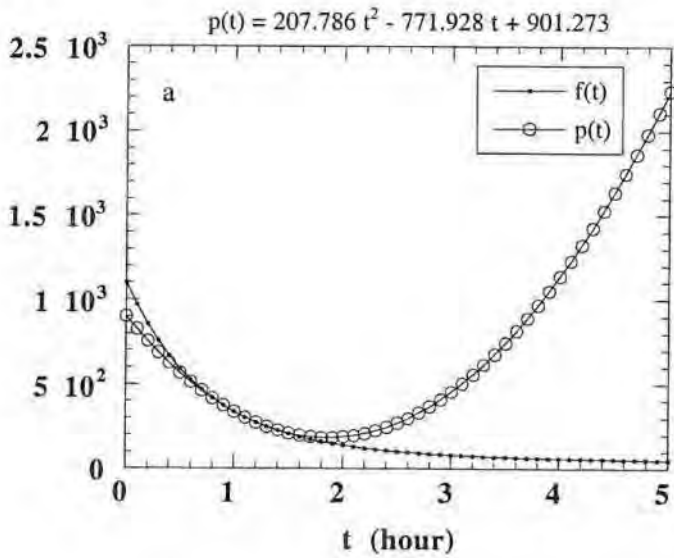
$$f(t) = 1000 \exp(-0.0231 t) + 100 \exp(-0.00231 t) \quad (6.9)$$

Data sets for these functions are simulated for $x = \ln t$ varying between 0 and 10 with $\Delta x = 0.1$ unit. The analyses, using the improved GGM method combined with a Gaussian low-pass filter with $\mu_d = 1.0$, result in the $g(\lambda)/\lambda$ vs λ spectra that are shown in Figs 6.8a and b for the eqs (6.6) and (6.9), respectively. In Fig. 6.8a, no reliable information about the positions of the real peaks can be deduced. In Fig. 6.8b, two equal intense peaks are clearly observable at the expected positions.

The second degree polynomials $p(t)$ that are used for the extrapolation in the interval $]0,1[$ are shown in Figs 6.9a and b. It can be seen that the polynomial, calculated for the extrapolation of the data set generated for eq (6.6) (Fig. 6.9a), is a poor approximation of the real data set. On the contrary, $p(t)$ (Fig 6.9b) calculated for the data set generated from eq. (6.9), corresponds very well to the real vales of $f(t)$.



Figs 6.8a,b : $g(\lambda)/\lambda$ vs λ spectra obtained with the improved GGM method combined with a Gaussian low-pass filter ($\mu_d = 1.0$) in the analysis of the data sets of eq.(6.6) when the time unit is one hour (a), and of eq.(6.9) when the time unit is one minute (b).



Figs 6.9a,b : Overlay plot of $f(t)$ and the computed polynomial $p(t)$ of the second degree for the data sets generated from eq. (6.6) when the time unit is one hour (a), and from eq. (6.9) when the time unit is one minute (b).

Keeping all these characteristics of the improved GGM method in mind, it can be concluded that carefully chosen experimental conditions can improve and simplify the analysis of the data.

6.2.2. Data in the presence of noise

In many applications, the observed multi-exponentials are the result of counting processes characterized by a Poisson distributed noise. The influence of such a noise has been studied on simulated mono- exponential decay functions :

$$f(t) = 10^6 \exp(-0.01 t) \quad , \quad \text{initially 0.1 \% noise} \quad (6.7)$$

$$f(t) = 10^4 \exp(-0.01 t) \quad , \quad \text{initially 1.0 \% noise} \quad (6.8)$$

Noise has been introduced on the values of the functions (6.7) and (6.8) by using a Poisson random number generator [VanR93].

The data sets are analyzed with the improved GGM method combined with a Gaussian filter ($\mu_d = 1.0$). The resulting $g(\lambda)/\lambda$ vs λ spectra are presented in Fig. 6.10. In the absence of noise, a signal to noise ratio of ca. 30 can be expected (Fig. 6.4). The spectra in Fig. 6.10 show that the signal to noise ratio decreases to a value of ca. 8 for an initial noise level of already 0.1 %. More dramatically is the signal to noise ratio for the data set generated from eq. (6.8), where the value is at most equal to 2. An improved spectrum can be obtained when a Gaussian low pass filter is used with a smaller μ_d . For example, if μ_d equals 0.6 in the analysis of eq. (6.8), the spectrum in Fig. 6.11 is obtained. The signal to noise ratio increases by a factor of two. But as a result of the lower resolution, the neighboring error ripples interfere with the real maximum at $\lambda = 0.01$. The improved GGM method is therefore well suited for experimental data which are characterized by low noise levels. The spectra obtained in the analysis of data sets with higher noise levels must be carefully interpreted.

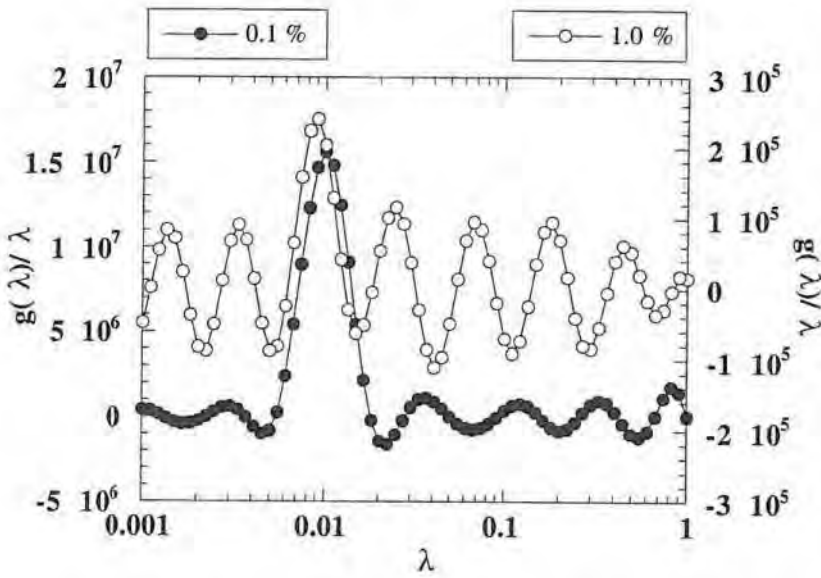


Fig. 6.10 : $g(\lambda)/\lambda$ vs λ spectra obtained from eqs (6.7) and (6.8) with initial Poisson distributed noise levels of 0.1 % and 1.0 % respectively, using the improved GGM method ($\mu_d = 1.0$).

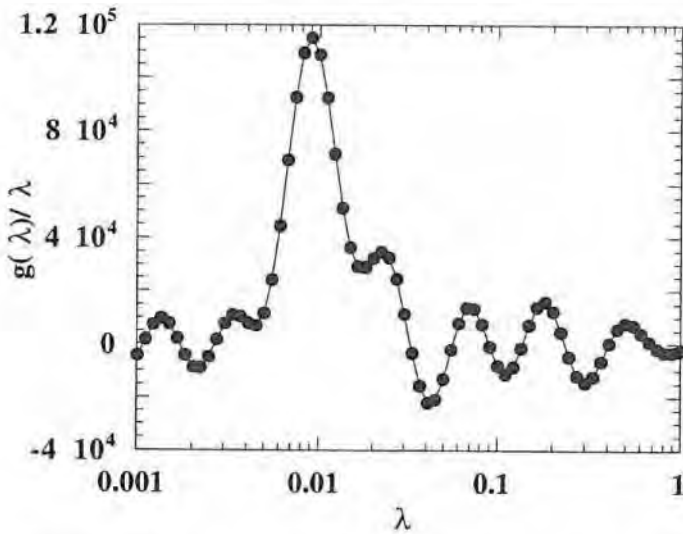


Fig. 6.11 : $g(\lambda)/\lambda$ vs λ spectrum obtained from eq. (6.8) with an initial 1.0% Poisson distributed noise using the improved GGM method ($\mu_d = 0.6$).

6.3. Evaluation of the improved method of Prony

6.3.1. Noise-free data

The improved method of Prony requires a data set (t_i, f_i) at constant time intervals Δt . In order to obtain some characteristics of the technique, this data set is analyzed several times using the recurrence version of Prony's improved method in different ways. In the present discussion, the results are used that have been obtained in the analyses of the data sets from eqs (6.1 - 6.4) simulated at points t_i in a range $[0, 1000]$ with $\Delta t = 20$.

a. Input of the number of components n

An important parameter is the input of the number of components n . Therefore, the data set from eq. (6.4) is analyzed on the assumption that it is composed of 3, 4, and 5 exponential functions, respectively. The optimized (N_i^o, λ_i) values for each component i are given in Table 6.1.

Table 6.1 : Optimized (N_i^o, λ_i) values from Prony's improved method for the data set generated from eq. (6.4) on the assumption that it is composed of 3, 4, and 5 exponential functions, respectively.

Input n	N_i^o	Output λ_i
3	151	0.0114
	279	0.0533
	4519	0.2100
4	100	0.01
	100	0.02
	1000	0.10
	3750	0.50
5	0	0.2148-0.571i
	100	0.01
	100	0.02
	1000	0.10
	3750	0.50

If the number of components is correct, the program calculates the exact (N_i^o, λ_i) values. When n is too large, a component with an unreal (complex or negative) decay constant and zero intensity is found. Apparently, this has no effect on the calculation of the (N_i^o, λ_i) values for the other components. However, if n is too small, the optimized decay constants and pre-exponential factors can deviate a lot from the true values.

b. Influence of starting values

The improved method of Prony can be used with or without starting values for the decay constants. For simulated decay curves in the absence of noise the program itself can generate a set of good starting values (see Table 6.1). However, when the operator gives an input set with an unknown accuracy, the program is obliged to start the iteration with these parameters. Therefore, the influence of the starting λ_i values on the accuracy of the final (N_i^o, λ_i) values has been investigated. Table 6.2 shows the results that are obtained with two different sets of starting λ_i values (the data sets generated from eqs (6.1-6.4) have been used).

Table 6.2 : Optimized (N_i^o, λ_i) values from Prony's improved method on the data sets generated from eqs (6.1 - 6.4) with two different sets of starting λ_i values.

Eq.	n	Input λ_i	Output	
			N_i^o	λ_i
(6.1)	1	a. 0.01	100	0.02
		b. 0.04	100	0.02
(6.2)	2	a. 0.02	100	0.01
		0.2	1000	0.1
		b. 0.005	100	0.01
		0.05	1000	0.1
		c. 0.02	100	0.01
		0.05	1000	0.1
(6.3)	2	a. 0.02	100	0.01
		0.2	100	0.1
		b. 0.005	100	0.01
		0.05	100	0.1
		c. 0.02	100	0.01
		0.05	100	0.1
(6.4)	4	a. 0.011	100	0.01
		0.022	100	0.02
		0.11	1000.1	0.1
		0.55	3749.9	0.5012
		b. 0.011	20.5+47.7i	0.0020 - 0.0831i
		0.022	20.5-47.7i	0.0020 + 0.0831i
		0.09	21.8	0.0006 - 0.1571i
		0.45	4787.9	0.0829

Even a deviation of 10% can result in complex values for the decay constants and hence, also in inaccurate pre-exponential factors. Thus, starting values given as input ought to be accurate : λ values from the literature or from the improved GGM method should be used.

c. Influence of the number of data points

Experimentally, the process is followed at constant time intervals in a given time period. The number of data points depends upon the size of the interval. For a small size, a better description of the function $f(t)$ is obtained and as a result, a better analysis of the data set can be expected. This statement is tested by simulating three different data sets with the function (5). The size of the interval is equal to 20, 10, and 2, so that over a time period of $[0,1000]$, a number of data points is collected equal to 50, 100, and 500, respectively. For $\Delta t = 20$, the optimized (N_i^o, λ_i) values for each component i are already given in Table 6.2. Table 6.3 shows the results returned by Prony's improved method when Δt is decreased to 10 and 2. An improvement can be observed when the set is enlarged to 100 data points. A further increase to 500 data points has an opposite effect, which is not caused by the input data set itself but rather by the numerical computations. In the improved method of Prony, the n decay constants λ_i are found from the roots $\rho_i = e^{-\lambda_i/N}$ of the characteristic polynomial $P_\delta(z)$ (eq.(5.29)). For large N , this is an ill-conditioned problem because the ρ_i cluster near one.

Table 6.3 : Optimized (N_i^o, λ_i) values obtained by Prony's improved method on the data sets generated from eq. (6.4) over a time period of $[0,1000]$ at Δt equal to 10 (100 input points) and 2 (500 input points).

number of input points, N	n	Input λ_i	Output	
			N_i^o	λ_i
100	4	0.011	102.0	0.0101
		0.022	98.70	0.0203
		0.09	1001	0.1002
		0.45	3748	0.5012
500	4	0.011	-2.150	0.0068-1.571i
		0.022	162.0	0.0120
		0.09	1165	0.0970
		0.45	3653	0.5585

6.3.2. Data in the presence of noise

The influence of a Poisson distributed noise has been quantitatively studied on the data sets generated from eqs. (6.7) and (6.8) at constant time intervals ($\Delta t = 10$) over a time period [0,1000]. Prony's improved method has been able to analyze these data sets without an initial estimate for the decay constant.

The optimized parameters in the presence of 0.1 % noise are : $\lambda = 0.010004$ and $N^{\circ} = 1.0002 \times 10^6$. The deviations from the true values of the parameters in eq. (6.7) are small compared to the initial noise level. In the presence of 1.0 % noise, the program returns the following optimized values : $\lambda = 0.009633$ and $N^{\circ} = 9.9734 \times 10^3$. Here the value for the decay constant differs by 3.7% from the true value in eq. (6.8). The analysis of a second data set simulated from eq. (6.8) at time intervals $\Delta t = 2$ shows that more accurate results ($\lambda = 0.010041$ and $N^{\circ} = 1.0075 \times 10^4$) could be obtained with Prony's improved method if the function values, characterized by higher noise levels, are simulated at smaller time intervals.

6.4. Conclusions

The improved methods of GGM and Prony are evaluated individually using simulated data.

The study of the characteristics of the improved GGM method included the following topics : (a) the influence of the Gaussian low-pass filter, (b) its performance on multicomponent decay curves, (c) the influence of the model function $kk(x)$, and (d) the choice of the time scale.

It has been found that with the use of a Gaussian low-pass filter, the intensities of the noise ripples strongly decrease. Further, it has been illustrated that smaller μ_d values of the Gaussian low-pass filter improve the signal to noise ratio exponentially but diminish the resolution. Hence, a compromise between both effects leads to an optimum choice of the μ_d value.

In the study of multicomponent exponential decay curves, it has been shown that the improved GGM method, combined with a Gaussian low-pass filter, will only be able to retrieve components with similar N_i°/λ_i ratios, and the N_i°/λ_i value should be large compared to the expected signal to noise ratio.

A criterium has been formulated for the correct choice of the model function $kk(x)$: "if the model function $kk(x)$ is chosen correctly, a symmetric peak can be found at the corresponding λ value in the $g(\lambda)/\lambda$ vs λ spectrum".

The choice of the time scale is a critical factor in the experimental set-up for measuring exponential decay curves. It has been illustrated that if a certain λ_j is larger than 1, an extrapolation using a polynomial of the second degree does not give accurate f values in the last n_x-1 points. As a result no reliable information is present in the resulting $g(\lambda)/\lambda$ vs λ spectrum. A simple solution for this problem has been offered : "use a smaller time scale for gathering the experimental data".

The impact of some important parameters of Prony's improved method of are studied, i.e. the input of the number of components n , the influence of the starting values for λ_j , and the influence of the number of data points N .

It has been found that for a correct input of the number of components, the program is able to calculate the exact (N_i^o, λ_i) values. However, when n is too large, the program finds a component with an unrealistic (complex or negative) decay constant and zero intensity ; when n is too small, the program returns inaccurate decay constants and pre-exponential factors.

In the study of the influence of the starting values, it has been shown that even a deviation of 10% can result in complex values for the decay constants, and hence, also in inaccurate pre-exponential factors. Thus, starting values given as input ought to be accurate : " λ values from the literature or from the improved GGM method should be used".

The quality of the results depends also upon the number of data points N . The larger the set of data points, the better the f function is described over a certain range. However, for large N , the problem becomes ill-conditioned. Therefore, the number of data points should be limited (for example to 100).

Finally, for both techniques, the impact of an initial Poisson distributed noise level of 0.1 and 1.0 % is checked. It has been found that an initial noise level of 1% has a strong impact on both methods. It has been recommended that the $g(\lambda)/\lambda$ vs λ spectra obtained with the improved GGM method combined with a Gaussian filter with a small μ_d value, should be interpreted carefully, and that a large data set gathered at small time intervals for the quantitative analysis with Prony's improved method should be used.

The general conclusion is that carefully chosen experimental conditions can improve and simplify the analysis of multicomponent decay curves.

Chapter 7

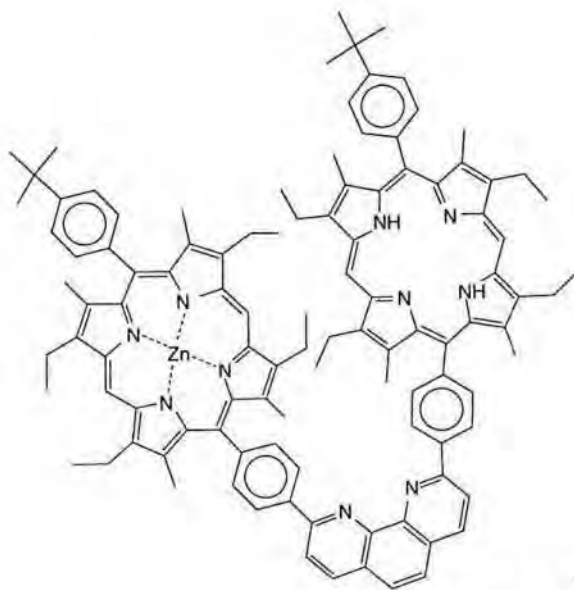
Qualitative and quantitative applications

During the extensive evaluation of our software described in Chapter 6, we could explore its capabilities and limitations. Also, we were able to formulate some practical tips for the analysis of experimental data. Keeping this knowledge in mind, we applied the combined use of the improved methods of Gardner et al. and Prony to experimental data, obtained from fluorescence decay, free induction decay (solid state ^1H NMR) and radioactivity decay measurements. The results are compared with those obtained by using common algorithms for the specific disciplines, i.e. the Marquardt-Levenberg [LevK44] algorithm for the analysis in fluorescence and NMR spectrometry, and Cumming's method [CumJ62] in nuclear chemistry.

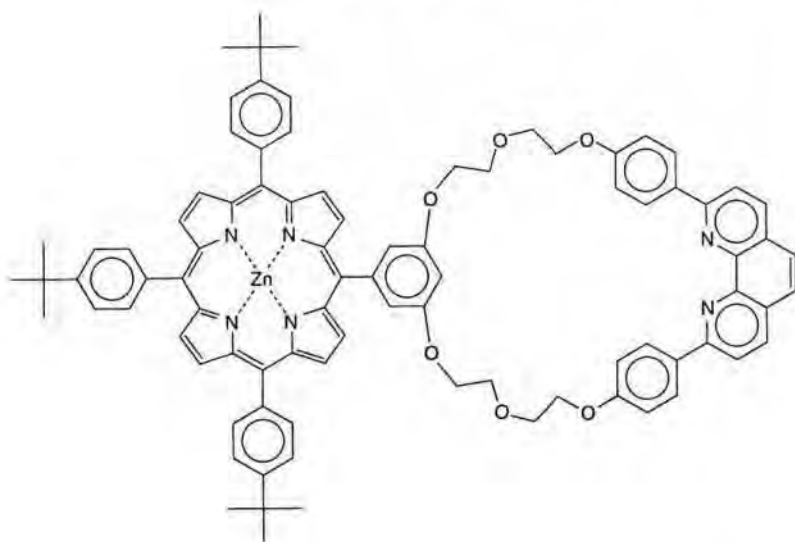
7.1. Fluorescence decay curves

Interlocked macrocyclic species (catenanes) are very interesting from a photochemical and photophysical point of view due to the electronic interactions between the various subunits in the ground and excited states. Catenanes with coordinating ability (catenands) can give rise to metal complexes (catenates) where the photochemical and photophysical properties are profoundly affected by the nature of the coordinated metal [ArmN93].

In this section, the fluorescence emissions of two porphyrin substituted catenanes I and II (Fig. 7.1) containing Zn and/or Cu ions are studied. First, the problems arising during the analysis of the fluorescence decay curves of compound I, are illustrated. In spite of these problems, the improved methods of Gardner and Prony have proven to be useful to analyze fluorescence decay as will be shown in the study of compound II where they allowed a successful analysis of the decay curves with a minimum of a priori information.



Compound I



Compound II

Fig. 7.1 : Structures of compound I and II

7.1.1. Experimental set-up

7.1.1.1. Determination of the fluorescence decay curves

The time-correlated single photon counting technique [KhaM91, O'CoD84] allows to record fluorescence decays with a dynamic range of 10^4 . Furthermore, as the data are obtained directly in digital form as discrete counts, the statistical error content of each data point (channel) is known a priori. Therefore, it is the method of choice to provide information on the mechanism of excited-state interactions of fluorescing species. High repetition rate, picosecond tunable dye lasers [SpeK78, KoeV78] and microchannel plate multipliers [YamI85, KumH88, BebD86, BoeN90] have improved the time resolution of the technique, allowing to determine decay times of less than 10 ps. Those developments allowed furthermore to collect in a very short time multidimensional fluorescence decay surfaces as a function of excitation/emission wavelength, quencher, concentration, pH, time increment,... When the excited state kinetics can be described as a series of coupled first order processes, the fluorescence decays are a linear combination of exponentials. Under these conditions, all decays obtained in a set of varying experimental conditions of excitation or emission wavelength or time increment per data point (channel width), have the same number of exponentials n with the same values of the decay constants λ_i , and the experimental conditions influence only the amplitudes of exponentials N_i^0 . Therefore, a simultaneous analysis of related decay traces, i.e. of the fluorescence decay surface, can be performed by linking the common fitting parameters [EisJ79, KnuJ83, LöffJ85, BeeJ85, AmeM85, JanL90, BoeN89]. The recently introduced global compartmental analysis [BeeJ85, AmeM91, AndR91] allows to link rate constants over the decay data surface and to analyze simultaneously decays obtained not only at different excitation or emission wavelengths, but also at different concentrations or different temperatures.

In the present study, the fluorescence decay of two porphyrin substituted catenanes is studied at different emission wavelengths. It should be mentioned that the experiments were set up at an earlier date, so that no guidelines could be given to optimize the data collection for the combined use of the improved methods of Gardner et al. and Prony. The fluorescence decay curves of compound I in dichloromethane, measured at emission wavelengths of 582, 630, 665, and 695 nm are obtained at constant time intervals of 0.04280 ns over a time period of 0 to 20.373 ns after an excitation pulse at 540 nm. The fluorescence decay curves of compound II in butyronitrile measured at emission wavelengths of 610, 630, 650, 670, and 690 nm are recorded after an excitation pulse at 597 nm at constant time intervals of 0.0207 ns over a time period of 0 to 9.6048 ns.

The finite width of an excitation pulse (8 ps) and the spread of the transit time of the photo-electrons in the microchannel plate detection (40 ps) make the observed fluorescence decay a convolution of the true decay curve with the instrumental response function (IRF), which is itself a convolution of an excitation pulse (delta-response) and detector response [BirJ67]. The response can therefore be written as

$$y(t, \lambda_{em}) = \int_0^t \text{IRF}(t', \lambda_{ex}, \lambda_{em}) f(t-t') dt' \quad (7.1)$$

with

$$f(t) = \sum_{i=1}^n N_i^0 \exp(-t/\tau_i) \quad (7.2)$$

where n is the number of components, and N_i^0 and τ_i are the amplitude and decay constant of the i th component, respectively.

Fig. 7.2 shows a portion of the resulting decay curve (y) of compound II obtained at $\lambda_{em} = 630$ nm together with the IRF obtained at 540 nm using a scattering solution.

Since the data are distorted due to the convolution with the IRF function, serious problems occur in the quantitative analysis of the fluorescence decay curves using the improved methods of Gardner et al. and Prony. These problems will be discussed in each of the experimental studies.

7.1.1.2. Analysis of the fluorescence decay curves

Each of the recorded data sets are analyzed using the following procedure. After a cubic spline interpolation, the improved method of Gardner combined with a Gaussian low-pass filter is applied in order to determine the number of components and to estimate the decay constants. Secondly, the Prony's improved method is used with starting values (obtained from the previous improved method of Gardner) on a subset of the data set in order to quantify the parameters τ_i and N_i^0 for each component i .

The final results are compared with those obtained from the application of the Marquardt-Levenberg algorithm under the same conditions as used for the optimization of Prony's improved method. Finally, the results from the global analysis are presented.

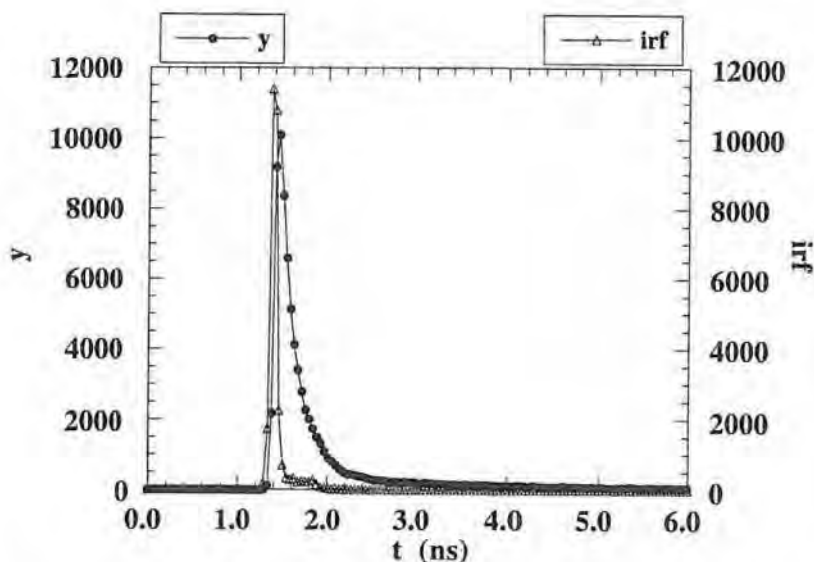


Fig. 7.2 : Fluorescence-emission (●) of compound II recorded at $\lambda_{em} = 630$ nm together with the IRF (Δ).

7.1.2. Study of compound I

7.1.2.1. Problems

a. Interpretation of the $g(\lambda)/\lambda$ vs λ spectra

The original data sets are collected at time units of ns. However, decay times of ps can be expected in fluorescence decay curves of catenanes. Hence, decay constants larger than unity can be expected, and consequently, the time scale is multiplied by a factor of 100 before the cubic spline interpolation algorithm is applied. A data set in constant logarithm time scale $x = \ln t$ over an interval $[0,6.8]$ with $\Delta x = 0.1$ is obtained.

The $g(\lambda)/\lambda$ vs λ spectra resulting from the improved GGM method combined with a Gaussian low-pass filter ($\mu_d = 0.55$) are superimposed in Fig. 7.3. The interpretation of the maxima is difficult : the number of maxima and their positions are different for each spectrum. The positions of potential peaks in the resulting $g(\lambda)/\lambda$ vs λ spectra are $\lambda_1 = 0.3$ and $\lambda_2 = 1.0$ and $\lambda_3 = 2.0 - 3.0$ ns⁻¹. The intensity of the peaks differs for each λ_{em} . Possibly, there are also some small peaks present at $\lambda > 5$ ns⁻¹, but these can hardly be distinguished from error ripples.

Furthermore, due to the convolution of the original response with the IRF, the area of $(\lambda/100)$ from 1 to 0,1 ns^{-1} in the $g(\lambda)/\lambda$ vs λ spectra contains no relevant information, and consequently, it can be stated that components with very short decay times cannot be retrieved.

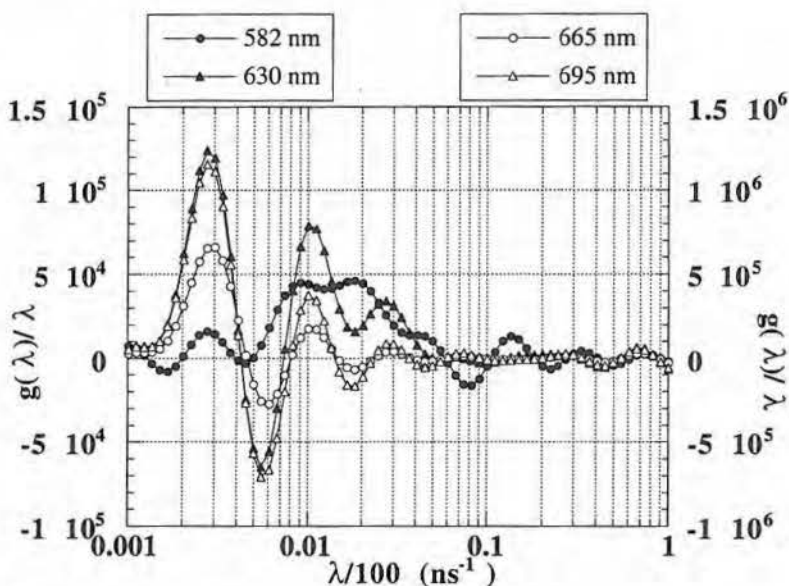


Fig. 7.3 : $g(\lambda)/\lambda$ vs λ spectra in the analysis of the fluorescence decay curves of compound I measured at different λ_{em} .

Due to the limited amount of product, the experiments could not be repeated under better conditions by using e.g. smaller Δt (as for compound II, see further).

Consequently, one is confronted with the problem that no reliable information concerning the number of components and of their decay constants can be deduced from the $g(\lambda)/\lambda$ vs λ spectra. This will hamper the quantification which is performed by using Prony's improved method.

b. Quantification

Since the influence of the IRF function is already small at one point after the maximum in the fluorescence decay curve (see Fig. 7.2), the fitting of the experimental points is started at this position. The data file contains many points. The evaluation of Prony's method (see Chapter 6) showed that a set of 100 points is preferred in order to

produce good results. Therefore, a subset of 100 points at $\Delta t = 0.1284$ ns is selected from the original data set. The analyses have been repeated several times with different number of components, and with or without starting values (deduced from the individual $g(\lambda)/\lambda$ vs λ spectrum). The plausible solution for each decay curve is chosen based on the standard residual plots and on the fact that no complex or unrealistic parameters are returned by the program. With the same input conditions, the decay curves have also been analyzed by using the Marquardt-Levenberg algorithm.

The results of both analyses are collected in Tables 7.1 and 7.2. In general, a good agreement is found between both analyses. Only for the decay curve measured at $\lambda_{em} = 630$ nm, three components are found. The first component, near 2 ns^{-1} , is only found in the analysis of the decay curves recorded at 582 and 630 nm. This could also be expected from the $g(\lambda)/\lambda$ vs λ spectra shown in Fig. 7.3 where the contribution of this component is only significant at these two λ_{em} . A second component has a value $\lambda_2 = 0.44$ and 0.34 ns^{-1} at $\lambda_{em} = 582$ and 695 nm, respectively. The second component found at $\lambda_{em} = 630$ and 665 nm has a value $\lambda_2 = 0.8 \text{ ns}^{-1}$. Probably, these are two different components corresponding to the two peaks (at a 0.3 and a 1.0 ns^{-1}) in the $g(\lambda)/\lambda$ vs λ spectra in Fig. 7.3. A last component is characterized by a λ of $0.1 - 0.2 \text{ ns}^{-1}$. The growing contribution of this peak at higher λ_{em} (Fig 7.3) might indicate that it could also be related to the peak at $\lambda = 0.3 \text{ ns}^{-1}$ in the $g(\lambda)/\lambda$ vs λ spectra in Fig. 7.3. Nevertheless, the intensity of this peak in the $g(\lambda)/\lambda$ vs λ spectrum at $\lambda_{em} = 630$ is also large and its contribution, calculated using the methods of Prony and Marquardt-Levenberg is rather small. In general, it can be stated that the fraction of the first component diminishes strongly and that the fraction of the third component increases as the decay curves are recorded at higher emission wavelengths.

7.1.3. Study of compound II

7.1.3.1. Qualitative analysis

For the second compound, decay constants larger than unity could also be expected. Therefore, the time scale was multiplied by a factor 100 before a cubic spline interpolation algorithm was applied in order to obtain a data set in a constant logarithm time scale $x = \ln t$ over an interval $[0,6.8]$ with $\Delta x = 0.1$.

The improved GGM method is combined with a Gaussian low-pass filter ($\mu_d = 0.55$) in order to reduce the experimental and computational noises. The resulting $g(\lambda)/\lambda$ vs λ spectra obtained in the analysis of the fluorescence decay curves recorded at $\lambda_{em} = 610$, 650 and 690 nm are superimposed in Fig. 7.4. Two peaks at $\lambda_1 \approx 0.4$ and $\lambda_2 = 1.2 \text{ ns}^{-1}$ are

present in all three spectra, and a third peak at $\lambda_3 \approx 2.5 - 3.0 \text{ ns}^{-1}$ in only two of the three spectra. This is a first indication that it is probably an large interfering error ripple. All other maxima are error ripples since their positions are variable and their intensity, relative to the intensity of a real peak, is very small. Similar to the spectra of compound I, the $\lambda/100$ area from 1 to 0.1 ns^{-1} in the $g(\lambda)/\lambda$ vs λ spectra contains no relevant information (due to the convolution), and consequently, it can be stated that components with very short life times cannot be retrieved.

Table 7.1 : Results obtained with Prony's optimized method.

λ_{em} (nm)	λ_1 (ns^{-1})	λ_2 (ns^{-1})	λ_3 (ns^{-1})	N°_1 (counts)	fraction ₁ (%)	N°_2 (counts)	fraction ₂ (%)	N°_3 (counts)	fraction ₃ (%)
582	1.51	0.44	-	8835	94.7	498	5.3	-	-
630	1.72	0.81	0.11	6614	69.9	2023	21.4	824	8.7
665	-	0.79	0.18	-	-	2272	23.0	7590	77.0
695	-	0.34	0.11	-	-	2360	24.2	7375	75.8

Table 7.2 : Results obtained with the Marquardt-Levenberg algorithm.

λ_{em} (nm)	λ_1 (ns^{-1})	λ_2 (ns^{-1})	λ_3 (ns^{-1})	N°_1 (counts)	fraction ₁ (%)	N°_2 (counts)	fraction ₂ (%)	N°_3 (counts)	fraction ₃ (%)
582	1.50	0.30	-	8909	83.9	1715	16.1	-	-
630	1.75	0.65	0.11	7450	78.8	1236	13.1	766	8.1
665	-	0.46	0.17	-	-	3893	37.4	6511	62.6
695	-	0.34	0.11	-	-	2625	27.0	7094	73.0

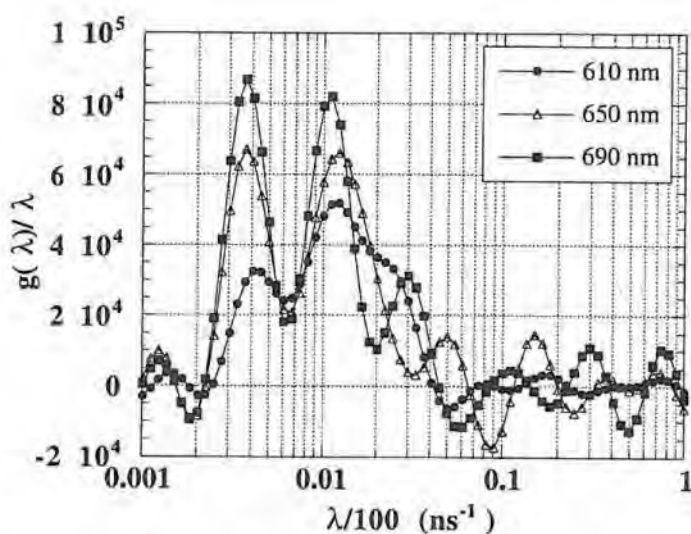


Fig. 7.4 : $g(\lambda)/\lambda$ vs λ spectra in the analysis of the fluorescence decay curves of compound II measured at different λ_{em} .

7.1.3.2. Quantitative analysis

Since the data are distorted due to the convolution with the IRF function, the quantitative analysis can only give tentative results. The influence of the IRF function can be limited by starting the fitting procedure one point after the maximum in the fluorescence decay curve (see Fig. 7.2). Prony's improved method is applied to a subset of 100 points at $\Delta t = 0.0621$ ns from the original data set. Using the information about the decay constants (3 components and their approximate decay constants) deduced above from the improved GGM method, the program returns a complex value for λ_3 with an intensity near 0. This is a second proof that only two components are present. Therefore, the improved Prony algorithm is repeated with and without starting values for λ_1 and λ_2 . The optimized (N_i^0, λ_i) values and the calculated fractions of each component are collected in Table 7.3. The first component corresponds to the peak found in the $g(\lambda)/\lambda$ vs λ spectra at $\lambda_1 \approx 0.4$ ns⁻¹, and the second one to the peak at $\lambda_2 \approx 1.2$ ns⁻¹. It can be noticed that if λ_{em} increases, the decay constants decrease instead of being constant. The fractions vary for different experimental conditions (e.g. 17 to 27% for the first component). These tendencies are also present in the results obtained with the classic Marquardt-Levenberg method [LevK44] (Table 7.4). Here, the fraction of the first component increases for larger values of λ_{em} .

Table 7.3 : Results obtained with Prony's optimized method.

λ_{em} (nm)	λ_1 (ns ⁻¹)	λ_2 (ns ⁻¹)	N ^o ₁ (counts)	fraction ₁ (%)	N ^o ₂ (counts)	fraction ₂ (%)
610	0.59	1.55	1984	20.9	7516	79.1
630	0.48	1.42	1607	16.6	8064	83.4
650	0.48	1.43	2624	26.8	7167	73.2
670	0.44	1.39	2143	21.7	7712	78.3
690	0.41	1.31	2499	24.8	7566	75.2

Table 7.4 : Results obtained with the Marquardt-Levenberg algorithm.

λ_{em} (nm)	λ_1 (ns ⁻¹)	λ_2 (ns ⁻¹)	N ^o ₁ (counts)	fraction ₁ (%)	N ^o ₂ (counts)	fraction ₂ (%)
610	0.54	1.49	1620	17.2	7813	82.8
630	0.49	1.41	1598	16.6	8021	83.4
650	0.41	1.29	1830	19.0	7817	81.0
670	0.41	1.32	1848	18.9	7929	81.1
690	0.38	1.24	2104	21.1	7864	78.9

In Fig. 7.5, the experimental fluorescence decay curve and the calculated fitted bi-exponential function are depicted together with the standard residual plot of the data set, recorded at $\lambda_{em} = 630$ nm (only 1/3 of the experimental points are shown). The fitted function describes the data set very well, resulting in a perfect standard residual plot without outliers.

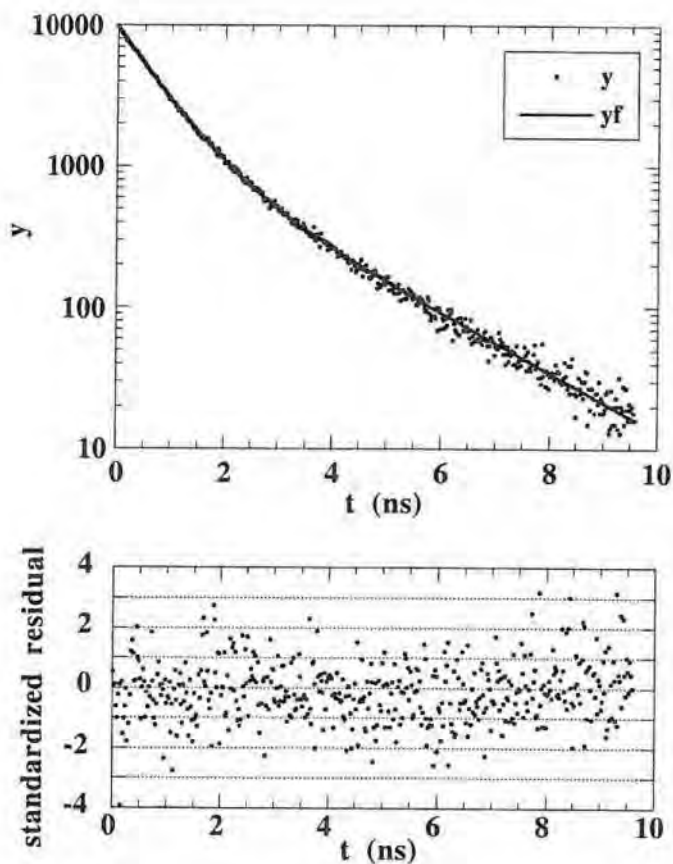


Fig. 7.5 : Experimental decay curve, fitted bi-exponential function, and the corresponding standard residual plot of the data set recorded at $\lambda_{em} = 630$ nm.

7.1.4. Conclusions

The study of the fluorescence decay curves of two catenanes illustrated that the proposed combination of the improved GGM method and Prony's method sometimes has to deal with serious problems, e.g. the interpretation of complex $g(\lambda)/\lambda$ vs λ spectra, and the further quantification based on poor reliable information.

Furthermore, the importance of a prior discussion between the operator and the analyst in such difficult research topics which are further hampered by the limited supply of the studied products, has been stressed in the study of compound I.

Due to the convolution with the IRF function, the quantitative analysis can only give tentative results. Since, in the qualitative analysis with the improved GGM method, the $(\lambda/100)$ range from 1 to 0.1 ns⁻¹ in the $g(\lambda)/\lambda$ vs λ spectra contains no relevant information. Furthermore, in the quantitative analysis with Prony's improved method or with the Marquardt-Levenberg algorithm, the fitting procedure was started at one point after the maximum in the fluorescence decay curve in order to limit the influence of the IRF. Hence, some valuable information was lost.

However, it could be proven in the study of compound II, that only two compounds are present, and the corresponding contributions and decay constants could be quantified. The consideration of several curves, obtained in a set of various experimental conditions (here : λ_{em}) was a crucial part in the success of these analyses.

Finally, it can be concluded that the combination of the improved GGM method and Prony's method can be a useful technique for the analysis of multicomponent fluorescence decay curves.

7.2. Free induction decay analysis

Solid state proton wideband (broadband) NMR provides a sensitive probe for the molecular state of a nuclear environment through the short range nature of magnetic dipolar interactions. For heterogeneous polymer systems (physical or chemical), the molecular mobility of each component and the fraction of the component can be directly estimated from the measurement of the spin-spin relaxation time T_2 [FukK90]. A solid echo technique provides a way to collect the complete response of the system to a 90° pulse near the resonance frequency without influence of the system recovery time. The recorded Free Induction Decay (FID) curve is a multicomponent decay curve having for each component a characteristic line shape, a spin-spin relaxation time T_2 , and an intensity depending on the characteristics of the corresponding phase. Unfortunately, the analysis of the recorded FID curve is a difficult task. Up till now, there is still uncertainty about the number of components and on their mathematical model functions in the decay curve.

7.2.1. Experimental set-up

Proton wideline measurements of isotactic polypropylene (iPP) films and atactic PVA grains (< 50 μm cross section) were performed on a Varian Inova 400 spectrometer in a wideline probe equipped with a 10 mm coil. Measurements as a function of temperature were done on the same sample, starting after a 30 min thermal stabilization time for each temperature. To determine the precision (stability) of the proposed method, three consecutive FID curves of iPP were recorded under identical spectrometer settings on a fresh sample. On-resonance FID's were acquired by means of the "solid echo" technique ($90^\circ_x - \tau - 90^\circ_y$) developed by Powles and Strange [PowJ63] in an effort to overcome the effects of the dead-time of the receiver, with an echo delay of 8.5 μs . According to these authors, the NMR signal, τ μsecs after the second pulse, is a good approximation of a standard free induction decay after a 90° pulse. The 90° pulses were of 2.3 μs duration. The dwell time during acquisition (sampling rate) is 0.5 μs allowing a very accurate determination of the data point with maximum intensity. This maximum of the "echo" FID has been calibrated to time zero. All FID curves were accumulated with 350 scans and a preparation delay of 5 sec. After recording, the number of experimental data points (sampling rate) has been reduced to 25% (only one point out of four points has been used). These data reduced FID curves were converted into an ASCII file and read into the Mac Kaleidagraphe 3.0.2 program for the NLLS fit (Marquardt Levenberg algorithm) or the MatLab 4.2c1 programs for the improved methods of Gardner et al. and Prony.

Temperature studies of iPP and PVA were made above their glass-transition temperature T_g (65°C for PVA, 16°C for PP).

The FID curves of the iPP sample at 40, 60, 80 and 100 °C were recorded at constant time intervals of 2 μs between over a period of 650 μs . Fig. 7.5 shows the FID curve obtained at 60 °C on both linear and semi-logarithmic (natural) scale.

In the study of the PVA sample, the FID curves were recorded between 100 and 160 °C (with increments of 10 °C), and with constant time intervals of 2 μs . In these experiments, the number of counts at $t = 0$ is almost two magnitudes lower than that in the study of iPP. Consequently, a higher noise level limits the time period during which the FID curves were recorded (500 μs).

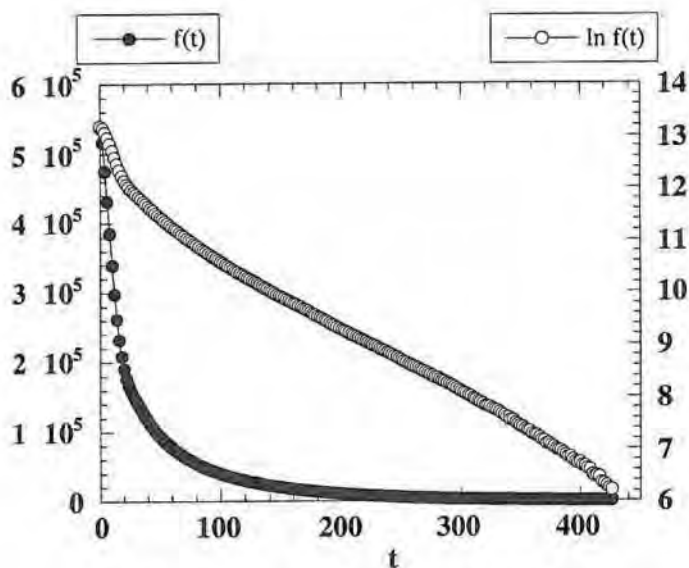


Fig. 7.5 : FID curve of an iPP sample at 60 °C on both linear and semi-logarithm (natural) scales.

7.2.2. Data handling

The model function (7.3)

$$M(t) = \sum_{i=1}^n M_i \exp \left(- \left(\frac{1}{a_i} \right) \left(\frac{t}{T_{2i}} \right)^{a_i} \right) \quad (7.3)$$

can be used for fitting to the experimentally measured NMR signal, where M_i , T_{2i} , a_i are the magnetization, spin-spin relaxation time, and shape parameter for the i -th component, respectively. If all a_i are equal to 1, the model function $M(t)$ simplifies to a sum of exponential functions which will be noted furtheron in the general form of a multicomponent exponential decay curve $f(t)$

$$f(t) = \sum_{i=1}^n N_i^{\circ} \exp(-\lambda_i t) \quad (7.4)$$

where N_i° and λ_i are the pre-exponential factor and the decay constant of component i , respectively. Comparison of eqs (7.3) and (7.4) shows that $M_i = N_i^{\circ}$ and $T_{2i} = 1/\lambda_i$ for each component i , if $a_i = 1$.

These multicomponent decay curves contain information about the physico-chemical structure of the polymer sample : each component is characterized by a specific model function containing a spin-spin relaxation time T_2 , and an intensity as parameters depending on the properties of the corresponding state. In general, in T_2 measurements the FID for polymer segments below their glass-transition temperature T_g (the rigid glassy or crystalline state) can be approximated by a Gaussian function, while the decay for polymer segments well above their glass-transition temperature can be approximated by an exponential function. Only for very rigid systems or low temperatures, the fastest decaying part can be fitted by an Abragamian function [FedV89] rather than by a Gaussian one. Hence, for systems having rigid and mobile components, a linear combination of these functions is used in order to obtain an NLLS fit of the free induction decay. The form of the fitted equation for an NMR signal $M(t)$, given by eq.(7.3), consists of several decay function types depending on the shape parameter a_i of the i -th component ($a_i=1$, exponential ; $a_i=2$, Gaussian ; $1 < a_i < 2$, Weibullian).

Still a lot of discussion is going on concerning the determination of the number of components n used to fit the FID curve. For iPP, regions with high structural order (crystalline phase (C)) and low molecular mobility behave differently from other regions with low structural order (elastomeric phase (E)) and high molecular mobility. As a transition between these regions, an intermediate phase (I) is assumed having a lower molecular mobility compared to that of the E phase but a lower ordering compared to that of the C phase. According to Tanaka [TanH82, TanH93] the FID curve of iPP is a superposition of three distinct curves, corresponding to the C, E, and I regions. The existence of a third intermediate component was proposed by Fujimoto et al. [FujK72] for low density polyethylene (LDPE), in agreement with the two spin-lattice relaxation times T_1 found in the amorphous phase by Peterlin et al. [CriB69]. Furthermore, it is generally accepted that in the 40-100°C thermal range the component having the shortest T_2 shows a Gaussian type decay and may be ascribed to the crystalline phase while the component having the largest T_2 decays exponentially and can be ascribed to the elastomeric phase (glass well above T_g). The complete FID curve can then be represented by either eq. (7.5) or (7.6) :

$$f(t) = N_C^0 e^{-0.5(t/T_{2C})^2} + N_I^0 e^{-0.5(t/T_{2I})^2} + N_E^0 e^{-t/T_{2E}} \quad (7.5)$$

$$f(t) = N_C^0 e^{-0.5(t/T_{2C})^2} + N_I^0 e^{-t/T_{2I}} + N_E^0 e^{-t/T_{2E}} \quad (7.6)$$

The analysis of these multicomponent decay curves consists of two separate parts. In the first part, the improved GGM method is used as a qualitative technique for the

determination of the number of components, and the best model function of the intermediate phase and for the estimation of the decay constants (T_2 values). This method can also validate the exponential ($a_i = 1$) or Gaussian ($a_i = 2$) character of each component i . In the second part, the recurrence version of Prony's improved method is used to quantify the parameters $T_{2i} = 1/\lambda_i$ and the fractions N_i^o/N^o ($N^o = N_C^o + N_I^o + N_E^o$) for each exponential component i in the complete FID curve.

7.2.3. Study of isotactic polypropylene films

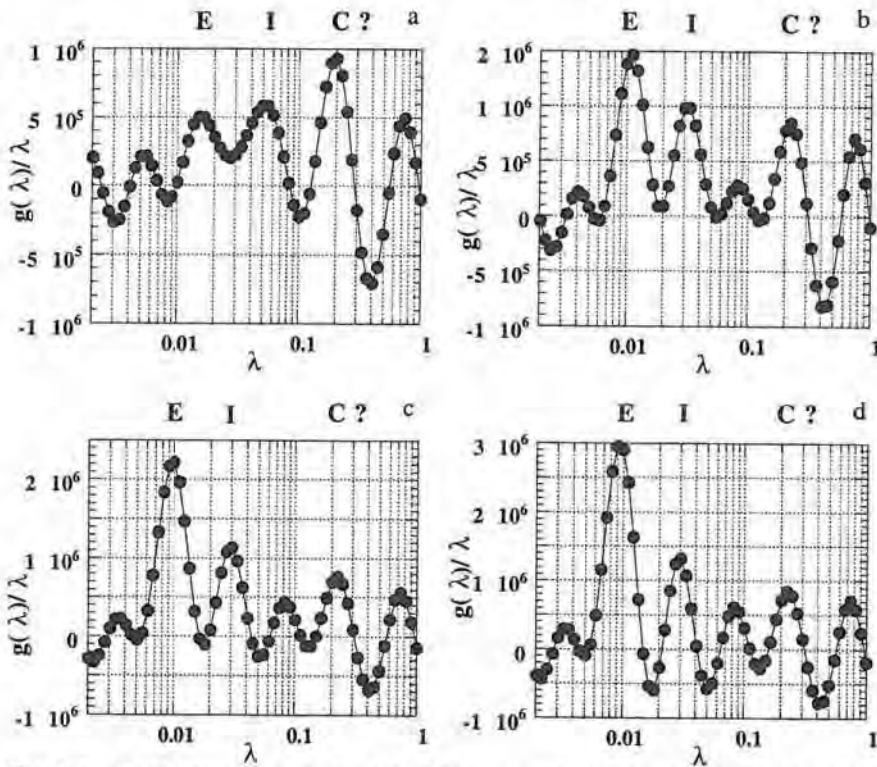
In this section, we present the analysis of Free Induction Decay curves of an isotactic polypropylene (iPP) film obtained at different temperatures. The improved method of Gardner et al. has been used to obtain information about the number of components (phases), to predict the best fitted model function (line shape), and to estimate the decay constants (T_2 values). In addition, the improved method of Prony and the Marquardt-Levenberg algorithm were applied to quantify the contributions (fractions) of each component in the complete FID curve. The influence of the temperature on the fractions of the components is examined and related to the physicochemical structure of the polymer. The precision of the computed parameters is discussed for the analyses of three consecutively measured FID curves of iPP at 60 °C.

7.2.3.1. Qualitative analysis : the improved GGM method combined with a Gaussian low-pass filter

In the improved GGM method, the choice of the model function $kk(x)$ depends upon the functional relation between the variable t and the response $f(t)$ of the decay curve. Eqs. (7.5) and (7.6) suggest that a mixture of Gaussian and exponential components can be expected.

The experimental FID curves are collected at constant time intervals. Since the input data set of the function $f(t)$ in the improved GGM method combined with a Gaussian filter should be gathered at constant intervals of $x = \ln t = 0.1$, a new data set is calculated using a cubic spline interpolation method on the original data set. The model function $kk(x)$ in eq.(5.10) is set to $\exp(-\exp(x))$ in order to evaluate the exponential components and to $\exp(-\exp(x^2))$ in order to locate the Gaussian components. In all analyses, the implementation of a Gaussian low-pass filter was necessary for reducing most of the experimental and computational noises.

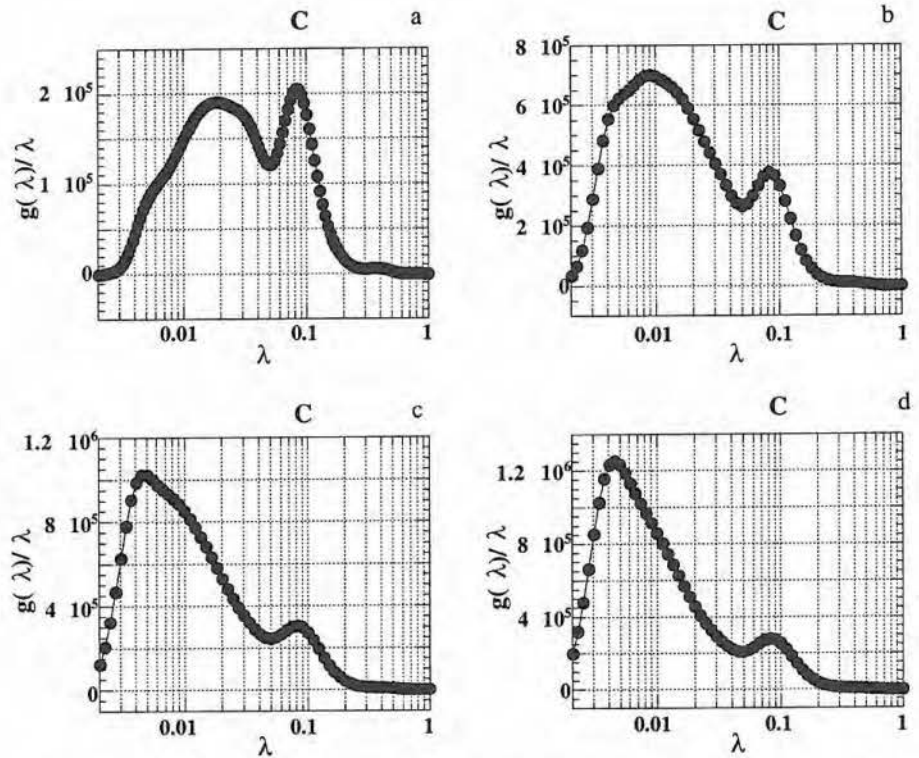
The $g(\lambda)/\lambda$ vs λ spectra obtained from a first analysis of the FID curves, in order to determine the exponential components are given in Figs 7.6a-d. Besides the expected error ripples (see Chapter 6), which are now additionally amplified by noise present in the experimental data, three significant peaks can be observed by considering the four Figs 7.3a to d. A first exponential component is situated at $\lambda \approx 0.0095\text{-}0.015 \mu\text{s}^{-1}$ (or a $T_2 \approx 67\text{-}105 \mu\text{s}$) and can therefore be assigned to the elastomeric phase (E). The central peak at $\lambda \approx 0.03\text{-}0.05 \mu\text{s}^{-1}$ can for the same reason be attributed to the intermediate phase (I). The third peak is asymmetric and has a large negative lobe at the right side. Analogous to the case illustrated in Fig. 6.7a, the third signal should be related to a Gaussian component.



Figs 7.6a-d : Qualitative analysis of the FID curves obtained at (a) 40, (b) 60 (c) 80, and (d) 100 °C by using the improved GGM method with $kk(x) = \exp(-\exp(x))$ in order to identify the exponential components.

To confirm that conclusion, a second analysis of the FID curves is carried out using the improved GGM method in which the model function $kk(x) = \exp(-\exp(x^2))$ is used in conjunction with the same Gaussian filter. The resulting $g(\lambda)/\lambda$ vs λ spectra are plotted in Figs 7.7a-d. A narrow symmetric peak at $\lambda \approx 0.08 \mu\text{s}^{-1}$ or $T_2 = (\lambda\sqrt{2})^{-1} \approx 8.8 \mu\text{s}$ is

superimposed on a broad composite feature. This symmetric peak is related to the Gaussian component in the FID curve and can be assigned to the crystalline phase (C).



Figs 7.7a-d : Qualitative analysis of the FID curves obtained at (a) 40, (b) 60, (c) 80, and (d) 100 °C by using the improved GGM method with $kk(x) = \exp(-\exp(x^2))$ in order to identify the Gaussian components.

The results obtained with the improved GGM method indicate that eq.(7.6) is the best model function for the studied FID curves of the iPP film over the temperature range 40-100°C. The multicomponent decay curves are superposition of a single Gaussian component and two exponential components. The estimated T_2 values for each component at the specific temperatures are summarized in Table 7.5.

7.2.3.2. Quantitative Analysis : Prony's improved method

It should be noted that Prony's improved method can only unravel multicomponent exponential decay curves. Therefore, the Gaussian function belonging to the crystalline phase (C), was first quantified using the Marquardt-Levenberg algorithm with model function (7.6) and subtracted from the original signal. Then, the intermediate (I) and elastomeric (E) components in the remaining signal have been quantified using the recurrence version of Prony's improved method.

Table 7.5 : Estimates of the T_2 values obtained with the improved GGM method

phase	T_2 value (μs)			
	40 °C	60 °C	80 °C	100 °C
C	8.8	8.8	8.8	8.3
I	20.0	31.3	33.3	33.3
E	66.7	100	100	111

a. Crystalline phase

The improved GGM method shows that the crystalline phase is represented by the Gaussian component in eq.(7.6). Furthermore, starting values for the T_2 values could be determined (Table 7.5). However, the Marquardt-Levenberg algorithm requires also starting values for the parameters N_i^0 of each component i . These are empirically set to 50, 30 and 20 % of the initial intensity of the FID curve at a specific temperature for the crystalline, intermediate and elastomeric phase, respectively.

The optimized Gaussian functions obtained in this fitting problem are collected in Table 7.6. A T_2 value of ca. 8 μs remaining almost constant over the 40-100°C temperature range agrees nicely with that reported by Tanaka et al. [TanH93]. The Gaussian components are subtracted from the initial responses. The complete removal of the Gaussian was checked by applying the improved GGM method with $kk(x) = \exp(-\exp(x^2))$. The $g(\lambda)/\lambda$ vs. λ spectrum at 60 °C is shown in Fig. 7.8. Comparing Figs 7.7b and 7.8 shows that only a very small fraction of the Gaussian component remains. The curves obtained after subtracting the Gaussian components in Table 7.6 are therefore good approximations for superpositions of two pure exponential functions. Hence, they meet the requirements of Prony's improved method.

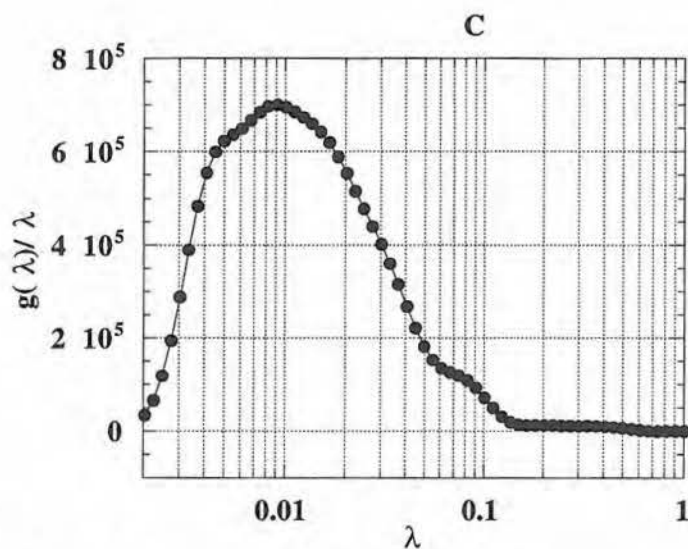


Fig. 7.8 : $g(\lambda)/\lambda$ vs λ spectrum after subtraction of the Gaussian component.

Table 7.6 : Optimized Gaussian functions, obtained with the Marquardt-Levenberg algorithm, describing the crystalline phase in a FID curve recorded at a number of selected temperatures.

T (°C)	$f_C(t)$
40	$2.26 \times 10^5 \exp\left(-0.5 \left(\frac{t}{8.03}\right)^2\right)$
60	$2.29 \times 10^5 \exp\left(-0.5 \left(\frac{t}{7.93}\right)^2\right)$
80	$2.05 \times 10^5 \exp\left(-0.5 \left(\frac{t}{7.90}\right)^2\right)$
100	$1.92 \times 10^5 \exp\left(-0.5 \left(\frac{t}{7.79}\right)^2\right)$

b. Intermediate and elastomeric phases

Prony's improved method requires the number of exponential components, which was for all the analyzed FID curves equal to two, as known from the results obtained with the improved GGM method. This latter method provides also the starting values of the decay constants listed in Table 7.5. The decay constants are optimized with Prony's method and the pre-exponential factors are evaluated. The results obtained from these analyses are shown in Table 7.7. The T_2 values and fractions of the intermediate (I) and elastomeric (E) phases are calculated. They are found to be in good agreement with the results obtained from the non-linear regression analyses presented in Table 7.8. Moreover, it is worthwhile to mention that also for the NLLS fit, the errors and especially the χ^2 are smaller when eq.(7.6) is used instead of eq.(7.5).

With the combined application of the improved GGM method and Prony's method, the existence of an intermediate phase has been proved now and quantified. The results show that its participation is not negligible in a FID signal recorded in a temperature range of 40 to 100 °C. Furthermore, the combination of both methods in the analysis of FID curves performs equally well as the common used non-linear regression methods. However, in our technique no a priori information is needed concerning the model functions describing the different phases, their number, characteristic decay constants and contributing fractions.

Table 7.7 : Results obtained using Prony's improved method

T (°C)	phase	λ (μs^{-1})	N° ($\times 10^5$)	T_2 (μs)	fraction (%)
40	I	0.0452	1.90	22.1	40.4
	E	0.0166	0.55	60.2	11.6
60	I	0.0372	1.92	26.9	35.8
	E	0.0119	1.16	84.0	21.6
80	I	0.0379	1.41	26.4	27.7
	E	0.0106	1.64	94.8	32.2
100	I	0.0431	1.05	23.2	21.9
	E	0.00980	1.81	102.0	37.8

Table 7.8 : Results obtained with the Marquardt-Levenberg algorithm

T (°C)	phase	T ₂ (μs)	fraction (%)
40	C	8.04	48.0
	I	22.2	40.5
	E	60.6	11.5
60	C	7.93	42.6
	I	26.9	35.8
	E	84.1	21.6
80	C	7.90	40.2
	I	27.5	28.6
	E	96.3	31.2
100	C	7.79	40.2
	I	23.3	22.0
	E	102.1	37.8

7.2.3.3. Influence of the temperature on the fractions of the phases

Table 7.7 shows nearly constant values for T_{2C} with increasing temperature, indicating that molecular motion is almost unchanged in the crystalline regions over the temperature range covered in this experiment. On the other hand, T_{2E} increases with rising temperature, indicating that molecular mobility in the non-constrained (decoupled from crystalline regions) amorphous regions is enhanced as the temperature is raised. Fig. 7.9 shows the influence of temperature on the fractions of each phase. The contribution of the elastomeric (E) phase increases fast when the temperature increases. An opposite tendency can be observed for the intermediate (I) phase. The contribution of the crystalline (C) phase asymptotically tends to the real crystallinity. At lower temperatures the C and I phases are difficult to distinguish from each other due to a comparable rigidity, and therefore, the fractions found are rather totals of the fractions of the C phase and parts of the I phase with very low mobility. Only at higher temperatures (from 80°C for the C phase, constant fraction of 40% crystallinity), the fraction is representing the real C phase content. Concerning the molecular mobility (determining the line shape) below 80°C, part of the E phase is clearly not far enough above T_g to give a pure Lorentzian line shape, resulting in an overestimation of the C and I phases. From 80°C on, the Gaussian line shape is better defined allowing a subtraction of the response of the crystalline species. At higher temperatures, a decrease of the I phase contribution and an increase of the fraction of the E phase can be seen towards their two limiting values, yielding the intrinsic contribution of the E and I phases.

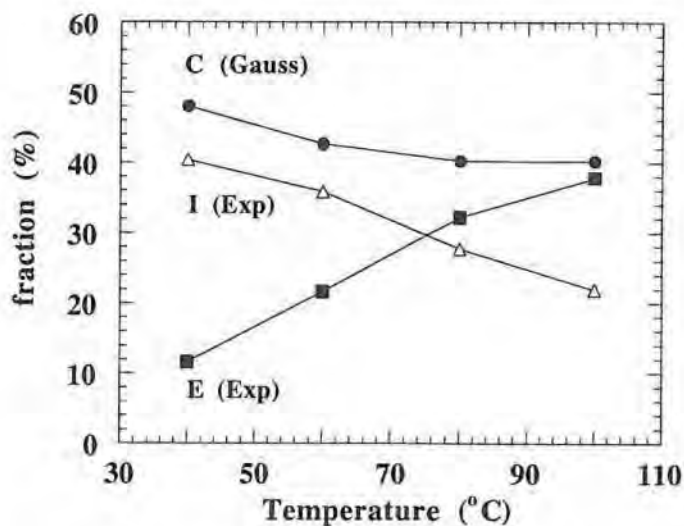


Fig. 7.9 : Influence of temperature on the fraction of a phase.

7.2.3.4. Precision of the parameters

When several FID curves are recorded under the same spectrometer conditions and are analyzed using the same methods, one can get an idea about the precision of the parameters found which accounts for both instrumental and computational errors. Therefore, a series of three FID curves of polypropylene is recorded at 60 °C. The T_2 values and the fractions of the corresponding phases are quantified using the procedure described above. The mean values and the 95% confidence intervals of the parameters obtained in these three analyses are : (a) for the crystalline phase, $T_2 = (7.12 \pm 0.01) \mu\text{s}$ and a fraction of $(40.5 \pm 0.2) \%$; (b) for the intermediate phase, $T_2 = (22.8 \pm 0.2) \mu\text{s}$ and a fraction of $(39.55 \pm 0.05) \%$, and (c) for the elastomeric phase, $T_2 = (80.3 \pm 0.7) \mu\text{s}$ and a fraction of $(19.9 \pm 0.2) \%$. Thus, for all the parameters a high precision could be reached. However, the values obtained in the thermal study described previously (see Tables 7.7 and 7.8) for a iPP sample at 60 °C are quite different, e.g. in Table 7.7, $T_2 = 26.86 \mu\text{s}$ for the intermediate phase (I) at 60°C, which is far outside the 95% confidence interval that has been calculated here. This could be due to experimental conditions like e.g. heterogeneities in the iPP film, folding of the film into the NMR tube, thermal stabilization, etc.. Therefore, the confidence level that can be obtained in individual measurements is much lower (deviations of more than 1 % are realistic). Thus, it can be concluded that the procedure used to analyze the FID curves is

numerical stable since it is able to determine the parameters within the entire experimental precision of the recording of the multicomponent decay curves.

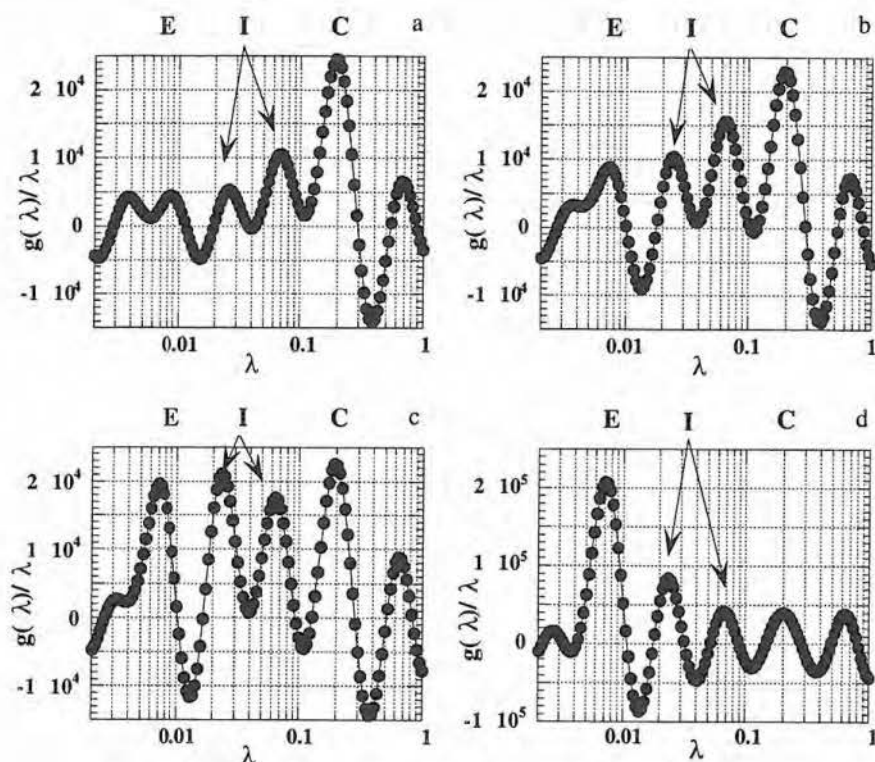
7.2.4. Study of atactic PVA grains

After the successful study of iPP (Section 7.2.3.), we applied the combined use of the improved methods of GGM and Prony for the analysis of Free Induction Decay curves of atactic PVA grains (< 50 μm cross section) obtained at different temperatures above T_g . The qualitative information, concerning the number of components (phases), the best fitted model functions (line shape), and the corresponding decay constants (T_2 values), is obtained using the improved GGM method. In addition, the improved method of Prony and the Marquardt-Levenberg algorithm were applied to quantify the contributions (fractions) of each component in the complete FID curve. Again, the influence of the temperature on the fractions of the components is examined and related to the physicochemical structure of atactic PVA.

7.2.4.1. Qualitative analysis : the improved GGM method combined with a Gaussian low-pass filter

As in the study of isotactic polypropylene (Section 7.2.3.), the number of components and the model functions of the phases are determined using the improved GGM method. The FID curves are also collected at constant time intervals, so that for each temperature, a new data set is calculated using the cubic spline interpolation method on the original data set. The model function $k(x)$ in eq.(5.10) is taken as $\exp(-\exp(x))$ in order to evaluate the exponential components and as $\exp(-\exp(x^2))$ for identifying the Gaussian components. In all the analyses, a combination with a Gaussian low-pass filter was necessary for reducing most of the experimental and computational noises. Due to the higher noise level in the data of PVA than in those of iPP, the $g(\lambda)/\lambda$ vs λ spectra are harder to interpret.

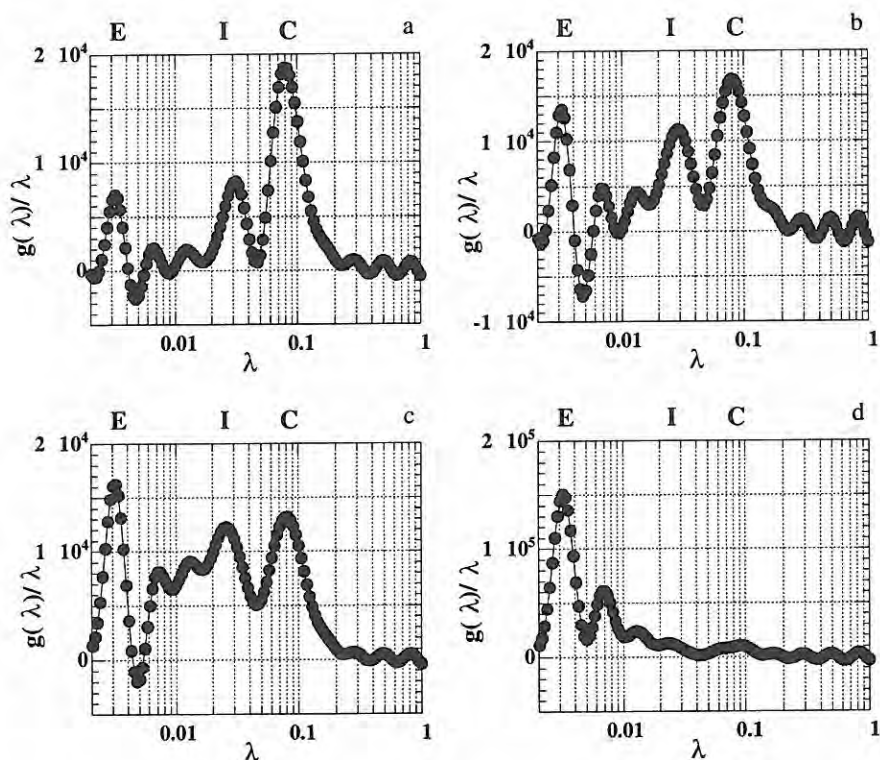
The characteristic $g(\lambda)/\lambda$ vs λ spectra obtained from a first analysis of the FID curves (recorded at 100, 120, 140 and 160 $^\circ\text{C}$) in order to determine the exponential components are given in Figs 7.10a-d.



Figs 7.10a-d : Qualitative analysis of the FID curves obtained at (a) 100, (b) 120, (c) 140 and (d) 160 °C by using the improved GGM method with $kk(x) = \exp(-\exp(x))$ in order to identify the exponential components.

Besides the expected error ripples (see Chapter 6), which are now supplementary enhanced by the noise present in the experimental data, four significant peaks can be observed. A first component is situated at $\lambda \approx 0.007\text{-}0.0087 \mu\text{s}^{-1}$ (or a $T_2 \approx 115 - 143 \mu\text{s}$) and can therefore be assigned to the elastomeric phase (E). Two central peaks are located at $\lambda \approx 0.025 \mu\text{s}^{-1}$, and $0.065\text{-}0.07 \mu\text{s}^{-1}$; one of them should be assigned to the intermediate phase (I). The peak at $\lambda \approx 0.2 \mu\text{s}^{-1}$ is asymmetric and has a large negative lobe at its right side. Analogous to Fig. 6.7a this signal should due to a Gaussian component. To confirm this conclusion a second analysis of the FID curves is carried out using the improved GGM method in which the model function $kk(x) = \exp(-\exp(x^2))$ is used in conjunction with the same Gaussian filter. The resulting $g(\lambda)/\lambda$ vs λ spectra are plotted in Figs 7.11a-d. An intense peak is present in the $g(\lambda)/\lambda$ vs λ spectra at $\lambda \approx 0.08 \mu\text{s}^{-1}$ or $T_2 = (\lambda\sqrt{2})^{-1} \approx 8.8 \mu\text{s}$ for the data collected at 100 to 140 °C. This Gaussian component can be assigned to the crystalline phase (C). However, in this case the Gaussian component is not superimposed on a broad composite feature as it was the case in the iPP study. Instead,

some minor (error ?) peaks are located between the two signals of the I and E phases. The shape of the E component is asymmetric indicating that it cannot be described by a Gaussian model function as could be expected from its form in the $g(\lambda)/\lambda$ vs λ spectra in Figs 7.10a-d. The slight asymmetrical shapes of the lines in the previous spectra are probably caused by the larger statistical fluctuations and by the resulting computational noise. Therefore, an exponential is used as model function for the elastomeric phase. At 160 °C, the intensities belonging to the C and I phases become small compared to the one of the E phase.



Figs 7.11a-d : Qualitative analysis of the FID curves obtained at (a) 100, (b) 120, (c) 140 and (d) 160 °C by using the improved GGM method with $kk(x) = \exp(-\exp(x^2))$ in order to identify the Gaussian components.

As in the iPP study, eq. (7.6) is the best model function for the recorded FID curves of PVA over the temperature range 100-160°C. The multicomponent decay curves are a superposition of a single Gaussian component and two exponential components. However, the situation is a little bit more complicated since there are two candidates for the T_2 value of the intermediate phase. The estimated T_2 values for each component at the specific

temperatures are summarized in Table 7.9. Furthermore, in the quantitative analysis it can be expected that the contribution of the C phase becomes very small at the highest temperature.

Table 7.9 : Estimates of the T_2 values obtained in the modernized method of Gardner

phase	T_2 value (μs)			
	100 °C	120 °C	140 °C	160 °C
C	8.8	8.8	8.8	8.3
I	14.9 or 38.5	15.6 or 40.5	15.6 or 42.6	14.9 or 42.6
E	116	134	141	141

7.2.4.2. Quantitative Analysis : Prony's improved method

The problem that Prony's improved method can only unravel multicomponent exponential decay curves, is also in this study solved by first quantifying the Gaussian function, belonging to the crystalline phase (C), using the Marquardt-Levenberg algorithm with the model function (7.6), and then subtracting it from the original signal. Afterwards, the intermediate (I) and elastomeric (E) components in the remaining signal have been quantified using the recurrence version of Prony's improved method.

a. The crystalline phase

The quantification and subtraction of the Gaussian component in eq.(7.6), has been done by using the same procedure as that described in Section 7.2.3.2 for iPP. The optimized Gaussian functions obtained in this fitting problem are collected in Table 7.10. The T_2 value of ca. 7.7 - 7.8 μs remains almost constant over the 100-160°C temperature range and is furthermore in good agreement with the expected T_2 value for a C phase [FedV89].

The Gaussian components obtained with the Marquardt-Levenberg algorithm (Table 7.10) are subtracted from the initial response. The resulting curves are now good approximations for the superpositions of two pure exponential functions. Hence, they meet the requirements of Prony's improved method.

Table 7.10 : Optimized Gaussian functions, obtained with the Marquardt Levenberg algorithm, describing the crystalline phase in a FID curve recorded at a number of selected temperatures.

T (°C)	$f_C(t)$
100	$1.51 \times 10^4 \exp\left(-0.5\left(\frac{t}{7.86}\right)^2\right)$
110	$1.43 \times 10^4 \exp\left(-0.5\left(\frac{t}{7.79}\right)^2\right)$
120	$1.41 \times 10^4 \exp\left(-0.5\left(\frac{t}{7.76}\right)^2\right)$
130	$1.37 \times 10^4 \exp\left(-0.5\left(\frac{t}{7.72}\right)^2\right)$
140	$1.36 \times 10^4 \exp\left(-0.5\left(\frac{t}{7.67}\right)^2\right)$
150	$1.24 \times 10^4 \exp\left(-0.5\left(\frac{t}{7.74}\right)^2\right)$
160	$1.18 \times 10^4 \exp\left(-0.5\left(\frac{t}{7.46}\right)^2\right)$

b. The intermediate and elastomeric phase

The improved method of Prony is used with starting values for the decay constants deduced from Table 7.9, in order to fit a bi-exponential function to one fourth of the data points between 0 and 500 μ s. The method has been used twice since for the intermediate phase, two possible T_2 values are given in Table 7.9. If the largest value for the spin-spin relaxation time of the intermediate phase is taken as a first estimation, the system always converges to a value near the smallest one. Therefore the latter is used in all optimizations resulting in the final decay constants and pre-exponential factors (see Table 7.11). The T_2 values and fractions of the intermediate (I) and elastomeric (E) phases are calculated. They agree very well with the results obtained from the non-linear regression analyses presented in Table 7.12.

Finally, it should be emphasized that also in the study of PVA, the combined application of the improved GGM method and Prony's method could be applied with success. The existence of an intermediate phase has been proved again and quantified. The results show that its participation is not negligible in a FID signal recorded of PVA in a temperature range of 100 to 160 °C.

Table 7.11 : Results obtained using Prony's improved method

T (°C)	phase	λ (μs^{-1})	N° ($\cdot 10^4$)	T_2 (μs)	fraction (%)
100	I	0.0837	1.37	12.0	46.9
	E	0.00773	0.042	129.4	1.4
110	I	0.0702	1.43	14.2	49.3
	E	0.00563	0.039	177.7	1.4
120	I	0.0611	1.44	16.4	49.8
	E	0.00560	0.048	178.6	1.7
130	I	0.0537	1.41	18.6	49.3
	E	0.00667	0.074	149.9	2.6
140	I	0.0444	1.32	22.5	46.6
	E	0.00691	0.15	144.7	5.3
150	I	0.0453	1.30	22.1	47.4
	E	0.00935	0.20	107.0	7.4
160	I	0.0460	0.55	21.7	17.6
	E	0.00649	1.40	154.1	44.8

7.2.4.3. Influence of the temperature

Table 7.10 shows nearly constant T_{2C} values, slightly increasing T_{2I} values and strongly fluctuating T_{2E} values with increasing temperature. For T_{2C} , this indicates that molecular motion is almost unchanged in the crystalline regions over the temperature range covered in this experiment. The fluctuations for the spin-spin relaxation time T_{2E} can be caused by its high value compared to the measured time period (500 μs) and the relative larger noise level than that in the iPP study.

Table 7.12 : Results obtained with the Marquardt-Levenberg algorithm

T (°C)	phase	T ₂ (μs)	fraction (%)
100	C	7.86	51.7
	I	12.0	46.9
	E	129.4	1.4
110	C	7.79	49.3
	I	14.2	49.3
	E	177.7	1.4
120	C	7.76	48.6
	I	16.4	49.8
	E	178.6	1.6
130	C	7.72	48.1
	I	18.6	49.3
	E	149.9	2.6
140	C	7.67	48.1
	I	22.5	46.6
	E	144.7	5.3
150	C	7.74	45.2
	I	22.1	47.4
	E	107.0	7.4
160	C	7.46	37.6
	I	21.7	17.6
	E	154.1	44.8

Fig. 7.12 shows the influence of temperature on the fractions of each phase. The contributions of all phases remain almost constant up to 140 °C. At higher temperatures, the contribution of the elastomeric (E) phase increases, and the fraction of the intermediate (I) phase decreases very fast. The contribution of the crystalline (C) phase diminishes only slightly at the highest temperature.

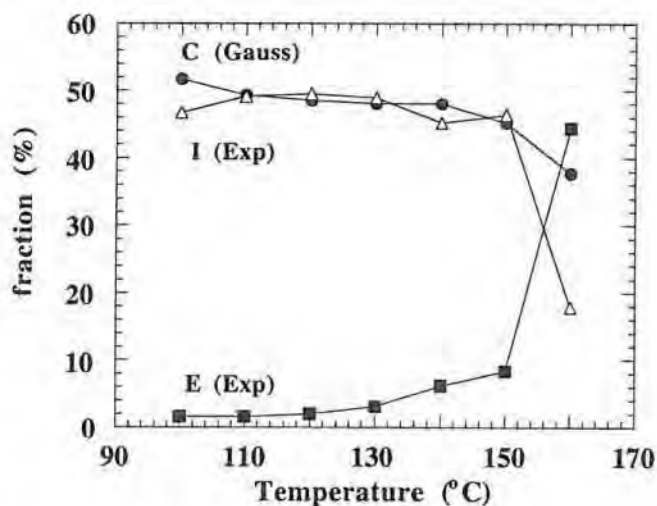


Fig. 7.12 : Influence of temperature on the fraction of a phase.

7.2.5. Conclusions

The combined use of the improved GGM method and Prony's method is proposed as a new technique for analyzing Free Induction Decay curves. The improved GGM method is able to identify the three components as well as their model functions, and to estimate the decay constants related to the T_2 values. The recurrence version of Prony's improved method is used to optimize the decay constants and to calculate the pre-exponential factors.

In a temperature study of iPP films and PVA, their Free Induction Decay curves are analyzed using these methods. The results are in good agreement with those obtained with the Marquardt-Levenberg algorithm ; however, less a priori information is needed in our proposed method. For both materials, the presence of an intermediate phase (I) could be proved unambiguously and quantified at the different temperatures. The influence of temperature on the fractions of the phases is discussed. In the study of iPP, the precision of the quantification of the parameters is shown to be much smaller than the one that can be reached with the recording of the FID curves.

7.3. Radioactive decay curves

7.3.1. Study of pure positron emitters

Decay curve analysis (DCA) is a very valuable tool for the instrumental, qualitative identification of a radionuclide and quantitative measurement of its contribution in mixtures of pure positron emitters. A possible alternative is to perform a radiochemical separation which provides better precision and detection limits. On the other hand, the development of such a radiochemical procedure is a lasting procedure because the selectivity and quantitiveness (yield) should be checked for each particular matrix. Moreover, this is not possible for very short-lived radionuclides.

Charged particle activation (CPA) of light elements (Li, B, C, N, O) induces pure positron emitters, with short half-lives (≤ 110 min), in contrast to most charged particle induced reactions (e.g. a (p,n) reaction) producing β^+, γ emitters. By γ -spectrometry, one can identify these β^+, γ emitters and their half-life. However, for a mixture of pure positron emitters, one has to measure the decay curve and analyze it without any foreknowledge about the number of components and their half-lives. Decay curve analysis should therefore be able to resolve a sum of exponential functions in order to reveal the number of components and, for each component, the half-life related to the decay constant of the exponential function $\lambda_i = \ln(2)/(T_{1/2})_i$ (qualitative analysis), and the corresponding initial activity A_i^0 , which is equal to the pre-exponential factor of each exponential function (quantitative analysis). Applying CPA analysis for the determination of light elements leads to short-lived pure β^+ emitters ($T_{1/2} < 110$ min), for which the counting statistics are less favorable. This quite difficult case, pure positron emitters and short half-lives, will be studied now. Moreover, a critical comparison will be made between the recurrence version of the improved method of Prony and Cumming's method [CumJ62] for the analyses of simulated and experimental radioactive decay curves of a mixture of pure β^+ emitters.

7.3.1.1. Experimental set-up

a. Production of ^{15}O , ^{11}C , and ^{18}F

Pure positron emitters produced in CPA for the determination of light elements are: ^{17}F , ^{15}O , ^{13}N , ^{11}C , and ^{18}F . As shown in Table 7.13, the short half-lives of ^{17}F and ^{15}O make a radiochemical separation nearly impossible. In the experimental study, only mixtures of ^{15}O , ^{11}C , and ^{18}F have been made. Therefore, each of these three radionuclides has been produced separately, with high radionuclidic purity. Three samples were taken in a

well known ratio (e.g. 1/2/3) and measured separately to know the initial activity of each component. They were measured then together in order to obtain the decay curve to be analyzed. As these three components should be available at the same time, ^{18}F was produced by nuclear reactor (Thetis, Univ. Gent) irradiation, and ^{11}C and ^{15}O (in that order) by cyclotron (CGR-MeV 520, Univ. Gent) irradiation.

Fluorine-18 was produced by neutron irradiation of Li_2CO_3 in a nuclear reactor. Tritons were formed by a (n, α) reaction on ^6Li . These secondary tritons induced then a (t,n) reaction on ^{16}O producing radionuclidic pure ^{18}F . The yield was 10^5 Bq for an irradiation of 10 mg of Li_2CO_3 in an epithermal neutron fluency rate of 10^{11} cm^{-2} s^{-1} during 30 min. After irradiation, Li_2CO_3 was dissolved in 1 ml water and NaF carrier added.

Carbon-11 [VanT83] was produced by proton irradiation of pure N_2 gas (with traces of O_2) by a (p, α) reaction on ^{14}N . The ^{11}C formed was trapped in a coil immersed in liquid Ar, then released by increasing the temperature, and finally trapped in 0.5 M NaOH. This procedure provided excellent radionuclidic purity, by removing all ^{13}N . The yield was 10^8 Bq for a 18 MeV proton irradiation under 'thick target' conditions at 1 μA beam intensity during 1 min, so that a $1/10^3$ sample was taken.

Oxygen-15 [StrK85] was produced by deuteron irradiation of a N_2/CO_2 gas mixture (97.5/2.5 v/v) by a (d,n) reaction on ^{14}N . The ^{15}O formed was trapped in 1 M NaOH, while ^{13}N passes. Only a negligible (< 0.1 % for $t = 0$) contamination of ^{11}C remained. The yield was 10^9 Bq for a 7.5 MeV deuteron irradiation under 'thick target' conditions at 3 μA beam intensity during 1 min, so that a $1/10^2$ sample was taken.

All three radionuclides were now available as a solution, so that they could be sampled with an Eppendorf pipette in order to obtain four predefined ratios (1/1/1, 1/2/2, 1/2/3 and 3/2/1) for $t = 0$ (i.e. start of a decay curve, start of a simultaneous measurement of the three components). The three samples of ^{18}F , ^{11}C , and ^{15}O were measured separately, so that the uncertainty on the initial activity (RSD = 0.5 %) was negligible as compared to that obtained from DCA (RSD from 2 to 10 %). Moreover, the activity level was limited to 10^4 counts min^{-1} , so that the dead-time correction was less than 1 % (< 3 % for ^{15}O), and consequently, potential systematic errors due to dead-time correction were negligible as compared to the random errors due to counting statistics.

The timing of the whole procedure was as follows. First, ^{18}F was produced by neutron irradiation in the nuclear reactor. Then, ^{11}C by proton irradiation with the cyclotron, and finally ^{15}O by deuteron irradiation with the cyclotron. During the ^{11}C production, ^{18}F

was sampled in order to obtain the predefined ratio (e.g. 1/2/3) and to obtain a total activity of 10^4 counts min^{-1} for the three radionuclides at $t = 0$, i.e. the start of the measurement of the multi-component decay curve. The single-component decay curve of the ^{18}F sample was measured. The same procedure was executed for ^{11}C and ^{15}O , respectively, so that the single-component decay curves were measured one after the other, in order to calculate the initial activity of each of the three components at $t = 0$. Finally, the three samples were put together in the counting set-up (the reproducibility of this protocol was tested previously). Then, at $t = 0$, measurement of the three-component decay curve was started.

The radionuclidic purity of all three components was checked in separate experiments, both by γ -spectrometry and DCA (Cumming's method).

b. Positron counting

The positrons were counted by a γ - γ coincidence set-up consisting of two NaI(Tl) scintillation detectors (diameter: 7.6 cm, height: 7.6 cm) in 180° geometry. A timing single channel-analyzer (SCA) selected the 511 keV photopeak in each detector (window: 400 to 600 keV). Only when the two photopeaks were detected within 40 ns (observed by a time-to-pulse-height-converter/SCA module coupled to the fast SCA output) the counter increased with one unit. The dead-time of the set-up was 1 μmin per count, as experimentally determined by measurement of a pure ^{11}C source. Due to the coincidence principle the background was very low (0.5 counts min^{-1}). Detectors and electronics were all EG&G Ortec. For convenient handling of the large number of measurements (200), a multi channel-analyzer (MCA) in the multi-scaling mode was used. All multicomponent radioactive decay curves are obtained at constant time intervals of 1 min over time periods of 200 min (except for those mixtures containing ^{17}F where the time periods were 100 min).

7.3.1.2. Data handling

The experimentally determined counts c_j of a radioactive sample over N constant time intervals can be transformed into a data set of N counting rates y_j at certain points in time t_j in the specific interval j (see further). If m independent species are present, a sum of m exponential functions, symbolized as $f(t)$ (eq. (7.7)), can be fitted to the data set (t_j, y_j)

$$f(t) = \sum_{i=1}^m A_i^0 \exp(-\lambda_i t) \quad , \quad t \geq 0 \quad (7.7)$$

where the pre-exponential factor A_i^0 is the contribution of component i to the total activity at time $t = 0$ and the decay constant λ_i is related to the half-life $(T_{1/2})_i$ of component i as $\lambda_i = \ln(2)/(T_{1/2})_i$.

In the multicomponent decay curve analysis, the linear (A_i^0) and non-linear (λ_i) parameters are to be determined for each of the m components in the best fitted model function $f(t)$.

a. Simulation of decay curves

Before using the recurrence Prony algorithm on experimental data, its performance is evaluated on simulated data sets representing potential difficult experimental situations. The most cumbersome radioactive decay curves to analyze are those obtained for mixtures of pure β^+ emitters with short half-lives. Pure β^+ emitters, produced by CPA of light elements, are given in Table 7.13. Their half-lives vary from 1 to 110 min.

In our experiments, the measuring time period Δt was limited therefore to 1 min at most. The dead time correction in our experimental set-up was less than 1% so that the selected activity level was below 10^4 counts min^{-1} . Because all counting processes are accompanied by a Poisson distributed noise so that the standard deviation $\sigma(c) = \sqrt{c}$ (c : number of counts), an initial noise level of ca 1% can be expected. Hence, realistic simulations have been made for mixtures of pure positron emitters with an initial total activity of 10^4 counts on which a Poisson distributed noise is superimposed. For each examined combination of pure β^+ emitters, five data sets of 200 points are simulated at constant time intervals of 1 min (except for those mixtures that contain ^{17}F , where $\Delta t = 0.5$ min). The counts c_j obtained in the j th time interval Δt can be found by the following theoretical relationship

$$c_j = \sum_{i=1}^m \left[A_i^0 \exp(-\lambda_i \Delta t (j-1)) \left(\frac{1 - \exp(-\lambda_i \Delta t)}{\lambda_i} \right) \right] + e_j \quad (7.8)$$

with e_j the noise term.

It should be remarked that the Prony algorithm requires the count rate at N equidistant points in time. When $\Delta t < 0.5 * T_{1/2}$, the following inequalities hold

$$1 < \frac{c_j / \Delta t}{y_j} < 1.005 \quad (7.9)$$

where y_j is the count rate at a time in the middle of the interval j . Hence, the c_j values are first divided by Δt in order to obtain good approximations for the count rates y_j at the middle of each interval j .

Table 7.13 : Half-life of pure positron emitters

Radionuclide	$T_{1/2}$ (uncertainty) in min*
^{17}F	1.075 (3)
^{15}O	2.037 (3)
^{13}N	9.965 (4)
^{11}C	20.39 (2)
^{18}F	109.77 (5)

* found in the NuDat data base on <http://www.nndc.bnl.gov/nndc/nudat/>

b. Analysis procedure

Prony's improved method can be used with and without starting values for the decay constants. Cumming's method, on the other hand, requires always starting values for the half-lives. To compare the output of both methods, it is necessary that the same procedure is followed and the same input is used.

Both simulated and experimental (see further) data sets have been analyzed separately with Cumming's method and with the recurrence version of the improved Prony method using the following procedure. In an initial part, it has been assumed that all five pure positron emitters (^{17}F , ^{15}O , ^{13}N , ^{11}C , and ^{18}F) are present with their tabulated λ_i values. This first preliminary analysis returns real decay constants with positive contributions for the components that are present in the sampled data. The other ones are characterized by a negative or small pre-exponential factor and, only for the improved Prony method, by a complex decay constant. The output of this first analysis has been used in order to obtain the true number and nature of the components. With this information a second analysis has been performed in order to refine the results quantitatively.

The results obtained for the simulated decay curves have been compared. Since for each examined combination of pure positron emitters, five data sets have been simulated and analyzed, the following null hypotheses could have been tested for each of the parameters : (1) $H^0 : x_c - x_p = 0$; (2) $H^0 : x_c/x_p = 1$; (3) $H^0 : (x_c - x_p)/x_{sim} = 0$, where x_c and x_p are the optimized values for the tested parameter obtained with Cumming's method and

Prony's improved method and x_{sim} is the input value for the parameter in the simulations. The level of significance α of these tests has been set to 0.05.

7.3.1.3. Analysis of simulated decay curves

A first series of simulated decay curves with an A_i^0 ratio of ca 1/3 has been composed of two out of the five positron emitters from Table 7.13. The decay curves have been analyzed applying the previously described procedure. Table 7.14 shows the input values (λ_i , A_i^0) and the results (mean (sd)) obtained with the methods of Cumming and Prony for five data sets for each of the combinations $^{15}\text{O}/^{17}\text{F}$, $^{11}\text{C}/^{13}\text{N}$, $^{13}\text{N}/^{15}\text{O}$, $^{13}\text{N}/^{17}\text{F}$, and $^{11}\text{C}/^{15}\text{O}$. Cumming's method retrieved both components in all sets. The improved method of Prony yielded a wrong number of exponentials for the combination $^{15}\text{O}/^{17}\text{F}$. This could be caused by the small difference in the values of the decay constants. However, since the analysis of the decay curve for the combination $^{11}\text{C}/^{13}\text{N}$ could be performed without difficulties, the just mentioned cause could not be the only one. The analyses of additional simulated decay curves for the combination $^{11}\text{C}/^{13}\text{N}$ with longer counting periods ($\Delta t = 5$ min), $A^0(^{11}\text{C}) = 600$ counts min^{-1} , and $A^0(^{13}\text{N}) = 2000$ counts min^{-1} , returned also a wrong number of components for all curves. Hence, a second important difficulty seems to be the relatively large sampling step or counting period Δt compared to the $T_{1/2}$'s of the decaying species. When the $T_{1/2}/\Delta t$ ratio is small (e.g. 2), only a few (2) data points are available within each half-life period, and hence, the total number of data points, which are characterized by a low relative noise level, is limited.

Comparing the mean values with the true values of the (λ_i , A_i^0) parameters for the other combinations ($^{11}\text{C}/^{13}\text{N}$, $^{13}\text{N}/^{15}\text{O}$, $^{13}\text{N}/^{17}\text{F}$, and $^{11}\text{C}/^{15}\text{O}$), it can be concluded that accurate results can be obtained with both methods. Testing the null hypotheses for each of the parameters shows that only for the $^{13}\text{N}/^{15}\text{O}$ combination the optimized (λ_i , A_i^0) values obtained by using Cumming's method are different from those obtained from Prony's improved method. For the $^{13}\text{N}/^{15}\text{O}$ combination, additional null hypotheses ((1) $H^0 : \mu_C = x_{sim}$, and (2) $H^0 : \mu_P = x_{sim}$, where μ_C and μ_P are the mean values of (λ_i , A_i^0) obtained for the five analyses with Cumming's and Prony's method, respectively) are tested on a significance level $\alpha = 0.05$, in order to find the most accurate method. These additional null hypotheses show that for the method of Cumming H^0 must be rejected, but that for the improved method of Prony H^0 must be accepted. In other words, the additional null hypotheses show that only Prony's improved method returns (λ_i , A_i^0) values for $^{13}\text{N}/^{15}\text{O}$ which are consistent within a 95 % confidence level to the input values.

The standard deviations in Table 7.14, calculated from the results of the analyses of the five decay curves for each of these experiments, show that no significant additional systematic errors are introduced by the applied methods. A closer look shows that for the $^{15}\text{O}/^{17}\text{F}$ combination Cumming's method can still distinguish two components but only with a poor precision. For the $^{11}\text{C}/^{13}\text{N}$ combination larger deviations are obtained with Prony's improved method due to the small differences in the half-life values. If the $T_{1/2}$'s of the two components differ more than a factor of 2 (the $^{13}\text{N}/^{15}\text{O}$, $^{13}\text{N}/^{17}\text{F}$, and $^{11}\text{C}/^{15}\text{O}$ combinations), relative standard deviations of ca. 1% have been found for both the $T_{1/2}$'s and A_i° 's. It should further be noted that for the $^{13}\text{N}/^{15}\text{O}$ combination, although very small standard deviations have been found from both methods, the tested null hypotheses, stated above, show that only Prony's method is able to retrieve the set of input values (λ_i, A_i°) of each component i within a 95% confidence interval.

In general, it can be concluded from the preceding analysis that good results can be obtained from the analysis of bi-exponential decay curves in the presence of initially ca. 1% noise if the differences in the λ values and/or the $T_{1/2}/\Delta t$ ratios are large enough (>2). In experimental conditions the Δt value can be chosen, but a compromise must be found between a good $T_{1/2}/\Delta t$ ratio and a larger noise level for smaller counting periods. Cumming's method performs better for the decay curves of $^{15}\text{O}/^{17}\text{F}$ mixtures (see Table 7.14) although with large standard deviations; Prony's improved method returns more accurate results for the combination $^{13}\text{N}/^{15}\text{O}$. In general, the standard deviations, obtained for the five data sets for each of the combinations with Cumming's method, are smaller than those obtained in the analyses with Prony's improved method.

Second series of simulated decay curves with an A_i° ratio of ca 1/3/9 have been composed of three out of the five positron emitters from Table 7.13. They have also been analyzed applying the previously described procedure. Table 7.15 shows the input parameters (λ_i, A_i°) and, the final results (mean (sd)) obtained with both Cumming's and Prony's method. For all selected combinations, both methods could retrieve the exact number of components, identify the components, and quantify their contributions. The combination $^{18}\text{F}/^{11}\text{C}/^{17}\text{F}$ gives the largest deviations due to the imprecise determination of the longest lived component. After testing the null hypotheses it could be concluded that the optimized parameters of both methods are equal on a significance level $\alpha = 0.05$. It can also be seen that the precision of the results obtained with both methods are very alike for all combinations. Both methods are therefore equally suited for the qualitative and quantitative analysis of tri-exponential decay curves.

Table 7.14 : Results for the analysis of simulated bi-exponential decay curves

Components	Input Simulation		Output			
	λ_i (min ⁻¹)	A_i^0 (counts min ⁻¹)	Method of Cumming		Improved method of Prony	
	λ_i (min ⁻¹)	A_i^0 (counts min ⁻¹)	λ_i (min ⁻¹)	A_i^0 (counts min ⁻¹)	λ_i (min ⁻¹)	A_i^0 (counts min ⁻¹)
¹⁵ O/ ¹⁷ F	0.340	6000	0.351 (19)	6898 (1538)	0.422 (28)	22115 (1135)
	0.645	20000	0.660 (32)	19172 (1385)		
¹¹ C/ ¹³ N	0.0340	3000	0.0345 (9)	3184 (354)	0.0349 (20)	3380 (706)
	0.0696	10000	0.0705 (17)	9857 (336)	0.0713 (30)	9671 (679)
¹³ N/ ¹⁵ O	0.0696	3000	0.0706 (5)	3056 (43)	0.0694 (8)	2969 (70)
	0.340	10000	0.344 (3)	9988 (71)	0.339 (5)	10030 (82)
¹³ N/ ¹⁷ F	0.0696	6000	0.0698 (6)	6028 (51)	0.0696 (10)	6004 (105)
	0.645	20000	0.654 (9)	20133 (248)	0.650 (17)	20104 (252)
¹¹ C/ ¹⁵ O	0.0340	3000	0.0341 (2)	2989 (30)	0.0342 (4)	2996 (48)
	0.340	10000	0.339 (7)	10053 (84)	0.341 (7)	10067 (83)

Table 7.15 : Results for the analysis of simulated tri-exponential decay curves

Components	Input Simulation		Output			
	λ_i (min ⁻¹)	A_i^0 (counts min ⁻¹)	Method of Cumming		Improved method of Prony	
			λ_i (min ⁻¹)	A_i^0 (counts min ⁻¹)	λ_i (min ⁻¹)	A_i^0 (counts min ⁻¹)
¹⁸ F/ ¹³ N/ ¹⁷ F	0.00631	2000	0.00622 (28)	1981 (45)	0.00622 (42)	1984 (72)
	0.0696	6000	0.0692 (19)	5976 (118)	0.0692 (28)	5973 (130)
	0.645	18000	0.643 (16)	18082 (162)	0.642 (18)	18069 (156)
¹⁸ F/ ¹¹ C/ ¹⁷ F	0.00631	2000	0.0045 (20)	1609 (426)	0.0048 (15)	1662 (318)
	0.0340	6000	0.0321 (20)	6327 (381)	0.0324 (16)	6281 (274)
	0.645	18000	0.646 (5)	18140 (134)	0.646 (4)	18120 (135)
¹⁸ F/ ¹³ N/ ¹⁵ O	0.00631	1000	0.00624 (8)	969 (46)	0.00622 (15)	982 (24)
	0.0696	3000	0.0696 (27)	3058 (118)	0.0683 (28)	3009 (178)
	0.340	9000	0.346 (12)	9012 (143)	0.345 (20)	9090 (128)
¹⁸ F/ ¹¹ C/ ¹⁵ O	0.00631	1000	0.00641 (53)	1021 (92)	0.00658 (39)	1054 (68)
	0.0340	3000	0.0346 (18)	2995 (62)	0.0355 (15)	3011 (45)
	0.340	9000	0.341 (6)	9006 (53)	0.342 (6)	8927 (98)

7.3.1.4. Analysis of experimental decay curves

Four experimental decay curves measured from a mixture of ^{15}O , ^{11}C and ^{18}F in a well known ratio (1/1/1, 1/2/2, 1/2/3, and 3/2/1) have been analyzed. In an initial part of the analyses, it has been assumed that all five β^+ emitters (^{17}F , ^{15}O , ^{13}N , ^{11}C , and ^{18}F) are present in the sample. This preliminary analysis using Prony's method, returns real decay constants with positive contributions for those components that are present in the accumulated data. Radionuclides which are not present in the samples are characterized by complex decay constants and negative or small pre-exponential factors. Then, Prony's improved method is applied again with the correct number of components and starting values for the decay constants in order to obtain more accurate results. The same procedure has been followed in the analyses using Cumming's method. In Table 7.16, λ_i values, calculated from the $T_{1/2}$ data listed in Table 7.13, are collected together with A_i^0 values found in three single component analyses by Cumming's method (decay corrected for $t = 0$, the reference) ; the optimized (λ_i , A_i^0) parameters obtained from the multicomponent decay curve analyses by using Cumming's method and Prony's improved method are also included. Very similar results are found with both methods. For all experiments, the methods could give the correct number of components, could identify the species in the mixtures, and were able to quantify accurately the contribution of each species to the total activity for all the considered ratios. More in detail, it can be seen that the decay constant of the short-lived component was better determined by Cumming's method in experiment 1, 3, and 4. Prony's improved method could quantify more accurately the other two decay constants. The contribution A_i^0 of each component i to the total activity was slightly better retrieved by Prony's improved method in the analyses of experiments 1, 2, and 4. In experiment 3 the short-lived component has the largest pre-exponential factor and since Cumming's method can determine the corresponding decay constant more accurately, it will also be able to optimize this pre-exponential factor in the best way. Consequently, this method returns the best optimized values for the A_i^0 parameter of the other components. Except for these minor differences the performance of both methods in these analyses is very similar. Hence, the experimental decay curves could be analyzed both qualitatively and quantitatively by using the two proposed programs. Fig. 7.10 shows the experimental and fitted decay curves of experiment 3 together with the standard residual plots for both analyses. Only one fifth of the fitted points are superimposed on the experimental data points. These plots show that with both methods the experimental decay curve could be analyzed within the limits of the statistical fluctuations.

It can be concluded that the performances of the methods of Prony and Cumming are comparable and that they are equally well suited for the analyses of multicomponent radioactive decay curves.

Table 7.16 : Results for the analysis of experimental decay curves composed of ^{15}O , ^{11}C , and ^{18}F

exp.	species	reference mono-exponential decay curve		multicomponent decay curve			
		Cumming's method		Cumming's method		Prony's improved method	
		λ [NuDat] (min ⁻¹)	A_i^0 (counts min ⁻¹)	λ (min ⁻¹)	A_i^0 (counts min ⁻¹)	λ (min ⁻¹)	A_i^0 (counts min ⁻¹)
1	^{18}F	0.00631	2044	0.00588	1883	0.00642	2069
	^{11}C	0.0340	2819	0.0309	2851	0.0336	2723
	^{15}O	0.340	1872	0.289	2131	0.276	2081
2	^{18}F	0.00631	716	0.00663	761	0.00643	738
	^{11}C	0.0340	2075	0.0366	2139	0.0357	2126
	^{15}O	0.340	1730	0.396	1737	0.358	1814
3	^{18}F	0.00631	1516	0.00625	1506	0.00627	1525
	^{11}C	0.0340	3032	0.0340	3049	0.0342	3051
	^{15}O	0.340	4167	0.350	4380	0.354	4389
4	^{18}F	0.00631	3105	0.00622	3057	0.00634	3130
	^{11}C	0.0340	2054	0.0330	2105	0.0339	2035
	^{15}O	0.340	1124	0.352	1020	0.361	1044

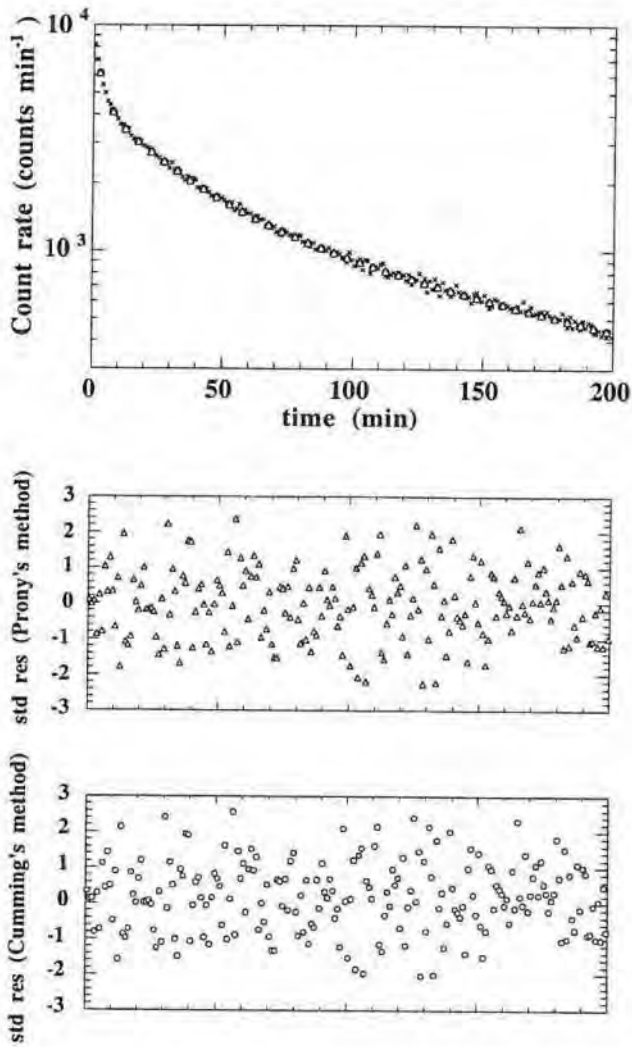


Fig. 7.10 : Experimental (x) and fitted decay curves with Cummings method (o) and with Prony's improved method (Δ) for experiment 3 together with the standard residual plots for both analyses

7.3.1.5. Conclusions

A procedure for the qualitative and quantitative analysis of radioactive decay curves is proposed. The improved method of Prony has been evaluated on both simulated and experimental data. It has been found that this technique was able to determine the number of components, to identify the species, and to quantify the contribution of each component to the total activity of a mixture of pure positron emitters. For the analysis of data with initially ca. 1% noise, the ratio of the decay constants and/or the $T_{1/2}/\Delta t$ ratio must be large enough (>2). Only the last condition can be experimentally adjusted. Comparing the final results with those obtained with the classical least squares method of Cumming, it can be stated that the results are of equal quality. The major advantage of the proposed procedure is that the number of positron emitters in the mixture must not be known in advance.

References Part II

- [AmeM85] Ameloot M, Beechem JM, and Brand L (1986) *Biophys Chem* 23 : 155
- [AmeM91] Ameloot M, Boens N, Andriessen R, Van den Bergh V, and De Schryver FC (1991) *J Phys Chem* 95 : 2041
- [AndR91] Andriessen R, Boens N, Ameloot M, and De Schryver FC (1991) *J Phys Chem* 95 : 2047
- [ArmN93] Armaroli N, De Cola L, Balzani V, Sauvage JP, Dietrich-Buchecker CO, Kern JM, and Bailal A (1993) *J Chem Soc, Dalton Trans* pp. 3241
- [BarH87] Barkhuijsen H, De Beer R, and van Ormondt D (1987) *J Magn Resonance* 73 : 553
- [BebD86] Bebelaar D (1986) *Rev Sci Instrum* 57 : 1116
- [BeeJ85] Beechem JM, Ameloot M, and Brand L (1985) *Anal Instrum* 14 : 379
- [BeeJ85] Beechem JM, Ameloot M, and Brand L (1985) *Chem Phys Lett* 120 : 466
- [BirJ67] Birks JB and Munro IH (1967) *Prog React Kinet* 4 : 239
- [BoeN89] Boens N, Janssens LD, and De Schryver FC (1989) *Biophys Chem* 33 : 77
- [BoeN90] Boens N, Tamai N, Yamazaki I, and Yamazaki T (1990) *Photochem Photobiol* 52 : 911
- [CohS75a] Cohn-Sfetcu S, Smith MR, and Nichols ST (1975) *Proc IEEE* 63 : 326
- [CohS75b] Cohn-Sfetcu S, Smith MR, Nichols ST, and Henry DL (1975) *Proc IEEE* 63 : 1460
- [CooJ65] Cooley JW, and Tukey JW (1965) *Math Comp* 19 : 297
- [CriB69] Crist B, and Peterlin A (1969) *J Polym Sc, i Part A-2*, 7 : 1165
- [CumJ62] Cumming JB (1962) Application of computers to nuclear and radiochemistry. Proceedings of a Symposium, Catlinburg Tennessee, Office of Technical Services, Dept. of Commerce, Washington 25, D.C., 25
- [EisJ79] Eisenfeld J, and Ford CC (1979) *Biophys J* 26 : 73
- [FedV89] Fedotov VD, and Schneider H (1989) *Structure and Dynamics of Bulk Polymers by NMR-Methods*, Springer-Verlag Berlin Heidelberg 58
- [FujK72] Fujimoto K, and Nishi T (1972) *Polym J* 3(4) : 448
- [FukK90] Fukumori K, Sato N, and Kurauchi T (1990) *Rubber Chemistry and Technology* 64 : 522
- [GarD59] Gardner DG, Gardner JC, and Meinke WW (1959) *J Chem Phys* 31 : 978
- [HunG69] Hunt GE, and Grant IP (1969) *J Atmospheric Sci* 26 : 963

References Part II

- [JanL90] Janssens LD, Boens N, Ameloot M, and De Schryver FC (1990) *J Phys Chem* 94 : 3564
- [KhaM91] Khalil MMH, Boens N, Van der Auweraer M, Ameloot M, Andriessen R, Hofkens J, and DeSchryver FC (1991) *J Phys Chem* 95 : 9375
- [KnuJ83] Knutson JR, Beechem JM, and Brand L (1983) *Chem Phys Lett* 102 : 501
- [KoeV78] Koester VJ, and Dowben RM (1978) *Rev Sci Instrum* 49 : 1186
- [KumH88] Kume H, Koyama K, Nakatsugawa K, Suzuki S, and Fatlowitz D (1988) *Appl Opt* 27 : 1170
- [KunS83] Kung SY, Arun KS, and Bhaskar DV (1983) *J Opt Am Soc* 73 : 1799
- [LanC56] Lanczos C (1956) *'Applied analysis'*, Prentice-Hall, Englewood Cliffs, New York p. 272
- [LevK44] Levenberg K (1944) *Quart Appl Maths* 2 : 164
- [LöfJ85] Löfroth JE (1985) *Eur Biophys J* 13 : 45
- [LupM95] Lupu M, and Todor D (1995) *Chem and Int Lab Sys* 29 : 11
- [ManP70] Mancini P, and Pilo A (1970) *Compt Biomed Res* 3 : 1
- [MarD63] Marquardt DW (1963) *J Soc Indust Appl Maths* 11 : 431
- [MooW73] Moore WS, and Yalcin T (1973) *J Magn Resonance* 11 : 50
- [NuDat] NuDat data base, <http://www.nndc.bnl.gov/nndc/nudat/>.
- [O'CoD84] O'Connor DV, and Phillips D (1984) *Time-Correlated Single Photon Counting*, Academic Press: London
- [OsBM75] Osborne MR (1975) *SIAM J Numer Anal* 12 : 571
- [OsBM91] Osborne MR, and Smyth GK (1991) *SIAM J Sci Stat Comput* 12 : 362
- [OsBM95] Osborne MR, and Smyth GK (1995) *SIAM J Sci Comput* 16 : 119
- [PaaP69] Paatero P (1969) *Annales Academiae Scientiarum Fennicae series A : VI Physica*, 319 : 1
- [PowJ63] Powles JG, and Strange JH (1963) *Proc Phys Soc London* 82 : 6
- [ProR95] Prony R (1975) *Journal de l'Ecole Polytechnique* 1: 24
- [SchJ73] Schlesinger J (1973) *Nucl Instrum Methods* 106 : 503
- [SchS96] Schreurs S (1996) *'Studie van gecombineerde analytische - numerieke methode voor de analyse van multicomponent exponentiële vervalcurven'* thesis MCT, Limburgs Universitair Centrum, Diepenbeek
- [SchS98] Schreurs S and François JP (1998) *Chem and Int Lab Sys* 43 : 107
- [SchSx1] Schreurs S, Adriaensens P, Gelan J and François JP, *J Phys Chem*, submitted
- [SchSx2] Schreurs S, Strijckmans K and François JP, *Nucl Instrum Methods*, submitted
- [SmiM74] Smith MR, and Cohn-Sfetcu S (1974) *Nucl Instrum Methods* 114 : 171
- [SmiM75] Smith MR, and Buckmaster HA (1975) *J Magn Resonance* 17 : 29
- [SmiM76] Smith MR, Cohn-Sfetcu S, and Buckmaster HA (1976) *Technometrics* 18 : 467

- [SpeK78] Spears KG, Cramer LE, and Hoffland LD (1978) Rev Sci Instrum 49 : 225
- [StrK85] Strijckmans K, Vandecasteele C, and Sambre J (1985) Appl Radiat Isot 36(4) : 279
- [TanH82] Tanaka H (1982) J Appl Polym Sci 27 : 2197
- [TanH93] Tanaka H, and Inoue Y (1993) Polymer International 31
- [VarJ85] Varah JM (1985) SIAM J Sci Comput 6 : 30
- [VanR93] Van Grieken RE, and Markowicz AA (1993) *Handbook of X-ray Spectrometry, Methods and Techniques*, Marcel Dekker, Inc., New York
- [VanT83] Vandewalle T, and Vandecasteele C (1983) Appl Radiat Isot 34 : 1459
- [YamI85] Yamazaki I, Tamai N, Kume K, Tsuchiya H, and Oba K (1985) Rev Sci Instrum 56 : 1187

Summary and final conclusions

The aim of the present thesis is stated in its title : the qualitative and quantitative analysis of spectral data and multicomponent decay curves using digital filtering techniques. Because of the diversity of the studied data, the present manuscript is divided into two main parts : Part I describes the analysis of spectral data, and Part II deals with the unraveling of multicomponent decay curves. Both parts have the same structure : one chapter deals with the theory and implementation of the applied software in detail ; the following chapter presents the results of the procedures which are extensively tested on simulated data and are interpreted in order to formulate guide lines for a successful analysis ; and in a final chapter, the applicability of the proposed methods is illustrated in several experimental studies.

In the **first part**, the FORTRAN 77 program ASDAP (Automated Spectral Data Analysis Program) developed by Dr. F. Janssens in our lab, has been further optimized, and its application on simulated and experimental studies is evaluated.

The most important optimization is the use of analytical expressions for the partial derivatives of the Voigt function with respect to the parameters $I_{V,0}$, t_0 , α_G , α_L and a . In this context, it has been found that the expressions for the partial derivatives of the Voigt function with respect to α_L and α_G published by Boumans are incorrect.

The evaluation of ASDAP using simulated spectral data has been divided into two parts. First, the evaluation of the peak detection procedure, based on the construction of the first and second order convolution signals using a zero-area Gaussian filter, resulted in the definition and visualization of the spectral detection limit. This spectral detection limit represents an important characteristic of ASDAP, namely the ability of determining the exact number of lines under a spectral envelop. Furthermore, it is shown that ASDAP is able to analyse both qualitatively and quantitatively multiplets using the following procedure. After the peak detection procedure, the parameters of the reduced sum function used as model function for a peak (the centroid t_0 , the intensity I_0 , at this centroid, the FWHM and a lineshape parameter) are estimated using information from the convolution signals and Zimmermann's method (see Chapter 1). Since the direct optimization using the Voigt profile is very sensitive to the initial estimates of the parameters, a previous fitting is done with the reduced sum function. The optimized values for the parameters of the reduced sum function are transformed into more accurate starting values for the Voigt function, and a second optimization is started. It has been found that the results obtained with the Voigt function are

Summary and final conclusions

much better than those obtained with the reduced sum function. The influence of noise is also studied. It has been found that reliable results can be obtained for rather noisy spectra (3%) when repeated data under the same conditions are available.

After the extensive evaluation of ASDAP on simulated data, its performance is tested in experimental studies.

It has been demonstrated that ASDAP can analyze both qualitatively and quantitatively complex IR spectra of carbon clusters trapped in solid Ar and Kr matrices at temperatures of 13, 30, and 35K. The resolved IR bands could be assigned to specific C_n cluster species based on data obtained via quantum chemical computations and from tunable diode laser IR spectroscopy of C_n species in the gas phase as referred to in the literature.

The analysis of ICP-OE spectra of standard reference materials using ASDAP and software of the Jobin Yvon-138 Ultrace, showed that the latter one could obtain good results in the absence of interferences. However, the calculation of the 95% confidence limits is only based on the precision of the measurements of the samples, not on the reliability of the calibration curves, resulting in underestimated values. The analyses performed with ASDAP, resulted in accurate determinations of the analyte concentrations, compared to the corresponding certified values. More realistic 95% confidence limits are obtained using the MatLab program based on linear least squares regression. Solid reference steel samples have also been analysed using the combined spark ablation - ICP-OES techniques. Solid sample introduction has the advantage to be a fast technique with a minimum of preparations. However, it has also been illustrated that the complexity of the spectra, resulting from the reference materials, and the low reproducibility hamper the success of this technique. Finally, the determination of boron in steel is studied using a certified reference material. Six spectral lines of boron have been selected. After the construction of the calibration curves with both weighted and non weighted linear regression using the results of ASDAP, and considerations about the sensitivity of these lines, it could be concluded that the 2089.59, 2496.78 and 2497.73 Å lines are the most suitable ones for the quantitative determination of B in steel.

The **second part** of the present work deals with a completely different universal problem, the qualitative and quantitative analysis of multicomponent decay curves. A first attempt to analyze these curves by digital filtering techniques, as they were used in ASDAP, showed promising results; nevertheless, it had to be abandoned.

The extensive study of two existing techniques (the methods of Gardner et al. and Prony), and their further improvements, induced the idea that the combination of both could result in a powerful technique for the qualitative and quantitative analysis of multicomponent decay curves. Digital filters fulfill only a small task in the improved method of Gardner et al. (GGM), however, their influence upon the final result should not be underestimated. Since nowadays, MatLab is the software language of choice of many chemometricians, the combination of the improved methods of Gardner and Prony has been programmed completely in MatLab 4.2c1.

The evaluation of this combination is also divided into two parts. First, the characteristics of the improved GGM method are illustrated by studying the influence of the Gaussian low-pass filter, the performance on multicomponent decay curves, the influence of the model function $kk(x)$, and the choice of the time scale. The general conclusion is that carefully chosen experimental conditions can improve and simplify the analysis of the data. The impact of some important parameters of Prony's improved method is studied, i.e. the input of the number of components n , the influence of the starting values λ_i , and the influence of the number of data points N . Finally, for both techniques, the impact of initial Poisson distributed noise levels of 0.1 and 1.0 % has been checked.

The combined use of the improved methods of Gardner et al. and Prony on experimental data, obtained from fluorescence spectrometry, free induction decay (solid state ^1H NMR) and radioactive decay curves is presented in the last chapter. The results are compared with those obtained by using common algorithms in the specific disciplines, i.e. the Marquardt-Levenberg algorithm in fluorescence and NMR spectrometry, and Cumming's method in nuclear chemistry.

The study of fluorescence decay curves of two catenanes illustrated that the proposed combination of the improved GGM and Prony's methods sometimes has to deal with serious problems : for example, the interpretation of complex $g(\lambda)/\lambda$ vs λ spectra, and the further quantification based on poor reliable information. Nevertheless, in the study of the so-called "compound II", it could be proven that only two compounds were present, and that the corresponding contributions and decay constants could be quantified. The consideration of several curves obtained in a set of various experimental conditions (here : emission wavelength λ_{em}) was a crucial part in the success of these analyses. Finally, it could be concluded that the combination of the improved GGM and Prony's methods can be a useful technique for the analysis of multicomponent fluorescence decay curves.

Summary and final conclusions

The free induction decay curves in a temperature study of iPP (isotactic polypropylene) films and PVA (atactic poly (vinyl alcohol)) grains, could also be analyzed with the combination of the improved methods of GGM and Prony. The results are in good agreement with those obtained with the Marquardt-Levenberg algorithm ; however, less a priori information is needed in our method. For both materials, the presence of an intermediate phase (I) could be proved unambiguously and quantified at the different temperatures. The influence of temperature on the fractions of the phases is discussed. In the study of iPP, the precision of the quantification of the parameters is shown to be much smaller than the one that can be reached with the recording of the FID curves.

For the qualitative and quantitative analysis of radioactive decay curves, a procedure based on only Prony's improved method is proposed. It has been evaluated on both simulated and experimental data, and it was found that this technique was able to determine the number of components, to identify the species, and to quantify the contribution of each component to the total activity of a mixture of pure positron emitters. Comparing the final results with those obtained with the classical least squares method of Cumming, it can be stated that the results are of equal quality. The major advantage of the proposed procedure is that the number of positron emitters in the mixture must not be known in advance.

Finally, it can be concluded that the qualitative and quantitative analysis of spectral data and multicomponent decay curves could be performed with success using digital filtering techniques. It has been illustrated that the introduction of some minor adjustments to a method can result in a wide applicability. The problems occurring in many disciplines of chemistry (and other sciences like biology, physics, statistics, economy, medicine, etc..) can often be solved using the same basic mathematical model, and therefore, also with the same software. Hence, the applicability of the proposed methods is not limited to the illustrated topics.

Samenvatting en algemeen besluit

In dit werk werden methoden, gebaseerd op digitale filtertechnieken, voor de kwalitatieve en kwantitatieve analyse van spectra en multicomponent vervalcurven, uitgebreid onderzocht. Omwille van de diversiteit van de bestudeerde data werd dit werk in twee delen opgesplitst : Deel I behandelt de analyse van spectra en Deel II beschrijft de studie van multi-component vervalcurven. Elk van de beide delen is opgebouwd op identieke wijze. Eerst wordt een theoretische uiteenzetting gegeven van de aangewende methode samen met een gedetailleerde beschrijving van de geïmplementeerde software. Vervolgens worden de karakteristieken van de algoritmen aangetoond in een evaluatiestudie op gesimuleerde data waarbij ook richtlijnen worden geformuleerd voor een succesvolle analyse. Tenslotte wordt de toepasbaarheid van de vooropgestelde methode geïllustreerd aan de hand van diverse experimentele studies.

In **Deel I**, werd het reeds in onze onderzoeksgroep ontwikkelde programma ASDAP (Automated Spectral Data Analysis Program) verder geoptimaliseerd en bestudeerd.

De belangrijkste optimalizatie was het gebruik van analytische uitdrukkingen voor de partiële afgeleiden van de Voigt functie naar de parameters $I_{V,0}$, t_0 , α_G , α_L en a . Hierbij kon vastgesteld worden dat de door Boumans gepubliceerde uitdrukkingen voor de partiële afgeleiden van de Voigt functie naar de parameters α_L en α_G verkeerd zijn.

De evaluatie van ASDAP voor gesimuleerde data werd opgesplitst in twee delen. In het eerste deel werd de piekdetectie procedure gebaseerd op de berekening van de eerste en tweede orde convolutie signalen (**R** en **S**) met behulp van een 'zero-area' Gaussiaanse filter, bestudeerd. Dit resulteerde in de definiëring en visualisering van een belangrijke karakteristiek van ASDAP : de spectrale detectielimiet die een maat is voor het oplossend vermogen van ASDAP. Bovendien werd geïllustreerd dat ASDAP complexe multipletten op een correcte wijze kan ontrafelen. In het tweede deel werd de fitting procedure geëvalueerd. De volgende voorgestelde procedure resulteerde in een succesvolle analyse van multipletten. Na de piekdetectie, worden de initiële schattingen voor de parameters van de gereduceerde somfunctie afgeleid uit de convolutiesignalen en de methode van Zimmermann. Na deze preliminaire fitting worden uit de geoptimaliseerde parameters accurate initiële schattingen voor de parameters van de Voigt functie bepaald en wordt een tweede definitieve fitting uitgevoerd met de Voigt functie als modelfunctie. De invloed van ruis werd ook onderzocht. Er werd besloten dat betrouwbare resultaten kunnen bekomen worden voor datasets met een

beduidend ruisniveau (3%) wanneer herhaalde data bekomen onder identieke omstandigheden, ter beschikking zijn.

Tenslotte werd ASDAP toegepast in twee uitgebreide experimentele studies.

Complexe IR spectra van koolstofclusters ingebed in vaste Ar en Kr matrices bij temperaturen van 13, 30 en 35K werden kwalitatief en kwantitatief geanalyseerd. De individuele IR lijnen werden toegekend aan specifieke koolstofclusters gebaseerd op uitgebreide literatuurgegevens. De invloed van temperatuur en matrix werden uitgebreid besproken.

ICP-OE spectra van referentie staalsoorten werden geanalyseerd met zowel ASDAP als met de standaard Jobin Yvon software. De kritische vergelijking toonde aan dat deze laatste in staat is goede resultaten te leveren in de afwezigheid van interferentie. Er diende echter opgemerkt te worden dat deze software de 95% betrouwbaarheidsintervallen enkel berekent op basis van de precisie van de metingen van het onbekende staal en geen rekening houdt met de constructie van de ijklijn. De analyse van ASDAP resulteerde in een accurate bepaling van de analietconcentraties. Realistische betrouwbaarheidsintervallen werden bekomen met het MatLab programma gebaseerd op de lineaire kleinste kwadraten methode. Referentie staalsoorten werden ook in de vaste toestand geanalyseerd met de gecombineerde techniek van vonkablative-ICP-OES. Deze techniek maakt een snelle analyse mogelijk met een minimum aan monstervoorbereiding, maar resulteert in nog complexere spectra voor het standaardmateriaal en dus ook in een kleinere betrouwbaarheid van de kwantitatieve analyses van onbekende monsters. Tenslotte werd de analyse van boor in een referentie staalsoort bestudeerd. Voor zes spectraal lijnen werden calibratiecurven opgesteld met zowel gewogen als ongewogen lineaire regressiemethodes uitgaande van de resultaten van ASDAP. In deze studie werd na het bepalen van de gevoeligheid van deze lijnen en de bijhorende detectielimieten, besloten dat de 2089,59, 2496,78 and 2497,73 Å lijnen het meeste geschikt zijn voor de kwantitatieve bepaling van boor in staal.

Deel II behandelt de kwalitatieve en kwantitatieve analyse van multicomponent vervalcurven. In een eerste poging om deze curve te analyseren, werd gebruik gemaakt van 'zero-area' Gaussiaanse filters zoals geïmplementeerd in ASDAP. Alhoewel veelbelovende convolutesignalen bekomen werden, konden geen praktische wiskundige uitdrukkingen afgeleid worden die de kwantitatieve bepaling van de individuele componenten toelaten.

Een uitgebreide studie (Schreurs S (1996) '*Studie van gecombineerde analytische - numerieke methode voor de analyse van multicomponent exponentiële*

vervalcurven' thesis MCT) van twee bestaande methoden (de methoden van Gardner et al. (GGM) en van Prony) en hun verdere verbeteringen, resulteerde in het idee dat de combinatie van beide wellicht een kwalitatieve en kwantitatieve analyse mogelijk maakt. Beide methoden werden geprogrammeerd in MatLab4.2c1. Bovendien werd voor deze combinatie een MatLab programma ontwikkeld om uitgaande van één dataset (nodig voor de verbeterde methode van Prony) de dataset voor de verbeterde methode van GGM te berekenen via kubieke splines. Alhoewel digitale filters slechts een klein aandeel in deze globale techniek hebben, moet hun invloed op het uiteindelijke resultaat niet onderschat worden.

Beide methoden werden apart geëvalueerd op gesimuleerde vervalcurven. De karakteristieken van de verbeterde GGM methode kwamen tot uiting in de grondige studie naar de invloed van het gebruik van een Gaussiaanse filter, naar de performantie van de methode op ingewikkelde multicomponent vervalcurven, naar de invloed van de keuze van de modelfunctie $kk(x)$ en van de tijdschaal. De impact van een aantal parameters nodig als input in de verbeterde methode van Prony, zoals het aantal componenten n , de startwaarden λ_i en het aantal datapunten N . Bovendien werd voor beide methoden de invloed van een initieel ruisniveau van 0.1 en 1.0% ruis bestudeerd. De algemene conclusie is dat goed overwogen experimentele condities de uiteindelijke analyse kunnen vereenvoudigen en verbeteren.

De combinatie van de verbeterde methoden van GGM en Prony werd toegepast in drie experimentele studies : fluorescentie vervalcurven, free induction decay curves (vaste stof ^1H NMR) en radioactief verval. In iedere studie werden de bekomen resultaten vergeleken met de standaard algoritmen die gebruikt worden in de betrokken domeinen.

In de kwantitatieve analyse van porfyriene gesubstitueerde catenanen werd aangetoond dat de gecombineerde methode van GGM en Prony soms moet kampen met ingewikkelde problemen omtrent de interpretatie van de complexe $g(\lambda)/\lambda$ vs λ spectra. Als gevolg hiervan dient de verdere kwantificatie te gebeuren met slechts een povere informatie betreffende het aantal componenten en de λ_i startwaarden. Nochtans kon in de studie van component II aangetoond worden dat twee componenten aanwezig zijn en waren de geoptimaliseerde parameters in goede overeenstemming met de resultaten die bekomen werden met behulp van het klassieke Marquardt-Levenberg algoritme.

De combinatie van de GGM en Prony methoden voor de analyse van free induction decay (FID) curven bij vaste stof proton NMR studies van iPP (isotactisch polypropyleen) filmen en PVA (atactisch poly (vinyl alcohol)) korrels leidde tot het bewijs

van de aanwezigheid van een intermediaire fase voor beide materialen, het bepalen van de beste modelfunctie van elke fase en het kwantificeren van de spin-spin relaxatietijden en fracties van elke component. Deze laatste waren bijna identiek aan de waarden die bekomen werden met het klassieke Marquardt-Levenberg algoritme. In deze studies werd bovendien de invloed van de temperatuur op deze parameters besproken. In de studie van iPP werd de precisie van de berekende parameters onderzocht. Deze bleek veel kleiner te zijn dan de precisie die bereikt kon worden met de registratie van de FID curven zelf.

Tenslotte werd een geheel nieuwe procedure met de verbeterde methode van Prony opgesteld en uitgetest voor de analyse van radioactieve vervalcurven van een mengsel van zuivere positronstralers. Ook hier waren de geoptimaliseerde parameters, halveringstijden en initiële activiteiten, in goede overeenstemming met de resultaten bekomen met het klassieke Cumming algoritme.

Als algemeen besluit kan gesteld worden dat de vooropgestelde methoden gebaseerd op digitale filtertechnieken in staat zijn spectra en multicomponent vervalcurven zowel kwalitatief en kwantitief te analyseren. In de inleiding van dit werk werd reeds aangehaald dat kleine aanpassingen aan een bestaande techniek kunnen resulteren in een uitgebreide toepasbaarheid. Dit werd ook bewezen in dit werk. De geboekte resultaten in de bovenstaande studies bewijzen immers reeds het multidisciplinair karakter van dit onderzoek. Toch zijn er zeker nog andere toepassingsdomeinen waarbinnen het onderzoeken van de bruikbaarheid van deze software de moeite waard is, zoals in de biologie, fysica, statistiek, economie, geneeskunde, ...

Doctoraatsopleiding : LUC - UIA

I. Cursussen en seminaries

1.1. Voortgezette academische opleiding : MCT / LUC

Cursussen :

- Sequentiële Algoritmen (INF) : Prof. Dr. P. Verbaeten
duur : 5 dagen van 6u. in de periode 2/10/1993 - 30/10/1993
examen : 19/11/1993 : quotering 14/20
- Numerieke Matrixmethoden (NA) : Prof. Dr. F. Lemeire
duur : 5 dagen van 6u. in de periode 6/11/1993 - 11/12/1993
examen : 14/1/1994 : quotering 18/20
- Structuur en Organisatie van Computersystemen (INF) : Prof. Dr. P. Verbaeten
duur : 5 dagen van 6u. in de periode 18/12/1993 - 5/2/1994
examen : 4/3/1994 : quotering 14/20
- Numeriek Oplossen van Differentiaalvergelijkingen (NA) : Prof. Dr. L. Wuytack
duur : 5 dagen van 6u. in de periode 12/2/1994 - 19/3/1994
examen : 22/4/1994 : quotering 16/20
- Statistiek en Gegevensanalyse (STAT) : Prof. Dr. M. Aerts
duur : 4 dagen van 6u. en 2 dagen van 3u. in de periode 21/5/1994 - 18/6/1994
examen : 1/7/1994 : quotering 16.5/20
- Wiskundige Optimalisatie zonder Beperkingen (OPON) : Prof. Dr. F. Lemeire
duur : 5 dagen van 6u. in de periode 1/10/1994 - 29/10/1994
examen : 18/11/1994 : quotering 16/20
- Computer Graphics (INF) : Prof. Dr. E. Flerackers
duur : 5 dagen van 6u. in de periode 5/11/1994 - 10/12/1994
examen : 13/1/1995 : quotering 16/20
- Experimenteel Proefopzetten (STAT) : Prof. Dr. M. Aerts
duur : 5 dagen van 6u. in de periode 25/3/1995 - 6/5/1995
examen : 19/5/1995 : quotering 16/20
- Wiskundige Optimalisatie met Beperkingen (OPON) : Prof. Dr. F. Lemeire
duur : 5 dagen van 6u. in de periode 13/5/1995 - 17/6/1995
examen : 30/6/1995 : quotering 16/20

- Stochastische Processen (OPON) : Prof. Dr. F. Lemeire
duur : 5 dagen van 6u. in de periode 30/9/1995 - 21/10/1995
examen : 24/11/1995 : quotering 17/20
- Grafen en Netwerken (INF) : Prof. Dr. M. Gijsens
duur : 5 dagen van 6u. in de periode 6/1/1996 - 3/2/1996
examen : 16/3/1996 : quotering 14.5/20
- Parallele Programatie en Computernetwerken (INF) : Prof. Dr. P. Verbaeten
duur : 5 dagen van 6u. in de periode 30/3/1996 - 4/5/1996
examen : 22/6/1996 : quotering 16/20

Proefschrift MCT opleiding :

Titel : "Studie van gecombineerde analytische - numerieke methoden voor de analyse van multicomponent exponentiële vervalcurven"
Subtitel : "Detectie van fasen in polymere systemen via de analyse van free induction decay (^1H NMR) curven"

Promotoren : Profs. M. Aerts en J.-P. François
Verdediging op 3/7/1996, quotering 17.5/20

Diploma MCT - opleiding : geslaagd met grote onderscheiding

1.2. Cursus "Spectroscopische technieken" : UIA

- Capita Selecta Analytische Chemie : Prof. Dr. J.A.C. Broekaert
duur : 20 uren in de periode van 25/2/1994 - 22/4/1994

1.3. Cursus Octrooirecht : Universitair Bedrijvencentrum Antwerpen (UBCA)

duur : 15 uur in de periode 12/2-7/5/1998

2. Andere activiteiten

Publicatie in tijdschrift met referee-systeem en/of proceedings met referee-systeem

- "Analysis of IR spectra of carbon clusters trapped in noble gas matrices using algorithms based on digital filtering technique",

S. Schreurs en J.-P. François, Fresenius J Anal Chem (1996) 355 : 726

- "Complete analysis of IR spectra of small carbon clusters trapped in noble gas matrices",

S. Schreurs en J.-P. François, in redactie

- "The combined use of the modified methods of Gardner and Prony for the qualitative and quantitative analysis of multicomponent decay curve",

S. Schreurs en J.-P. François, Chem Int Lab Sys (1998) 43 : 107

- "Analysis of free induction decay (^1H NMR) curves of polypropylene by using the modified methods of Gardner and Prony",

S. Schreurs, J. Gelan en J.-P. François, J Phys Chem B, 1999 aanvaard

"Analysis of multicomponent radioactive decay curves using an improved method of Prony"

S. Schreurs, K. Strijckmans en François, J.-P., Nuclear Instruments and Methods, ingediend

"Automated Spectral Data Analysis Program ASDAP"

Schreurs, S.; Janssens, F. en François, J.-P., Applied Spectroscopy, in redactie

Actieve deelname congres

- XXIX Colloquium Spectroscopicum Internationale (CSI), Leipzig, BRD,

periode : 27/8/1995 - 1/9/1995,

Posterpresentatie : "Analysis of IR spectra of carbon clusters trapped in noble gas matrices using algorithms based on digital filtering technique"

- 2d Chemometrics Symposium, Arenberg kasteel, Leuven, 27/9/1996

Voordracht : "Analysis of multicomponent exponential decay curves" (1/2 u.)

Posterpresentatie : "Analysis of free induction decay (^1H NMR) curves of polypropylene by using the modified methods of Gardner et al. and Prony"

- 3d Chemometrics Symposium, Centre de recherches agronomiques, Gembloux,

17/10/1997,

Posterpresentatie : "Analysis of fluorescence decay curves by using the modified methods of Gardner et al. and Prony"

Passief bijwonen van voordrachten, seminars, en/of zomerscholen

- 2 lezingen door Prof. Dr. H.W. Kroto i.v.m. C₆₀, Buckminsterfullereen, LUC, 27/5/1993
- Doctoraatsverdediging F. Janssens : *'Development of a computer program based on digital filtering techniques for qualitative and quantitative analysis of spectral data'*, LUC, 18/6/1993
- KVCV-Jongerencongres,UIA, 9/3/1994
- Chemometrics in Belgium, UIA, 16/6/1995
- 1st Chemometrics Symposium, Solvay, Brussel, 17/11/1995
- 4d Chemometrics Symposium, Tervuren, 11/1998
- lezing door Prof. Dr. A. Verschoren (UA) : "Genetische algoritmen of wat er gebeurt als je een bioloog met wiskunde laat spelen", LUC, 25/2/1997

